UNIVERSIDADE DE LISBOA
FACULDADE DE CIÊNCIAS

The relevance of tissue temperature in planning Tumor Treating Fields (TTFields) treatment for glioblastoma

" Documento Definitivo"

Doutoramento em Engenharia Biomédica e Biofísica

Nichal Gentilal

Tese orientada por:
Prof. Dr. Pedro Cavaleiro Miranda

Documento especialmente elaborado para a obtenção do grau de doutor

2022

UNIVERSIDADE DE LISBOA

FACULDADE DE CIÊNCIAS

The relevance of tissue temperature in planning Tumor Treating Fields (TTFields) treatment for glioblastoma

Doutoramento em Engenharia Biomédica e Biofísica

Nichal Gentilal

Tese orientada por:

Prof. Dr. Pedro Cavaleiro Miranda

Júri:

Presidente:

- José Manuel de Nunes Vicente e Rebordão, Investigador Coordenador e Presidente do Departamento de Física da Faculdade de Ciências da Universidade de Lisboa

Vogais:

- Doutor Luis Javier Reina Tosina, Catedrático de Universidad, Escuela Técnica Superior de Ingeniería da Universidad de Sevilla
- Doutor Axel Thielscher, Professor, Department of Health Technology da Technical University of Denmark
- Doutora Helena Catarina de Bastos Marques Pereira, na qualidade de Individualidade de Reconhecida Competência na Área Científica
- Doutor Pedro Michael Cavaleiro de Miranda, Professor Associado com Agregação, Faculdade de Ciências da Universidade de Lisboa (orientador)
- Doutor João Miguel Pinto Coelho, Investigador Auxiliar, Faculdade de Ciências da Universidade de Lisboa

Documento especialmente elaborado para a obtenção do grau de doutor

Bolsa financiada através de um contrato de investigação com a Novocure

2022

Acknowledgments

Well, this is it. The last thing that I am writing before I have to submit my thesis tomorrow. When I started this PhD three years ago, I never thought that I would have to ask so many times if everyone could see my screen. Without any doubt, a pandemic can really put things into perspective, and it can show you that life is much more than just working towards an academic degree. At the end of the day, what really matters is the process and what one learns going through it. And this includes especially going through the unexpected things, which might be the most difficult but also the most rewarding ones. That being said, I would like to add that some things are much easier to overcome when they are shared. This PhD is no exception and thus there are a couple of people that I need to thank, without whom these last three years would have been an even bigger challenge.

My first words have to go to my parents for always supporting me and believing that I could achieve higher goals. A special thanks to my mom, Indira, who even though does not understand much of what I do, always gets excited for me. Thank you to my sister, Meha, for always being the first one to tell me that I can do everything, and for making the best cakes I have ever eaten. Thank you to my brother, Miro, for always being so caring about my future. I only got to this point as you two so willingly bought me a lot of things that I needed throughout the years when I could not afford them, without me even having to ask you. A thank you will never be enough.

A special thanks to Hijino Leite, Samuel Conde, and David Leitão. You three are some of the best people I know and I truly believe that I am lucky that I can call you my best friends. Thank you for always being there for me. I hope we can share much more experiences together and that life brings you nothing but happiness because you really deserve it.

Thank you to my friends that helped me see that life is much more than just work. Thank you to Alexandra, for always being so supportive for the last 15+ years, to Duarte and Rafa, for our weekly lunches and funny discussions, to Nino and Stefan, my party buddies, and to Rita. Thank you to everyone that directly or indirectly helped me to improve myself even when they were not aware of it.

Thank you to Novocure for paying this PhD. A special thanks to you, Ze'ev, for believing in this project, for all the opportunities you gave me to present my work and for all the important ideas that allowed me to significantly improve this thesis. This work was only possible because of you. I would also like to acknowledge the importance that Tal had on this work. Thank you for being so willing to help me and for the opportunities you gave me to collaborate with the different Novocure departments. And thank you to Ariel for his helpful suggestions and very intelligent contributions to our work.

A big and warm thank you to everyone that works in IBEB, which is, without any doubt, where you can find the highest density of nice people per square meter in the

world. Thank you to João Coelho and Nuno Matela, my internal thesis committee, not only for their suggestions to significantly improve this thesis, but also for all the years that I was a student and during which they were always so available to answer all my questions. Thank you to all the other people which I had the pleasure to work with in the last years and that made my days better, especially Mariana Pereira, João Meneses and Daniela Godinho. Thank you to Raquel Conceição for finding me the opportunity to teach during one semester and for being one of the most caring professors I have ever had. To my office colleagues, Sofia Fernandes and Margarida Mota, a very special thank you for all the lunches, every coffee, every mcflurry, and every laugh.

People usually say that what the reader remembers the most is the last thing that is written. In that case, I would like to save the last, but definitely not the least, thank you to the best supervisor I could have asked for. To you, Pedro, my most sincere thank you. In these last 4.5 years, I really learned a lot from you. Thank you for always being so supportive and available even when you were so busy with all your own work. Thank you for always reading my texts and so patiently correcting every "in" that should have been an "on", every "on" that should have been an "in", and every "in" and "on" that should have been neither (I promise I will work harder "in" that). I hope you are as proud of this work as I am.

This is for all of you. Thank you!

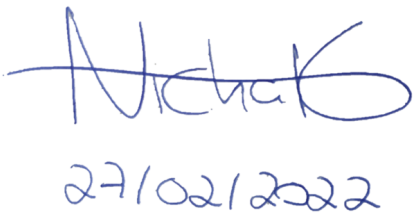

27/02/2022

Abstract

Tumor Treating Fields (TTFields) is an anti-mitotic cancer treatment technique used for solid tumors. It consists in applying an electric field (EF) with an intensity of 1 V/cm and frequency between 100 and 500 kHz to affect the mitotic process of tumoral cells. In patients, transducer arrays are placed on the shaved scalp in strategic regions that maximize the EF in the tumor using an FDA-approved software named NovoTAL. Patients should be under the action of these fields for at least 18 hours per day. To avoid any thermal harm, the amount of current injected varies depending on the temperature of the scalp. The aim of this thesis was two-fold: 1) to study how accounting for the temperature increases might affect the choice of the best regions to place these arrays; and 2) to predict TTFields thermal impact.

This work was performed using a realistic head model to which a virtual tumor was added to mimic a glioblastoma. Different array positionings obtained from the NovoTAL system were considered. To predict the electric field distribution in the head Laplace's equation was solved, whereas the temperature distribution was estimated using Pennes' equation.

The results obtained suggest that there is a minimum distance of 1 cm between arrays that should be accounted for during planning to avoid the occurrence of temperature hotspots that might limit treatment efficacy. The choice of the best layout was also shown to be sensitive to the criterion used to rank the available options. These conclusions might vary significantly depending on the values assigned to the physical parameters and on the heat transfer mechanisms modelled. Based on the maximum temperature predicted for each tissue, no unexpected physiological changes were predicted according to what is reported in the literature and thus TTFields seem to be safe from a thermal point of view.

Keywords: Glioblastoma multiforme (GBM); Realistic head model; Tissue heating; Treatment planning; Tumor Treating Fields (TTFields).

Resumo

Glioblastoma multiforme (GBM) é um dos tipos de cancro mais agressivos que ocorrem no cérebro. Apesar de nas últimas três décadas se ter assistido a uma melhoria significativa na aplicação das técnicas de tratamento de cancro com recurso a ferramentas computacionais, este avanço não se traduziu numa melhoria do prognóstico associado a esta doença. Hoje em dia, é esperado que uma pessoa com glioblastoma viva em média 15 meses com tratamento ótimo, sendo que a taxa de sobrevivência a cinco anos é de apenas 5%. Mesmo nos pacientes em que é possível destruir completamente o tecido tumoral, a probabilidade deste reincidir é muito elevada, pelo que a terapia é realizada de forma paliativa com o intuito de tentar melhorar a qualidade de vida do doente. Durante muitos anos, cirurgia, terapia com radiação e quimioterapia foram consideradas como sendo a melhor linha de tratamento no combate a este tipo de cancro. No entanto, em 2004, surgiu uma nova opção que rapidamente mostrou inúmeros benefícios em oncologia quando usada de forma concomitante com quimioterapia. Os Tumor Treating Fields (TTFields) consistem na aplicação de campos elétricos alternados, com uma frequência entre 100 e 500 kHz, através de transdutores que são colocados na cabeça do doente. Os primeiros estudos publicados mostraram que se a intensidade do campo elétrico no tumor for de pelo 1 V/cm, então esta técnica consegue afetar significativamente o processo mitótico das células cancerígeneas. Apesar dos mecanismos de ação ainda não serem totalmente entendidos, os resultados obtidos através de experiências em laboratório e em ensaios clínicos mostraram a sua importância e os parâmetros que mais contribuem para a sua eficácia. Com base nestes estudos, hoje em dia os campos elétricos são aplicados em duas direções perpendiculares de forma alternada e durante pelo menos 18 horas por dia, todos os dias. De modo a que estes dois parâmetros sejam tidos em conta, foi criado um sistema específico, denominado de Optune, que consiste num gerador de campo elétrico e quatro *arrays*, cada um com 9 transdutores, que funcionam aos pares. Estes são colocados em posições específicas da cabeça em regiões definidas pelo sistema NovoTAL. A metodologia seguida por este software de planeamento do tratamento consiste em injetar 900 mA de corrente elétrica em cada par de *arrays* e calcular o campo elétrico médio no tumor, sendo a melhor opção aquela que induz o valor mais elevado. Dada a frequência destes campos elétricos e o tempo de tratamento, a temperatura dos tecidos biológicos da cabeça vai aumentar, devido ao efeito de Joule, e manter-se em níveis superiores ao valor basal durante grande parte do dia. De modo a garantir a segurança e o bem-estar do doente, a temperatura do escalpe é monitorada e mantida a um valor máximo de 39.5 ℃ variando a corrente injetada.

Os objetivos desta tese consistiram em investigar como se podem estimar estes aumentos de temperatura e como é que este parâmetro adicional pode afetar a escolha da posição dos *arrays* se também fosse incluído no sistema NovoTAL. As variações dos processos fisiológicos como consequência da aplicação da terapia também foram estimadas

com base no aumento de temperatura em cada tecido biológico.

Este trabalho foi realizado com um recurso a um modelo realista da cabeça, criado previamente para outros estudos de TTFields, com base em imagens de ressonância magnética. O modelo foi segmentado em escalpe, crânio, líquido cefaloraquidiano (CSF), cérebro, dividido em substância cinzenta e substância branca, e ventrículos laterais. Foi ainda adicionada uma lesão fictícia para representar um glioblastoma. A modelação numérica foi feita no software COMSOL Multiphysics que usa o método dos elementos finitos (FEM) para resolver as equações que modelam os processos físicos de interesse. A distribuição do campo elétrico foi obtida através da equação de Laplace, enquanto que a temperatura foi estimada resolvendo a equação de Pennes.

Os resultados obtidos através das simulações realizadas foram comparados com dados clínicos de um doente tratado com TTFields. Com base nos valores observados concluiu-se que, no modelo usado, a corrente elétrica que leva a uma previsão de uma temperatura máxima de 39.5 ℃ no escalpe é um bom indicador da corrente média que é injetada durante o tratamento. Assim, esta foi a metodologia seguida para se proceder ao estudo de como é que a temperatura pode afetar a escolha da posição dos *arrays* durante o planeamento. Para tal, foi utilizado o sistema NovoTAL e, para o modelo usado nestes estudos, foram obtidos cinco posicionamentos diferentes (*layouts*) para a colocação dos *arrays*. Para cada caso, previu-se os valores de corrente elétrica que se podiam injetar em cada par e calculou-se o campo elétrico médio nessas condições. Estes valores foram depois comparados com os que seriam obtidos se se seguisse a abordagem implementada no NovoTAL em que a corrente injetada em cada par de *arrays* é constante. A análise dos valores obtidos mostrou que, independentemente do *layout* usado, não é possível injetar 900 mA devido às restrições térmicas da terapia. Num dos pares, a corrente elétrica teve que ser reduzida, em média, 36%, enquanto que no par complementar, cuja impedância era menor, foi observado um decréscimo médio de 14%. Num dos *layouts*, dois transdutores de pares diferentes estavam a 3 mm um do outro o que levou a que ocorresse um aumento temperatura localizado entre eles e consequentemente a uma redução significativa da corrente injetada. No entanto, de acordo com a abordagem implementada no NovoTAL, este *layout* é o que induz um campo elétrico mais elevado no tumor e seria por isso a melhor opção de entre as 5 possibilidades analisadas. Este resultado justifica a importância de se considerar a temperatura durante o planeamento. Nos restantes 4 *layouts*, os transdutores de pares diferentes estavam a pelo 8 mm uns dos outros o que foi suficiente para evitar a ocorrência destas regiões quentes que poderiam limitar a corrente elétrica injetada. Com base nestes resultados, recomenda-se uma distância mínima de 1 cm entre *arrays* de modo a maximizar a eficácia da terapia. A sensibilidade dos resultados foi também avaliada recorrendo-se a diferentes métricas reportadas na literatura por outros autores. A escolha do melhor *layout* mostrou ser significativamente afetada pelo critério usado, o que reforça a ideia de serem necessários mais estudos para se averiguar qual é a melhor quantidade física para se classificarem as diferentes opções disponíveis. Os resultados também podem variar significativamente dependendo dos valores atribuídos aos parâmetros físicos e aos mecanismos de transferência de calor modelados. Mais especificamente, a condutividade elétrica do escalpe e do crânio e a condutividade térmica e perfusão sanguínea do escalpe foram as propriedades cuja incerteza no seu valor levou a uma maior variação na temperatura máxima prevista em cada tecido biológico. Por outro lado, a modelação das perdas de energia através do suor também mostrou ser um parâmetro significativo na estimativa do aumento de temperatura. A limitação inerente à modelação deste mecanismo prende-se com o facto de não existirem equações que

consigam prever com precisão a energia que é transferida.

O aumento de temperatura nos tecidos biológicos foi praticamente o mesmo para todos os *layouts* testados, uma vez que a temperatura máxima do escalpe, que controla quanta corrente pode ser injetada, foi também a mesma. Em cada tecido, o aquecimento devido à aplicação dos campos elétricos ocorreu apenas nas regiões que se encontravam por debaixo dos *arrays* e foi muito superficial. Este fenómeno é justificado pelo facto de, em cada tecido, o campo elétrico máximo ser atingido à superfície e consequentemente o efeito de Joule ser também mais acentuado nessas regiões. A temperatura máxima prevista no escalpe foi de 39.5 ℃, o que corresponde a um incremento de 5.5 ℃ comparativamente à sua temperatura máxima inicial. Nos restantes tecidos estes valores foram menores: no crânio a temperatura máxima prevista foi de 39.4 ℃ (+3.5 ℃), no CSF 37.8 ℃ (+0.2 ℃), no cérebro 37.7 ℃ (+0.1 ℃), e no tumor 38.2 ℃ (+0.2 ℃). Para estas variações de temperatura, as únicas alterações fisiológicas expectáveis de ocorrerem são variações na perfusão sanguínea de cada tecido e na atividade metabólica. No entanto, estes efeitos correspondem a processos biofísicos que promovem uma maior eficiência nas trocas de calor, assegurando assim a homeoestasia do corpo. Com base nestes resultados foi possível concluir que os TTFields são seguros do ponto de visto térmico.

Palavras-chave: Aquecimento de tecidos biológicos; Glioblastoma multiforme (GBM); Modelo realista da cabeça; Planeamento de tratamentos; TTFields (do inglês Tumor Treating Fields).

Disclosure

This 3-year PhD grant (March 2019- February 2022) was funded by a research agreement with Novocure.

This agreement contemplated a clause in which Novocure could share information to the author but that information could not be disclosed to third parties due to its confidential nature. Thus, in some parts of the work described throughout this thesis the amount of results and their discussion is kept to the minimum to respect this agreement.

The analysis and discussion of all results presented in this document are the author's own and do not necessarily represent the views of Novocure.

Contents

List of figures

List of tables

List of abbreviations

A-R^2 ..... **A**djusted-**R**^{2}

AP ..... **A**nterior-**P**osterior

ATV ..... **A**bove-**T**hreshold **V**olume

ATV1 ..... **A**bove-**T**hreshold [**1** V/cm] **V**olume

ATV1$_{eff}$ ..... **Eff**ective **A**bove-**T**hreshold [**1** V/cm] **V**olume

AV ..... **A**rray **V**ector

BBB ..... **B**lood-**B**rain **B**arrier

CEM 43 °C .. **C**umulative Number of **E**quivalent **M**inutes at **43 °C**

CNS ..... **C**entral **N**ervous **S**ystem

CSF ..... **C**erebro**s**pinal **F**luid

CT ..... **C**omputed **T**omography

DNA ..... **D**eoxyribo**n**ucleic **A**cid

DTI ..... **D**iffusion **T**ensor **I**maging

ECT ..... **E**lectro**c**onvulsive **T**herapy

EF ..... **E**lectric **F**ield

EQS ..... **E**lectro**q**uasistatic **A**pproximation

FDA ..... **F**ood and **D**rug **A**dministration

FEM ..... **F**inite **E**lement **M**ethod

GABA ..... **G**amma-**A**mino**b**utyric **A**cid

GBM ..... **G**lio**b**lastoma **M**ultiforme

GM ..... **G**rey **M**atter

IEC ..... **I**nternational **E**lectrotechnical **C**ommission

LAPD ..... **L**ocal **A**verage **P**ower **D**ensity

LMiPD ..... **L**ocal **M**inimum **P**ower **D**ensity

LR ..... **L**eft-**R**ight

max ..... **Max**imum

min ..... **Min**imum

MR ..... **M**agnetic **R**esonance

MRI ..... **M**agnetic **R**esonance **I**maging

MST ..... **M**ost **S**ignificant **T**ransducer

NIBS ..... **N**on-**I**nvasive **B**rain **S**timulation

NovoTAL .... **Novo** **T**ransducer **A**rray **L**ayout

OS ..... **O**verall **S**urvival

PD ..... **P**ower **D**ensity

PET ..... **P**ositron **E**mission **T**omography

PFS ..... **P**rogress **F**ree **S**urvival

PRiDe ..... **P**atient **R**eg**i**stry **D**atabas**e**

RHM ..... **R**ealistic **H**ead **M**odel

rTMS ..... **R**epetitive **T**ranscranial **M**agnetic **S**timulation

SAR ..... **S**pecific **A**bsorption **R**ate

SHM ..... **S**implified **H**ead **M**odel

std ..... **St**an**d**ard

sTMS ..... **S**ingle-pulse **T**ranscranial **M**agnetic **S**timulation

tDCS ..... **T**ranscranial **D**irect **C**urrent **S**timulation

TMS ..... **T**ranscranial **M**agnetic **S**timulation

TMZ ..... **Te**m**oz**olomide

TTFields ..... **T**umor **T**reating **Fields**

USA ..... **U**nited **S**tates of **A**merica

WHO ..... **W**orld **H**ealth **O**rganization

WM ..... **W**hite **M**atter

Physical quantities

Physical parameters

The parameters in bold represent vectorial quantities. In parentheses, the SI units are provided.

- c: specific heat at constant pressure (J/(kg K))
- $\boldsymbol{E}$: electric field intensity (V/m)
- f: frequency (Hz)
- h: convection factor (W/(m^2 K))
- I: electric current (A)
- $\boldsymbol{J}$: electric current density (A/m^2)
- k: thermal conductivity (W/(m K))
- R: resistance (Ω)
- t: time (s)
- T: temperature (K)
- ϵ: emissivity (1)
- ϵ_r: relative permittivity (1)
- ρ: density (kg/m^3)
- σ: real electric conductivity (S/m)
- σ^*: complex electric conductivity (S/m)
- ϕ: electrostatic potential (V)
- ω: angular frequency (rad/s)
- ω^*: blood perfusion rate (1/s)

Constants

- ϵ_0: electric permittivity of free space ($\epsilon_0 \approx 8.854 \times 10^{-12}$ F/m)
- σ_{SB}: Stefan Boltzmann constant ($\sigma_{SB} \approx 5.668 \times 10^{-8}$ W/(m^2 K^4))
- j: imaginary constant ($j = \sqrt{-1}$)

Chapter 1

Introduction

1.1 Glioblastoma Multiforme

Glioblastoma multiforme (GBM) is the most agressive type of tumor that appears in the brain. It is ranked by the World Health Organization (WHO) as a grade IV glioma, which is the highest and therefore the most dangerous classification assigned to a central nervous system (CNS) disease [1]. More specifically, GBM is a type of astrocytoma, which as the name indicates, affects the normal functioning of the astrocytes. The astrocytes are a type of glial cells, hence the name glioma, that are responsible for a handful of different tasks that ensure a correct and organized functioning of the nervous system [2]. Some of their main functions include structural and biochemical regulation of the CNS, regulation of the cerebral blood flow, maintenance of the blood-brain barrier (BBB), clearance of neurotransmitters at the synapses, support of myelin structures in the white matter (WM) tracts, and inflammatory reactivity after injury [3].

Thus, it is not surprising that any injury to these cells can significantly compromise the quality of life of people who have a GBM. The most common symptoms result from an increased pressure in the brain due to the tumor's rapid growth. As the tumor grows, the heathly tissue is progressively compressed against the skull. The increase in intracranial pressure blocks the normal cerebrospinal fluid (CSF) flow in the brain and leads to headaches, nausea, vomiting and drowsiness [4]. Very often, there are also more specific symptoms that depend on the region of the brain where the tumor appeared. For instance, tumors located in the motor cortex might lead to psychomotor slowing, hemiparesis and aphasia, whereas tumors located at the occipital region might result in double vision.

According to the work by Ostrom et al [5], the global incidence of GBM was around 3.20 per 100 000 people and it accounted for 47.1% of all primary malignant brain tumors diagnosed in the USA between 2010 and 2014. The same study showed that the incidence increased with age and sex. The highest incidence rates were observed in people between 75 and 84 years and it was 1.58 times more common in males compared to females. The likelihood of developing a GBM was also shown to be significanlty enhanced following long exposures to ionizing radiation [6]. Despite the most recent advances in medicine, the aetology of GBM is still not known and the prognosis remains very poor [7]. The median survival rate with optimal treatment is only 15 months from diagnosis [8] and the five-year survival rate is only 5% [5]. The impact of the problem is agravatted considering that the incidence of glioblastoma will most likely increase in the next years. As the

average life expectancy increases in highly developed countries, so does the group of people which are at a high risk of developing a GBM. According to the predictions made by Johnson [9], it is expected that by 2050, this group of people will increase by 120% and that the number of diagnoses will rise by 72% in the USA. This highlights the need of an early diagnosis and of a more efficient treatment.

In terms of diagnosis, as the general symptoms described above are common to different diseases, it might be difficult to quickly predict the presence of a glioblastoma based only on questionnaires such as the mini mental state examination – MMSE – or the Montreal cognitive assessment – MoCA [10]. Usually, imaging techniques are the quickest option to investigate the lesion and therefore are also the first approach to the problem. Among these, neuroimaging techniques such as contrast enhanced computed tomography (CT), contrast enhanced magnetic resonance imaging (MRI) and/or positron emission tomography (PET) are the most used ones (figure 1.1). In the case of suspected GBM, the first line of management is surgical resection to improve neurological functioning. Based on the histopathological analysis of the excised tissue, the best treatment options are then defined. A more detailed description of the workflow of the diagnosis and management of GBM can be found in McKinnon et al [10].

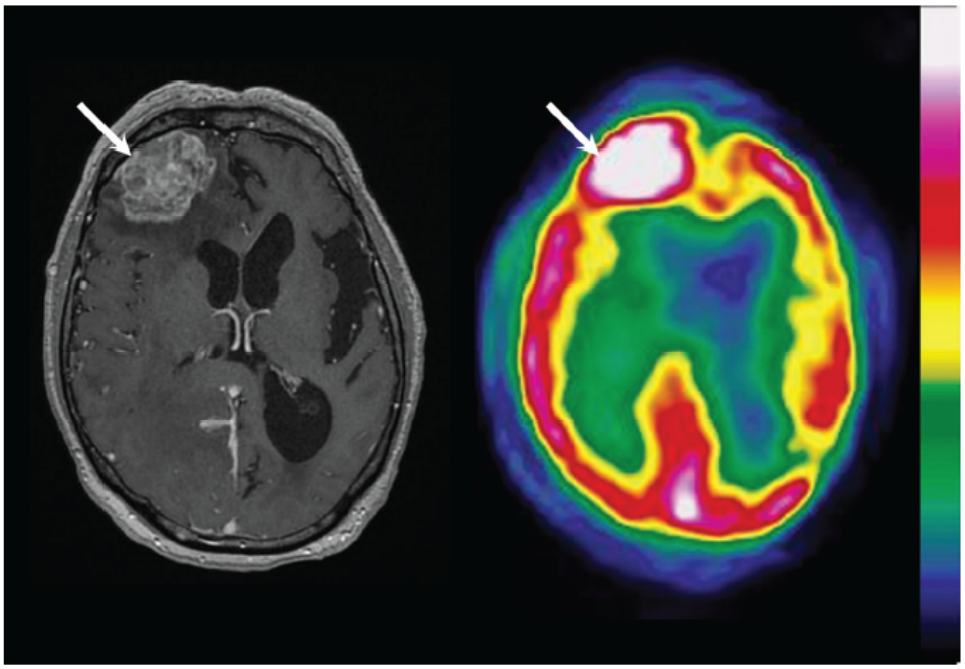

Figure 1.1: Diagnosis of a right frontal glioblastoma following acquisition of T1-weighted gadolinium-enhanced MRI (left, white arrow) and ^{18}F-FDG PET (right, white arrow). In the latter, the white color indicates a high uptake of the radiotracer, which is directly related to an increased metabolism, characteristic of tumors. Image taken from [11].

Once GBM is confirmed, the choice of the best treatment plan depends on several factors such as which biomarkers were identified during the histopathological analysis, tumor location, patient's health condition and whether it is a reoccurrence or not. Given the complexity of the workflow, planning is made by a neuro-oncology multidisciplinary team that is responsible for defining the best approach for each patient. For newly-diagnosed GBM cases, surgery is the first line of treatment whenever possible and it consists in removing as much as possible of the gross tumor volume. For recurrent GBM, surgery can be performed multiple times whenever possible. Radiation therapy and chemotherapy might

be used next. The first consists in destroying tumoral cells that could not be removed during surgery using high-energy beams for the course of several weeks. Depending on each case, chemotherapy might be used concurrently or after radiation therapy and it refers to medication that is adminstrated to the patient usually in the form of a pill, although other application types can be used. The most used drug is temozolomide (TMZ), which was approved by the Food and Drug Administration (FDA) in 2005 following the results from the clinical trial performed by Stupp et al [12]. Other than TMZ, carmustine is also FDA-approved for both new and recurrent GBM cases since 2003, whereas lomustine is only approved for reincident tumors, since 1976 [13]. For recurrent cases, bevacizumab can also be used in treatment. The latter was approved by the FDA in 2009 and it is used as anti-angiogenic therapy, with the goal of inhibiting cell growth by decreasing tumor's blood supply. Most recently, Tumor Treating Fields (TTFields) was also FDA-approved for recurrent and newly-diagnosed GBM cases. This technique consists in applying an electric field to affect tumoral cell proliferation, as described in detail in the next section. A more detailed description of glioblastoma standard of care can be found in the work by Fernandes et al [14].

Due to the agressiveness of this type of tumor, treatment is only performed with a palliative intent to improve the quality of life of both the patient and caregiver. The therapies mentioned above could only add a couple of months to patient's life in some cases despite the improvements in their application. Thus, it is not surprising that the overall survival (OS) and the progression free survival (PFS) did not increase significantly in the past 30 years. According to the National Cancer Institute (NCI) [15], the OS is defined as the length of time from diagnosis until the patient passes away from the disease. The PFS is defined as the length of time during and after treatment that the patient lives with the disease but it does not get worse. As mentioned by Fernandes et al [14], the patient with GBM is simultaneously a subject with cancer and with a progressive neurological disease and thus it is of the utmost importance to improve his quality of life.

1.2 Tumor Treating Fields (TTFieds)

Tumor Treating Fields is a non-invasive cancer treatment technique that consists in the application of electric fields (EFs) to affect the mitotic process of cells. This technique was first investigated in 2004 by Kirson et al [16]. In that study, low-intensity (1-3 V/cm) and intermeadiate-frequency (100-500 kHz) alternating electric fields were shown to have an inhibitory effect on the growth rate of animal and human tumoral cells in *in-vitro* studies. Work published in the following years showed an increase in the potential of this technique and nowadays it is considered to be a fourth-line of cancer treatment, after surgery, radiaton therapy and chemotherapy. In 2011, TTFields were approved by the FDA for the treatment of recurrent GBM after the promising results of the EF-11 clinical trial [8]. Three years later, in 2014, the technique also got approval for the treatment of newly-diagnosed GBM cases after the results of the EF-14 clinical trial [17].

1.2.1 Mechanisms of action

The study published by Kirson et al [16] reported that the mechanisms by means of which TTFields interact with cells were two-fold. The first one occurs at early stages of mitosis and consists in the inhibition and/or prolongation of cell division. Under the

effect of an alternating EF, all charges and polar molecules within the cells are subjected to forces of alternating direction [18], which leads to ionic flow and dipole rotation (figure 1.2A). During cell division, in pre-telophase, tubulin polymerization-depolymerization drives the proliferation process. At this stage, the induced EF can reorientate tubulin dimers according to its own direction due to their large intrinsic dipole moment [19]. As these dimers are one of the major components of the microtubules, the mitotic spindle is not able to form properly and thus to correctly align and separate the chromossomes. This leads to cellular arrest in mitosis for several hours and to a failure at the spindle assembly checkpoint (SAC). The latter ensures that the chromossomes are aligned correctly and attached to the mitotic spindle before separation of the sister-chromatids. Failure at this checkpoint might lead to aberrant metaphase exit, as well as to abnormal chromossome segregation and multinucleated cells and thus to cell death [20]. In the *in-vitro* study by Kirson et al [16], application of an electric field with an intensity between 1.0 and 1.4 V/cm to a culture with mouse melanoma cells led to a mitotic rate that was two-times slower, 124 min vs. 62 min, compared to the control group.

The second mechanism suggested by Kirson et al [16] occurs during cytokinesis when the dividing cell acquires an hourglass morphology. The application of an external EF gives rise to a non-uniform intracellular field, with a high density at the cleavage furrow [19]. Due to a physical phenomenom known as dielectrophoresis, polarizable macromolecules and ions contained in the cell are pulled towards the furrow, regardless of the field polarity. An accumulation of these components leads to membrane blebbling and consequently to cell destruction (figure 1.2B).

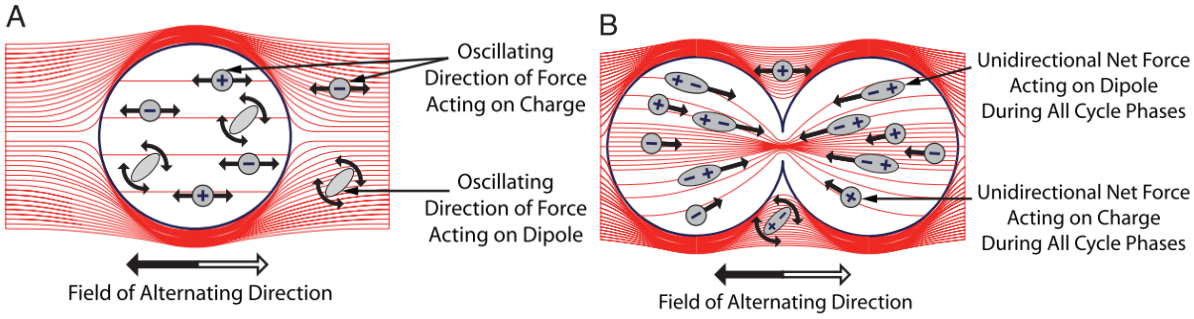

Figure 1.2: TTFields mechanisms of action: (A) during the early stages of mitosis the application of an external EF leads to an inhibition and/or prolongation of cell division by changing the spatial orientation of tubulin subunits due to their large intrisinc dipole moment. As those dimers are the main components of the microtubules and given that tubulin polymeratization-depolymeratization drives the proliferation process at this stage, the mitotic spindle is not able to form properly and thus to correctly align and separate the chromossomes; (B) an external EF applied during cytokinesis gives rise to a non-uniform intracellular field, with a high density at the clevage furrow due to cell's hourglass morphology. Polar macromolecules and ions are attracted towards this region due to a physical phenomenom known as dielectrophoresis. An accumulation of these components leads to membrane blebbling and thus to cell destruction. Image taken from [18].

Throughout time, the mechanisms of action were further investigated and new hypotheses were suggested to explain how TTFields affect cell division. The *in-vitro* study by Gera et al [21] suggested an additional mechanism of action based on the role of septin. The latter is a protein whose main function within cells is to coordinate cell division by associating with actin and microtubules cytoskeletal networks and acting to recruit and integrate certain proteins to specific locations to allow for a correct cell division [22]. The hypothesis proposed by Gera et al [21] is based on the fact that septins have a high dipole moment and thus are also affected by the applied EFs in the same manner as the tubulin

dimers are. Given the importance of septin in cell division, both in pre-telophase and during cytokinesis, this interference could also contribute to the aberrant spindle formation observed by Kirson et al [16]. However, the calculations performed by Tuszynski et al [19] showed that, although TTFields might indeed affect cell division during cytokinesis, the first mechanism of action might not be accurate. According to that study, the predicted torque excerted on the microtubules is around 1000 times weaker than the necessary value and consequently the force induced is also lower than the threshold to disrupt cell division. The conclusions regarding the second mechanism of action were further corroborated by a combined *in-vitro* and *in-silico* analysis performed by Berkelmann et al [23]. To induce an EF intensity of 1 V/cm at the cleavage furrow, the temperature augments 0.5 ℃ and the specific absorption rate (SAR) increases by 57% when TTFields are applied. This local increase might be enough to damage the dividing cell and consequently to affect the mitotic process.

In the work by Giladi et al [24], a delay in the repair of radiation-induced deoxyribonucleic acid (DNA) damage when TTFields were applied was observed. In that *in-vitro* study, the number of glioma cells with DNA damage was 40% higher when TTFields were applied after radiotherapy compared to when the latter was applied as a monotherapy. These results suggest that using TTFields concurrently with radiotherapy might be beneficial to improve patient's quality of life. The work by Chang et al [25] also provided more evidence that might support the use of concomitant TTFields and chemotherapy, instead of chemotherapy alone. In that *in-vitro* study, the membrane permeability of glioma cells increased significantly for 24 hours when TTFields were applied before returning to basal values. This indicates that cells were temporarily more sensitive to chemotherapeutic agents, which might allow to use other drugs that were not considered up until now due to their inability to overcoming this barrier. These results point to the possibility of using TTFields at earlier stages of treatment.

The uncertainty on the mechanisms of action suggests that further investigation is needed to understand and thus to optimize the technique. A more detailed discussion on this topic can be found in the work by Rominiyi et al [20]. One of the points that is already well established and confirmed is that quiescent cells are not affected by these EFs [16, 18]. This makes TTFields one of the most selective techniques for the treatment of brain cancer as it is thought that the cells that compose the brain no longer divide themselves or divide very slowly at an adult age [26]. The impact of the technique in other healthy cells division was still not discussed in detail, but the effect might be very limited. The optimal frequency to affect division depends on cell size and cell doubling time. For glioma cells, the latter is 24 hours and the optimal frequency is 200 kHz [16]. For instance, as the doubling time for skin cells is around 2.5 times higher, 62.5 hours [27], the frequency of the fields that maximizes cell division arrest is most likely different.

1.2.2 Application of TTFields

The way TTFields are applied in patients nowadays is a result of the conclusions drawn from several *in-vitro* and *in-vivo* studies. Kirson et al [16] showed that the number of cells affected by the technique increases significantly when the direction of the external field and the axis of cell division are parallel to each other. According to the mechanisms of action discussed above this result is not surprising given that a perpendicularity between these two axis would not lead to a significant electric field gradient at the cleavage furrow and thus the cell would divide normally. One way to increase the number of cells affected

by the EFs is by applying them in two different directions. The same authors showed that the technique could affect 20% more cells if the fields were applied in two perpendicular directions alternately with a switching between 0.25 and 1 seconds compared to when just one direction was used. The time that the cells were under the action of the fields, the frequency used and the intensity of the electric field were also shown to affect the results [18]. The proliferation rate of cells slowed down during exposure and gradually recovered after the application of the fields was ceased (figure 1.3A). For each cell line there was also an optimal frequency that led to a higher number of cells affected (figure 1.3B). In particular, for glioma cells the ideal frequency was 200 kHz. *In-vitro* results also showed that TTFields can significantly affect more tumoral cells for EF intensities of at least 1 V/cm at the tumor bed (figure 1.3C).

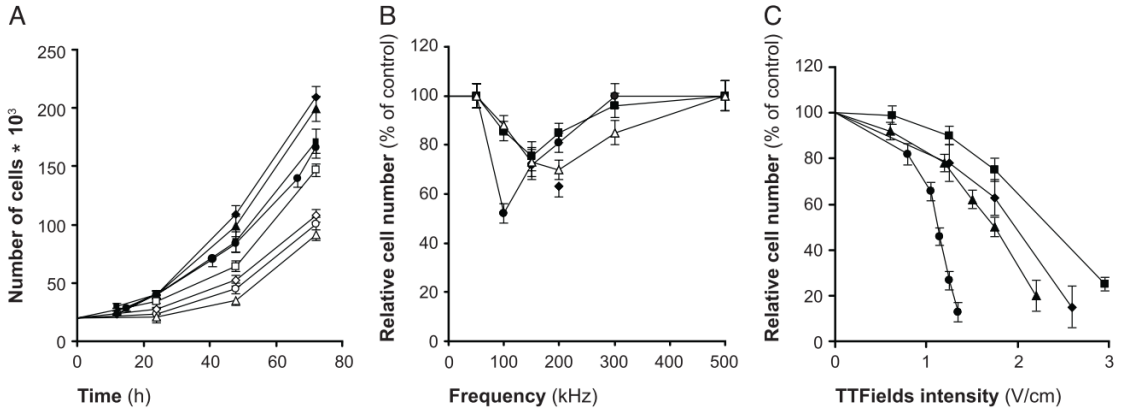

Figure 1.3: Impact of different parameters on TTFields effectiveness. Each symbol represents a cell line. Filled symbols represent untreated cultures, whereas unfilled symbols represent cell lines treated with TTFields for 24 hours. (A) The number of cells in an untreated culture is higher than in one treated with TTFields; (B) There is an optimal frequency for each cell line that maximizes the number of cells affected by the EFs; and C) There is an EF intensity (∼1 V/cm) above which TTFields are highly effective in arresting cell proliferation. Image taken from [18].

To apply TTFields in patients, Novocure® created the Optune™ device (figure 1.4), registered under patent number WO 2017/175116 A1 [28]. This device, formely known as NovoTTF-100A™, consists in an electric field generator coupled to four transducer arrays that work in pairs. Optune was FDA-approved in 2011 for recurrent GBM as a monotherapy and as a last line of treatment when the remaining techniques fail to be effective in improving patient's quality of life. In 2014, it was also approved for newly-diagnosed cases, to be used jointly with chemotherapy with TMZ. It also received a CE mark in 2015, and, as of 2021, it has also been approved to treat GBM in Israel, Japan and China [29]. To allow for long periods of application of the EFs, the patient can carry this device in a bag, in which case the former is powered by portable batteries. Each battery lasts for two to three hours. Alternatively, if the patient plans on staying in the same place for a long time period, the device can also be plugged into a socket.

The arrays are placed on patient's shaved scalp at specific regions that induce the highest EF possible in the tumor in two perpendicular directions at 200 kHz. Each array is a 3x3 matrix of ceramic transducers, whose centers are separated by 33 mm in one direction and by 22 mm in the other. In the most recent generation of arrays, the 33 mm were increased to 44 mm. Between the transducers and the scalp, a thin layer of conductive gel with a thickness of 0.6 mm is used, which comes already embedded in the arrays, to optimize current flow into the head.

Figure 1.4: Components of the Optune™ device. The electric field generator can be powered by portable batteries, which can last between two to three hours, or by plugging it into a socket. The generator is connected to four arrays with 9 transducers each that work in pairs. These arrays are placed on the patient's shaved scalp in specific regions to induce the highest EF possible in two perpendicular directions alternately. Image taken from [30].

There are some contraindications to the use of Optune due to the limitated number of conditions in which it has been tested [31]. Patients that fall within one or more of the following categories can not use TTFields in their treatment:

1. Patients who are 21 years old or younger;
2. Patients with active electronic devices such as deep brain stimulators, spinal cord stimulators, vagus nerve stimulators, pacemakers, defribrillators and programmable shunts;
3. Women who are or might be pregnant or that are trying to get pregnant. Women of child-bearing age must use a birth control while using TTFields;
4. Patients who have a known sensitivity to conductive hydrogels;

The eligible patient must be followed by a doctor and a physician regularly. Very often, a family member or a friend also plays a significant part in treatment as a caregiver, helping, e.g., in placing the arrays in the right regions. As discussed in the next subsection, the arrays should be replaced at least twice every week. Both the caregiver and the patient receive training from qualified personnel (e.g.: the doctor, the physician, etc) who have completed a training course given by Novocure.

1.2.3 Clinical trials outcomes and TTFields improvement

The results observed in clinical trials also allowed to improve how TTFields are applied in patients. The two main pilot studies were the phase III EF-11 [8] and the phase III EF-14 [17] clinical trials, whose results led to TTFields FDA-approval for the treatment of GBM.

The goal of the first one was to compare the efficacy and safety of TTFields in recurrent GBM patients in comparison with physician's best chemotherapy choice, both used as

a monotherapy [8]. This study was performed following the results from the phase II clinical trial with 10 patients reported by Kirson et al [18]. In the EF-11 trial, patients were randomised at a 1:1 ratio to receive either therapy (120 patients received TTFields and 117 received chemotherapy) with the end-points of the experiment being disease progression or intolerance to treatment. The results obtained indicated that although no significant improvements were seen in the overall survival of patients when TTFields were applied, there was an increase in the median survival (6.6 vs. 6.0 months) and progression-free survival rate at 6 months (21.4% vs. 15.1%). In general, the quality of life in the group of patients who received TTFields was also improved as a better cognitive response and emotional functioning were observed and some of the effects that could be directly attributed to chemotherapy were avoided (e.g.: fatigue, nausea, vomiting and pain). The most common side-effect due to the use of Optune was contact dermatitis on the scalp underneath the regions where the arrays were placed in 16% of patients. This condition was associated with the use of the hydrogel and it was easily treated using topical corticosteroids.

After the EF-11 clinical trial was concluded, a handful of different studies were performed to better understand how TTFields application could be improved. The *post-hoc* analysis performed by Kanner et al [32] showed that the overall survival of the sub-group of patients who completed at least one course of TTFields treatment, i.e., that were under continuous treatment for 28 consecutive days, was significantly improved compared to those patients who received chemotherapy (7.7 vs. 6.0 months). Another factor that contributed to an enhanced OS was the time that patients were under the application of the EFs, i.e., the compliance. The sub-group whose daily compliance was at least 75% (18 hours) had a median OS of 7.7 months, whereas the median OS of the complementary group was 4.5 months. In 2014, Mrugala et al [33] published the patient registry database (PRiDe) in which data regarding recurrent patients who received TTFields were compiled. Compared to the EF-11 clinical trial, this larger database included more patients as the evaluation period was bigger, from 2011 to 2013, and the analysis of the data yielded more favorable predictions compared to that trial. The OS increased from 6.6 to 9.6 months and the one- and two-year survival rates rose from 20 to 44% and from 9 to 30%, respectively. The conclusions drawn by Kanner et al [32] were also corroborated by this study.

The EF-14 clinical trial [17] followed a preliminary phase II trial performed by Kirson et al [34] in which the goal was to investigate the benefits of adding TTFields as an adjuvant therapy to chemotherapy with TMZ instead of TMZ alone in newly-diagnosed GBM patients. In the EF-14 clinical trial patients were randomized at a 2:1 ratio (466 vs. 229) to receive either TTFields plus TMZ or just TMZ, respectively. The results showed that adding TTFields leads to an improvement on the median progression free survival (6.7 vs. 4.0 months) and of the median overall survival (20.9 vs. 16.0 months), with no additional side-effects reported. Similarly to what was observed in the EF-11 clinical trial, the only adverse effect that resulted from the use of Optune was mild to moderate skin toxicity underneath the arrays in 52% of the patients. The *post-hoc* analyses of the data carried out by Toms et al [35] showed that the sub-group of patients whose daily compliance was at least 50% had an extended PFS and OS and those whose compliance was higher than 90% had maximal survival benefits with a median PFS of 8.2 months compared to the 4.0 months observed in the group that received TMZ alone. For this sub-group of people, the OS also increased from 16.0 to 24.9 months. The efficacy of the combined therapy in newly-diagnosed cases in elderly patients ($\geq$ 65 years) that

participated in the EF-14 clinical trial was investigated by Ram et al [36]. In this subgroup, the OS survival was 17.4 months and the PFS 6.5 months. These values were higher than the 13.7 and 3.9 months observed in the group of patients treated with TMZ alone, thus proving that TTFields as an adjuvant therapy is also beneficial for the age group with the highest incidence rate.

In both clinical trials there were some dermatologic adverse events at the skin level. In 2014, Lacouture et al [37] published a first investigation on this problem based on the results of the EF-11 trial. In 2020, this analysis was further extended with information concerning the results from the EF-14 trial as well [38]. The high majority of these adverse effects were graded with a level 1 (mild effect) or 2 (moderate), which means that they were manageable without substantial treatment breaks and resolved completely after treatment was stopped [38]. These adverse events included, among others, dermatitis, skin infection, and skin ischemia (figure 1.5).

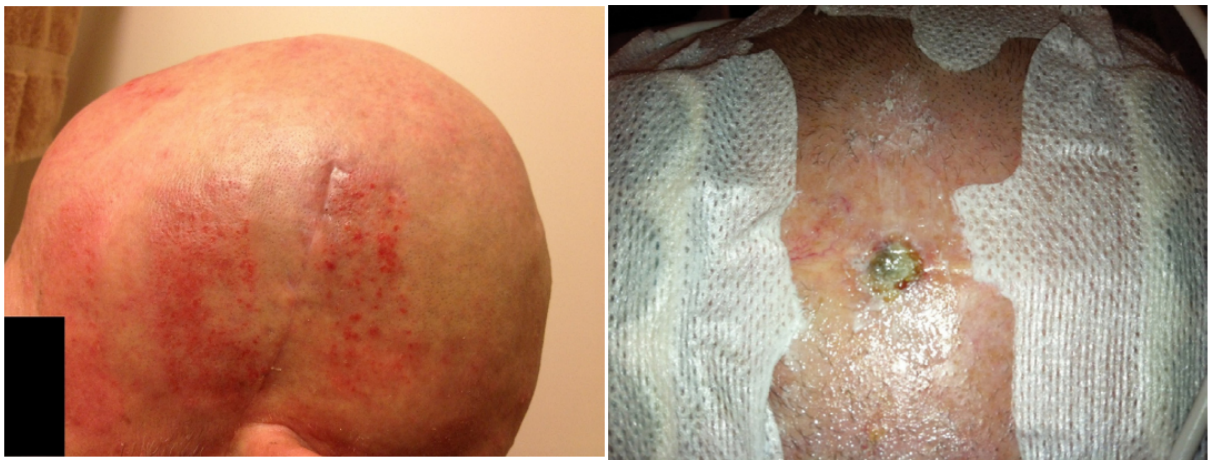

(a) Dermatologic erosion and skin infection

(b) Skin ulceration

Figure 1.5: Examples of dermatological adverse effects that occurred due to the use of Optune. The image on the left corresponds to a 60-year old patient treated with TTFields+TMZ for 3 months. The image on the right corresponds to a 61-year old patient who was treated with TTFields for 2 weeks. Images taken from [37].

To manage these dermatologic events, different strategies were suggested by Lacouture et al [37, 38] in terms of how to properly prepare the head (shaving, cleaning, washing, etc) and how to place and remove the arrays. As mentioned by the authors, these arrays should be replaced every 3 to 4 days to minimize skin problems.

The results discussed up until now allowed to ascertain which were the most important parameters when a patient was treated with TTFields. Nowadays, the arrays are placed on patient's shaved scalp by the treating physician or the caregiver. To assist in this task, Novocure created the Novo Transducer Array Layout (NovoTAL™) system. This FDA-approved software [39] uses MRI data of each patient and suggests the best regions to place the arrays based on geometric measurements of the head and on the results of computational simulations. Given the importance of applying the fields in more than one direction, four arrays that work in pairs are used, which allows to inject current in two perpendicular directions alternately, with a switching time of one second. Based on what is reported in the literature, the total amount of current injected into each pair is 900 mA [39]. However, as it will be seen in chapter 7, this value is not constant and it varies throughout treatment. It is recommended that the patient completes at least one complete

cycle of treatment, which lasts for one month. Ideally, the patient should continue to use TTFields indefinitely unless there is a strong contraindication. The daily treatment time should also be maximized, with a minimum compliance of 18 hours per day. However, such high daily treatment times leads inevitably to an increase of the temperature of the head, which explains why Optune's current injection depends on this parameter. Based on the literature, to avoid any thermal harm to the patient, the temperature of the transducers is monitored and kept below 41 ℃ [38] by shutting down the injected current. However, as it will be discussed in chapter 7, the temperature limit is lower than this value and current is not completely shut down. According to Mrugala et al [33], 11.3% of the patients that were part of the PRiDe experienced a heat sensation when using TTFields. This was one of the most common adverse events in patients treated with this technique, only second to skin reaction, which was reported in 24.3% of the cases.

1.3 Context of the thesis

The heat sensation felt by patients is still an understudied side-effect. Due to the continuous application of the electric fields the temperature of head tissues increases as a result of a physical phenomenom known as Joule effect and it will remain above basal values for most part of the day. The studies published in the literature failed to accurately investigate this issue, either because the geometry used and the modelling of the problem were far from a real case [40], or because the conditions in which treatment is performed and the Optune device were not accurately represented [41]. The prolonged exposure to the these EFs might induce physiological changes that were not reported in patients yet. This PhD thesis is a continuation of the work that began with a MSc thesis [42], presented in 2018, whose main goals were to quantify the temperature increases in the head and predict the thermal impact when TTFields were applied. The results obtained in that work were very promising and were later on published in a peer-reviewed journal [43]. Due to the novelty of that work, Novocure sponsored a 3-year grant to continue this investigation in more detail thus leading to this PhD thesis. The organization of this work can be divided into two parts, with the separation line being the visit made to Novocure's headquarters, in Haifa, in December of 2019.

The first part (chapters 4, 5 and 6) was more focused in investigating ways to improve the computational results obtained during the MSc thesis and to suggest new ways to improve how treatment was modelled. During the visit made, Novocure shared more information (chapter 7), which was very useful as it allowed to understand better how treatment was done in patients. In that same meeting, future work was also defined that could simultaneously increase the novelty of this PhD and also help the company on working towards their own goals. Some of the main tasks planned included, among others, an experimental part and building a phantom to validate the heat transfer model. However, three months later the WHO declared covid-19 as a pandemic and thus the main goals and the workplan had to be rethought to something that could be done remotely, exclusively. The main concern was to redirect the goals to something that would still maintain the originality of the work and that could still help Novocure improving the technique.

As mentioned previously, treatment planning should be fast and accurate to provide the best quality of life as possible to the patient. One aspect of treatment planning is related to array positioning, which is performed by the NovoTAL system. This software

suggests the best regions to place the arrays based on the average EF that is induced at the tumor bed using computational simulations. The results obtained during the MSc thesis and in chapters 4, 5 and 6 clearly showed the importance of the temperature increases when the EFs were applied. As it will be seen throughout this thesis, accounting for the temperature during treatment planning is also of the utmost importance as it significantly reduces the values of the metrics used to evaluate treatment effectiveness and thus might affect the choice of the best layout to use. Thus, the general goal of this work was changed to improving treatment planning by investigating how the temperature of head tissues might affect the conclusions obtained from the NovoTAL system (chapters 8 and 9). Even though the general aim had to rethought halfway through this work, the conclusions drawn from each chapter were useful to the final goal.

1.3.1 Thesis overview

This thesis is divided as follows:

- Chapter 2: Biological tissue heating. In this chapter a general overview of the impact of biological tissue heating in other medical techniques is discussed, both as a side-effect, as in MRI and non-invasive brain stimulation (NIBS) techniques, and as a part of the final goal in treatments such as hyperthermia. The physiological changes that occur are analysed, as well as the different metrics that can be used to quantify the thermal effects in each one of these techniques. Based on this investigation, the thermal impact predicted when TTFields are applied is presented alongside with the main results from the MSc thesis;

- Chapter 3: Modelling TTFields. In this chapter, a description of the workflow on how to model TTFields treatment is presented. More specifically, the realistic head model used for the most part of this thesis and its limitations are discussed. As all computational results were obtained using COMSOL Multiphysics, a general overview of the finite element method (FEM) is also discussed as well as the necessary equations to predict both the electric field and the temperature distributions;

- Chapter 4: Sensitivity analysis of the physical parameters. As computational modelling implies specifying parameters that might not be accurately known, the sensitivity of the results discussed in chapter 2 is evaluated by accounting for the uncertainty in the electric and thermal parameters assigned to each physical property;

- Chapter 5: Sweat as an additional cooling mechanism. In this chapter, an additional step towards a more accurate representation of the heat processes that occur during TTFields treatment is taken by accounting for the contribution of sweat losses. As sweating was reported to occur in patients, in this chapter one possible way model this additional mechanism and the main challenges in doing it are provided;

- Chapter 6: Study of a new current injection mode. In this chapter a different approach to inject current to maximize the time that the patient is effectively under treatment is investigated. The temperature distribution and the thermal impact of this new method is also evaluated and compared with the current injection mode of the Optune device;

- Chapter 7: Improving TTFields modelling: Analysis of Optune's current injection algorithm and log files. In this chapter, the information shared by Novocure is presented and discussed as much as possible based on the confidentiality agreement. From the analysis of these data, it was possible to know which keypoints had to be improved to model TTFields treatment more accurately and to study the limitations of the model used throughout this thesis;

- Chapter 8: Tissue temperature during TTFields treatment planning: simplified head model. This chapter represents a first approach towards the final goal of the thesis. The impact of adding information regarding the temperature increases in the head during treatment planning is considered using a simplified head model. Additionally, more suitable metrics to predict treatment effectiveness are also discussed based on papers published recently in the literature;

- Chapter 9: Tissue temperature during TTFields treatment planning: realistic head model. The work described in this chapter compiles all the relevant conclusions drawn from the previous chapters to investigate how to add information about the temperature of tissues during TTFields treatment planning. To achieve this goal, a realistic head model with array positions suggested by the NovoTAL system is used in the simulations. Different methods to rank the layouts are considered and the impact of the temperature in the metrics used to choose the best layout is evaluated. The thermal impact of TTFields is predicted once again in a much more accurately manner;

- Chapter 10: Final considerations. An overview of the main outcomes of this thesis, the general limitations of this work as well as future work that can be done to improve the results obtained here are presented. The future of TTFields in oncology is also discussed based on what was observed in the last 15 years;

- Chapter 11: Scientific output: Full list of published and presented work. A detailed list of the scientific outcome that resulted from this PhD thesis is presented;

Chapter 2

Biological tissue heating

In most medical techniques, biological tissue heating is an undesirable side-effect and therefore it should be controlled to keep the patient safe. However, in some medical procedures, such as hyperthermia and ablation techniques, the main goal is to kill or remove tumoral cells by overheating them and thus it is desirable to increase the temperature as much as possible in a controlled manner.

For non-invasive brain stimulation techniques, the frequency used is lower than 10 kHz. In this frequency range, the electromagnetic radiation can depolarize cells membrane but it is not high enough to significantly heat tissues up. As the frequency increases, the main effect of these fields at the cellular level is no longer membrane depolarization and thus stimulation does not occur and the medical applications start to change as well. In techniques such as hyperthermia, frequencies in the order of the hundreds of kHz and higher are used in cancer treatment with the final goal of overheating tumoral cells. Frequencies of few MHz and higher are also used for diagnostics in techniques such as MRI and microwave imaging in which anatomical images of a part of the human body are produced. For the latter three medical procedures, heating occurs whether it is desirable or not even for low exposure times due to the Joule effect. This phenomenom, also known as resistive heating or ohmic losses, occurs when current passes through a conductor. The induced electric field gives kinetic energy to the electrons which collide with the particles of the conductor, thereby increasing their temperature. For frequencies higher than that of the visible light (> 1 PHz), the electromagnetic radiation is strong enough to ionize cells and affect chemical bonds. This type of radiation finds its most valuable use in cancer treatment where techniques such as radiotherapy have been developed based on this type of interaction. Another common application of such type of radiation is in diagnostics namely through X-ray imaging, mammography, and CT.

The frequency range in which TTFields operates, between 100 and 500 kHz, is too high to stimulate cells but it can cause significant temperature increases as a result of the Joule effect with tissues temperature remaining above basal values for most part of the day due to the high daily compliance. As patients that use Optune in their treatment should be under the application of the electric fields for as long as possible, the temperature increases might have some negative impact on their health that was not reported yet. In this chapter, a brief discussion is made in terms of the temperature increases in three different cases: 1) NIBS and similar techniques; 2) MRI; and 3) hyperthermia. The rationale to discuss the first is that the frequency used is relatively close to the one considered for TTFields treatment and the way current is injected can also be very similar. Tissue

heating in MRI is discussed as in this technique it is also an undesirable effect that should be accounted for and for which there are already several studies published and metrics that are widely accepted to quantify these increases. Lastly, hyperthermia is considered due to the frequency used and in order to investigate ways to predict the thermal impact when TTFields are applied. The conclusions drawn from this analysis are extrapolated to discuss what might occur temperature-wise when TTFields are applied. In this context, thermal impact is defined as short- and/or long-lasting physiological changes that occur due to the temperature increases that result directly or indirectly from the application of the technique. As it will be seen by the end of this chapter, there are several limitations on trying to use metrics from other medical procedures to quantify TTFields thermal impact. Thus, the results from this analysis only represent an initial attempt towards the study of the impact of the temperature increases in TTFields patients. Although the metrics used in the aforementioned three cases are discussed to some extent in this chapter, their quantification in the rest of the thesis is limited.

2.1 Tissue heating in other medical techniques

2.1.1 NIBS and related techniques

Non-invasive brain stimulation and other similar techniques aim to induce an electric stimulation in a specific region of the brain to modulate its excitability, due to a phenomenom known as neuroplasticity [44]. This refers to the ability of the brain to change and modulate cortical activity beyond the stimulation period. One of the better known techniques that fall within this category is transcranial magnetic stimulation (TMS). This technique is FDA-approved for the treatment of medication-resistant depression since 2008 and for migraine with aura since 2013. It consists in a strong (4 to 8 kA) and rapidly changing (in the order of the tenths of ms) electric current that circulates through a set of coils strategically placed above patient's head. This current gives rise to a time-varying magnetic field that penetrates the cranium and induces a time-varying electric field in the brain. The induced EF can stimulate excitable tissues located in the regions underneath the coils, thus generating a neurophysiological change in the brain [45]. Depending on the final goal, the way these fields are applied is different. Single-pulse TMS (sTMS) consists in discharging pulses with a duration between 0.25 and 0.75 ms separated by intervals of at least 4 seconds and it is mainly used for diagnostics [45]. TMS is also used as a therapy when many pulses are delivered with a time interval of 2 seconds or less and is referred to as repetitive TMS (rTMS). It might be applied for time periods as long as 30 minutes. Another well-known NIBS technique is tDCS in which electrodes are placed on patient's scalp and a constant direct current, generally lower than 2 mA, is injected [46]. This technique is applied to modulate cortical excitability to enhance human cognitive process [47] and each session might last for up to 30 minutes. As of 2021, this technique is not approved by the FDA and it is only used for investigational or experimental purposes.

Similarly to rTMS, electroconvulsive therapy (ECT) is also used to treat depression, but it is not considered to be a NIBS technique. In ECT, two electrodes are placed on specific regions of the scalp and a current with a frequency between 20 to 120 Hz and intensity between 500 and 900 mA is injected for time periods of up to 8 seconds [48]. Typically, each treatment lasts around 20 minutes, including current set-up, and should be performed 2 to 3 times a week until patient's condition improves (usually within 6 to

12 sessions).

In these techniques, the main outcomes in patients are changes in the cortical activity that last for some time after application ceases [47, 49, 50]. According to the guidelines published by Rossi et al in 2009 [51], and later on updated in 2021 [52], the most common side-effects reported to occur due to rTMS include hearing problems, as well as headache, pain and discomfort. Physiological changes due to temperature increases were not reported in any case. For rTMS, scalp's temperature might rise up to 37 ℃ [45], whereas the temperature rise due to a single-pulse is estimated to be less than 0.1 ℃ in the brain [53], with the values quickly returning to their initial temperature. Computational studies also showed that both ECT [48] and tDCS [54] are safe from a thermal point of view, as the predicted temperature increases were very low. These results indicate that NIBS techniques and ECT do not lead to significant temperature increases in the head and thus that the thermal impact due to their application is most likely to be negligible.

2.1.2 MRI

Magnetic resonance imaging is a non-invasive technique used to produce high-resolution tomographic images of the human body. One of its important applications is in oncology where it is one of the first options to confirm the presence of a tumor. Typically, an MR imaging session lasts for twenty minutes to one hour. As all nuclei within the human body are randomly oriented, the net magnetization vector is null. The rationale to create images in MRI is to intentionally induce variations in this vector and study them. More specifically, these variations are studied for hydrogen atoms due to their abundance in the body. The first step consists in applying a strong static magnetic field. This field aligns nuclei according to its own direction and creates a non-null and constant magnetization vector. At this stage, the number of nuclei aligned parallel with the direction of the static field is slightly higher than those who are in an anti-parallel state. Electromagnetic radiation is then applied in two different ways: spatially and temporally variable magnetic fields, known as gradients, and high-frequency radiofrequency waves. The first are applied to induce temporary gradients in the static field, which are needed to add information about the spatial distribution of the individual MR signals [55]. The frequency of these gradients is typically in the few kHz range. The radiofrequency pulses are used to cause a transition of nuclei from the parallel to the anti-parallel energy states. The energy difference between these two is defined by two parameters: 1) the intensity of the static field, which in common clinical practice is either 1.5 or 3.0 T; and 2) the gyromagnetic ratio of hydrogen atoms (γ=42.58 MHz/T). These field intensities translate into a resonant frequency of 64 and 128 MHz, respectively [55]. This is also known as the Larmor frequency for hydrogen, and it corresponds to the frequency of the radiofrequency pulses that allows nuclei to transit between two levels of energy. This leads to a variation in the direction of the magnetization vector and the study of these variations allows to built MR images.

The main side-effects that result from the application of the static field include drowsiness, metallic taste, headaches, nausea and dizziness, which only last for as long as the patient is subjected to the field [56]. There is no tissue heating due to its application given that, as described by the laws of Maxwell (equations (A.1) to (A.4), appendix A), to induce an electric field within the human body the magnetic field should vary with time, which is not the case. Tissue heating also does not occur when the gradient magnetic fields are applied. As their frequency is within the few kHz range, nerves and muscles

stimulation might occur. Thus, it is not surprising that sensations such as tingling are felt by patients [56]. The short-lasting RF pulses, which are applied in specific intervals that depend on the sequence used to produce the final image, are the ones that lead to the temperature rises that occur during image acquisition [57].

In MRI, the specific absorption rate (SAR) is used as a surrogate for the temperature increases. The SAR measures the energy (in W/kg) that is absorbed by the human body. It is mathematically described as:

$$SAR = \frac{1}{V}\int_V \frac{\sigma||\boldsymbol{E}||^2}{\rho}dV \tag{2.1}$$

where σ (S/m) is the electric conductivity of the tissue, $\boldsymbol{E}$ the electric field vector (V/m) and ρ the density of the tissue (kg/m^3). This calculation is made within a specific volume V (m^3), whose value depends on the guidelines followed.

An estimation of the SAR at the surface of the body might be obtained using a simple loop model as reported by Panych et al [58]. The authors showed that the electric field is proportional to the Larmor frequency, which in turn is proportional to the strength of the static magnetic field. Based on the expression to calculate the SAR, this means that doubling the intensity of the static field, e.g. from 1.5 to 3.0 T, leads to a power deposition increase of four times for a given MR pulse sequence [59]. Depending on factors such as the type of pulse used, repetition time, type of coil, volume of tissue contained within the coil, among others, this increase might lead to significant temperature variations [57].

Thresholds for the SAR were defined in directives produced by international agencies, based on experiments on healthy human subjects (e.g.: [60, 61]) (table 2.1). Later, in 1998, the FDA published guidelines, under the name of "Guidance for the submission of premarket notifications for magnetic resonance diagnostic devices" in which safety thresholds were defined. In terms of whole volume limits, a maximum value of 4 W/kg, averaged over 15 minutes, for the body, and of 3 W/kg, averaged over 10 minutes, for the head were considered to be safe exposure limits for patients. As for local SAR, the safety values for one gram of tissue and averaged over 5 minutes were 8 W/kg, for the head and torso, and 12 W/kg for extremities. These limits are different from those defined later by the International Electrotechnical Commission (IEC) under the reference IEC 60601-2-33, first published in 2002 and last updated in 2015. In this guideline, the limits were divided into three different categories, all averaged over 6 minutes. In level 0, also known as the normal mode, the risk of ill-effects to patients is minimised and the limits are defined to prevent a whole-body temperature rise higher than 0.5 ℃. According to this guideline, the SAR value for the body is limited to 2 W/kg, whereas for the head this value is increased to 3.2 W/kg. In terms of local energy absorption, calculations should be performed over 10 grams of tissue and should not exceed 10 W/kg in the head and torso and 20 W/kg in the extremities. In level 1, also known as the controlled mode, most of these thresholds are doubled and are defined to limit whole-body temperature increases to 1 ℃. Level 2, the experimental mode, is only used for research purposes and MRI experiments made at this level have to be approved by the local institutional review board. Currently, there are no upper limits when working on this operating mode, but whole-body temperature increases are recommended to stay within 2 ℃. Nowadays, both IEC and FDA thresholds are in use.

Table 2.1: Specific absorption rate limits according to the guidelines defined by the FDA in 1998 and by the IEC in 2015. These limits concern whole volume and local SAR values. For the first, there is a difference in the SAR limits for the body and for the head, whereas for the second the SAR values are averaged over a specific amount of tissue (one gram following the FDA guidelines and 10 g following the IEC recommendations) and are different for the head, torso and extremities. Adittionally, the IEC defines three different levels of exposure: level 0 (the normal mode), level 1 (the controlled mode) and level 2 (the experimental mode), depending on the limits for the whole-body temperature increases that are allowed for the patient.

		Whole volume		Local		
		Body	Head	Head	Torso	Extremities
FDA		4 W/kg 15 min	3 W/kg 10 min	8 W/kg 5 min 1 g of tissue	8 W/kg 5 min 1 g of tissue	12 W/kg 5 min 1 g of tissue
IEC	Level 0	2 W/kg 6 min	3.2 W/kg 6 min	10 W/kg 6 min 10 g of tissue	10 W/kg 6 min 10 g of tissue	20 W/kg 6 min 10 g of tissue
	Level 1	4 W/kg 6 min	3.2 W/kg 6 min	20 W/kg 6 min 10 g of tissue	20 W/kg 6 min 10 g of tissue	40 W/kg 6 min 10 g of tissue
	Level 2	>4 W/kg	>3.2 W/kg	>20 W/kg 10 g of tissue	>20 W/kg 10 g of tissue	>40 W/kg 10 g of tissue

One of the main challenges of using SAR comes from the variety of ways that are used to apply sequences of radiofrequency pulses, which increases the uncertainty in terms of temperature variations. As reported by Collins et al [62], there is not a good overall spatial correlation between SAR values and temperature increases as blood perfusion and conduction also play a significant role in the thermoregulation of tissues. According to the calculations made by Shellock and Schaefer [57], the maximum SAR that could be deposited in the brain to increase its temperature by 1 ℃ is 31 W/kg, whereas in the skin this value could be as high as 87 W/kg. Both these SAR values are significantly higher than what was defined in the safety guidelines discussed above. Other studies also corroborate the lack of a good correlation between the SAR and the temperature increases. In the work by Boss et al [59], a 3.0 T scanner was used to investigate the temperature increases due to different radiofrequency pulses in healthy volunteers. These pulses consisted in a six-minute T1-weighted 3D gradient-echo sequence followed by a four-minute T2-weighted 2D multislice fast spin-echo sequence. The average SAR induced in the head was 1.17 W/kg for the first and 2.53 W/kg for the second, which translated into an average total temperature increase of around 1.2 ℃ in the head. Thus, even though the SAR limits were within what was defined by the FDA and IEC (level 1), the temperature increases were not limited to 1 ℃. In this study, patients experienced a heat sensation due to the application of the radiofrequency pulses, but no side-effects were attributed to the temperature increases.

The results described above highlight that the SAR might not be the best indicator to evaluate temperature increases for MRI. Nonetheless, throughout this chapter this metric is still used to predict TTFields safety.

2.1.3 Hyperthermia

Hyperthermia represents an additional line for cancer treatment. It was approved by the FDA in 2011 for the treatment of cervical carcinoma used in conjunction with radiation therapy for those patients who are not eligible for chemotherapy [63]. This technique is used to heat up the tumor to a temperature around 45 ℃ to damage or kill cancer cells [64]. Hyperthermia can also be used to sensitise cancer cells to other treatments, such as radiotherapy and chemotherapy, in which case the target temperature might be lower than 45 ℃. Tumor heating can be performed in different ways and at different frequencies. Very often, radiofrequency (300 kHz to 300 MHz) or microwave (300 MHz to 300 GHz) electromagnetic radiation is used for a period of one hour or more [65], although there are other options such as, e.g., ultrasounds and hot water perfusion blankets [66]. Depending on the type and stage of the tumor, presence of metastases and patient's health condition, hyperthermia might be applied locally, regionally or to the whole-body. The temperature range in which each one operates is different, as the latter is used mainly to sensitise cancer cells to the action of chemotherapy and radiation therapy, whereas the first two are used to overheat tumoral cells to kill or damage them (figure 2.1).

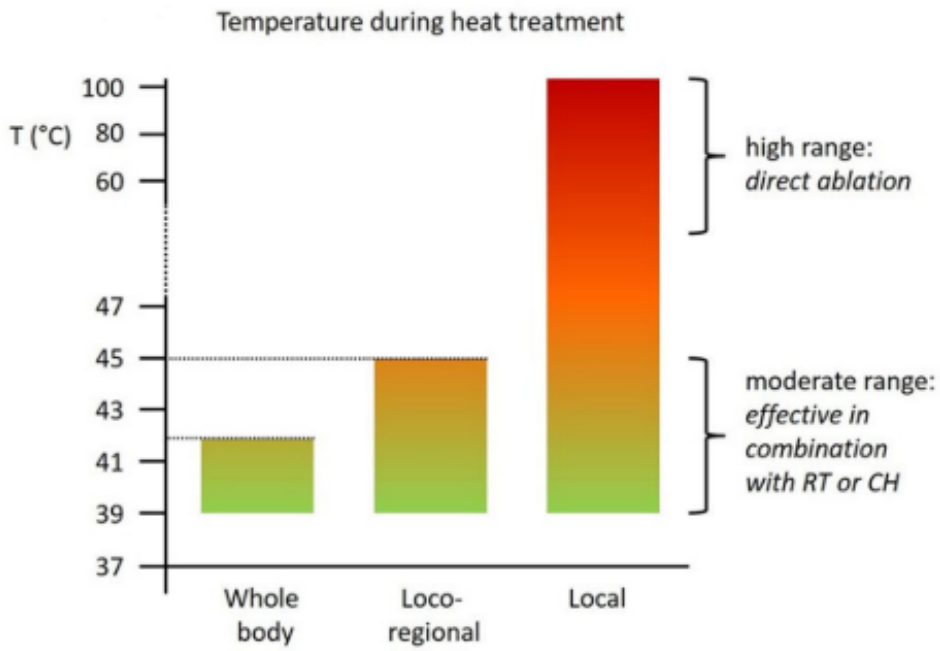

Figure 2.1: Different temperature ranges at which each hyperthermia procedure operates. Whole-body treatment is applied for 6 hours to maintain body's temperature between 39-40 ℃ or for 60 minutes to keep it around 41-42 ℃. It is applied to sensitise cells to the action of chemotherapy and/or radiation therapy. Regional hyperthermia is used mainly at the abdominal level and limbs and the maximum target temperature is 45 ℃. Local hyperthermia is the most specific one and it consists in increasing the temperature of cancer cells to values around 45 ℃ as well. Both the regional and local methods are used to kill cancer cells by overheating them. In thermal ablation techniques, the local temperature can reach values higher than 50 ℃ for a few minutes in a single session to destroy cancer cells by heat. Image taken from [67].

Local hyperthermia is used for small tumors with a maximum diameter of 6 cm located superficially or within an acessible body cavity [66]. In this type of treatment, the temperature can increase significantly in a short period of time. As seen in the work by

Chiche et al [66], one of the most used commercial hyperthermia equipments can raise the temperature of a tissue by 5 ℃ after just 25 seconds using an interstitial applicator operating at 915 MHz. The main advantage of this approach is that it is possibe to minimise heating of normal tissue surrounding the tumor, thus ensuring patient's safety. A less localised heating is seen in regional and whole-body hyperthermia. The first is used to heat the tumor plus an additional margin that includes healthy tissue. The main regions in which this method is applied are the abdominal cavity and the limbs [66]. The second might be used when the patient has multiple metastases and it consists in increasing the body core temperature to 39-40 ℃ for 6 hours or to 41-42 ℃ for 60 minutes [67]. The main limitation of the latter approach is that it is the one that offers the greatest probability of complications in terms of thermal stress to tissues. The most immediate side-effects include transient diarrhoea, nausea and vomiting [66]. An extensive discussion and review of the main benefits and disadvantages of the different types of hyperthermia treatment can be found elsewhere (e.g.: [67]).

The long-term impact of hyperthermia treatments has been a subject of study since this technique started being applied in oncology. Due to the different heating regimes and to the different ways that there are to increase the temperature of tissues, it is not easy to investigate and define thermal thresholds to compare treatments and predict what physiological changes might occur. It is known that the time that it is necessary to reach a certain thermal effect is inversely related to the maximum temperature that the tissue reaches. This means that it is possible to heat up the tumor to a high temperature for a small period of time or to heat it up at a lower temperature but during more time to reach the same effect. Sapareto and Dewey [68] were the first authors to investigate a metric that could convert the time at a certain temperature to an equivalent time at a reference temperature using data from the literature. The latter was chosen to be 43 ℃ as *in-vitro* work showed that for most tissues there is a variation in the rate of cell death for temperatures below and above that value [68]. This variation was explained by a change in cellular thermotolerance and the metric was named as the cumulative number of equivalent minutes at 43 ℃ (CEM 43 ℃). Its mathematically expression is:

$$CEM\,43℃ = \int_0^t R(T)^{43-T} dt \tag{2.2}$$

where t (min) is the time interval of interest and T (℃) is the mean temperature in that period of time. R is the constant related to the thermotolerance acquired by cells when heated and its value is given by:

$$R(T) = \begin{cases} 0.25 \Leftarrow T \leq 43^oC \\ 0.50 \Leftarrow T > 43^oC \end{cases}$$

These expressions imply that the same thermal effect is obtained when heating a tissue during 4 hours at 42 ℃, 1 hour at 43 ℃, or 30 minutes at 44 ℃.

The values of CEM are affected by the value assigned to the factor R and to the choice of the reference temperature. Additional *in-vivo* studies indicated that for human cells the breakpoint temperature at which there is a change in cells sensibility to heat should be 43.5 ℃ and that the value of R should be 0.13 and 0.72 for temperatures lower and higher than that value, respectively [69]. Nonetheless, equation (2.2) with a R value of 0.25 or 0.50 has been widely used in the literature to define the relevant thresholds for

hyperthermia treatments. The first work that compiled the information available in the literature to deduce these thresholds was published by Dewhirst et al in 2003 [69]. An updated version of the thresholds was produced by Yarmolenko et al and published in 2011 [70]. In total, more than 250 papers were considered to deduce thresholds for several tissues using data from animal and human experiments. The relevant values that can also be used to predict the thermal impact for TTFields are presented in table 2.2. The original papers used by the authors are not here referenced, but can be easily found in [69, 70]. Two additional papers with relevant information that were not included in those two works were also considered in this analysis: Leon et al [71] (with CEM 43 ℃ values for bone) and Frosini [72] (with CEM 43 ℃ values for the CSF). As discussed by Dewhirst et al [69] and Yarmolenko et al [70], the uncertainty associated with these values may be high. This is explained by the lack of uniformity in the heating regime, differences in the species on which the experiments were performed, whether anaesthesia was used or not and the post-exposure damage assessment time. This uncertainty is increased by the fact that most papers only report acute changes (tissues evaluated 0 to 30 days after exposure) rather than chronic effects (tissues evaluated more than 30 days after exposure). A more extensive discussion on the limitations of using CEM 43 ℃ can be found in [73].

Table 2.2: CEM 43 ℃ thresholds reported in Dewhirst et al [69], Yarmolenko et al [70], Leon et al [71] and Frosini [72] that led to physiological changes in the tissues of interest to predict TTFields thermal impact. In some cases, more than one value is presented given that more than one study reported the same physiological effect but for a different threshold, or because two opposite variations of the same physiological change were seen for different thresholds. The studies from which these values were based on are not here referenced but they can be easily found in the aforementioned works.

Tissue	Physiological change	CEM 43 ℃ (min)	Species
Skin	Acute and minor changes	<20	Mouse
	Erythema and functional changes	112	Human
	Necrosis	288	Human
Bone	Resorption	16	Rabbit
	Density	45	Rabbit
CSF	Taurine, GABA and ion levels	0.78	Rabbit
Brain	BBB permeability	0.03 and 1.30	Rats
	Cerebral blood flow	0.03 and 16 (increase)	Humans Rats
		1 and 34 (decrease)	Rabbits Rats
	GABA, glycine and glutamate levels	0.115 and 1.290	Rats
	Metabolism	1.07	Rats
	CNS damage	2	Rats
	Coagulative necrosis, oedema and atrophied neurons	30	Monkey

In the case of TTFields the scalp is the tissue that heats up the most as it is the one closest to the transducers. For the skin, it was seen that for low values of CEM 43 ℃ ($<$ 20 min) only minor and acute changes occurred like superficial burns, which could be easily treated. Skin damage was observed for values higher than 20 minutes. Other studies also showed significant erythema for CEM 43 ℃ values as high as 112 minutes and variations at a functional level. The latter included an increase of the thresholds for cold

and warm detection, while heat and mechanical pain thresholds decreased returning to their basal state after four hours. Complete skin necrosis occurred for CEM 43 ℃ values higher than 288 minutes.

In the case of bone, there was one study that reported changes at the resorption level at 16 CEM 43 ℃. This is a natural process that occurs in the human body to control the calcium blood levels, but also to maintain and remodel bone's structure and integrity [74]. This phenomenon occurs due to the action of the osteoclasts and is compensated by the action of osteoblasts that create bone tissue. Studies with rabbits showed that heat can induce irreversible bone resorption for CEM 43 ℃ values as low as 16 minutes with the percentage of damage increasing for higher exposure times. Another *in-vivo* study made with rabbits showed that when the temperature of the femur was maintained around 43 ℃ for 45 minutes, more and denser bone deposition occurred after 3 weeks [71]. This indicates that hyperthermia might promote bone deposition and that it could be used in the regenerative process of some injuries.

Frosini [72] showed that when the rabbit body is subjected to heat stress at 0.78 CEM 43 ℃, CSF levels of two neurotransmitters, GABA (gamma-aminobutyric acid) and taurine, increased significantly compared to the basal levels to protect neurons and to decrease body temperature. As described by the author, some studies found that taurine and GABA can induce hypothermia through mechanisms like vasodilation, which can be a possible explanation for these observations. Other neurotransmitters such as aspartate and glutamate, whose action can lead to heat production, did not increase their concentration in this study. In the case of ions it was seen that sodium, magnesium and potassium concentrations did not change significantly but calcium's did. This can be explained by the fact that calcium also plays a role in down-regulating the human body temperature.

Contrary to what occurred with the CSF, there are several studies that investigated the impact of heat in the brain at a vascular and functional levels as well as in cell death. Although the thresholds varied between studies all of them showed an increase of the BBB permeability. The main function of the BBB is to control the components that pass from the systemic circulation to the brain and thereby to prevent the entrance of any molecule or bacteria that can be harmful. An increase of its permeability occurs under certain conditions like inflammation, injuries or stroke and can be dangerous to the patient if not quickly controlled. In some cases it might be desirable to temporarily increase it to facilitate drug delivery in certain treatments, as discussed previously. Not so consistent results were found for the cerebral blood flow. Two studies showed an increase on brain's blood irrigation for CEM 43 ℃ of 0.03 and 16 minutes, while two other papers reported an opposite effect for 1 and 34 CEM 43 ℃. Theoretically, an increase in brain's blood perfusion for higher temperatures would be expected, to remove heat more efficiently [75].

Cell death was observed in the brain for values around 2 CEM 43 ℃ in brain cells, nerves and glial cells. Heating also led to variations in the concentration of some neurotransmitters in the brain: the levels of GABA, glutamate and glycine increased for 0.115 CEM 43 ℃, but decreased for values above 1.29 CEM 43 ℃. GABA is the major inhibitory neurotransmitter in the CNS and has the capability of reducing neuronal excitability by binding to specific transmembrane receptors which lead to cell hyperpolarization. A deficiency of GABA can lead to insomnia, depression, hypertension, panic disorders, low growth of hormone levels, convulsions, amid other problems, while high levels of GABA are related to tiredness and affect cognitive thinking. Glutamate is the major excitatory neurotransmitter in the brain and is related to cognitive function, mem-

ory, learning, as well as other functions. While low levels of this neurotransmitter have been associated with some diseases such as autism, high levels of glutamate are related to other brain diseases, cognitive impairments and brain motor malfunction. Furthermore, traumatic brain injuries where an increase of the BBB permeability was seen led to more glutamate entering the brain, thus increasing its damage [76]. Glycine is an inhibitory neurotransmitter of the spinal cord and it participates in the processing of motor and sensory information. Changes related with an increased glycine concentration can lead to anxiousness, low mood, stress and immune issues.

Finally, changes in metabolism were also observed in some studies. Some of them include an increased activity of lactate dehydrogenase (LDH) and succinate dehydrogenase (SDH), as well as in ribonucleic acid (RNA) content in three different clusters of cells in the hypothalamus: supraoptic nucleus (that produces some neuropeptide hormones), paraventricular nucleus (that has an important role in the regulation of some autonomic functions), and median preoptic nucleus (involved in thermoregulation). It was seen that, for 1.07 CEM 43 ℃, metabolism had increased at least 20 times compared to the basal values, with lactate being the one whose levels augmented the most, reaching values 35 times higher on average. Regarding the concentration of lactate, pyruvate, glutamate and glycerol, another study showed an increase in these levels in the brain for increasing CEM 43 ℃. The choice to evaluate these specific metabolites is justified by the fact that their concentration in the extracellular compartment of the brain might be an important biomarker in oncology. In the study of Roslin et. al [77] higher glutamate levels were observed in necrotic tumors than in non-necrotic ones, although more investigation is needed to understand these observations. Glycerol levels were also higher in patients with necrotic tumors which can be explained by a degradation of cell-membrane glycerophospholipids. The fact that an increase of these components was observed with increasing CEM 43 ℃ suggests that for long exposures to hyperthermia tumor cells oxygenation might be compromised. Still in regard to the brain, Matsumi et al [78] performed a histological evaluation of monkeys' brain after exposing it to heat at different temperatures for a time period of 60 minutes. Their results showed the existence of an oedema in the white matter and atrophied neurons as well as coagulative necrosis of brain cells for a temperature of 44 ℃ or higher ($>$ 30 CEM 43 ℃). According to the authors, the brain oedema can be related with a BBB disregulation and can lead to an increase in intracranial pressure.

As noted by Dewhirst et al [69], the physiological changes in response to heat stress that were reported by the different authors may or may not be related to thermal damage. For example, an increase in the cerebral blood flow reflects a biophysical mechanism that helps to dissipate heat more efficiently when the brain is subjected to a thermal stimulus. Similarly, other effects reported in table 2.2 might also represent biological responses to heat stress.

2.2 Tissue heating during TTFields therapy

In this section, the temperature increases during TTFields are quantified through *in-silico* work and the thermal impact is predicted based on three different metrics: SAR, CEM 43 ℃ and maximum temperature variation.

In order to model a TTFields treatment based on the information described at the end of subsection 1.2.3, a realistic head model was used. This model is presented and described in detail in section 3.1 and it was the same one used in the MSc thesis [42] and

in the paper published with those results [43]. Briefly, it was built from MR images and divided into scalp, skull, CSF and brain. The latter consisted in grey matter (GM) plus white matter. The lateral ventricles were also segmented and were assumed to be filled with CSF. A spherical virtual lesion to mimic a glioblastoma was also added to the model and it was divided into a necrotic core surrounded by an active shell. This tumor was placed in the right hemisphere of the brain, totally embedded in the WM, and near the lateral ventricles (figure 3.1). The four arrays were also added to the model to mimic the Optune device (shown in figure 3.2). The first six minutes of treatment were simulated using COMSOL Multiphysics, which solves the relevant equations through the FEM. A detailed discussion of the software used and the electric and thermal equations is provided in sections 3.2 through 3.5. The simulation time was around 36 hours to compute.

2.2.1 The electric field in the head

As Optune is a current source, the 900 mA that are injected into each array are not equally divided by each transducer. Given that the array is an isopotential surface more current is injected at the four outer transducers and less at the central one due to a phenomenom known as edge effect [79] (figure 2.2). As the head is more resistive in the anterior-posterior (AP) direction, a higher potential difference between these two arrays is necessary to inject the same current compared to the left-right (LR) pair. To inject 900 mA the potential difference between the first two was 91.2 V, whereas for the second pair this value was 68.2 V. The higher the potential of the surface the more pronounced are the edge effects as seen in figure 2.2.

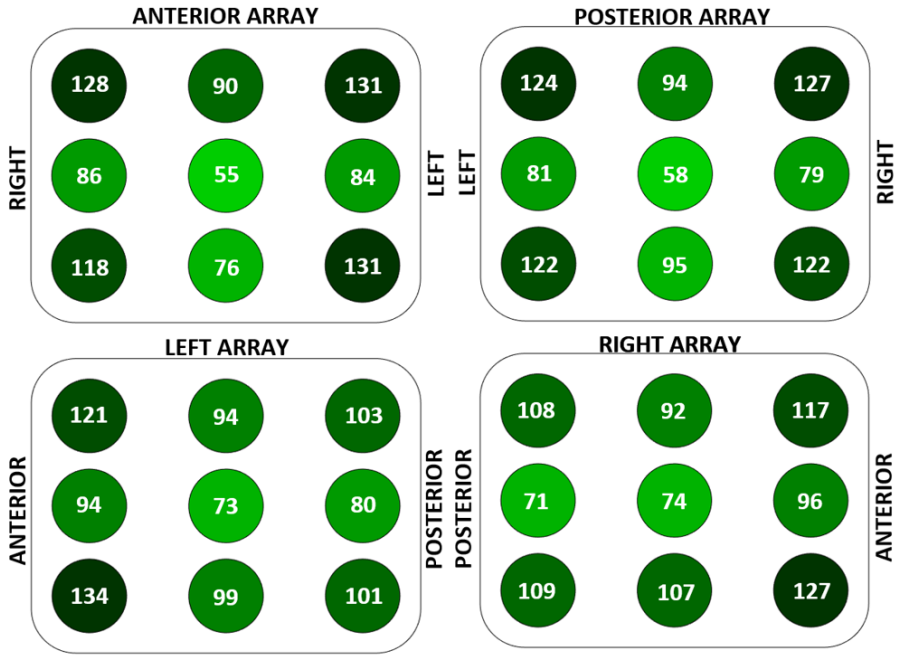

Figure 2.2: Amplitude of the current, in mA, injected into each transducer. Each array can be seen as an isopotential surface where the edge effects are evident as more current is injected in the outer transducers of each array and less in the central one. As the head is more resistive in the anterior/posterior direction, the potential difference between these two arrays was higher (91.2 V) than between the left and right arrays (68.2 V) and thus the edge effects were more pronounced. The sum of the current injected into each array might not yield exactly 900 mA due to the approximations made. Image taken from [80].

For the most superficial tissues, the heteregenous current injection seen in the previous figure is responsible for inducing a more pronounced non-uniform electric field distribution. The deepest the tissue, the less significant the edge effects become. The study of the EF distribution in the head can be divided into two components: the primary and the secondary EFs. The primary depends on the distance to the transducers, and on the dielectric properties of tissues. The closest to the arrays, the highest the EF values and the highest the electric conductivity of a tissue, the lowest the EF there. The secondary EF occurs in regions where the applied current is perpendicular to the interface of two tissues [81]. There is an accumulation of electric charges in those regions that depends only on the ratio of the electric conductivity between the two adjacent tissues and it is proportional to the strength of the normal component of the applied EF for purely resistive tissues. As discussed in subsection 3.3, this approximation holds at 200 kHz, which is the frequency Optune uses to treat GBM. Electric field maxima in the scalp, skull and CSF when 900 mA were injected in the AP pair was 46.9, 96.9 and 15.8 V/cm, respectively. For the complementary pair these values were 40.0, 155.5 and 4.3 V/cm. The values of the EF in the tumor are discussed in more detail below.

In figure 2.3 the EF in the brain is presented when 900 mA of current were injected in the AP (left column) and LR (right) pairs in an axial (upper row), saggital (middle), and coronal (lower) slices. The EF exceeds 1 V/cm over large areas in the brain as clearly seen. As discussed in Miranda et al [81], the EF distribution is slightly more uniform in the AP direction as the effect of the lateral ventricles, filled with CSF, is less marked and due to the higher coverage of the head's cross-section when current is injected in that pair. The secondary EF is also well observed in this figure when current was injected in the LR pair as the magnitude was enhanced in regions close to the lateral ventricles due to the difference in the electric conductivities of the white matter (σ_{WM}=0.12 S/m) and CSF (σ_{CSF}=1.79 S/m).

As mentioned in subsection 1.2.2, for EF intensities above 1 V/cm the number of tumoral cells affected by TTFields increases significantly. The insets in figure 2.4 shows the EF distribution in the tumor's necrotic core and active shell. As it is noticeable, the regions in which the threshold of 1 V/cm was surpassed in the active shell was different for both pairs. Another important effect that is visible in this figure is the impact of the distance between the tumor and the arrays. As the tumor is located midway between the anterior and posterior pairs, the EF was weaker there compared to when current was injected in the LR pair given that the tumor is relatively close to the right array. In the necrotic core, the EF was low because its electric conductivity is high ($\sigma_{necrotic\,core}$= 1 S/m) compared to the active shell and brain tissue (table 4.1).

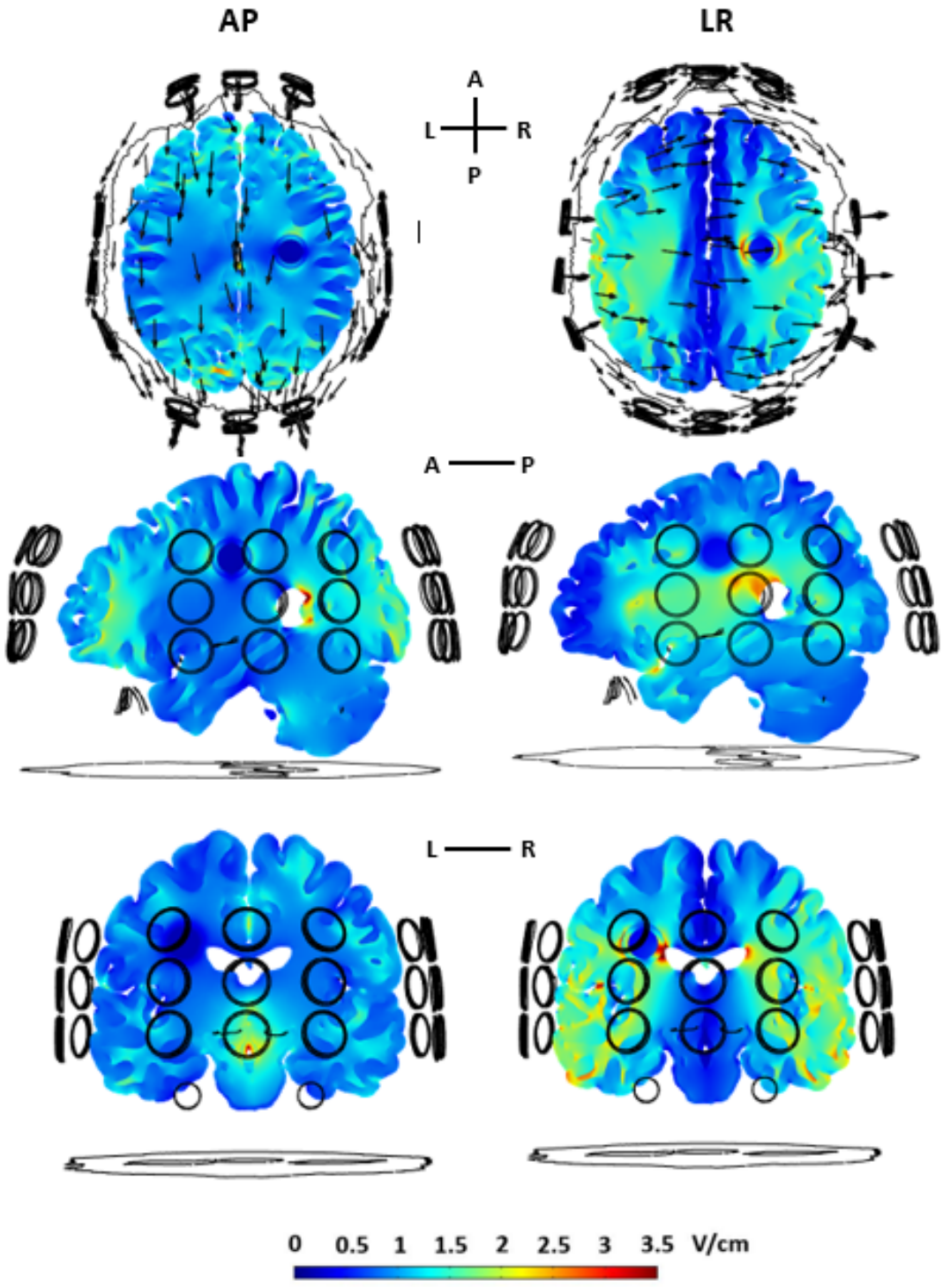

Figure 2.3: Electric field distribution in the brain and tumor when 900 mA were injected into the AP (left column) and LR (right) pairs. Three different views are presented: axial (first row), saggital (second), and coronal (third). In the first, the arrows indicate the direction of the alternating electric field. The size of these arrows is the same for both cases and it is not proportional to the current that passes through each region of the brain and tumor. The secondary EF is observed clearly by the red color in the coronal slice on the right (LR pair active) when current goes from the WM to the ventricles (not repreented), filled with CSF. As the ratio of the electric conductivities between these two tissues was high, a significant acummulation of charges occurred at this interface. The circles represent the regions where the transducers were placed on scalp's surface. Values greater than 3.5 V/cm are colored in dark red.

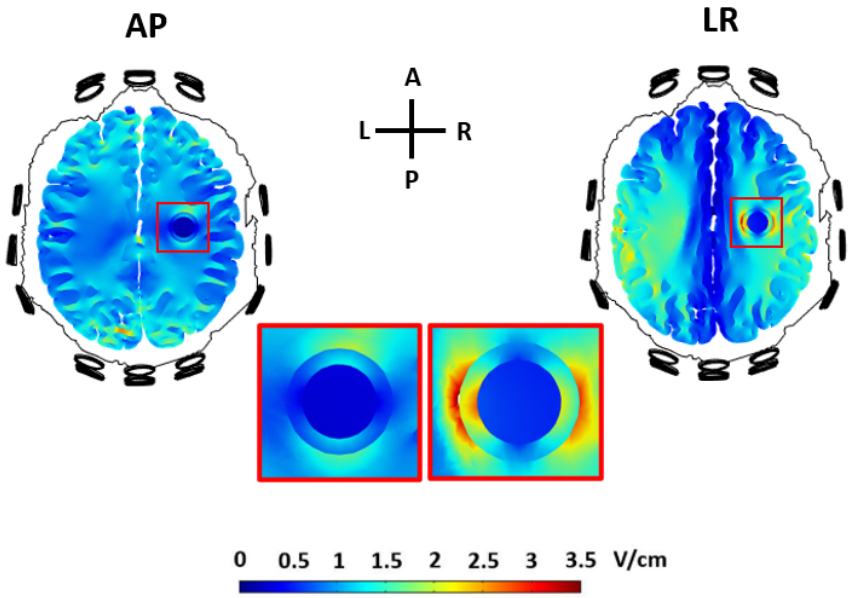

Figure 2.4: Axial view of the electric field distribution in the brain and tumor when 900 mA were injected into the AP (left) and LR (right) pairs. The insets show the EF in the necrotic core (inner circle) and in the active tumor shell (outer circle). As the electric conductivity of the first is high compared to the second, the EF was lower there. The regions of the active tumor that reached the therapeutic threshold of 1 V/cm were different for both pairs. Due to tumor's position, the EF in the LR direction was higher than when current was injected in the AP's. Values greater than 3.5 V/cm are colored in dark red.

To help quantify treatment effectiveness, Wenger et al [82] defined a metric, named as the above-threshold volume (ATV), that evaluates how much of the active tumor volume is above 1 V/cm (ATV1). Due to the reasons mentioned above, the ATV1 for each pair was very different and it yielded 13% for the AP pair and 72% for LR's. This means that the latter pair is contributing more for treatment effectiveness than the former.

2.2.2 The duty cycle

The current injected in this study was equal to what was assumed that was considered in a real treatment where 900 mA are injected into each array pair alternately with a switching time of one second. It was assumed that the temperature of the transducers should be kept below 41 ℃ to avoid any thermal harm to the patient. In this work, the critical temperature was considered to be 40.4 ℃ as it corresponded to having around 5% of the transducer volume above 41 ℃, which was assumed to be the volume occupied by the thermistor. At this point, there was no additional information available regarding Optune's temperature sensor dimensions. This 5% corresponded to having a sensor with an area of 12.7 mm^2 and a thickness of 1 mm, which is within the range of the commercial sensors available in the market (e.g.: [83, 84]).

The temporal evolution of the average temperature of all 18 transducers of the anterior-posterior pair is shown in figure 2.5, whereas the same analysis for the left-right pair is presented in figure 2.6.

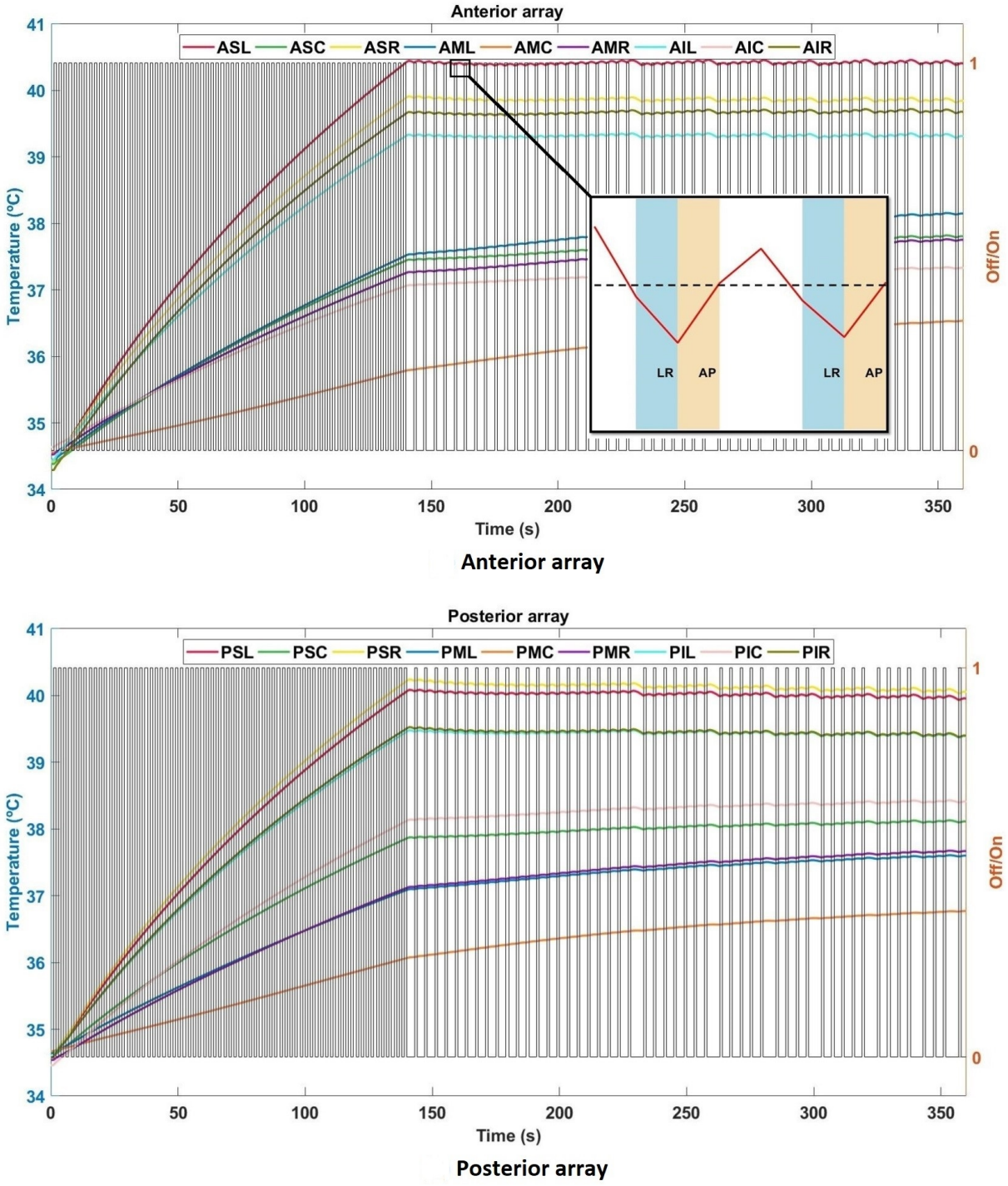

Figure 2.5: Temporal variation of the average temperature (left y-axis) of the 18 transducers that compose the anterior (above) and posterior (below) arrays. Each transducer is identified by a three letter combination. The first letter indicates the array (A: Anterior; P: Posterior), the second represents the row within the array (S: Superior; M: Middle; I: Inferior) and the third represents the position within the row (L: Left; C: Central; R: Right). These temperature variations suggest an intermittent operation mode of Optune. When the device is on (1 in the right y-axis, represented by the vertical bars) it means that current was injected in the AP pair. This occurred when the average temperature of each of the 18 transducers from the AP and LR pairs was not higher than 40.4 ℃. The temperature variation of the MST during intermittent operation is shown in the inset, with additional information concerning current injection in the perpendicular pair as well. In this inset, the red line represents the temperature variation of the MST and the black dashed line the 40.4 ℃. The AP and LR bars mean that current was injected in that respective direction for one second. The absence of these bars means that current was not being injected. These periods lasted between 3 to 4 seconds. Image taken from [43].

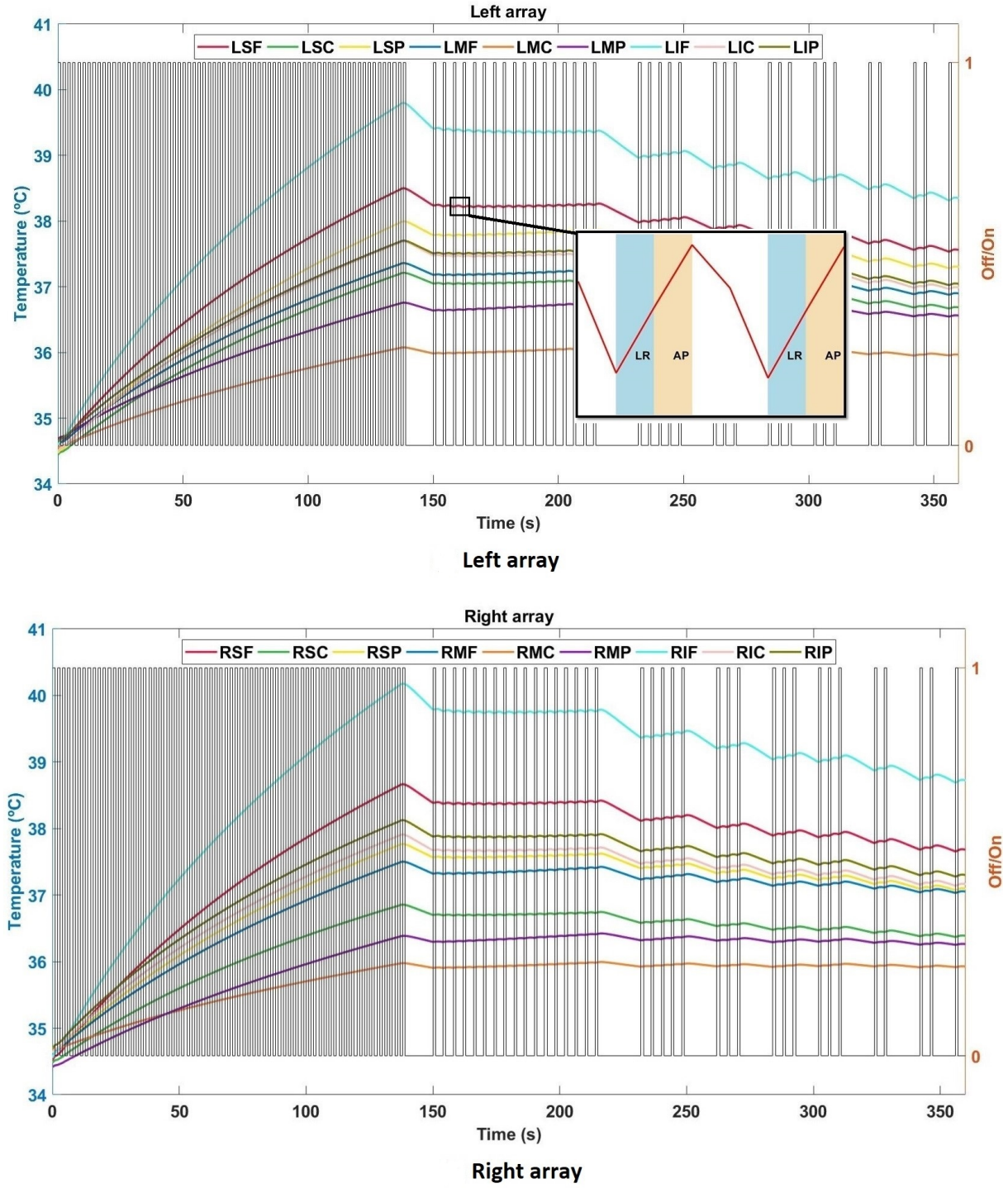

Figure 2.6: Temporal variation of the average temperature (left y-axis) of the 18 transducers that compose the left (above) and right (below) arrays. Each transducer is identified by a three letter combination. The first letter indicates the array (L: Left; R: Right), the second represents the row within the array (S: Superior; M: Middle; I: Inferior) and the third represents the position within the row (F: Frontal; C: Central; P: Posterior). These temperature variations suggest an intermittent operation mode of Optune. When the device is on (1 in the right y-axis, represented by the vertical bars) it means that current was injected in the LR pair. The latter occurred when the average temperature of each of the 18 transducers from the AP and LR pairs was not higher than 40.4 ºC. The temperature variation of one transducer from the LR pair during intermittent operation is shown in the inset, with additional information concerning current injection in the perpendicular pair as well. This inset corresponds to the same time interval as the one of the previous figure. In this inset, the red line represents the temperature variation of the transducer LSF. The AP and LR bars mean that current was injected in that respective direction for one second. The absence of these bars means that current was not being injected. These periods lasted between 3 to 4 seconds. Image taken from [43].

At the beginning of the simulation, the head was in thermal equilibrium with the environment at 24 ℃. Based on these plots, a couple of conclusions can be drawn. It took around 150 seconds of alternate application of the EFs for a transducer to first reach 40.4 ℃. In this case, it was the one placed in the anterior array, superior row, left side (ASL) (figure 2.5). After this threshold was surpassed, current was completely shutdown in both directions. It then took between 3 to 4 seconds for the temperature of this transducer to drop down again to a value below 40.4 ℃. After that, current injection was resumed and it took 2 seconds of alternate application of the fields (1 s AP and 1 s LR) for its temperature to once again surpass the critical value. As this was the only transducer whose temperature controlled current injection, it was named the most significant transducer (MST). As it can be seen in figures 2.5 and 2.6, the temperature of the other transducers remained practically constant and equal to the value that they reached when current was first shut down, as it occurred for the AP pair, or it decreased throughout time, as it happened for the LR pair. These results indicate that Optune works in an intermittent operating mode due to the thermal restrictions.

The importance of this current control is discussed in detail in Gentilal et al [43], in which it was shown that after just 6 minutes of alternate application of the EFs the temperature of 17 out of the 36 transducers already surpassed the 40.4 ℃ when no temperature control was implemented.

In this head model, the MST was one of the transducers in which more current was injected, thus increasing the Joule effect underneath it, which explains why it was the one that heated up quicker (figure 2.2). In other head models and for other array layouts, the MST could be one of the other transducers.

Another important result that can be drawn from the analysis of figures 2.5 and 2.6 is the time that each pair is effectively delivering current. For this 6-minute simulation and after the first current shutdown at around t=150 seconds, current was applied in the AP pair 47% of the maximum time it could have been (i.e., $ON_{AP} = 0.47$), while this value decreased to around 30% for the LR pair ($ON_{LR} = 0.30$). This means that, on average, Optune is effectively injecting current only 39% ($ON = 0.39$) of the time that the device is being used by the patient due to the thermal restrictions. This result might explain why such a high daily compliance is needed.

Based on the results of the previous subsection, it is possible to fine-tune the calculation of treatment effectiveness by adding information about how much time the fields are effectively being applied. Thus, the effective ATV1 ($ATV1_{eff}$) is defined as:

$$ATV1_{eff}(\%) = \frac{1}{2}\big(ON_{AP}\, ATV1_{AP}(\%) + ON_{LR}\, ATV1_{LR}(\%)\big) \tag{2.3}$$

where ON_X is the fraction of time that pair X is injecting current and the $ATV1_X$ the respective percentage of active's tumor volume above 1 V/cm. The factor of 1/2 is a normalization factor so the maximum is set to 100%.

For the data obtained and discussed previously this metric yielded:

$$ATV1_{eff}(\%) = \frac{1}{2}\big(0.47 \times 13\% + 0.30 \times 72\%\big) = 13.9\%$$

This metric combines information about the electric field in the tumor and the time

that current is injected into a single value and thus it might represent a more accurate quantity to evaluate treatment effectiveness than just the ATV1. The effective ATV1 is also useful to investigate and compare different treatment methodologies. Based on what is described in Gentilal et al [80], there are several ways to improve TTFields delivery:

1. Decreasing the injected by a factor of $1/\sqrt{2}$ (I $\approx$ 637 mA), but activating both arrays simultaneously increases the time that the patient is under treatment to 70%. As the injected current is reduced, the ATV1 in the active tumor was only 45%, which yielded an $ATV1_{eff}$ of 15.8%. Although this value is higher than the 13.9% obtained for Optune's standard operating mode, current is only injected in one direction because the EF is a vector quantity, and thus the net field is oriented at approximately 45°relative to the standard AP and LR directions. As discussed previously, injecting current in more than one direction can significantly improve treatment outcomes [16]. One possible way to do this while still injecting current in both pairs at the same time is to intentionally change the phase of the injected current so that more electric field directions are achieved;

2. Increasing the switching time between the two pairs to 2 seconds increases the $ATV1_{eff}$ to 17.5% (ON_{AP}=0.47 and ON_{LR}=0.40). Although this leads to a higher temperature increase of the MST and theoretically to longer periods in which the device has to be shutdown, the cooling rate is also augmented because it depends on the temperature difference with the environment. Thus, the device can apply current during more time. However, it is important to note that switching times different from one second might not be the most suitable to affect the mitotic process of GBM cells as seen in the *in-vitro* work by Kirson et al [16];

3. Having two independent current controllers significantly improves the results. This means that current is still injected alternately with a switching time of one second but there can be two MSTs, one for each pair. If one of them reaches 40.4 ℃, current can still be injected in the perpendicular pair until its MST reaches the critical limit. This operating mode was specially useful for the model and layout used in this work as current could be injected in the LR pair pratically the same amount of time that it was in the AP's (ON_{AP} = 0.47 and ON_{LR}=0.46). Under these conditions, the effective ATV1 yielded 19.6%.

4. Having a current controller for each transducer also increased the time that the fields were applied. The edge effects shown in figure 2.2 might be avoided if the same current, 100 mA, is injected in all transducers of the same array. Under these conditions, the MST changed and current was injected in the AP pair 46% of the time and in the LR's 42%. The electric field in the tumor was not affected and thus the $ATV1_{eff}$ yielded 18.0%;

These studies represent possible alterations that can be incorporated in the Optune device to enhance treatment outcomes. Although not all of them are easy to implement (e.g., having a current controller for each transducer might imply redesigning the whole array), they all led to a similar temperature distribution in tissues and transducers.

2.2.3 Temperature increases

In the absence of current control the temperature of the transducers would quickly rise and lead to severe thermal damage to the patient. After just six minutes of application

of the EFs the scalp would reach 47.5 ℃, the skull 42 ℃, the CSF 41 ℃ and the brain 39.2 ℃. These values would increase even more if more treatment time was simulated. However, as shown in figures 2.5 and 2.6, the control implemented in the Optune system sets a maximum temperature value for the transducers, and consequently for tissues, thus ensuring patient's safety. Six minutes after the treatment had started tissues temperature is already very close to a steady-state, as reported in Gentilal et al [43]. The temperature distribution on each tissue surface at the end of the simulation with current control is shown in figure 2.7.

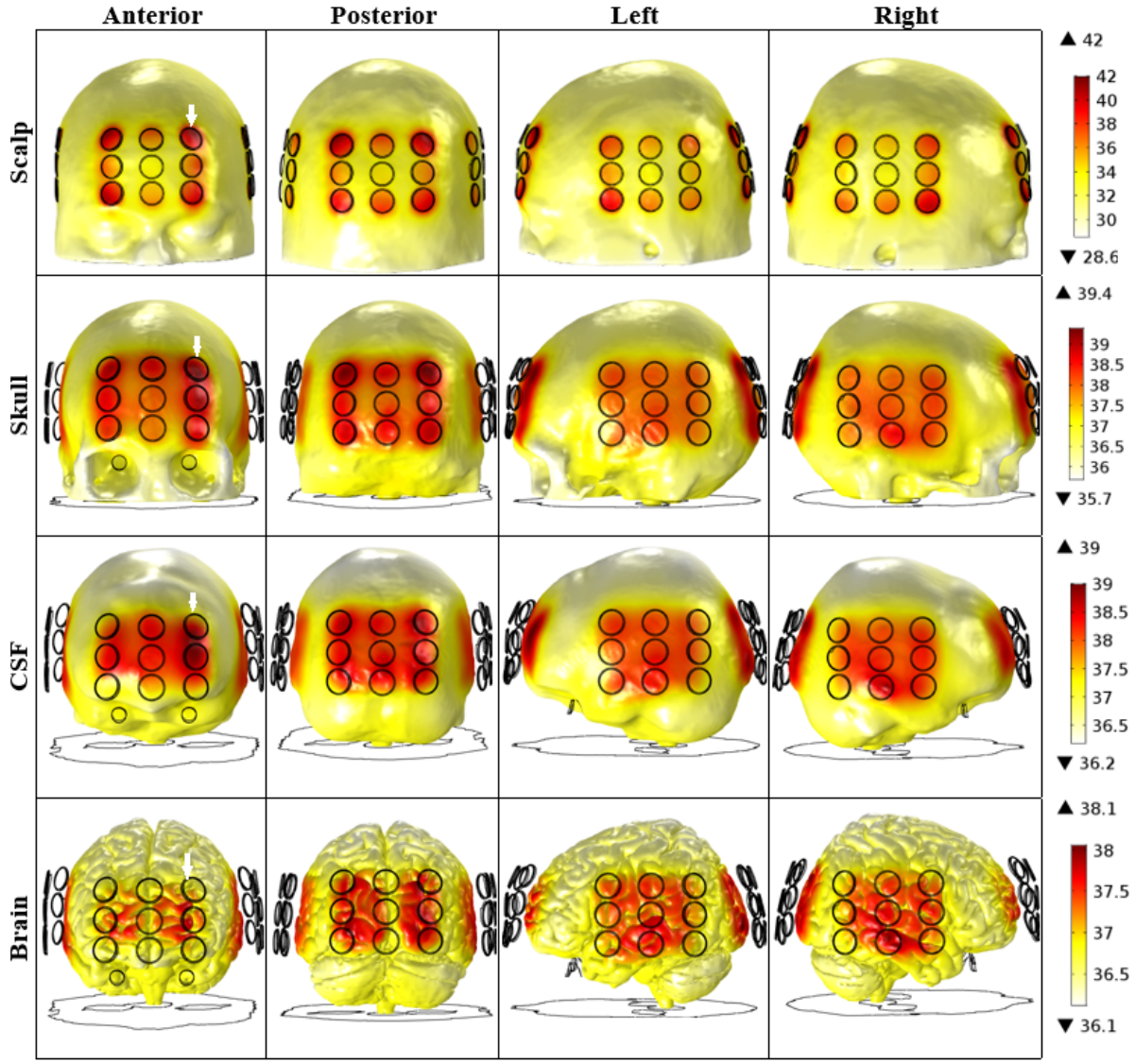

Figure 2.7: Temperature distribution, from four different perspectives, on each tissue surface at the end of the simulation with current control (t=360 seconds). The temperature increases occurred mainly underneath the arrays as clearly seen by the regions in red. More specifically, temperature maxima in each tissue was reached underneath the region where the MST was placed (white arrow, first column). Each circle represents the position of one transducer. First row: scalp; Second row: skull; Third row: CSF; Fourth row: Brain. In the latter, the maximum temperature was reached at the GM surface. The maximum temperature reached on the scalp was higher than Optune's threshold for current shutdown, 40.4 ℃, as there is no Joule effect in the transducers. Instead, they heat up by conduction from the scalp and gel. Scales are different for each row. All values are in ℃.

The temperature increases were very limited and they occurred mainly on the surface of each tissue as those were the regions where the EF reached its maximum and consequently where the Joule effect was the highest. The previous figure shows a localised heating when TTFields are applied, particularly on the scalp, as indicated by the regions colored in red. In this tissue, the edge effects led to a higher temperature increase underneath the outer transducers. As current flowed into the head, the EF became more homogeneous underneath the array leading to a more uniform Joule heating. The maximum temperature at end of the simulation on the scalp was 42 ℃, on the skull 39.4 ℃, on the CSF 39 ℃ and on the brain 38.1 ℃. The maximum temperature reached by the scalp was higher than Optune's threshold of 40.4 ℃ for current shutdown. This is explained by the fact that there is no Joule effect in the transducers as they are capacitively coupled to the scalp (i.e., they are not electric conductors). Instead, their temperature increased by thermal conduction from gel and scalp. The heat pathways are discussed in more detail in subsection 4.4.2 using quantitative data.

The variation of the temperature of the tumor is not shown as it only increased by 0.1 ℃ compared to its initial value. As discussed in subsection 1.2.1, the study by Berkelmann et al [23] suggested that one possible mechanism of action of TTFields is a very local, but significant increase of SAR at the cleavage furrow that might be enough to interfere with cell division. This hypothesis can not be corroborated or disproved by the data presented here as the simulations were not performed at a cellular level. On the other hand, as discussed in subsection 2.1.3, hyperthermia is used either to sensitise tumoral cells to the action of chemotherapy and radiation therapy by heating them (whole-body hyperthermia) or by overheating these cells to kill or damage them (regional and local hyperthermia). Based on the increase of 0.1 ℃ seen in the simulation, the second could not explain TTFields efficacy as the necessary temperature variation for those types of hyperthermia to be effective were not observed (figure 2.1). As for the first, more studies are needed to investigate if such a small, but prolonged, temperature increase is sufficient to sensitise cells. These studies might help to corroborate the conclusions by Giladi et al [24] and Chang et al [25] that were discussed in subsection 1.2.1.

As mentioned, the maximum temperature in each tissue was reached at its surface and it quickly dropped with depth. In figure 2.8 the regions that reached the percentile 90% or higher of the temperature distribution in each tissue at the end of the simulation are represented in red in two slices, one saggital (S1) and one coronal (C2). This percentile was calculated based on the maximum temperature reached in each one of these slices. In the coronal slice, a significant area of the skull reached this percentile as its thickness was small.

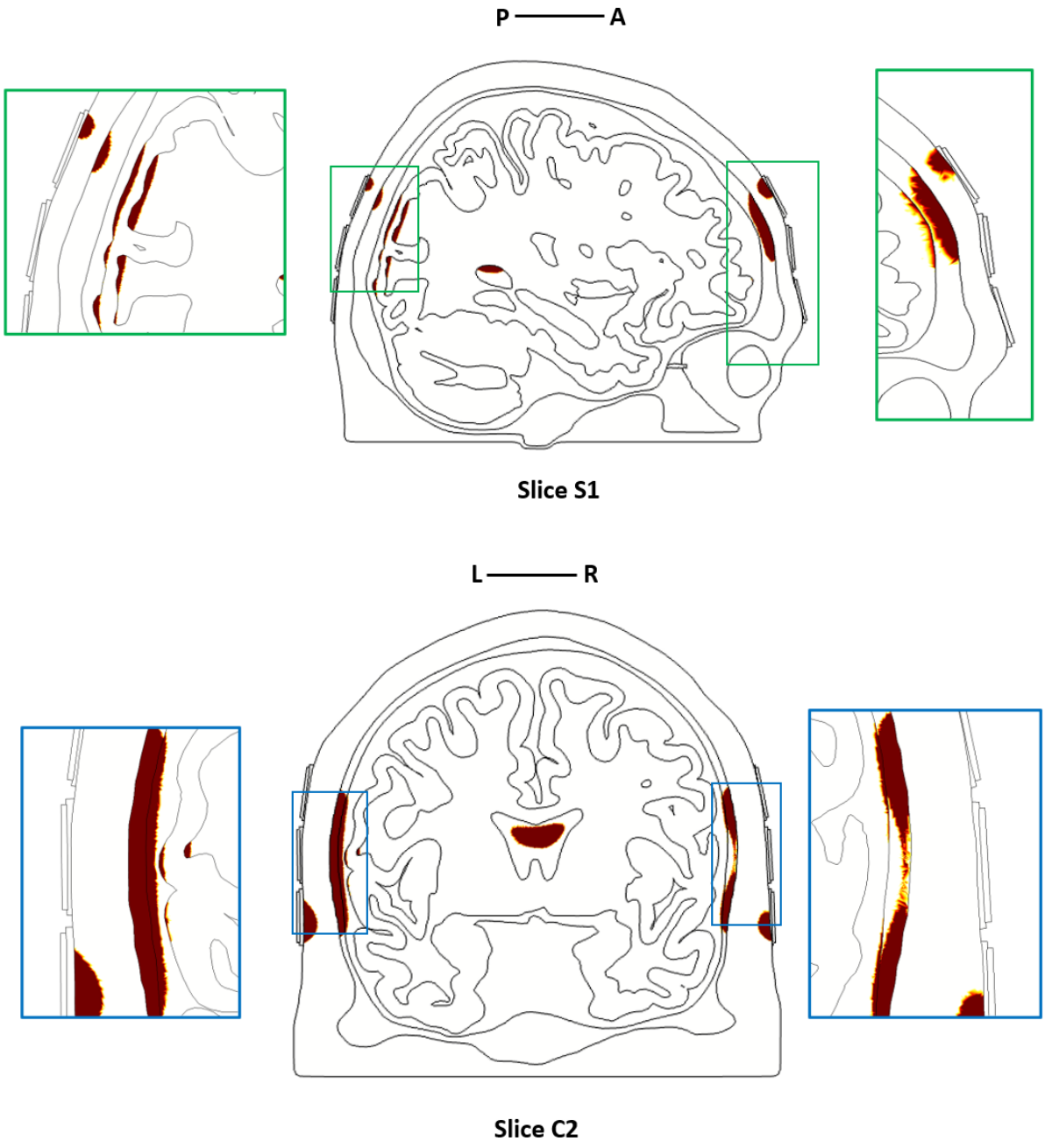

Figure 2.8: Regions that reached the percentile 90% or higher of the temperature distribution in each tissue at the end of the simulation (t=6 minutes). In each tissue, the temperature increases occurred underneath the arrays and were very superficial, as EF maxima was also reached there, and quickly decreased with depth. This percentile was calculated based on the maximum temperature reached in each one of these slices. The temperature increases in the lateral ventricles (not shown in the insets) also occurred in the regions underneath the arrays.

In figure 2.9 the temperature variation in the brain, which was the tissue that heated up the least, but the one in which most physiological changes are expected as discussed in the next subsection, is presented through four different slices. Two of these slices are the same ones considered in the previous figure.

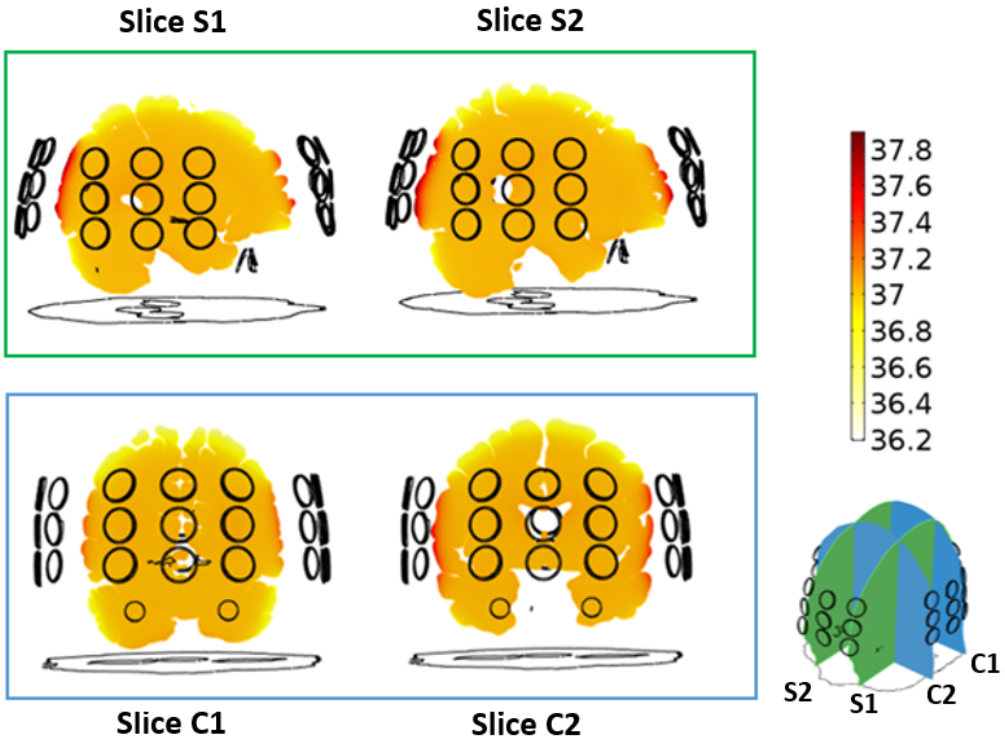

Figure 2.9: Temperature variation in the brain (GM+WM) at the end of the simulation (t=360 seconds) in two saggital (upper row) and two coronal (lower) slices. Temperature maxima, colored in red, were very superficial and quickly dropped with depth. The inset on the bottom right shows the relative position of these slices. Temperature scale is in ℃.

2.2.4 Prediction of the thermal impact

2.2.4.1 SAR

As TTFields are applied locally, the values of SAR were calculated following FDA and IEC guidelines for local exposure. In both cases, the point where the maximum electric field was reached in the head was retrieved and a cube that contained it was considered for the calculations. As the skull is the one with the lowest electric conductivity (see standard values, table 4.1), it was also there where the maximum EF was reached. As FDA guidelines are for one gram of tissue and IEC's for 10 grams, the volume of interest was different for both. For the first, a cube with a length of 10 mm was defined, which included scalp, skull, CSF and GM. For the second, this length was roughly 21 mm and it also included WM. A maximum SAR of 224 W/kg was obtained following FDA guidelines, and of 136 W/kg following IEC's. These two values are above the thresholds of 8 W/kg (FDA limit) and 20 W/kg (IEC limit, level 1) presented in table 2.1. This does not necessarily mean that TTFields are not safe for the patient, because, as discussed in subsection 2.1.2, there are several inconsistencies when SAR is used as surrogate for thermal impact. The need of redefining thresholds was further corroborated by Adibzadeh et al [85] who concluded that for the muscle SAR values as high as thirty times the ones defined by the international agencies might not cause significant thermal harm. If SAR is to be used to evaluate TTFields then the limits should be adjusted to reflect a more effective compromise between efficacy, which is quantified in terms of EF and should be at least 1 V/cm, and safety.

2.2.4.2 CEM 43 ℃

The very local increases makes it difficult to predict TTFields thermal impact based on volume temperature variations. As the temperature increases were very superficial and they occurred mainly underneath the transducers, in this work the average tissue temperature variations were evaluated inside a cylinder defined by the MST. This cylinder base had the area of the transducer, and the cylinder's axis was parallel to the transducer surface's normal. The CEM 43 ℃ for each tissue was then calculated based on this temperature. As only six minutes were simulated, the temperature at the end of the simulation was assumed to be constant for the remaining necessary time to complete the minimum daily compliance of 18 hours. As Optune was working in an intermittent operating mode 2.5 minutes after current injection started (figures 2.5 and 2.6), by the end of the first 6 minutes of treatment tissues were already very close to their steady-state temperature, which validates this approach as discussed in Gentilal et al [43]. The values obtained (second column, table 2.3) were then compared with the ones reported in table 2.2.

Table 2.3: Calculated CEM 43 ℃ values (second column) for each tissue inside a cylinder defined by the MST and comparison with the thresholds defined in the literature (third column) and for which some physiological change was observed (fourth column). The values presented in the second column were calculated for one day of treatment with the minimum compliance (18 hours) by considering that the temperature of each tissue at the end of the simulation (t = 6 minutes) remained constant.

Tissue	CEM 43 ℃ (min) Simulation	CEM 43 ℃ (min) Literature	Physiological change
Scalp	12.60	< 20	Acute and minor changes
Skull	3.47	–	–
CSF	0.45	–	–
Brain	0.33	0.03 and 1.30	BBB permeability increase
		0.03	Increase in cerebral blood flow
		1	Decrease in cerebral blood flow
		0.115	Increase on GABA, glycine and glutamate levels

Based on the results above, physiological changes due to the temperature increases were only predicted to occur in the scalp and brain. In the first, minor and acute changes like superficial burns were predicted. These were indeed reported to occur in patients treated with TTFields but only as a result of a misuse of the Optune device and not due to the technique itself [37, 38]. As reported by Mrugala et al [33], the most common side-effect in regard to temperature was the heat sensation that patients felt, which was not enough to cause scalp burns. In the large majority of patients, the most common acute and minor effect that occurred at the scalp level was dermatitis, although it was attributed to the use of the gel and not to heat. The values of CEM 43 ℃ presented in table 2.3 also showed that the threshold for significant skin erythema (112 min, table 2.2) was far from being reached. However, as reported by Lacouture et al [37, 38] minor skin erythema occurred in patients due to the adhesive tape, hydrogel or even as a combination of other factors such as high ambient temperature, increased humidity, excessive sweating,

and inappropriate patient sleeping position while using the device.

The physiological changes that were predicted for the brain included an increase of the BBB permeability. The latter was indeed suggested to be one of the possible mechanisms of action of TTFields by Chang et al [25], as explained in subsection 1.2.1, although the possibility of attributing those increases to heat was not discussed by the authors. In the case that the permeability is indeed increased, whether as a result of the temperature or not, it could allow the use of more powerful drugs when TTFields are applied as a concomitant treatment with chemotherapy. In terms of cerebral blood flow, the value of CEM 43 ℃ is within two thresholds for which two opposite variations were predicted. For TTFields in particular, an increase in blood perfusion in the brain would be expected to dissipate heat more efficiently as this is the main mechanism for this tissue to cool down, as discussed in detail in subsection 4.4.2 (chapter 4). The two contradictory effects expected for this value of CEM 43 ℃ are most likely due to the different conditions in which the studies to draw them were performed. Lastly, the results obtained also predict a local increase in the level of some neurotransmitters such as GABA, glycine and glutamate. Among the adverse events in patients with recurrent GBM treated with TTFields in PRiDe [33], 10.4% of them showed a neurological disorder, 8.9% had a seizure, 4.7% experienced pain and discomfort, 2.5% fatigue and 1.4% weakness. These effects might be related to this possible variation of neurotransmitter levels, although in the studies by Stupp et al [8, 17], both groups of patients treated with and without TTFields reported some of these effects and there was no statistical difference between them. Most likely, these effects are related to the disease itself and not with the therapy.

In the skull and CSF, the thresholds reported in the literature were not reached and thus changes in the bone density and resorption for the first and increased levels of ions, taurine and GABA for the second were not predicted to occur when applying TTFields.

It is important to note that all the calculations based on CEM 43 ℃ are only for one day of treatment. The fact that TTFields should be applied every day and for more than 18 hours might lead to a cumulative effect and consequently to an increase in the values predicted for this metric that might surpass the thresholds presented in table 2.2. The development of thermotolerance throughout treatment was also not accounted for but it might play a significant role.

2.2.4.3 Temperature variation

The third and final criterion used to predict the thermal impact of TTFields was the temperature variation. As shown in figure 2.7, after the first six minutes of treatment the scalp reached 42 ℃, the skull 39.4 ℃, the CSF 39 ℃ and the brain 38.1 ℃. These values are below the threshold of 45 ℃, which is the temperature at which protein and lipid denaturation starts to occur [75]. The maximum temperature reached on scalp's surface was also below the 44 ℃ reported by Moritz and Henriques [86] to cause skin burns for long exposures. The brain was the only tissue in which physyiological changes were predicted based on the temperature variation observed (+2 ℃). These include an increase of the cerebral metabolic rate of oxygen and of blood flow, which were reported to occur by different authors [87, 88]. As mentioned before, variations in these two mechanisms occur as a biophysical response to a heat stimulus and are not necessarily a side-effect [75]. Additionally, the studies by Volgushev et al [89, 90] showed that temperature variations can temporarily change the synaptic transmission in the neocortex and increase the probability of neurotransmitter release at the synapses. These two effects might be

related with what was discussed in the CEM 43 ℃ analysis concerning the variations in the levels of GABA, glycine and glutamate in the brain.

2.2.4.4 *In-silico* predictions vs. reports from clinical trials

Most of the predictions discussed above were not corroborated by what was reported in the EF-11 [8] and EF-14 [17] clinical trials. Some of the hypotheses that could explain this discrepancy include:

1. These changes do not occur during TTFields therapy: the conclusions drawn from the literature only apply to the conditions and techniques for which those specific studies were performed. This means that the way tissues heat up in MRI and hyperthermia can not be compared with the temperature increases that occur when TTFields are applied. In this case, the thresholds used in this work might not be valid and further investigation is needed in order to evaluate which physiological changes occur and how to measure them. Ideally, the thresholds should be obtained based on experiments made in humans and for exposure times that are representative of the compliance that is needed for this technique;

2. These changes do occur but are negligible: given that the temperature variations are not very high, the physiological effects predicted are only slight and can not be measured or their impact is so small that side-effects are not discernible. An additional factor that might contribute to this hypothesis has to do with biophysical changes, such as an increase in the basal blood perfusion, that could occur due to the high daily compliance and that might attenuate the temperature variations;

3. These changes do occur but were not measured: the biomarkers sensitive to the changes reported throughout this chapter were not acquired. In some cases, direct measurements can also be used to investigate this hypothesis. For instance, there are a handful of different methods to measure the cerebral blood flow (e.g.: [91]), although the approach taken and the best conditions in which it should be performed still needs to be investigated. Other studies already reported the physiological changes predicted here, such as an increase of the BBB permeability, but their cause was not attributed directly to the temperature increases;

4. These are long-term changes and are masked by the patient's health condition: these possible side-effects might not occur on the first months of treatment and only manifest themselves after some time. As glioblastoma is a fast-growing tumor, it is known that patients with this disease quickly lose their quality of life and experience several health problems. Thus, some of these physiological changes might occur, but they were not directly attributed to the temperature increases but rather to the disease;

5. The high daily compliance leads to a development of thermotolerance by cells: as the daily treatment compliance is very high, cells might become less sensitive to temperature variations and thus the thresholds to observe the physiological changes might increase and not be reached. A temporary increase of cells thermotolerance was already reported to occur by Sapareto and Dewey [68], although its duration for exposure times as high as the ones needed for TTFields was not investigated yet;

6. The predictions made are not accurate: the model used, its implementation and/or the metrics considered do not accurately mimic a real case scenario and thus the conclusions drawn are not correct due to a possible overestimation of the temperature distribution;

In this PhD thesis, the last hypothesis is investigated by improving the predictions made in different ways. In chapter 3 the assumptions made to drawn the conclusions presented in this chapter are discussed in detail. In chapters 4, 5 and 6, the accuracy of the model and of the predictions is tested and improved. In chapter 7 a detailed discussion of how to improve TTFields modelling based on information provided by Novocure is made and it is implemented in chapter 8 using a simplified head model. In the same chapter, different metrics to evaluate TTFields effectiveness are calculated and compared with the ones used in chapter 2. All these results are then considered in chapter 9, where, among other aspects, a more accurate prediction of the thermal impact is performed once again. Due to the limitations of the SAR and CEM 43 ℃, whenever the thermal safety and thermal impact are predicted only the absolute temperature variation will be used as a criterion. As most of the physiological changes are predicted to occur in the brain and given the fact that most of these effects are the same regardless of using the CEM 43 ℃ or the temperature increases as a metric, this choice should not affect the conclusions of the studies performed.

Chapter 3

General methods: Modelling TTFields

The study of Tumor Treating Fields is typically made through *in-silico* studies as it is not possible to non-invasively measure the electric field and temperature distributions inside the human head. The accuracy of the results is intrinsically related not only to an accurate representation of the geometry of the head, but also to the equations used to represent the physical processes of interest. In the large majority of TTFields computational studies, the first is addressed by using realistic head models (RHMs) that are built based on MR images. As for the second, the most general way to represent how electromagnetic radiation and matter interact is through Maxwell's equations. Under the conditions in which TTFields are applied, the electroquasistatic (EQS) approximation is valid, as discussed in more detail in appendix A. Thus, Laplace's equation can be used to calculate the electric field distribution in the head. The temperature distribution can then be predicted using Pennes' equation.

3.1 The realistic head model

Throughout this thesis, the same realistic head model was used. It was not built specifically for this project as the first studies performed with it were to predict the electric field distribution in the cortex during transcanial current stimulation (tCS). As described in detail in Miranda et al [92], this model was created using MR images available for the single-subject template Colin27 and provided by Brainweb. Based on the datasets available, T1 and proton density images, the relevant tissues for that work were segmented. Both these datasets were already aligned to the Montreal neurological institute (MNI) stereotaxic space using FSL FLIRT with voxel dimensions of 1x1x1 mm^3. The segmentation was performed using Brainsuite where T1 images were used to segment the CSF and the brain, which was divided into grey matter and white matter, whereas proton density images were used to segment the scalp and the skull. After the segmentation was completed, surface meshes were obtained and were then imported into Mimics where small irregularities in the CSF outer surface were smoothed out and additional detail was added manually. More specifically, the lateral ventricles were segmented by thresholding the data of the WM. Figure 3.1 shows the tissues that composed the model.

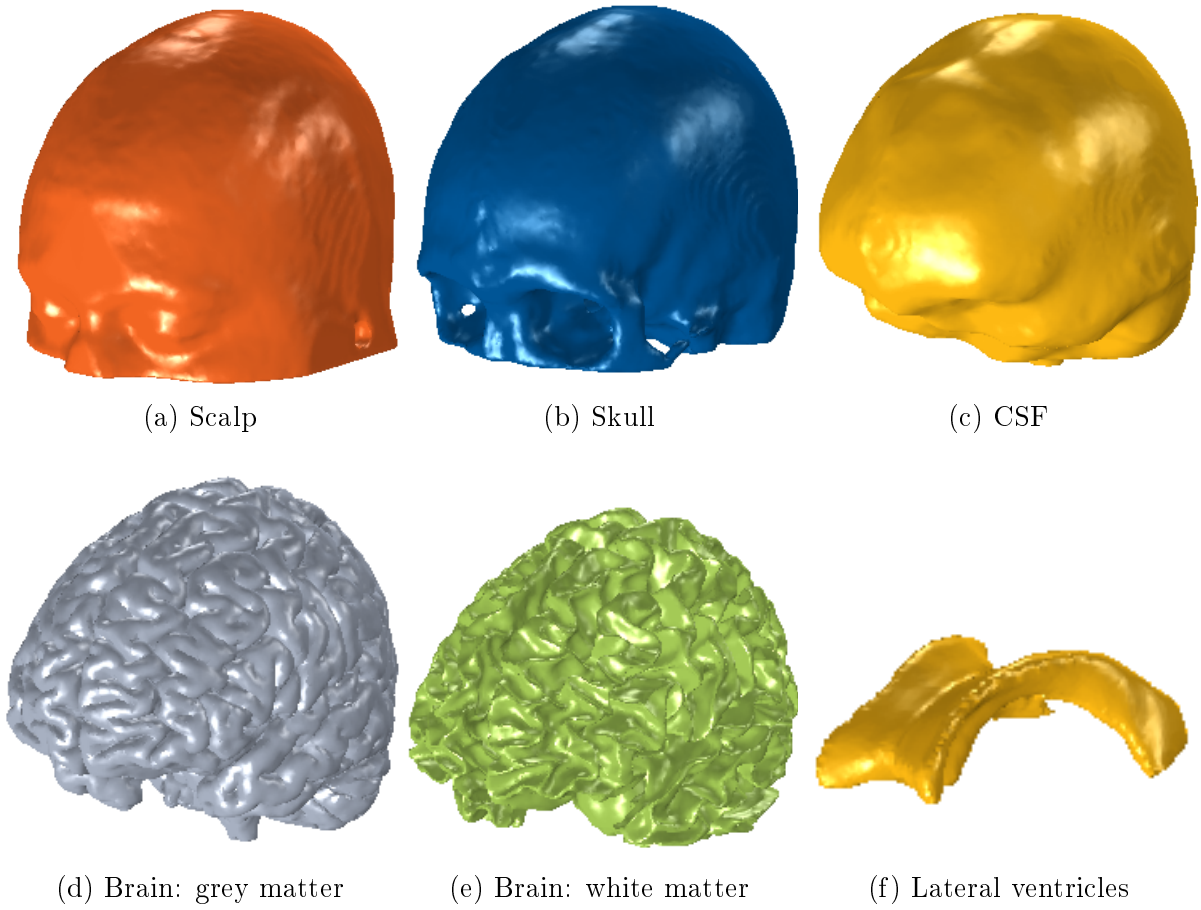

(a) Scalp (b) Skull (c) CSF

(d) Brain: grey matter (e) Brain: white matter (f) Lateral ventricles

Figure 3.1: Tissues segmented in this model from the outermost (a) to the innermost (f) tissue. The scalp and the skull were built based on proton density images, whereas the CSF, grey matter and white matter were created based on T1 images. The ventricles were added manually in a posterior step by thresholding WM data, as described in Miranda et al [92]. The relative size of the different tissues is not realistically represented.

In a subsequent work, this model was adapted for the study of the electric field distribution when TTFields were applied, as explained in Miranda et al [81]. In that work, four arrays were placed on the surface of the scalp to mimic the Optune system. Each array consisted in a matrix of 3x3 interconnected ceramic transducers with centers separated by 22 mm in one direction and 33 mm in the other. Each transducer had a thickness of 1 mm and a radius of 9 mm. Between each transducer and the scalp a thin layer of gel was added, in Mimics, with a thickness between 0.5 and 2.0 mm and a radius of 10 mm. One array pair was placed over the left and right temporal and parietal regions of the head (the LR pair), whereas the other was placed over the supraorbital region and at the back of the head (the AP pair), as shown in figure 3.2.

Lastly, a virtual lesion was added to mimic a glioblastoma multiforme. It consisted in a necrotic core, represented by a sphere with a radius of 7 mm, surrounded by an active concentric shell with a radius of 10 mm. This lesion was placed in the right hemisphere of the brain, totally embedded in the WM, and near the lateral ventricles, as depicted in figure 3.3.

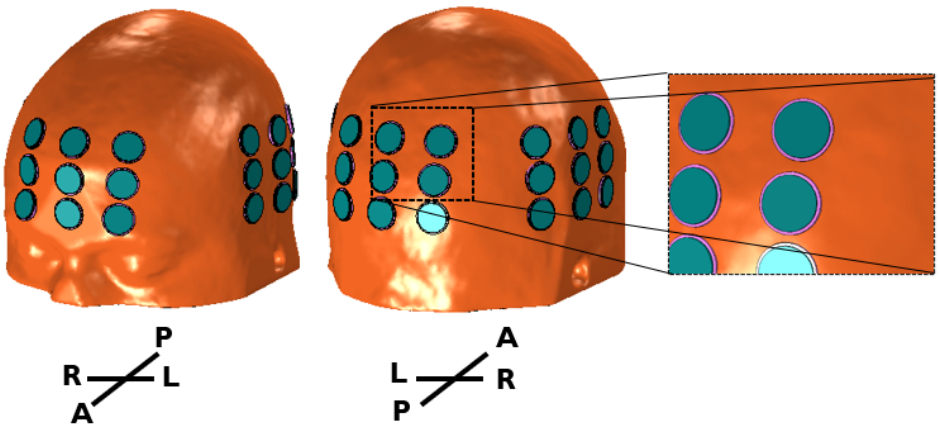

Figure 3.2: Placement of the two pairs of arrays. One pair was placed over the left and right temporal and parietal regions of the head (LR pair), whereas the other was placed over the supraorbital region and at the back of the head (AP pair). Between each transducer (in cyan) and the scalp (orange) there is a layer of gel (pink), with an average thickness between 0.5 and 2.0 mm. A: Anterior; P: Posterior; L: Left; R: Right.

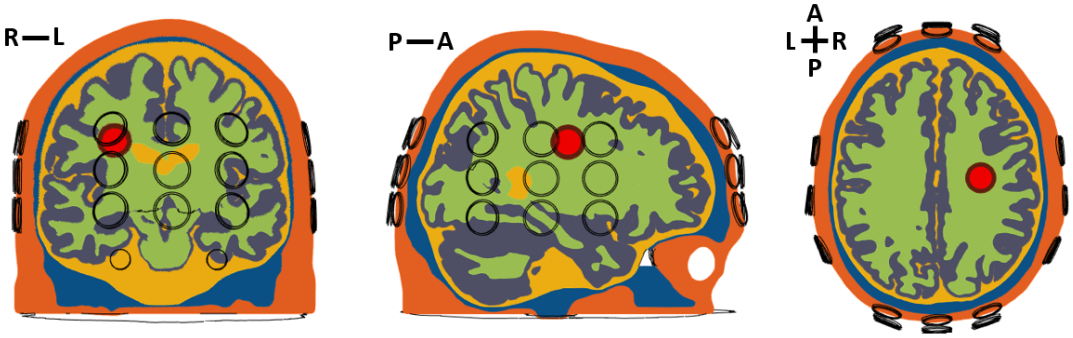

Figure 3.3: Coronal (left), sagittal (middle) and axial (right) sections of the head model through the center of the virtual lesion. Each color represents a different tissue: scalp (orange), skull (blue), CSF (yellow), grey matter (grey), white matter (green), tumor's active shell (brown) and tumor's necrotic core (red). The ventricles were assumed to be filled with CSF and thus are also colored in yellow. Placement of the transducers on the scalp is represented by the black circles.

As it can be clearly seen in the previous figures, this model was truncated at the nose level due to the limited coverage of the MR images that were used to built it. Although this might increase the EF distribution in tissues, it is not expected to significantly affect the results as the transducers were placed relatively far from the truncation level, as explained in Miranda et al [92].

3.2 The Finite Element Method (FEM)

After building the geometry, it is necessary to model the physical processes of interest. This can be done in a handful of different ways and with a variety of software. In this thesis, the software used was COMSOL Multiphysics which has also been used in several other TTFields computational studies (e.g.: [43, 81, 93, 94]). COMSOL uses the FEM to solve the necessary differential equations. Briefly, this method consists in discretizing the whole geometry into several small simple geometrical elements in which the solution

is calculated. The final solution is then obtained by combining the information of all elements of the geometry. The assembly of all these elements is known as the mesh (an example is provided in figure 3.4). In this head model, there were roughly 2.3 million tetrahedral elements (volume elements) and 564 thousand triangular elements (surface elements). The total number of points in which the solution was computed, the degrees of freedom, was around 6 million. A more detailed description of the FEM is presented in appendix B.

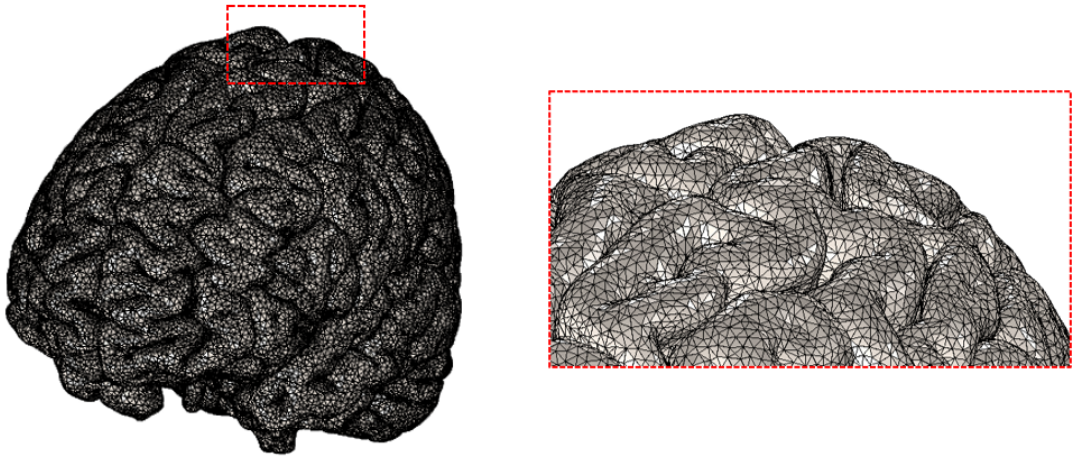

Figure 3.4: Representation of the surface mesh of the grey matter. In the inset on the right it is possible to see that this mesh is composed by several triangles in which the solution is calculated. These triangles are one of the 4 triangles of a tetrahedral element.

3.3 Predicting the electric field during TTFields

As the electric fields are applied in two directions, it is necessary to calculate the electric field distribution twice, once for each pair. For the frequency range at which TTFields operate, 100-500 kHz, the electromagnetic wavelength is significantly larger than the size of the head ($\approx$ 15 m vs. $\approx$ 20 cm, respectively) and thus the EQS approximation of Maxwell's equations holds (a more detailed discussion on this is provided in appendix A). Under this approximation, the electric field distribution within the human head can be obtained using Laplace's equation[1].

$$\nabla \cdot (\sigma^* \nabla \phi) = 0 \tag{3.1}$$

where σ^* is the complex electric conductivity (S/m) and ϕ the electrostatic potential (V). The first quantity is related to the real electric conductivity, σ (S/m), by:

[1] In appendix A, Maxwell's equations were used to derive Laplace's equation. In all those equations, the complex electric conductivity was represented by σ in order to use the same nomenclature as the one that is commonly found in the literature. However, throughout this thesis, there is a need to differentiate between the complex, σ^*, and the real, σ, electric conductivities. The relation between the two is clearly shown by equation (3.2).

$$\sigma^* = \sigma + j\omega\epsilon_0\epsilon_r \tag{3.2}$$

where j is the imaginary constant ($\sqrt{-1}$), ω is the angular frequency (rad/s), ϵ_0 is the permittivity of the vaccum ($\approx 8.854 \times 10^{-12}$ F/m) and ϵ_r the relative permittivity of each tissue (unitless). Throughout this thesis, all tissues were assumed to be isotropic and thus σ^*, σ and ϵ_r were scalar values. If anisotropic values had been used, these quantities would have been tensors and thus 3x3 matrices. In chapter 4, some considerations about this simpification are made.

Equation (3.2) reflects the existence of a resistive and a capacitive components of the current density, given by the first and second terms on the right-hand side, respectively. For the frequency at which TTFields are used the current density in the head is mainly resistive as $\sigma \gg \omega\epsilon_0\epsilon_r$ [95] for all tissues. The latter implies that σ^* and σ have pratically the same value. In table 4.1 the values of each physical parameter are presented for all tissues considered.

At the boundaries some conditions were also imposed to mimic how treatment was performed. As the Optune system is a current source all transducers of the same array are at the same potential. Thus, a Dirichlet boundary condition has to be imposed at these boundaries:

$$\phi = V_0 \tag{3.3}$$

The value of V_0 depends on how much current is injected into each pair.

At the remaining outer boundaries, namely on the scalp, gel and lateral boundaries of the transducers, the normal component of the current density is null. Thus, a Neumann boundary condition is used:

$$\boldsymbol{n} \cdot \boldsymbol{J} = 0 \tag{3.4}$$

where $\boldsymbol{n}$ is the normal to the surface and $\boldsymbol{J}$ is the current density (in A/m^2). This ensured that the head is electrically insulated.

At the internal boundaries, continuity of the normal component of the current density is imposed:

$$\boldsymbol{n_2} \cdot (\boldsymbol{J_2} - \boldsymbol{J_1}) = 0 \tag{3.5}$$

where $\boldsymbol{n_2}$ is the outward normal in medium 2, and current is flowing from medium 1 to medium 2.

Typically, it is assumed that all tissues and materials start at a null potential. Thus, the following initial condition can be used:

$$\phi^0 = 0 \tag{3.6}$$

Equations (3.1) to (3.6) realistically model how current is injected and how it interacts with the head during treatment. After the electric part of the problem is solved, the contribution of the EFs to the temperature increases is accounted for when predicting the temperature distribution.

Throughout this thesis all the electric parameters were assumed to be uniform and isotropic. A detailed discussion of the possible limitations of this approach is presented in the next chapter.

3.4 Predicting the temperature during TTFields

In computational studies, the temperature variation is typically studied and predicted using Pennes' equation [96]. This equation was developed by Pennes based on experimental data obtained from 9 patients whose forearm temperature was measured at different conditions and in different time points. Based on the results obtained the following equation was deduced:

$$\rho c \frac{\partial T}{\partial t} = \nabla \cdot (k \nabla T) + Q_{blood} + Q_{met} \tag{3.7}$$

where ρ is the density (kg/m^3), c is the specific heat at constant pressure (J/(kg ℃)), T the temperature (℃), t the time (s) and k the thermal conductivity (W/(m ℃)). The first term on the right-hand side is known as Fourier's law for thermal conduction and it accounts for the heat that is transferred through that process. The second and third terms, Q_{blood} and Q_{met}, both in W/m^3, represent the energy exchange with the blood and the heat generated by the metabolic activity of tissues, respectively. The first is given by:

$$Q_{blood} = \omega^* \rho_b c_b (T_b - T) \tag{3.8}$$

where ω^* is the blood perfusion rate (1/s). The subscript "b" stands for blood. A constant blood temperature, T_b, of 36.7 ℃, was assumed in simulations. This equation implies that when the temperature of tissues is below T_b, the blood acts like a heat source, whereas when it is above it acts like a heat sink.

The metabolic rate of each tissue, Q_{met}, was considered to be constant for the temperature range at which TTFields operate. A more detailed discussion of the limitations of this assumption is provided in the next chapter.

When applying TTFields, there is an additional term, that represents the Joule heating effect, that should be added to account for the contribution of the electric fields to the temperature increases. It is given by:

$$Q_{JH} = \boldsymbol{J} \cdot \boldsymbol{E} \tag{3.9}$$

where $\boldsymbol{E}$ is the electric field vector (V/m). Based on equation (A.7) (appendix A), for isotropic materials, the previous expression can be rewritten as:

$$Q_{JH} = \sigma ||\boldsymbol{E}||^2 \tag{3.10}$$

As current is injected in two perpendicular directions alternately with a switching time of one second, these power densities have to be taken alternately from each pair. Furthermore, as there is a limit on the maximum temperature, T_{lim}, that the transducers can reach, Q_{JH} can be rewritten:

$$Q_{JH} = \begin{cases} Q_{JH}^{AP}\, pulse(t) + Q_{JH}^{LR}\, pulse(t+1), & \text{if } \forall T_{transducers} \leq T_{lim} \\ 0, & \text{otherwise} \end{cases} \tag{3.11}$$

where T_{lim} is the maximum temperature that the transducers can reach while still applying the EFs and $pulse(t)$ evaluates to one for even time integers and zero otherwise. The choice to inject current in the AP or in the LR pair first is arbitrary and has no impact on the predicted temperature variation. The value of zero when the temperature is higher than T_{lim} means that current is not injected in any pair. As discussed in Gentilal et al [43] and in subsection 2.2.2, the value used for T_{lim} was 40.4 ℃ and it corresponded to the average temperature of the most significant transducer that controlled if current was injected or not. In those simulations, this value corresponded to having 5% of the transducer volume at 41 ℃, which was assumed to be the volume occupied by the thermistor.

Thus, Pennes' equation for TTFields studies is given by:

$$\rho c \frac{\partial T}{\partial t} = \nabla \cdot (k \nabla T) + \omega^* \rho_b c_b (T_b - T) + Q_{met} + Q_{JH} \tag{3.12}$$

In somes cases, studying the time-transient variation of the temperature of tissues might not be relevant for the work as only the maximum is of interest. In that cases, steady-state simulations can be used instead to compute the solution quicker. As time is not a variable in this type of studies, the term on the left-hand side of Pennes' equation is set to zero ($\frac{\partial T}{\partial t} = 0$). Under these conditions, the contribution of both array pairs can not taken alternately and thus current injection has to be made continously in just one pair. Steady-state studies imply that it is possible to reach a state in which the amount of heat flowing into a certain tissue/material equals the amount of heat that is flowing out of it.

At the external boundaries, there are also other cooling mechanisms, namely convection and radiation, that allow tissues and materials to cool down. Convection is mathematically given by:

$$F_{conv} = h(T_{surface} - T_{room}) \tag{3.13}$$

where h is the convection factor (W/(m^2 ℃)), $T_{surface}$ is the temperature of the surface (℃) that is in contact with the environment at a temperature T_{room} (℃).

On the other hand, radiation is given by Stefan-Boltzmann's law:

$$F_{rad} = \epsilon \sigma_{SB} ((T_{surface} + 273.15)^4 - (T_{room} + 273.15)^4) \tag{3.14}$$

where ϵ is the emissivity factor (unitless) and σ_{SB} is the Stefan-Boltzmann constant ($\approx 5.668 \times 10^{-8}$ W/(m^2 ℃^{4})). In the simulations performed in this work, T_{room} was considered to be constant and equal to 24 ℃. The environment is acting like a heat source when $T_{surface}$ is lower than the room temperature and as a heat sink otherwise. Both F_{conv} and F_{rad} are in W/m^2.

When setting up the simulations it is necessary to define an initial temperature for all tissues and materials. One possible way to do it is to consider the initial temperature of all tissues equal to blood's temperature and the initial temperature of the gel and transducers equal to the room's temperature:

$$T^0_{tissues} = T_{blood} \tag{3.15}$$

$$T^0_{materials} = T_{room} \tag{3.16}$$

In practice, the initial temperature does not change the minimum/maximum temperature reached by each tissue and material, but it can significantly affect how much time has to be simulated to reach it, especially in time-transient simulations. To reduce the computational time, a steady-state simulation can be performed first in which the electric fields are not applied (i.e., $Q_{JH} = 0$). This allows a state to be reached where the head is in thermal equilibrium with the environment. The temperature distribution obtained from this simulation can then be used as an initial condition to solve Pennes' equation when TTFields are applied in time-dependent studies.

Throughout this thesis all the thermal parameters were assumed to be uniform and isotropic. A detailed discussion of the possible limitations of this approach is presented in the next chapter.

3.5 Software and workstations used

The following software was used in this thesis:

- COMSOL Multiphysics (www.comsol.com) - version 5.2a
  - To solve all the equations presented throughout this chapter using the finite element method;
- Materialise 3-matic (www.materialise.com/en/software/3-matic) - version 9.0;
  - To build models and create surface and volume meshes that were then imported into COMSOL;
- MATLAB (www.mathworks.com/products/matlab.html) - versions 2017b and 2020a;
  - To analyse data and perform data curve fitting;

In COMSOL Multiphysics, the electric equations are solved using the electric currents (ec) interface of the AC/DC module. As the EQS approximation holds, frequency domain studies are performed. In this type of studies, the input is given in terms of amplitude (e.g.: V_0 in equation (3.3)), whereas the results obtained are given in terms of root mean square (RMS) values (e.g.: the electric field distribution, $\boldsymbol{E}$, in equation (3.9)).

The thermal equations are solved using the heat transfer in solids (ht) interface of the Heat Transfer module. Two different studies were used: time-dependent and stationary. The relative tolerance considered for the iterative solvers for both the electric and thermal problems was 10^{-6}.

Validation of the numerical calculations obtained through COMSOL Multiphysics was already performed during the MSc thesis by comparing the results of this software with the respective analytical solution for a similar problem involving a simpler geometry [42]. The results from that analysis allowed to conclude that this numerical tool is very accurate when solving the electric and thermal equations for TTFields therapy.

Three different workstations were used to run the simulations. As their specifications affect the computational time, the main differences between them are given below:

- Workstation 1: Computer with dual core Intel Xeon W5580 processors clocked at 3.2 GHz and 48 GB of RAM;
- Workstation 2: Computer with dual core Intel Core i7-9800X X-series processors clocked at 4.5 GHz and 64 GB of RAM;
- Workstation 3: Computer with dual core Intel Core i9-10900X X-series processors clocked at 3.7 GHz and 64 GB of RAM;

Chapter 4

Sensitivity analysis of the physical parameters

Published work

The results presented in this chapter resulted in the following work:

1. **Nichal Gentilal** and Pedro Cavaleiro Miranda. Heat transfer during TTFields treatment: influence of the uncertainty of the electric and thermal parameters on the predicted temperature distribution. *Computer Methods and Programs in Biomedicine*, 196, 105706, 2020. DOI: 10.1016/j.cmpb.2020.105706 – **Peer-reviewed paper #2**

2. **Nichal Gentilal** and Pedro Cavaleiro Miranda. The impact of the uncertainty of biological tissue thermal parameters on the estimated maximum temperature during TTFields therapy. *2020 42nd Annual International Conference of the IEEE Engineering in Medicine and Biology Society (EMBC)*, 2283-2286, 2020. DOI: 10.1109/EMBC44109.2020.9175372 – **4-page abstract #1**

3. **Nichal Gentilal** and Pedro Cavaleiro Miranda. The impact of the uncertainty of biological tissue thermal parameters on the estimated maximum temperature during TTFields therapy. *IEEE Engineering in Medicine and Biology Society (EMBC 2020)*, 20th-24th July 2020, virtual conference – **Oral presentation #6**

4. **Nichal Gentilal** and Pedro Cavaleiro Miranda. Influence of the thermal and electric properties of biological tissues on the maximum temperature during TTFields therapy. *American Association for Cancer Research 2020 (AACR 2020)*, 22nd-24th June 2020, virtual conference. DOI: 10.1158/1538-7445.AM2020-5484 – **Poster presentation #3**

5. **Nichal Gentilal** and Pedro Cavaleiro Miranda. The impact of the electric conductivity of tissues on the electric field intensity and power density during TTFields therapy for glioblastoma. *American Society for Radiation Oncology (ASTRO 2020)*, 23rd-29th October 2020, virtual conference. DOI: 10.1016/j.ijrobp.2020.07.715 – **Poster presentation #4**

4.1 Introduction

The temperature increases during TTFields treatment were predicted for the first time in the study by Gentilal et al [43]. In that work, it was shown that the scalp could reach a maximum temperature of 42 ℃, a value higher than the preset temperature limit of 41 ℃ of the Optune system. These temperature increases were shown to be very superficial and localised as in each tissue temperature hotspots occurred underneath the regions where the transducers were placed (figures 2.7 to 2.9, subsection 2.2.3). The brain was the tissue whose temperature was predicted to vary the least, from 36 ℃ to 38 ℃, but it was also the one where the most physiological changes were predicted. These included an increase of the blood-brain barrier permeability, variations in the neocortical activity and cellular properties. No side-effects that could have been caused by these changes were reported to occur in patients that participated in clinical trials [8, 17], as discussed in section 2.2. Among the several hypotheses presented in subsubsection 2.2.4.4, the easiest way to start investigating the discrepancy between what was predicted and what was observed in patients is to study the uncertainties and limitations that the model has.

As seen in chapter 3, all the equations that are necessary to solve involve physical parameters that must be specified in order to run the simulations. However, very often, the exact value of these parameters is not known and several values are found in the literature for the same physical property. For the study of heat transfer during TTFields, both the electric and thermal parameters play a significant role when predicting the temperature in each tissue. The impact of the uncertainty associated with the electric parameters in the EF distribution during TTFields was already studied by Wenger et al [93]. In that work, the same model as the one presented in figure 3.3 was used. The results showed that the average EF strength could vary by up 42% in the brain and by up to 68% in the active tumor when the dielectric properties were varied based on what was found in the literature. In general, the tissues whose electric conductivity led to the highest variations on the values of the average EF strength were the scalp, the skull and and tumor's active shell. On the other hand, changes in the relative permittivity of tissues led to a maximum variation of the EF strength of only 5% in the brain and tumor. This result is not surprising given that at 200 kHz the current in the head is mainly resistive.

The impact of the uncertainty of the physical parameters has already been shown to affect the maximum temperature predicted in tissues in other techniques such as electroconvulsive therapy. In the studies by Oliveira et al [48, 97], variations in the electric and thermal properties of the scalp and skull were shown to influence the temperature reached by each tissue. In some cases, variations of 1-2 ℃ in the maximum temperature predicted were seen in the most superficial tissues.

Thus, an investigation of how these uncertainties might affect the predicted temperature when TTFields are applied is of the utmost importance.

4.2 Aim

The goals of this work were:

1. Investigate the impact of the uncertainty of the electric and thermal parameters on the temperature predicted for each tissue and transducers during TTFields treatment through a sensitivity analysis;

2. Predict the thermal impact of TTFields based on the results obtained and compare it with what was discussed in section 2.2;

4.3 Methods

4.3.1 Current injection mode

The same head model as the one described in section 3.1 was used and the equations already presented in sections 3.3 and 3.4 were solved. As the goal of this work was to perform a sensitivity analysis, it would not be feasible to follow the same approach as in Gentilal et al [43]. Instead, steady-state simulations were performed to allow for reasonable computational times. As mentioned in section 3.4, this type of studies does not depend on time. Consequently, it was not possible to inject 900 mA in both pairs alternately with a switching time of one second. To make the predictions as realistic as possible, 450 mA were injected in the AP pair continously. This value is half the current that is typically injected in patients and it led to temperature values in the transducers and tissues that were near Optune's maximum operating temperature for the same physical parameters used in Gentilal et al [42, 43]. This ensured that, in a complete working cycle of 2 seconds, energy transfer mechanisms had similar magnitudes in both the transient and the steady-state simulations. In this work, current was injected in the AP pair given that in this head model the MST was located in the anterior array, as discussed before. Each study took around 10 minutes in workstation 1.

4.3.2 Literature review

A literature review was carried out to determine the range of reported values for the electric and thermal properties of tissues and other materials. The most commonly reported ones were taken to be the standard (std) values and they correspond to the values used in the simulations performed to draw the conclusions presented in section 2.2. In the sensitivity analysis, one parameter at a time was changed to its minimum or its maximum value while maintaining the other parameters constant and equal to their standard value. These values are presented in table 4.1. A total of 57 simulations were performed for this one-way sensitivity analysis.

In the case of the electric parameters, the work by Wenger et al [93] already showed that the uncertainty in the relative permittivity values does not significantly affect the EF in the head at the frequency at which TTFields are used. Thus, it will also not affect the temperature distribution as the Joule effect will remain unchanged. Because of that this source of uncertainty was not accounted for in this study. As for the electric conductivity values, the same minimum and maximum reported in that work for each tissue were used [93]. The only exception was skull's maximum electric conductivity as a higher value was reported in a subsequent paper: 0.080 S/m [98]. As the electric properties of the transducers and gel are well known and were provided by Novocure, a sensitivity analysis of those values was only made to investigate their impact on the maximum temperature.

As for the thermal parameters and as mentioned previously, in steady-state studies the term on the left-side of Pennes' equation, equation (3.7), is set to zero and thus a sensitivity analysis concerning the density and specific heat is not possible. However, the values assigned to these two physical parameters only affect how quickly tissues reach

a steady-state situation, but not the maximum temperature reached. Based on figures 2.5 and 2.6, it takes around 2.5 minutes for the transducers to reach the temperature limit, T_{lim}, when the standard parameters are used. As treatment should last for at least 18 hours, this initial increase only represents a small fraction of treatment time. The only specific heat and density values that were relevant for this work were blood's, as they might change the perfusion rate of each tissue, according to equation (3.8). For the other physical parameters an extensive literature review was carried out to perform this analysis. Most of the minimum and maximum thermal parameters were taken either from the IT'IS Foundation database [99] or from Duck's reference book [100], which are two of the most used sources for thermal values of biological tissues. Whenever a higher maximum or a lower minimum were found elsewhere those values were used instead. In particular, scalp [101] and skull's [102] minimum thermal conductivity, skull's minimum [103] and maximum [104] blood perfusion rate, WM's maximum perfusion rate [103] and the minimum metabolic rates of the scalp, GM and WM, all from [104], were changed. Given that information about the thermal parameters of GBM is very poor, the values used in this study were for other types of tumors and were taken from [105–107]. The minimum and maximum values were considered to be $\pm$ 10% the standard value. As for the boundaries, scalp's convection factor, h_{scalp} [108], and emissivity, ϵ_{scalp} [109], are well known and thus there was no uncertainty associated. Due to the lack of information in the literature, the same values were considered for the outer boundaries of the gel and transducers. The remaining thermal properties of the gel, which is mainly composed by water, and transducers are also accurately known. Following the same approach as before, for the thermal properties of these two, the maximum and the minimum values were considered to be twice and half the respective standard values to investigate their impact in the temperature distribution.

All the electric and thermal parameters considered in this study are indicated in table 4.1. In some cases, the standard value was already the minimum or maximum and thus only two values are presented. In other cases, the values of the parameters were not necessary for the simulations, such as the blood's thermal conductivity, and thus they are not considered.

4.3.3 Metrics used

The results of the sensitivity analysis were studied in terms of how much the temperature varied compared to when the standard values were used. As described in subsection 2.2.3, the maximum temperature reached by each tissue always occurred at its surface and mainly underneath the regions where the transducers were placed. More specifically, the maximum temperature in each tissue was reached in the regions underneath the MST. In this work, the percentile 99.99% of the temperature distribution in each tissue was calculated for each simulation. The reason why this quantile was used instead of the maximum temperature was to avoid possible numerical errors that could affect the results. However, for simplicity of discussion, this percentile is simply referred to as the maximum temperature, T_{max}, throughout this chapter. As for the transducers, the average temperature was quantified in each simulation instead of the maximum, to allow for a direct comparison of the results of the sensitivity analysis with those published in the first study [43].

Table 4.1: Standard (std) electric and thermal properties assigned to each tissue, gel and transducers. For the parameters considered for the one-way sensitivity analysis, minimum (min) and maximum (max) values are also presented based on what is reported in the literature. In total 57 simulation were performed.

Physical parameter			Scalp	Skull	CSF	Brain: GM	Brain: WM	Tumor: Active shell	Tumor: Necrotic core	Gel	Transducers	Blood
Electric	Electric conductivity σ (S/m)	Min	0.14	0.003	1.64	0.15	0.08	0.15	0.50	$0.5\sigma_{gel}^{std}$	–	–
		Std	0.25	0.013	1.79	0.25	0.12	0.24	1.00	0.10	0	
		Max	0.45	0.080	1.94	0.50	0.30	0.50	1.50	$2\ \sigma_{gel}^{std}$	–	
	Relative permittivity ϵ_r (1)	Std	10000	200	110	3000	2000	2000	110	100	10000	–
Thermal	Thermal conductivity k (W/(m °C))	Min	0.16	0.16	0.50	0.503	0.460	$0.9\ k_{tumor}^{std}$	$0.9k_{tumor}^{std}$	–	$0.5\ k_{transducers}^{std}$	–
		Std	0.34	1.16	0.60	0.565	0.503	0.550	0.550	0.6	6	
		Max	0.50	–	0.62	0.576	–	$1.1\ k_{tumor}^{std}$	$1.1\ k_{tumor}^{std}$	–	$2\ k_{transducers}$	
	Specific heat c (J/(kg °C))	Std	3150	1700	4200	3680	3600	3600	3600	4186	527	Min: 3300 Std: 3600 Max: 3930
	Density ρ (kg/m^3)	Std	1000	1500	1000	1036	1027	1030	1030	1000	6060	Min: 1025 Std: 1050 Max: 1064
	Blood perfusion rate ω^* (10^{-3} 1/s)	Min	0.91	0.040	–	11.69	3.30	$0.9\ \omega_{tumor}^{*,std}$	–	NA	NA	NA
		Std	1.43	0.143	0	13.30	3.70	1.72	0			
		Max	2.20	0.180	–	14.68	5.21	$1.1\ \omega_{tumor}^{*,std}$	–			
	Metabolic rate Q_{met} (W/m^3)	Min	271	–	–	10369	2491	$0.9\ Q_{met\,tumor}^{std}$	–	NA	NA	NA
		Std	363	70	0	16229	4518	58000	0			
		Max	2294	542	–	17859	5018	$1.1\ Q_{met\,tumor}^{std}$	–			
	Convection factor h (W/(m^2 °C))	Min	–	NA						$0.5\ h_{scalp}^{std}$		NA
		Std	4							h_{scalp}^{std}		
		Max	–							$2\ h_{scalp}^{std}$		
	Emissivity ϵ (1)	Min	–	NA						$0.5\ \epsilon_{scalp}^{std}$		NA
		Std	1							ϵ_{scalp}^{std}		
		Max	–							–		

Min: Minimum; Std: Standard; Max: Maximum; NA: Not Applicable.

4.4 Results and discussion

4.4.1 Temperature distribution

The temperature distribution when the standard electric and thermal parameters were used is shown in figure 4.1. As it is visible by the darker regions in that figure, the maximum temperature in each tissue was reached underneath the transducer located in the anterior array, superior row, left side which was also the MST in the first study [43]. The average temperature of the MST in this study was around 40.4 ℃. In the brain, the maximum temperature was reached on the surface of the grey matter, as before. These temperature distributions and range of values are similar to what is presented in figure 2.7 (page 31), in which 900 mA of current were injected alternately into each pair with a switching time of one second.

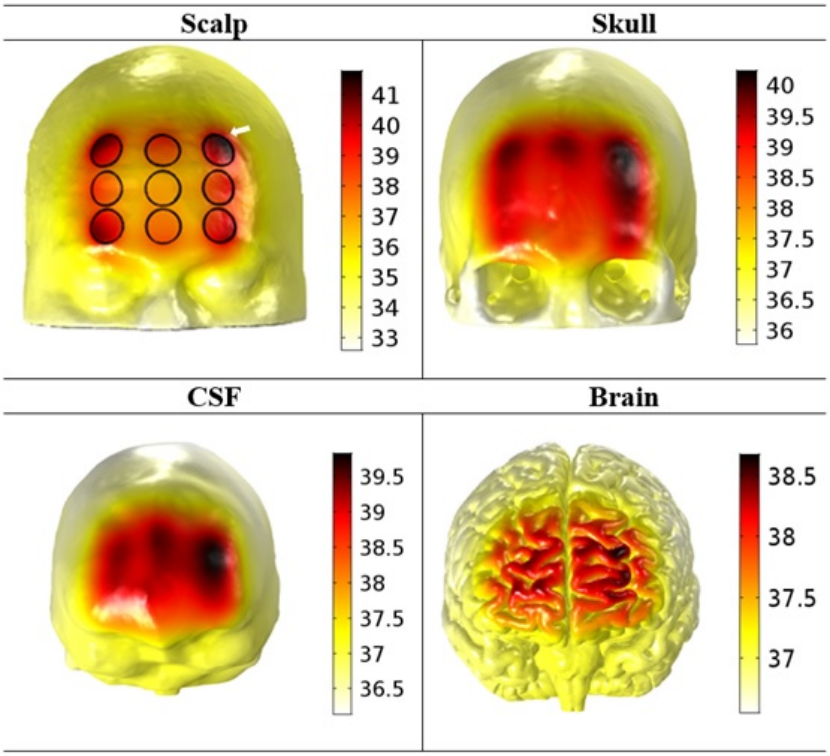

Figure 4.1: Anterior view of the temperature on each tissue surface when the standard electric and thermal parameters were used and when 450 mA of current were injected in the AP pair continuously. The black circles on the scalp represent where the transducers were placed. The localised heating underneath the regions where the array was placed is clearly visible. The hottest region, in dark red, occurred underneath the MST (white arrow, top row, left panel). The maximum temperature was 41.6 ℃ on the scalp, 40.2 on the skull ℃, 39.8 ℃ on the CSF, and 38.5 ℃ on the brain. In the latter, the maximum temperature occurred at the surface of the GM. Temperature scales are in ℃. Image taken from [80].

4.4.2 Importance of each heat transfer mechanism

Before investigating the data of the sensitivity analysis, it is important to understand first how each heat transfer mechanism contributes to increasing or decreasing the temperature of each tissue when the standard values were used. To perform this study it was first necessary to rearrange Pennes' equation considering a steady-state:

$$-\nabla \cdot (k\nabla T) = \omega^* \rho_b c_b (T_b - T) + Q_{met} + \sigma ||\boldsymbol{E}||^2 \tag{4.1}$$

At the hottest regions, i.e., underneath the MST, the maximum heat loss due to blood perfusion (first term on the right) in each tissue can be calculated if T is set to T_{max} (these values are reported in appendix C for every tissue). Throughout this work, the metabolic rate, Q_{met}, was assumed to be constant and thus its value was also known for every tissue (table 4.1). The maximum contribution of the Joule effect could also be predicted by considering a cylinder defined by the MST, following a similar approach as the one considered in subsubsection 2.2.4.2. The base of this cylinder had the area of the MST and its axis was parallel to the normal to transducer's surface. For these calculations, the percentile 99.99% of the power density within that cylinder was considered. Then, through equation (4.1) it was possible to estimate how much energy was transferred through conduction. Figure 4.2 depicts the contribution of each energy mechanism in cooling down or heating up tissues at the hottest regions after these calculations were performed.

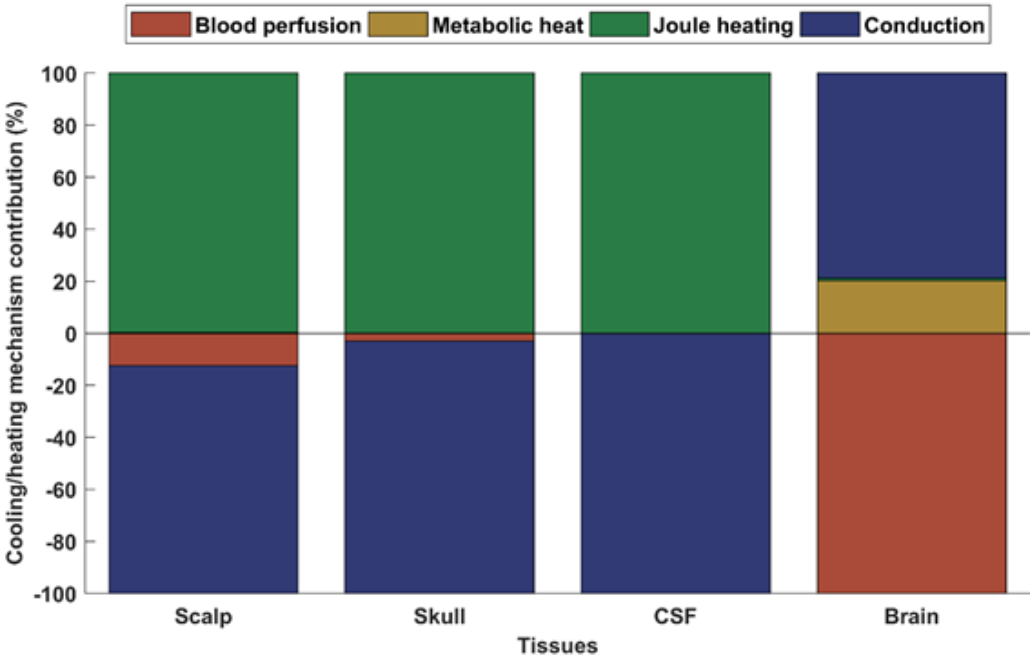

Figure 4.2: Relative contribution of each energy transfer mechanism for the temperature distribution and for each tissue in a cylinder defined by the MST, where tissues heated up the most. If the y-value is negative then that tissue is cooling down through that mechanism, whereas a positive value means that the tissue is heating up through that mechanism. As steady-state simulations were performed, the amount of energy that flows into one tissue through some mechanisms must equal the amount flowing out through others. Not all contributions are well observed given their low relative importance compared to others. In particular, the metabolic heat rate only explained 0.17% and 0.11% of the temperature increases in the scalp and skull, respectively, whereas Joule heating only explained 1.06% of the temperature increases in the whole brain. Image taken from [80].

In the previous figure, a positive y-value means that heat is flowing into the tissue, whereas a negative value means that it is flowing out. As steady-state simulations were performed the amount of energy that is flowing into one tissue through some mechanisms must equal the amount flowing out through others. Some of the mechanisms had a low contribution compared to others. In particular, the metabolic heat rate only explained

0.17% and 0.11% of the temperature increases in the scalp and skull, respectively, whereas Joule heating played a minor role in the brain (1.06%). Radiation and convection are not shown as the hottest region of the scalp was covered by the MST and thus it could not cool down through those mechanisms.

Figure 4.2 shows that the Joule heating term explained practically 100% of the temperature increases in the three most superficial tissues at the hottest regions. In the scalp, this heat will be dissipated mainly through conduction to the other regions of the scalp itself, to the gel and to the skull. In turn, gel transfers heat to the MST thereby increasing its temperature. Cooling in the skull and CSF followed the same rationale as in the scalp. Thus, energy flowed from the hottest and more superficial tissues to the brain, thereby increasing the temperature of the latter. However, blood perfusion in the brain is very efficient in removing this heat. This is not surprising given that this organ consumes around 25% of body's total glucose and 20% of the oxygen available [75], which requires a complex and efficient network of blood vessels.

The results from this study will be useful in the following analysis of the sensitivity results.

4.4.3 Influence of the uncertainty of the physical parameters of biological tissues

The impact that the variation of each parameter had on the temperature of tissues and MST is presented in appendix C. In that appendix, the absolute difference in the metrics evaluated is shown in regard to the temperature obtained when using the standard values. Based on that information, it was possible to investigate which biological tissues' parameters led to the highest variations. Figure 4.3 depicts the range predicted for the maximum temperature of each tissue and the average temperature of the MST when the electric (in black) and thermal (in red) properties of biological tissues were changed. Each line has three points that correspond to the lowest T_{max} (T^{-}_{max}) and highest T_{max} (T^{+}_{max}) predicted, as well as the value of T_{max} when the standard parameters were used (T^{std}_{max}). The values of the latter correspond to the temperature distribution shown in figure 4.1.

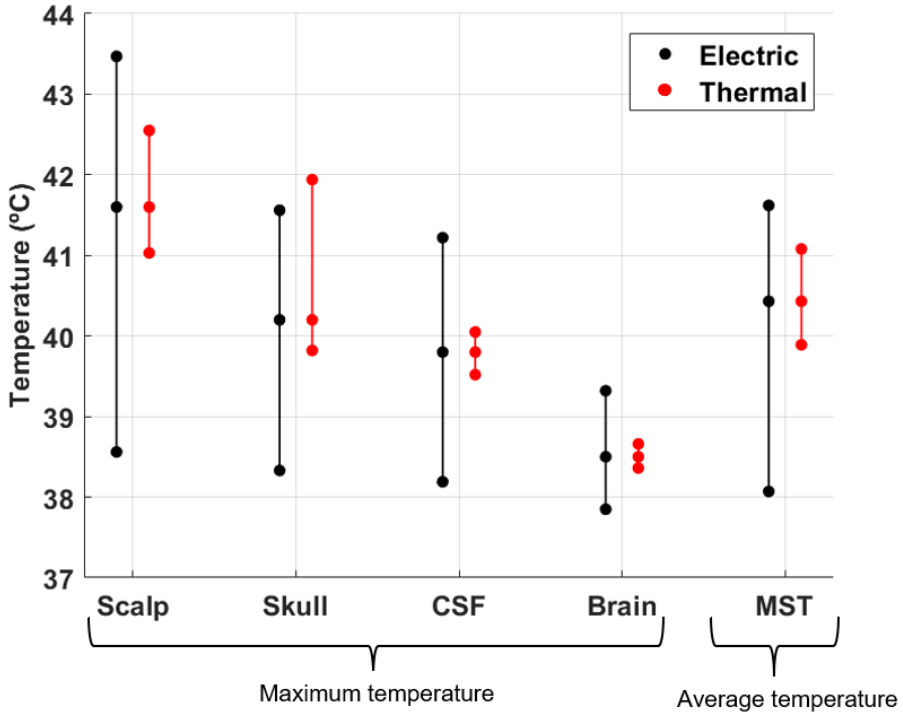

Figure 4.3: Range of variation of the temperature when changing the electric (in black) and thermal (in red) parameters. For each line and for each biological tissue, the lowest point corresponds to the lowest maximum temperature (T^{-}_{max}) predicted, the middle dot to the maximum predicted using the standard values (T^{std}_{max}), and the highest point to the highest maximum temperature value (T^{+}_{max}). Data is presented for the MST following the same rationale but considering the average temperature instead of the maximum. The absolute values are given in appendix C. Image taken from [80].

Table 4.2 shows which electric and thermal parameters change led to the highest variations in each tissue and MST.

Table 4.2: Electric and thermal parameters of biological tissues that led to the lowest and highest variation of the maximum temperature in tissues and average temperature in the MST.

Parameter evaluated	Tissue		T^{-}_{max} / T^{-}_{avg}	T^{+}_{max} / T^{+}_{avg}
Maximum temperature	Scalp	Electric	σ^{max}_{skull}	σ^{min}_{skull}
		Thermal	$\omega^{*,max}_{scalp}$	k^{min}_{scalp}
	Skull	Electric	σ^{max}_{skull}	σ^{min}_{scalp}
		Thermal	$\omega^{*,max}_{scalp}$	k^{min}_{skull}
	CSF	Electric	σ^{max}_{skull}	σ^{min}_{scalp}
		Thermal	$\omega^{*,max}_{scalp}$	k^{min}_{scalp}
	Brain	Electric	σ^{max}_{scalp}	σ^{min}_{scalp}
		Thermal	$\omega^{*,max}_{scalp}$	k^{min}_{scalp}
Average temperature	MST	Electric	σ^{max}_{skull}	σ^{min}_{scalp}
		Thermal	$\omega^{*,max}_{scalp}$	k^{min}_{scalp}

The previous table shows that the two electric parameters whose uncertainty led to the highest variations in the temperature were scalp and skull's electric conductivity (σ_{scalp} and σ_{skull}, respectively). Increases in these two led to lower temperature maxima in every tissue and MST. This was expected given that the higher the conductivity of tissues,

the lower the potential difference between the arrays to inject the same current (i.e., the lower the impedance of the head). Consequently, the Joule effect in all tissues is also reduced, as well as temperature maxima. On the opposite end, a decrease of the electric conductivity of the scalp and skull to the minimum found in the literature led to the highest temperature predicted everywhere. These results are in accordance with what is reported in figure 4.2. As the Joule effect is the main heat source in the most superficial tissues and that heat flows from those tissues to the cooler regions of the head, changing the magnitude of this mechanism also affects all tissues and transducers. The impact of the variations in the electric conductivity values of the remaining tissues (CSF, brain and tumor) was very limited, either because the values were well known or because the EF in these tissues was not high enough for the Joule effect to be significantly changed.

Table 4.2 indicates that scalp's thermal conductivity, k_{scalp}, and scalp's blood perfusion rate, ω^*_{scalp}, were the two most significant thermal parameters. Based on figure 4.2, these results are also not surprising as at the hottest regions the scalp cools down through conduction and blood perfusion. As this tissue is the one that heats up the most and as that heat flows from it to the deeper tissues, the temperature in all tissues is significantly affected by the magnitude of these two mechanisms. The only exception seen was skull's thermal conductivity, k_{skull}, whose uncertainty led to the highest temperature variation in the skull itself. This is explained by a decrease of 86% in the value of k_{skull}, from 1.16 to 0.16 W/(m ℃). As for the remaining thermal properties, lower metabolic rates, Q_{met}, and increases in the thermal conductivities, k, and in the blood perfusion rates, ω^*, of each tissue led to lower temperature maxima in all tissues as heat was dissipated more efficiently (tables C.1 and C.2, appendix C). In general, variations in the values of the thermal properties of blood and tissues other than the scalp did not significantly affect the temperature predicted, as the values did not change by more than 0.1 ℃ compared to when the standard parameters were used.

In figure 4.3 it is also possible to see that the uncertainty of the electric parameters led to highest variations in the temperature predicted than the uncertainty of the thermal parameters. An additional factor that contributed to this result was the narrower range of variation in most of the thermal parameters used in this study, which indicates that these are more accurately known than the electric ones. Among all tissues, scalp was the one that heated up the most, where the highest maximum temperature predicted (T^+_{max}) was 43.5 ℃ (range: 38.6 - 43.5 ℃) when skull's electric conductivity was reduced. This value is still below the 44 ℃ reported by Moritz and Henriques [86] to cause complete epidermal necrosis for long exposures. In the skull, T^+_{max} was almost 42 ℃ (38.3 - 41.9 ℃) and it occurred when k_{skull} was reduced. This value represents an increase of more than 2.5 ℃ compared to what was obtained and presented in figure 2.7 (page 31), but it was not sufficient to surpass the thresholds at which some physiological changes occurs. In the CSF, the highest maximum temperature predicted was around 41.2 ℃ (38.2 - 41.2 ℃) when σ_{scalp} was decreased. One of the main functions of this fluid is to give thermal support to the brain by acting as a thermal buffer [75]. To the best of the author's knowledge there is not any study that addressed the impact of this temperature range in the CSF, and thus possible physiological changes that might occur are not discussed here. The brain was the tissue in which temperature maxima varied the least, between 37.9 ℃ and 39.3 ℃ ($\Delta = +1.4$ ℃), but it is also the one that is more sensitive to thermal variations according to the literature [75]. In the studies performed in this chapter, the maximum temperature predicted for this tissue using the standard values was 38.5 ℃, which was slightly higher than the 38.1 ℃ predicted in the time-transient simulations (figure 2.7).

Extrapolating the results, this means that the lowest maximum temperature predicted for this tissue assuming an alternate application of the fields would be around 0.6 ℃ lower, i.e., 37.5 ℃, when the electric conductivity of the scalp is increased from 0.25 to 0.45 S/m. For this temperature variation an increased probability of neurotransmitter releases at the synapses [89, 90] and a possible increase on the blood-brain barrier permeability [110] are predicted. Other studies in rats reported that temperatures higher than 39 ℃ might injure brain cells [75], although the brain is not likely to reach this value when TTFields are applied. As for the tumor, its maximum temperature did not vary by more than 0.1 ℃ in any simulation, reaching a maximum of 38.1 ℃.

The physiological effects described in the previous paragraph are the sames ones that were predicted in the first study on heat transfer during TTFields therapy [43] and that are reported in subsection 2.2.4. This indicates that the discrepancy between what was predicted and what was reported could not be explained solely by possible inaccurate parameters used, even though the choice of these parameters can significantly affect the maximum temperature reached by each tissue. For instance, the maximum temperature predicted on the scalp can vary by up to 5 ℃ depending on the values assigned to physical properties, which highlights the importance of a performing a more thorough investigation on which are the most accurate values to use.

Lastly, the temperature of the MST was sensitive to practically the same parameters as the scalp. This was expected, given that the transducers heat up through conduction and that the heat goes from the scalp to the gel and from the gel to the transducers. The average temperature of the MST varied between 38.1 ℃ and 41.6 ℃, which might lead to significant changes in the main conclusions that were draw not only in Gentilal et al [43], but also in future works that might be published concerning how Optune injects current. For instance, in subsection 2.2.2, it was concluded that in an intermittent operation scenario Optune did not inject current during the same time in the AP and LR pairs due to the MST cooling down rate. If the values used for the four most sensitive physical parameters ($\sigma_{scalp}, \sigma_{skull}, k_{scalp}$, and ω^*_{scalp}) were higher, the time that the device was off could have been lower and thus current would be applied for longer periods of time and maybe even for the same time in each pair. This would lead to a more optimistic prediction of how Optune operates.

Based on these results, it would be important to do experimental measurements of the electric conductivity of the scalp and skull at 200 kHz, as well as scalp's blood perfusion and thermal conductivity for a temperature range between 20-45 ℃. To minimize the error of the predictions made in the next chapters, the standard values will be used, unless specified otherwise.

4.4.4 Influence of the physical parameters of the gel and transducers

In tables C.1 and C.2 (appendix C), the temperature variations when changing the properties of the gel and transducers are presented. An increase of the electric conductivity of the gel, from 0.1 S/m to 0.2 S/m, led to a decrease on the temperature predicted in tissues and in the MST. Even though this variation was not enough to significantly affect the impedance of the model, it was sufficient for the heat to dissipate more uniformly in the scalp and thus to decrease temperature maxima everywhere. Similarly, a decrease of σ_{gel} led to higher temperatures.

In terms of thermal parameters, an increase of the thermal conductivity of the transducers had a greater influence than a variation of the thermal conductivity of the gel, although both of them only had an impact on the temperature reached by the scalp. A greater impact was seen when the convection factor, h, and emissivity values, ϵ, of the gel and transducers were changed. As expected, the higher these two parameters the more energy is transferred to the environment (see equations (3.13) and (3.14)) and consequently the lower the temperature values in tissues and transducers.

These results indicate that if new materials are to be sought for these components to decrease temperature maxima then preference should be given to a gel with high electric conductivity and to a gel and transducers with a emissivity value as close to 1 as possible. In patients, the arrays, and consequently the transducers, gel and a part of the scalp, are covered by a medical tape that was not represented in the head model used in this work nor in the models used by other authors (e.g.: [94, 111]). A more detailed discussion of this limitation is provided in the next chapter.

4.5 Limitations and conclusions

In general, it is known that the physical properties vary with the temperature [87, 88, 112]. This means that, for instance, Q_{met} and ω^* should be in fact $Q_{met}(T)$ and $\omega^*(T)$. The importance of this temperature dependence was experimentally observed by different authors. For example, it was shown that the blood perfusion in the human forearm skin can increase as much as 15 times during heating [113]. Given the impact of ω^*_{scalp} in all tissues and MST (table 4.2), it might be possible that the predictions made are overestimating the real temperature distribution, not only in the scalp but in the remaining tissues as well. The sensitivity analysis performed showed that changes in the blood perfusion rate values can have a greater impact than changes in their metabolic heat (table C.2) and consequently if the dependence of the mechanisms on the temperature was accounted for it would possibly lead to lower temperatures in tissues. Despite the importance of accounting for this dependence, there are very few studies that investigated how to do it accurately. One possible approach is by considering a linear relation between each parameter and the temperature as discussed by McIntosh and Anderson [104] and by Rossmanna and Haemmerich [114]. However, as seen in the work by Wenger et al [115], this might not be necessarily true for all tissues as the electric conductivity of the GM and WM seems to vary exponentially with the temperature for a range between 20 and 35 ℃.

Another limitation of these simulations was the fact that the parameters were considered to be uniform and isotropic. Previous works showed that when heterogenous and anisotropic tensors were used for the physical parameters both the EF intensity and temperature maxima varied [48, 93, 116, 117]. For TTFields in particular, it was shown that accounting for the anisotropy of the electric conductivity of the GM and WM yielded variations on the average EF distribution of only 4% in the brain and 10% in the tumor [93] compared to when isotropic electric conductivities were used. Even though these differences are small, it is important to investigate how the temperature varies under these conditions. Including this anisotropy would lead to small changes in equations (3.1), (3.2) and (3.10), as σ^*, σ and ϵ_r would be 3x3 matrices. In electroconvulsive therapy, inclusion of the anisotropy of the skull's thermal conductivity only led to significant temperature changes in the skull itself [48]. In this tissue, the maximum temperature decreased by up

0.6 ℃ compared to when isotropic values were used for the same injected current, but the temperature of the remaining tissues was not significantly affected. Including this anisotropy would also change how the temperature is calculated through Pennes' equation, equation (3.12), as k would be a tensor. However, it is important to mention that using anisotropic physical parameters requires acquiring more data, such as DT images, that are necessary to estimate tensors. One major complication of this is that the results might vary depending on the approach followed [48, 93, 116, 117].

Chapter 5

Sweat as an additional cooling mechanism

Published work

The results presented in this chapter resulted in the following work:

1. **Nichal Gentilal**, Ricardo Salvador, and Pedro Cavaleiro Miranda. A thermal study of Tumor Treating Fields for glioblastoma multiforme. *Brain and Human Body Modeling 2020*, chap. 3, 37-62, 2020. DOI: 10.1007/978-3-030-45623-8_3 – **Book chapter #1**

5.1 Introduction

In the previous chapter, the thermal impact was predicted again accounting for the uncertainty associated with the values assigned to the physical parameters. Even though the results showed that the temperature of tissues and transducers might vary significantly depending on the values assigned to each parameter, the predicted thermal impact did not change compared to what was discussed in chapter 2. In this chapter, an additional study was performed towards a more accurate modelling of the therapy to investigate if the computational results could be corroborated by what was seen in the EF-11 [8] and EF-14 [17] clinical trials. As discussed in section 3.4, some cooling mechanisms that involve energy transfer to the environment, namely convection (equation (3.13)) and radiation (equation (3.14)), were modelled. However, there are others that might also play a significant role in decreasing the temperature of tissues and transducers. As reported by Lacouture et al [37, 38], occurence of sweat in TTFields patients is not an atypical situation. It was observed when the environment was hot and humid, when the patient wore a wig to cover the arrays and when certain medicaments were taken and certain ointments applied.

In hot environments, when the ambient temperature is higher than skin's temperature, sweat is the only way for the body to dissipate heat as it is the only cooling mechanism that is uni-directional [118]. According to Guyton and Hall [119], under normal conditions, the average amount of water lost through sweat is around 0.6 to 0.7 liters per day,

though this value can change depending on environment, physical activity and physiological conditions. As reported by Lim et al [118], the sweating rate can increase by up to 1.0 L per hour in hot conditions and even to 2.0 L per hour in well-trained athletes during exercise. One of the major factors that limits these values is air humidity. In very humid environments, the evaporative sweat losses are significantly reduced, which can compromise the thermal safety of people that are under these conditions for long periods of time. In addition, the type of clothing can also change how much energy is transferred to the environment.

Thus, finding a way to model the sweat losses might help to explain the discrepancies between theory and practice and to improve the accuracy of the results on the thermal impact that were predicted previously.

5.2 Aim

The goals of this work were:

1. Investigate how to model sweat and study its impact on the temperature reached by tissues and transducers when TTFields are applied;
2. Predict the thermal impact when this additional cooling mechanism is also considered and compare it with what was discussed in section 2.2;

5.3 Methods

5.3.1 Model and equations

For this work, the model described in section 3.1 was used and the equations described in sections 3.3 and 3.4 were solved. For the purpose of this study, sweat losses were also accounted for as described in the next subsection. This additional cooling mechanism was considered to occur at the outer boundary of the scalp. The values assigned to each physical parameter were the standard ones presented in table 4.1.

As in Gentilal et al [43], 900 mA of current were injected alternately into each array pair with a switching time of one second. The first 6 minutes of treatment were simulated which took around 36 hours in workstation 1.

5.3.2 Modelling sweat

An equation that could realistically model sweat losses has been sought for a long time. The first attempts could not satisfactorily predict these losses for a practical range of conditions, either environmental or considering all the remaining significant energy processes. Shapiro's equation [120] is typically considered to be the first mathematical expression to correctly model whole-body sweat losses in response to exercise, environment and clothing. In the study that derived this equation, 34 heat-acclimatized subjects walked in a treadmill in different room conditions and wearing distinct outfits [120]. The data obtained allowed the authors to deduce the following equation for sweat losses:

$$F_{sweat,Shapiro} = 18.7\, E_{req}\, (E_{max})^{-0.455} \tag{5.1}$$

where $F_{sweat,Shapiro}$ (W/m^2) are the heat losses through sweat, E_{req} (W/m^2) is the required evaporative cooling necessary to maintain thermal balance, and E_{max} (W/m^2) is the maximum evaporative capacity of the environment.
The values of E_{req} and E_{max} are bounded by the limits:

$$50 < E_{req} < 360\,\mathrm{W/m^2}$$
$$20 < E_{max} < 525\,\mathrm{W/m^2}$$

Both E_{req} and E_{max} are defined as in Givoni and Goldamn [121]. For a cooling effect to occur, the latter should be higher than the former, which is normally the case. In some situations, when air's vapor pressure is too high, such as in humid conditions, an increase in the skin vapor pressure and wetted area is not enough to cool down the body and thus heat storage occurs. Mathematically, E_{req} is defined as:

$$E_{req} = [M_{net} + (R + C)]/1.8 \tag{5.2}$$

The factor 1.8 represents the average surface of the human body (m^2). M_{net} (W) is the metabolic heat load given by the difference between body's total metabolism, M (W), and the external work performed by the subject walking in a treadmill:

$$M_{net} = M - (g\, m_t\, v\, G) \tag{5.3}$$

In the previous equation, g is the gravitational acceleration (≈ 9.8 m/s^2), m_t is the mass of the subject (kg), v the walking speed (m/s) and G the grade (in %) of the treadmill during the experiments. Metabolism can be calculated as:

$$M = m_t[(2.7 + 3.2(v - 0.7)^{1.65} + G(0.23 + 0.29(v - 0.7))] \tag{5.4}$$

At rest, i.e., when v=0 m/s, M is assumed to be 105 W.

The environmental heat load due to radiation, R, and convection, C (both in W), that appears in equation (5.2) is defined as:

$$R + C = \frac{11.6}{clo}(T_{room} - T_{skin}) \tag{5.5}$$

In the former expression, *clo* (1 clo = 0.155 (m^2 ℃/W)) represents the total thermal resistance of subject's clothes, which was a factor of interest in the experiment performed. A value of zero would correspond to a naked person, whereas a value of 1 corresponds to the insulating value of clothing needed to maintain a person at rest in comfort in a room at 21 ℃, with air movement of 0.1 m/s and humidity less than 50%. Typical values for

this parameter and for different outfits can be found in [122].

It is important to note that the metabolic head load, M_{net}, and the metabolism, M, both in W, in equations (5.2) to (5.4) are related to, but they are different than the metabolic heat rate, Q_{met}, in W/m^3, that appears in Pennes' equation, equation (3.7). As discussed in chapter 3, Q_{met} was assumed to be constant throughout the simulations, whereas the values of M_{net} and M vary depending on how fast the subject is walking on the treadmill. Similarly, the environmental heat load due to radiation, R, and convection, C, both in W, whose mathematical expression is given by equation (5.5), are calculated in a different manner compared to the convection and radiation processes expressed by equations (3.13) and (3.14), both in W/m^2.

The value of E_{max} in equation (5.1) is given by:

$$E_{max} = \frac{25.5}{1.8}\frac{i_m}{clo}(P_{skin} - P_{room}) \tag{5.6}$$

where P_{skin} and P_{room} are the vapor pressure in the skin and air (in mmHg), respectively. Similarly to the *clo* factor, the permeability index of clothing, i_m, also depends on subject's clothes [121]. A value of zero means that the fabric is impermeable, whereas a value of 1 means that all the moisture passes through the material. Typical values for different types of clothing can also be found in [122].

Shapiro's equation, equation (5.1), is valid for ambient temperatures between 20-54 ℃ and a relative humidity between 10-90%. This equation was largely used for more than 20 years to predict sweat losses. However, a more recent study [123] showed that this equation might be overestimating the real sweat losses. Additional experimental tests were made with 101 subjects for a wider range of conditions and a correction equation was deduced by Gonzalez et al [123]:

$$F_{sweat,Gonzalez} = 147e^{0.0012F_{sweat,Shapiro}} \tag{5.7}$$

In the latter equation both $F_{sweat,Gonzalez}$ and $F_{sweat,Shapiro}$ are in (g/(m^2 h)). To convert the result to W/m^2 it is necessary to multiply the value obtained from the previous equation by water's latent heat (2410 J/g at 37 ℃) and then by (1/3600 h/s). This correction proved to increase the accuracy of the results by 58% [123]. Additionally, a new sweat piecewise equation was also proposed based on the E_{req} and E_{max} quantities:

$$F^*_{sweat,Gonzalez} = 147 + 1.527E_{req} - 0.87E_{max} \tag{5.8}$$

The latter equation proved to be even more accurate (65%) in predicting sweat losses. The last two equations are valid for ambient temperatures between 15 and 46 ℃, water vapor pressure between 2-37 mmHg and wind speed of 0.4–2.5 m/s.

The large number of parameters that are necessary to specify to model sweat losses through equation (5.8) might lead to results that can be very sensitive to the values assigned to each one of them. In particular, for TTFields, the fabric of the medical tape that covers the arrays and a part of the scalp can retain some of the sweat [38] and thus the values of *clo* and i_m should be the ones of that material at those regions. However, to the best of the author's knowledge, this information is not available in the literature nor

in the datasheet of the most sold medical tapes available in the market (e.g.: [124, 125]).

Due to the lack of information of the most suitable values to use and to minimize the error of using an equation that was not specifically built for the purpose of this work and that is only 65% accurate in predicting sweat losses, constant values were assumed for each parameter that was necessary for the calculation of $F^*_{sweat,Gonzalez}$. The mass of the subject, m_t, was considered to be 70 kg. It was assumed that the patient does not perform intense physical exercise while on treatment and so the walking speed, v, was set to 1.4 m/s and the grade of the treadmill, G, to 0.05%. The thermal resistance of the medical tape, *clo*, was chosen to be 1 as at 21 ℃ the patient is most likely to be comfortable and not feeling hot nor cold in the head. Based on what was reported by Lacouture et al [38], the medical tape retains some of the sweat so it is not entirely permeable. Thus a value of 0.5 was assumed for the permeability index of clothing, i_m. Similar to what was used in equations (3.13) and (3.14), the temperature of the room, T_{room}, was assumed to be 24 ℃, whereas the temperature of the skin, T_{skin}, was assumed to be 33 ℃ which is around the temperature of the exposed scalp in the regions that would be covered by the medical tape if it was represented, according to figure 2.7 (page 31). The vapor pressure in the skin, P_{skin}, and air, P_{room}, were assumed to be 37 and 22 mmHg, respectively, and they were calculated for the aforementioned temperatures using Antonie's equation [126]. For all the values reported above, the sweat rate was calculated using $F^*_{sweat,Gonzalez}$ (equation (5.8)) and it yielded 125 W/m^2. This value was used in the simulations and the thermal impact was predicted once again considering this additional cooling mechanism.

5.4 Results and discussion

5.4.1 Temperature distribution

In figure 5.1, the temperature distribution when sweat losses were added to the model is presented. This figure is comparable with figure 2.7 (page 31), in which the temperature distribution was obtained accounting for the same heat transfer mechanisms except sweat.

Comparing these two figures, one can conclude that the maximum temperature reached by each tissue remained pratically the same as when sweat was not considered: 42 ℃ in the scalp (no change), 39.3 ℃ in the skull (-0.1 ℃), 38.9 ℃ in the CSF (-0.1 ℃), and 38.1 ℃ in the brain (no change). Due to this reason, the thermal impact predicted did not change compared to what was reported previously. The main difference was observed in terms of temperature minima in every tissue as a result of this additional cooling mechanism.

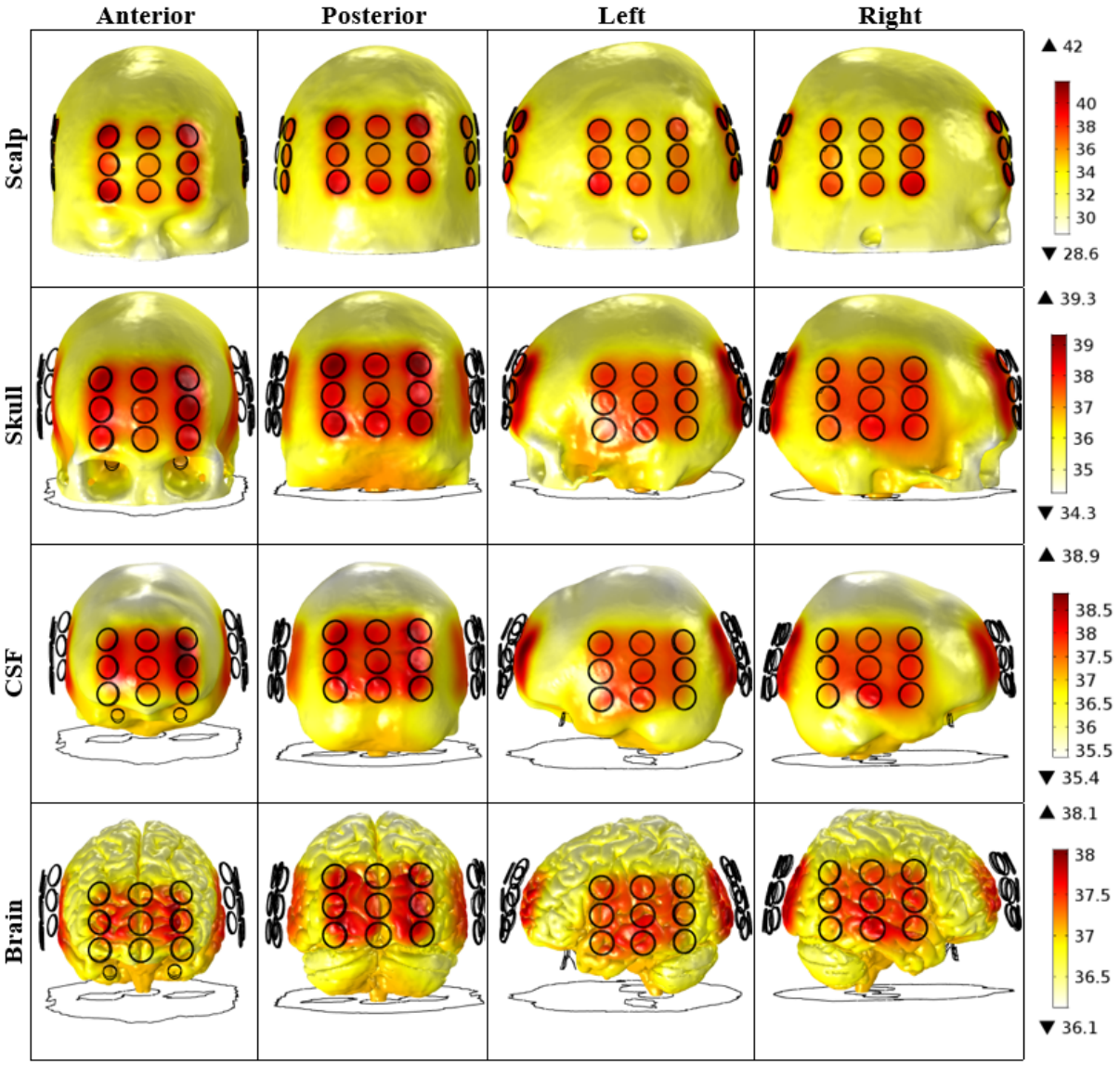

Figure 5.1: Temperature distribution, from four different perspectives, on each tissue surface at the end of the simulation (t=360 seconds) when sweat was considered for the outer boundary of the scalp. Once again, the temperature increases occurred mainly underneath the MST, which was the same as before, and were very localised. Each circle represents the position of one transducer. First row: scalp; Second row: skull; Third row: CSF; Fourth row: Brain. In the latter, the maximum temperature was reached at the GM surface. Scales are different for each row. All values are in ℃.

5.4.2 Effect of sweating on the duty cycle

The maximum temperature of the transducers, in general, and of the MST, in particular, did not change compared to what was presented in chapter 2, as the same value for T_{lim} was used in equation (3.11). However, adding sweat changed the amount of heat that flowed from the scalp to the gel and from the gel to the transducers. As the scalp cooled down through one more mechanism, the energy transfer between the system scalp-gel-transducer became more efficient and thus the cooling time to decrease the temperature of the MST to values below the 40.4 ℃ after an intermittent operation of the device was reached was reduced from 3-4 seconds, when sweat was not accounted for in the simulations, to 2 seconds, when it was. On the other hand, the heating time to increase

MST's temperature to a value above T_{lim} was 2 seconds in both cases. Under these conditions, current was injected the same amount of time in the AP and LR pairs. This means that both ON_{AP}^{sweat} and ON_{LR}^{sweat} were 0.5. Thus, the effective ATV1, calculated through equation (2.3), was:

$$ATV1_{eff}(\%) = \frac{1}{2}\big(0.5 \times 13\% + 0.5 \times 72\%\big) = 21.3\%$$

This value is higher than the 13.9% obtained when sweat was not considered and it provides a more optimistic prediction for treatment outcome. This implies that the modelled cooling mechanisms play a significant role when one wants to study the effectiveness of TTFields treatment based on the temperature variations.

5.5 Limitations and conclusions

In this work, energy exchanges through sweat were accounted for using Gonzalez's equation (equation (5.8)). One of the main limitations of this work was that there was no certainty that this equation was valid for the conditions in which it was used. Firstly, as mentioned in section 5.3.2, this equation was drawn for subjects walking on a treadmill under a controlled environment that does not mimic the circumstances in which treatment is performed in TTFields patients. It is also known that the number of eccrine glands varies depending on the region of the body, but it is commonly believed that the forehead has one of the highest density of these glands [127]. Thus, theoretically, the sweat rate would be higher if it was measured at this region and consequently the equation would most likely have different coefficients. For TTFields patients in particular, the arrays are placed on the forehead, and according to figure 5.1, this was also the region where the temperature increased the most as the anterior array was placed there. It was also discussed by other authors [37, 38] that sweating is one of the most significant adverse events that occurs in patients as it might partially liquify the gel. This might not only change how treatment is performed but also the heat transfer paths discussed before. Theoretically, the electric conductivity of the gel might also change under these conditions. The scalp also becomes drier underneath the regions where the arrays are placed and consequently changes in the electric properties of this tissue are also expected. Based on the impact of the electric conductivity of the gel and of the scalp on the maximum temperature predicted for tissues and MST (table C.1, appendix C), these variations might significantly influence the computational results. One of the main recommendations for these patients is to change the arrays more frequently (every 3-4 days) and slightly shift their position to avoid maceration, loose arrays due to the moisture and discomfort [38].

In the head model used in this work, the medical tape was not represented and thus the sweat losses could not be accurately modelled. If it was represented, it would be possible to improve the accuracy of the results by assigning specific values for i_m and clo, which still need to be investigated, at the regions where the scalp was covered and a different set of values for these two parameters in the regions where the scalp was in direct contact with the environment. Due to all the limitations described above, a constant value of 125 W/m^2 was assumed for the whole exposed scalp. It is possible to compare this value with the energy exchanges to the environment through convection (equation (3.13)) and radiation (equation (3.14)). Assuming the same values for T_{skin} and T_{room} as the ones

used to predict the sweat losses and using the standard values for the emissivity, ϵ, and convection factor, h, reported in table 4.1 one concludes that the energy exchange through convection is around 36 W/m^2, whereas it is slightly higher through radiation, around 56 W/m^2. This means that in this study, energy transfer to the environment occured mainly through sweat, which is most likely to be an overestimation of what occurs in a real case. In future work, and in the absence of a validated equation that models sweat losses for TTFields, it would be useful to perform a sensitivity analysis of the value used and investigate its impact. The value chosen for this mechanism might also significantly affect the conclusions drawn in terms of Optune's current injection time. Based on what is presented in subsection 5.4.2, the duty cycle improved and current was injected in both pairs for the same amount of time. If a higher value for the sweat rate was chosen the duty cycle could have been even higher and the effective ATV1 could be increased.

In terms of thermal impact, accounting for the sweat losses did not yield a different prediction compared to what was discussed in the previous chapters. As the temperature limit in the transducers, 40.4 ℃, was the same as before, temperature maxima in tissues remained unaltered, but the minima decreased. These results point out to the possibility that the discrepancies between *in-silico* data and the reports from clinical trials might be explained by a higher value used for T_{lim} compared to what is considered in a real treatment. This hypothesis is explored in more detail in chapter 7.

The results discussed in this chapter indicate that although modelling sweat can be very difficult, it is still relevant for the study of heat transfer during Tumor Treating Fields. However, as there is still a lot of uncertainty on how to do it, this cooling mechanism will not be considered in the next chapters to avoid an additional source of error in the results.

Chapter 6

Study of a new current injection mode

Published work

The results presented in this chapter resulted in the following work:

1. **Nichal Gentilal**, Ricardo Salvador, and Pedro Cavaleiro Miranda. A thermal study of Tumor Treating Fields for glioblastoma multiforme. *Brain and Human Body Modeling 2020*, chap. 3, 37-62, 2020. DOI: 10.1007/978-3-030-45623-8_3 – **Book chapter #1**

2. **Nichal Gentilal** and Pedro Cavaleiro Miranda. Continuous versus intermittent application of electric fields during TTFields for glioblastoma treatment. *2021 Global Medical Engineering Physics Exchanges/Pan American Health Care Exchanges*, 1-4, 2021. DOI: 10.1109/GMEPE/PAHCE50215.2021.9434835 – **4-page abstract #2**

3. **Nichal Gentilal** and Pedro Cavaleiro Miranda. Continuous versus intermittent application of electric fields during TTFields for glioblastoma treatment. *15th Global Medical Engineering Physics Exchanges (GMEPE) and Pan American Health Care Exchanges (PAHCE)*, 15th-20th March 2021, virtual conference – **Oral presentation #7**

6.1 Introduction

The first TTFields computational study was published in 2014 by Miranda et al [81] in which the authors quantified the electric field distribution in the head and predicted treatment effectiveness by injecting 900 mA of current into each array pair. The impact of the uncertainty of the values of the electric parameters on the EF distribution was published later on by Wenger et al [93] following the same approach. Similarly, a handful of other studies were published in which this specific amount of current was injected. Among these studies, the importance of personalized array placement was investigated by Wenger et al [82] and by Korshoej et al [94], the advantages of performing a craniectomy to enhance the EF in the head was studied by Korshoej et al [111], and the thermal impact was predicted by Gentilal et al [43]. In the NovoTAL system that is used to create personalized treatment maps for each patient, the best treatment layout is chosen based

on geometrical measurements of the head and on the results of computational simulations when 900 mA are injected [39].

However, the results presented in Gentilal et al [43] and that are depicted in figures 2.5 and 2.6 showed that injecting 900 mA alternately into each pair with a switching time of one second leads to an intermittent operation of the Optune device. This is a consequence of the thermal restrictions that are necessary to ensure patient's safety. Thus, the results presented in the studies described above might be seen as the best-case scenario as they assume that current is injected continously and that the EF in the tumor is constant during all treatment time. As seen in the *post-hoc* analyses performed by Kanner et al [32] and Toms et al [35], the time that the patient is under treatment significantly impacts the overall survival. Based on the results from these studies, the minimum recommended daily usage of TTFields is 18 hours. In the previous chapter, it was seen that even when sweat was accounted for the time that current was injected was only 50% of these 18 hours due to the thermal restrictions. This might explain why such a high daily compliance is needed in patients. Thus, investigating by how much does the current needs to be reduced compared to the 900 mA to allow for an uninterrupted treatment might help to improve TTFields therapy as the time that the patient is effectively under the action of the EFs is maximized.

6.2 Aim

The goals of this work were:

1. Investigate by how much current had to be reduced to reach an uninterrupted treatment and study if it might increase treatment efficacy based on the effective electric field in the tumor;

2. Predict the thermal impact for this new operating mode and compare it with what was discussed in section 2.2;

6.3 Methods

6.3.1 Model and equations

The model described in section 3.1 was used and the equations described in sections 3.3 and 3.4 were solved. For the purpose of this study, it was necessary to vary how much current was injected into the array pairs (equation (3.3)), and the current control condition (equation (3.11)), as described in the next subsection.

The values assigned to each physical parameter were the standard ones presented in table 4.1.

6.3.2 Current injection mode

The same amount of current was injected in both array pairs alternately with a switching time of one second. To investigate how much current could be injected for the temperature of the transducers to not surpass the critical value, T_{lim}, of 40.4 ℃, an iterative process

was followed. The value of V_0 in equation (3.3) was changed in each iteration based on the maximum temperature that the MST would reach if there was no current shutdown. Mathematically, this implies changing the Joule heating term to:

$$Q_{JH} = Q_{JH}^{AP}\, pulse(t) + Q_{JH}^{LR}\, pulse(t+1) \tag{6.1}$$

which is different from equation (3.11) as there is not any restriction on the application of the EFs based on the temperature of the transducers.

Each simulation took around 36 hours to compute in workstation 1. After each simulation was completed, the temperature variation of the most significant transducer was retrieved and a curve fitting was performed to that data. The general equation fitted was:

$$T = C_1(1 - exp(-t/C_2)) + C_3 \tag{6.2}$$

where C_1 (℃) represents the maximum contribution that the EFs have in increasing the temperature of the MST, C_2 (s) is a time constant related to how quick the transducer heats up and C_3 (℃) represents the initial temperature of the MST.

The maximum steady-state temperature, T_{max}, that the MST will reach can be predicted by:

$$T_{max} \equiv \lim_{t\to\infty} T = C_1 + C_3 \tag{6.3}$$

Curve fitting was performed using Matlab's curve fitting toolbox (cftool).

Several iterations were performed until the value of T_{max} was close to 40.4 ℃. The choice of the general form in equation (6.2) is justified by the results shown in the next section.

6.4 Results and discussion

6.4.1 Investigation of the critical current I_C

As discussed previously, in this model the MST was located in the anterior array. The variation of the average temperature of this transducer as a function of the total current injected into each array pair is presented in figure 6.1.

In table 6.1, the values obtained for each coefficient after curve fitting was performed are presented, as well as the adjusted-R^2 (A-R^2), for each case. As it can be seen, the value of current that led to a prediction of a T_{max} around 40.4 ℃ in the MST was 675 mA, which was named as the critical current, I_C.

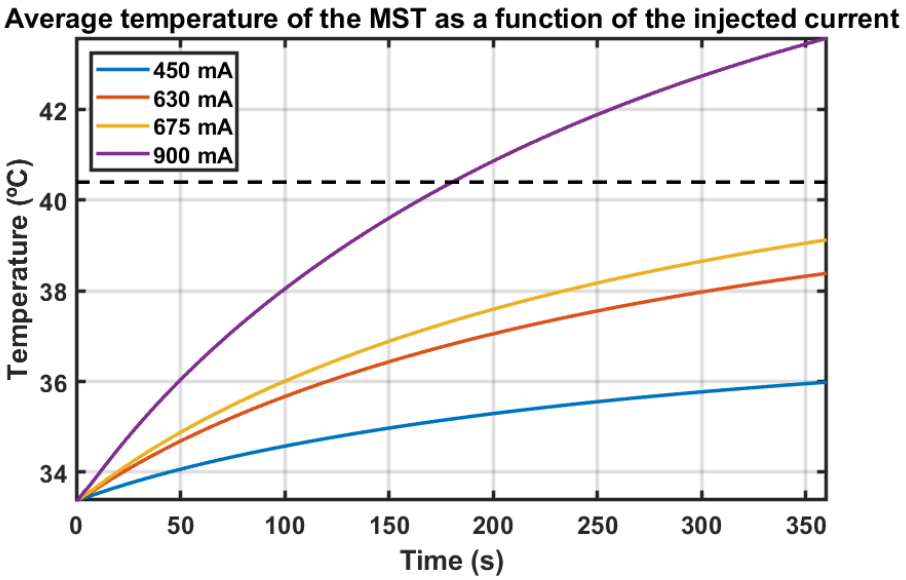

Figure 6.1: Variation of the average temperature of the MST as a function of the current injected when no current control was implemented. The same amount of current was injected in both pairs with a switching time of one second. The black dashed line represents the limit temperature, T_{lim}, of 40.4 ℃.

Table 6.1: Curve fitting parameters for the different simulations performed. The values of the adjusted-R^2, $A - R^2$, suggest that equation (6.2) can explain very well the temperature variation of the MST when TTFields are applied.

Injected current (mA)	C_1 (℃)	C_2 (s)	C_3 (℃)	A-R^2	T_{max} (℃)
450 (0.50 I_0)	3.19	222	33.4	0.9998	36.6
630 (0.70 I_0)	6.15	222	33.4	0.9998	39.6
675 (0.75 I_0)	7.17	222	33.4	0.9998	40.6
900 (I_0)	12.50	222	33.5	0.9998	46.0

The high values of A-R^2 indicate a very good agreement between equation (6.2) and the temperature increases when TTFields are applied. As before current injection the head was in thermal equilibrium with the environment, these increases are only due to the application of the fields. Other general equations were fitted to the data (first- and second-order polynomials and quadratic), but none of them led to better results.

The heat transfer pathways discussed in subsection 4.4.2 help to understand why the exponential variation was the most suitable one. The MST cools down through convection and radiation and it heats up through conduction. The heat comes from the scalp, which in its turn, heats up due to the Joule effect and metabolism and cools down through conduction and blood perfusion. When current starts to be injected, the Joule effect is immediately responsible for increasing the temperature of the tissue as it does not depend on a temperature difference (equation (3.7)). However, both cooling mechanisms depend on a temperature gradient. The heat transferred through conduction depends on the temperature difference between the hottest region of the scalp and the temperature of the skull, gel and coolest regions of the scalp itself. On the other hand, cooling through blood perfusion depends on the difference between scalp's and blood's temperature and only occurs when the temperature of the first is higher than 36.7 ℃ (equation (3.8)).

Thus, at the beginning of treatment, the temperature increases significantly due to the application of the fields. The more current is injected the quicker is this temperature rise, as it can be seen in figure 6.1 and by the value of C_1 in table 6.1. At some stage, the temperature gradient becomes high and more energy starts to be transferred through conduction and perfusion, which will result in a steady state temperature in the scalp that corresponds to the maximum temperature that this tissue reaches. Based on this behavior, the variation of the temperature of the transducers follows the same general equation. The main differences are that heating in the MST occurs only through conduction and cooling through convection and radiation. The latter two also depend on a temperature difference between the transducer and the environment. A comparison of the behavior of the temperature variation of the scalp, gel and MST when 675 mA were injected is presented in figure 6.2, which corroborates what was described above.

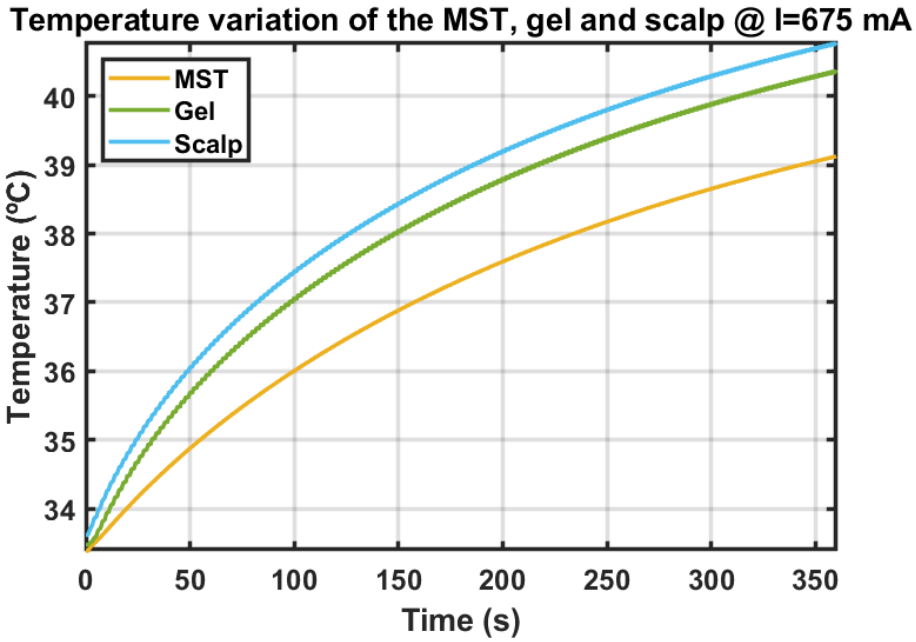

Figure 6.2: Variation of the average temperature of the MST and of the maximum temperature of the gel and scalp underneath that transducer when 675 mA were injected into each pair alternately with a switching time of one second. The temperature variation follows an exponential behaviour in all three cases.

In table 6.1, the value of C_3 was practically the same in all cases as it corresponded to the initial temperature of the MST. The reason why it was not kept constant during the curve fitting was because when it was done it led to a more pronounced underestimation of the temperature variation at the end of the simulation compared to when it was set as a free parameter (data not shown). The value of C_2 is related to how quickly this transducer reaches its maximum temperature. As it can be seen in figure 6.1 and table 6.1 it does not depend on the temperature difference with the environment, which increased as more current was injected, nor on the injected current itself. However, it does depend on the energy transfer from the scalp and gel, due to the temperature differences illustrated in figure 6.2. A similar behaviour to the one presented in the previous figure was observed when 450, 630 and 900 mA were injected. The fitted coefficients C_1, C_2 and C_3 might change depending on how much time is simulated, as shown by the results of study A in appendix D. Ideally, more treatment time should be simulated until the temperature variation of the MST reached a steadier value. However this would also increase the

simulation time and thus a trade-off had to be reached.

The exponential variation expressed by equation (6.2) is not unique for TTFields. The same temperature behaviour was seen in the computational work by Ozen et al [128] in which the authors investigated how skin's temperature varied when exposed to microwave radiation. The same work showed that when the application of the fields was ceased, the temperature variation also followed an exponential decay expressed by the following general equations:

$$T^{noEFs} = C_4\, exp(-t/C_5) + C_6 \tag{6.4}$$

$$T_{min}^{noEFs} \equiv \lim_{t\to\infty} T^{noEFs} = C_6 \tag{6.5}$$

in which C_4 (℃), C_5 (s), and C_6 (℃) are coefficients that can be obtained by fitting the data. The latter equations mean that when the fields are shutdown the temperature of tissues tends to their initial value, C_6. Other studies can be found in the literature that corroborate the exponential variation of the temperature of tissues for both heating and cooling [129, 130]. The same cooling behaviour was seen for the MST when current was shutdown at t=360 seconds, regardless of the injected current (figure 6.3).

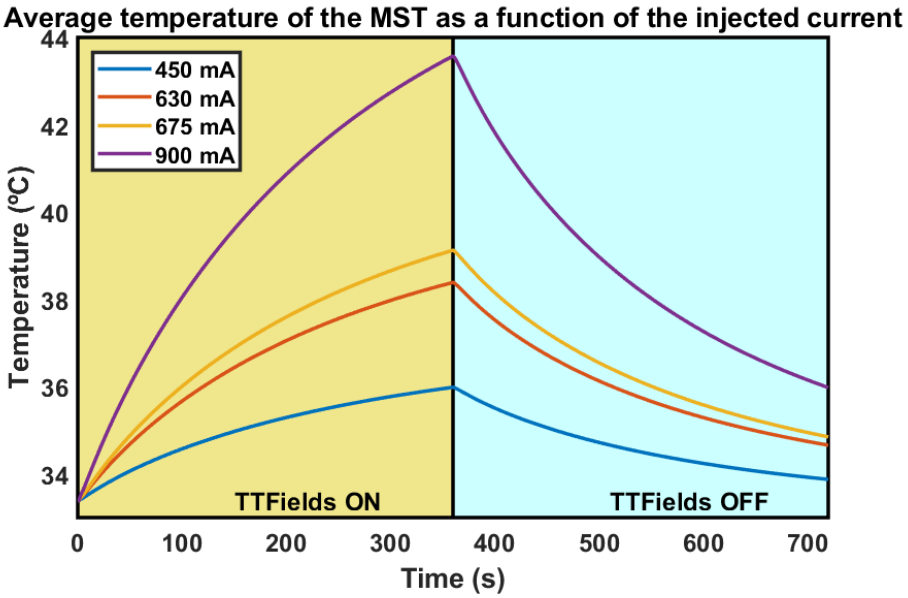

Figure 6.3: Variation of the average temperature of the MST when current injection was completely ceased (TTFields OFF). The temperature of the transducer tends to its initial temperature regardless of the current that was previously injected.

The coefficients C_4, C_5 and C_6, obtained from curve fitting, are presented in the next table for the temperature variation observed when the application of the fields was ceased.

Table 6.2: Curve fitting parameters for the different simulations performed. The values of the $A - R^2$, suggest that equation (6.4) can explain very well the temperature variation of the MST when current injection is ceased.

Injected current (mA)	C_4 (℃)	C_5 (s)	C_6 (℃)	A-R^2
450 (0.50 I_0)	2.50	203	33.5	0.9997
630 (0.70 I_0)	4.36	196	34.0	0.9997
675 (0.75 I_0)	5.02	199	34.1	0.9997
900 (I_0)	8.87	196	34.6	0.9997

The values of the A-R^2 indicate a very good agreement between the data obtained from the simulations and equation (6.4), thus indicating an exponential decay of the temperature when the EFs were shut down. In theory, the values of C_4 and C_6 should be the same ones as C_1 and C_3, respectively, because before current injection the head was in thermal equilibrium with the environment. The values of C_2 and C_5 do not need to be exactly the same as they depend on the overall contribution of the different energy mechanisms and during cooling there was no Joule effect. The reason why the values of C_4 and C_6, presented in the previous table, did not match the values of C_1 and C_3, reported in table 6.1, was investigated through an additional study, study B, which is discussed in appendix D. The results obtained from this study indicated that this discrepancy is mainly explained by an overestimation of the coefficient C_6 and consequently an underestimation of C_4. The analysis made based on when the fields were shutdown corresponds to a case in which the starting point does not correspond to the maximum temperature that the MST could have reached when the fields were applied. Consequently, the situation analysed is similar to what was mimicked in studies B1 to B4, in which the time-derivative of the temperature variation is lower compared to if the analysis was made with an initial temperature of T_{max}. This led to less accurate predictions of the values of the coefficients.

The importance of the current control discussed at the beginning of subsection 2.2.3 is corroborated by the values of T_{max} presented in table 6.1. In the absence of a temperature limit, the MST would reach 46.0 ℃ when 900 mA were injected after just 6 minutes. Under these conditions, the scalp would reach a maximum temperature around 47.5 ℃, which is enough to cause scalp burns and to compromise patient's safety, as discussed in Moritz and Henriques [86].

The data presented in the same table indicates that the maximum amount of current that can be injected in both pairs without the transducers reaching the temperature limit of 40.4 ℃ is around 675 mA. This critical current corresponds to a decrease of 25% compared to the 900 mA that are typically considered in TTFields computational studies. In terms of power density, this variation translates into a reduction of 44% in the Joule heating term (equation (3.10)) that appears in Pennes' equation (equation (3.12)).

6.4.2 Temperature distribution

The temperature distribution at the end of the simulation when the critical current was injected in both pairs alternately with a switching time of one second is presented in the next figure.

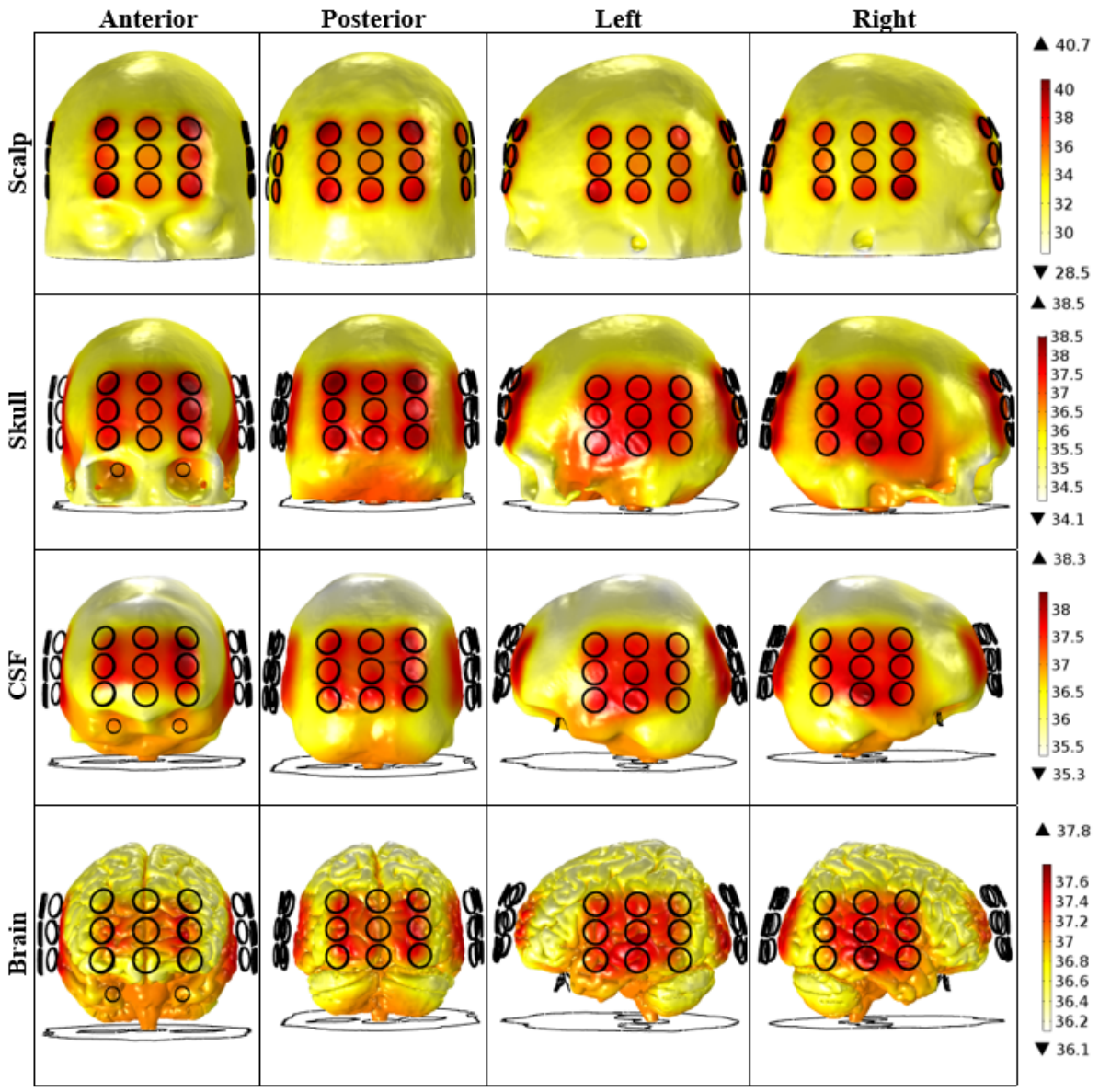

Figure 6.4: Temperature distribution, from four different perspectives, on each tissue surface at the end of the simulation (t=360 seconds) when 675 mA were injected in both pairs alternately with a switching time of one second. As before, the temperature increases occurred mainly underneath the arrays. Each circle represents the position of one transducer. First row: scalp; Second row: skull; Third row: CSF; Fourth row: Brain. In the latter, the maximum temperature was reached at the GM surface. Scales are different for each row. All values are in ℃.

The temperature increases follow the same pattern as the one observed in figure 2.7 (page 31) where temperature maxima occured at the surface of each tissue and mainly underneath the regions where the arrays were placed. When 675 mA of current were injected, temperature maxima at the end of the simulation were lower in every tissue compared to what was reported when 900 mA were injected (figure 2.7), as expected. According to equation (6.2) and the data presented in table 6.1, it takes 222 seconds, i.e., 3.7 minutes, for the contribution of the EFs in increasing the average temperature of the MST to reach 63% of its maximum. The same data allows to conclude that to reach 90% of the maximum value it takes just 8.5 min. For the critical current, this maximum temperature is around 40.4 ℃, which means that the temperature distribution

of tissues shown in figure 6.4 will tend quickly to the one presented in figure 2.7 in which Optune was working in an intermittent mode and MST's temperature was 40.4 ℃. Due to this reason, the thermal impact predicted for this new operating mode led to the same conclusions as before.

6.4.3 The duty cycle of a continuous treatment

The fraction of time that both pairs were active was 1 (100%) when the critical current was injected. However, the cost of reducing current was a decrease on the values of the ATV1 in the tumor in both directions. The ATV1 for the AP pair was already very low when 900 mA of current were injected, 13%, a value much lower than the 72% induced by the LR pair. When 675 mA were injected, the ATV1 for the first dropped down to 0%, thus leading to an ineffective pair for treatment, whereas the ATV1 for the complementary pair decreased to 39%. Thus, the effective ATV1 was:

$$ATV1_{eff}(\%) = \frac{1}{2}\big(1.0 \times 0\% + 1.0 \times 39\%\big) = 19.5\%$$

This value is higher than the 13.9% observed for an intermittent operating mode (chapter 2), but lower than the 21.3% reported in chapter 5 when sweat was also considered as a cooling mechanism. Thus, the choice of the best operating mode based solely on the value of the effective ATV1 is sensitive to the representation of the energy transfer mechanisms. An additional aspect that plays a crucial role on this choice is the ATV1 of each pair. As seen in the *in-vitro* work by Kirson et al [16], TTFields can significantly affect tumoral cells division when the EF intensity at the tumor bed is at least 1 V/cm. Furthermore, it was also shown in that study that applying the electric fields in two perpendicular directions alternately increases the number of cells arrested by 20%. Although a continuous application of the EFs was achieved in this study when current was reduced from 900 to 675 mA, the EF strength in the tumor was not enough to reach 1 V/cm in the AP direction, thus making this pair ineffective for therapy. The ATV1 produced by the LR pair decreased from 72% to 39%, which was enough for the value of the $ATV1_{eff}$ to be higher than the one obtained for the intermittent operating mode, even though a continuous application of current is not, most likely, the best treatment option. This shows that this metric might not be the best one to use to choose between operating modes as it might mask the inefficiency of one pair if the other contributes significantly more to treatment. A continuous operating mode might be beneficial for tumors located in more superficial regions of the brain as the electric field would most likely be higher for both pairs than what was seen in this study. In that case, a reduction in the injected current could be compensated by a longer application of the EFs.

6.5 Limitations and conclusions

The results obtained in this chapter were drawn by fitting the temperature variation observed to a general expression. Even though the adjusted-R^2 indicated a very good agreement between the current injected and the temperature reached by the MST, more work needs to be done to validate this equation and investigate its limitations. The results

presented in appendix D highlight that the time simulated might influence the values of the coefficients obtained and consequently it will also impact the conclusions in terms of how much current can be injected into the arrays. Ideally, simulations should be done in which the MST reaches a value very close to its steady-state. However, it is unfeasible to follow this approach for every study as the computational time would require a few days. Thus, there must a trade-off between the accuracy of the results and the time simulated to attain them.

The results of this work showed that it is still necessary to find better metrics to combine the important aspects of TTFields treatment. The electric field in the tumor, which is what defines whether the therapy is effective or not, has to be maximized. However, the more current is injected into the arrays the quicker the MST increases its temperature and consequently the more regularly the fields will be shutdown to ensure that the thermal restrictions of Optune are met. In this study, an alternative way to inject current was investigated and compared with the standard operating mode of the Optune device. The cost of applying the fields for longer periods of time was a reduction in the electric field in the tumor, which might compromise the applicability of this new current injection mode in some cases. For this head model in particular, the field intensity in the AP direction was the most affected one given the distance from the anterior and posterior arrays to the tumor, as discussed in subsection 2.2.1. Even though the effective ATV1 was higher for the continuous mode compared to an intermittent application of the fields when no sweat was considered, the efficacy of the therapy will most likely be higher for the latter as the ATV1 surpassed the therapeutic threshold in both directions. However, for other tumor positions, head models and array layouts, the decrease in the current injected might be compensated by the applications of the EFs for longer periods of time. In particular, more superficial tumors might benefit from this alternative current injection method.

As discussed in chapter 1, one important limitation in the efficacy of treatment is that the time that current is injected in both pairs depends only on the temperature of the most significant transducer. This leads to current being applied less time in the pair that does not include the MST, as it occurred with the LR pair in this head model. Another important question that remains unanswered has to do with the prediction of the thermal impact. The temperature increases reported in subsection 6.4.2 led to the same predictions as the ones reported in subsections 2.2.4 and 5.4.1. These results may not be surprising as the maximum temperature that each tissue will reach depends on the value of the critical temperature that the transducers are allowed to reach (equation (3.11)). Thus, before measuring the values of the physical parameters to improve heat transfer modelling and studying additional ways to inject current, it is necessary to investigate if the assumptions considered in chapter 3 have to be modified to improve the accuracy of the results obtained. This is the main focus of the next chapter.

Chapter 7

Improving TTFields modelling: Analysis of Optune's current injection algorithm and log files

Disclosure

Nine months after this thesis had started, a visit was made to Novocure's headquarters in Haifa, Israel. The main goal of that visit was to share the results that were obtained and discussed in the previous chapters, and also to get feedback to improve the computational modelling of heat transfer during TTFields, as well as to define future work that could be useful for the company. Due to the confidentiality agreement, some relevant information that was provided by Novocure could not be disclosed in detail in this chapter. For the same reason, the amount of results presented was kept to the minimum and, instead, a general discussion is provided to highlight the main outcome of this meeting and subsequent work. This discussion is divided into three parts: 1) A brief description of the main changes in the dimensions of the arrays; 2) An analysis of the current injection algorithm; and 3) An analysis of the log files from one patient.

7.1 Array dimensions

In the head model described in section 3.1, each array consisted in a 3x3 matrix of transducers, whose center was separated by 22 mm in one direction and by 33 mm in the other. As depicted in figure 3.2, these arrays covered a significant area of the scalp. However, head coverage was increased even more in the new generation of arrays, in which the 33 mm were augmented to 44 mm. This increment allows to reduce the current density in the head and thus might also allow to decrease temperature maxima in tissues for the same injected current. On the other hand, bigger arrays can also induce a more uniform electric field in the head. This might improve treatment outcomes in patients who have metastasis in different regions of the head as more tumoral cells are affected by the EFs. However, EF maxima can also be reduced in other regions of the head. Another difference in the arrays is the size of the transducers. The radius of each transducer increased from

9 mm to 10 mm, while its thickness remained at 1 mm.

7.2 Analysis of Optune's current injection algorithm

As described in chapter 3, the current injection algorithm was modelled through equation (3.11) in which the same amount of current, 900 mA, was injected alternately into each pair with a switching time of one second. Whenever the average temperature of any of the 36 transducers reached the critical limit, T_{lim}, of 40.4 ℃, current was completely shutdown and it was only resumed when the temperature of all transducers was below that value. To investigate how current is injected in patients, Novocure disclosed the algorithm implemented in the Optune system. Compared to the assumptions mentioned previously the main differences were:

1. The temperature is not monitored at the transducers, but on the surface of the scalp at the interface between this tissue and the gel. By considering the temperature of the scalp, temperature maxima will decrease everywhere compared to what was obtained in the previous chapters. As explained in chapter 2, there is no Joule effect in the transducers as they are capacitively coupled to the scalp. Instead, the temperature increases that occur there are explained by heat conduction from the scalp and gel as the latter two are at a higher temperature than the transducers. Thus, controlling the temperature of the scalp means that current injection depends on the highest temperature reached during treatment, which is a better and safer approach;

2. The optimal working temperature is 39.5 ℃ and not 41 ℃. As mentioned previously, the threshold of 41 ℃ was used based on the information available in the literature [37] at the time that the thermal studies started being performed. This higher temperature limit led to the prediction of some physiological effects that were presented and discussed in the previous chapters, but that were not corroborated by the results from clinical trials. Thus, based on this new information, the thermal impact predicted might not hold if this new threshold is considered in the computational studies;

3. Current injection is made independently for each array pair and it does not have to be necessarily the same. Up until now, all the studies performed assumed that there was a complete current shutdown in both directions whenever the MST reached the temperature limit, as shown in figures 2.5 and 2.6. In all studies already discussed, this implied that the current injected into the LR pair was also set to zero when the temperature limit was reached, even though the most significant transducer was located in the AP pair. Consequently, the predicted treatment efficacy was underestimated as the duty cycle was lower. For an independent current injection mode there will be two most significant transducers, one for each pair. As discussed at the end of subsection 2.2.2 this was also one of the methods suggested to improve current injection time. Under these conditions, current injection in the LR pair increased from 30% to 46% of the time that device was being used for treatment, whereas in AP's it remained at 47%;

4. The amount of current that is injected is not 900 mA if the temperature is below the optimal value and zero mA if it is above, but it can assume any value between 400

and 1000 mA. The current that is injected depends on the temperature of the scalp at the present and past moments. This approach allows for a more controlled current injection as it reduces the impact of temperature spikes due to technical problems that might occur (e.g.: due to a bad contact between the transducer and the scalp, which might lead to an incorrect temperature reading). Furthermore, significant changes on the injected current are also avoided when the patient goes from one environment to another in which the temperature might be very different. As a result, the temperature variations on the scalp, and consequently on the remaining tissues, are slower which is more comfortable and safer for the patient.

5. When the temperature is below the critical limit, the amount of current injected is not always varying. The main advantage of this approach is that it increases the lifetime of the electronic components and it avoids drastic variations in the electric field induced in the tumor when there are temperature spikes (e.g.: due to a bad contact between the transducer and the skin or when the patient changes between two very different environments);

6. Each array has only 8 thermistors, being the transducer placed at the center of the array the one whose temperature is not monitored. Based on what was reported in subsections 2.2.1 and 2.2.2 this transducer is the one whose temperature varies the least. Due to the edge effects, more current is injected in the outer transducers of each array and consequently the Joule effect underneath them is also higher compared to the remaining transducers of the same array. Thus, given that the region of the scalp underneath the central transducer is not where temperature maxima is reached, it is not necessary to control its temperature for current injection purposes. Additional information about the arrays and the remaining hardware can be found in Wasserman et al [131].

Based on the information provided by Novocure, the current injection algorithm implemented in the computational simulations was fine-tuned. To investigate whether it was possible to implement the real current algorithm in simulations or not, a simplified head model was created. This model consisted in two transducers, gel and a multi-layer sphere representing the scalp, skull, CSF and brain. The diameter of the outermost layer was 20 cm. To implement the algorithm, it was necessary to use the "events (ev)" interface in COMSOL Multiphysics, alongside with the ones described in subsection 3.5. This interface restarts the solver at given times specified by the user, which was necessary to reproduce Optune's algorithm. However, reinitializing the solver frequently significantly increases the computational time even for simple models. It took around 24 hours to simulate just the first 30 seconds of treatment in workstation 2. As the temperature varies more slowly when the real algorithm is used compared to the algorithm considered so far, it would take several weeks to have results from which some conclusions could be drawn. Thus, a different approach had to be considered, which could accurately represent the temperature variations, but that could also allow for pratical computational times. One possible way to do this is described in section 7.4.

7.3 Analysis of patients log files

Besides sharing the algorithm, Novocure also provided log files from a part of the treatment administered to patient 1020204. The log files are data that are stored in Optune's

memory bank and that are downloaded by the treating physician from time to time [98]. As reported by Hershkovich et al [132], these files contain information about the voltage, current and impedance of each array throughout therapy, as well as treatment compliance. The temperature recorded by each thermistor is also logged in regularly, among other data. By analysing these files it was possible to investigate and better understand not only how the temperature varies throughout treatment, but also some other important aspects of the therapy:

1. The impedance of each pair is not the same and it can vary throughout treatment. As it was discussed in chapter 2, the resistance of the head in the anterior-posterior direction is often higher than in the left-right direction. Furthermore, given that the dimensions of the head are different for each patient, there is also a significant inter-subject variability of the resistance values. However, an analysis of this parameter is useful to fine-tune the electric parameters assigned to each tissue of the head and to make sure that the impedance of the model is within what is seen during treatment. A similar approach was followed in the work by Hershkovich et al [132], in which TTFields were applied to the torso in patients with pancreatic cancer that participated in the panova clinical trial. In that study, the dielectric properties of tissues of the abdomen were investigated by comparing the impedance seen in the log files with the one obtained through computational models. For the head model described in subsection 3.1 and for the standard physical parameters presented in table 4.1, the impedance of the head in the AP direction was 104 Ω, whereas in the LR direction it was 77 Ω. Both these values are higher than the ones seen in the log files provided, which were around 60 Ω for both pairs in patient 1020204. Additional information shared by Novocure showed that, on average, the impedance of patient's head is around 70 Ω, although it can vary significantly throughout treatment and even surpass 100 Ω. These variations are most likely explained by changes in the contact between the scalp and the arrays due to, e.g., variations in the electric properties of the gel as a result of patient's sweating, or due to a drier skin underneath the arrays, as discussed in chapter 5.

2. There is not a most significant transducer. Throughout treatment the temperature of each thermistor varies differently and thus there is not one transducer whose temperature is always higher than the others. The rate at which the temperature increases and decreases is not only a function of how much current is injected into each array, but it also depends on the temperature of the environment in which the patient is in, if a physical activity is being performed, if the head is covered or not and even on how good the physical contact between the transducers and the head is. The analysis of the temperature variations allows to have an idea of the time constants associated with the heating and cooling of the scalp, which might be useful to fine-tune the thermal parameters.

Even though these log files have a lot of important information, the inter-subject variability makes it more difficult to know what to use in *in-silico* work. However, based on what was discussed previously some key aspects can be improved when modelling TTFields.

7.4 How to improve TTFields modelling

All the information described in the previous sections allowed to improve how TTFields were modelled. One of the limitations is that the real current injection algorithm is complex and it leads to very long simulation times even for simple models. Thus, an alternative approach had to be sought to improve how this algorithm was modelled that would also allow to compute the simulations in practical time. One method that proved to be a good alternative was to follow the same approach as the one considered in the previous chapter. In the latter, equation (6.2) was used to predict the maximum temperature that the MST would reach as a function of the injected current. Based on what was described until now and given that the MST and the scalp follow the same temperature variation behaviour (figure 6.2), this equation can be used to predict the maximum temperature that the scalp would reach for different values of injected current. The current that leads to a maximum steady-state temperature of 39.5 ℃ on the scalp surface underneath the transducers is a good indicator of the average current injected throughout treatment, as discussed with Novocure. Thus, for heat transfer studies during TTFields therapy, equation (3.11) has to be rewritten as:

$$Q^*_{JH} = Q^{*,AP}_{JH}\, pulse(t) + Q^{*,LR}_{JH}\, pulse(t+1) \tag{7.1}$$

where $Q^{*,AP}_{JH}$ and $Q^{*,LR}_{JH}$ are the power density distributions due to the application of the EFs in the AP and LR directions, respectively. The amount of current injected into each pair is the one that leads to a maximum steady-state temperature on the surface of the scalp of 39.5 ℃ underneath both pairs, predicted through equation (6.3) after an iterative process. The current injected into both pairs does not have to be necessarily the same, as it was assumed up until now, but it is bounded by 400 and 1000 mA.

The electric properties also need to be fine-tuned to decrease the impedance of the model given the difference observed between the computational data and the log files. According to Wenger et al [93], the parameters whose uncertainty leads to the highest variation in the values of the impedance are the electric conductivity of the scalp and skull. Thus, these are the two parameters that will be increased to match the computational impedance with the experimental one, as described in the next chapter. It is also noteworthy to mention that the sensitivity analysis discussed in chapter 4 showed that an increase in these two values leads to a temperature decrease in tissues and transducers. In terms of thermal parameters, the data retrieved from the log files did not allow to accurately conclude about which values to change. Thus, to minimize the error of the calculations, the standard values presented in table 4.1 will continue to be used.

7.5 Impact on the results reported previously

Ideally, the modifications aforementioned should be made to all the studies described until now in order to analyse their impact on the conclusions drawn so far. One of the main changes that might occur concerns the thermal impact predicted. As mentioned several times in the previous chapters, the physiological changes due to the temperature increases were not seen in patients, which can now be explained by an overestimation of the temperature distribution due to a higher value used for T_{lim} and by the fact that temperature was not being monitored in the right region. In terms of the duty cycle, the

values calculated for the $ATV1_{eff}$ might be an underestimation of the real value. This is justified by the independent current injection for both pairs that was not modelled correctly.

The results presented in this chapter represent an important step toward a more realistic modelling of how a TTFields treatment is performed. The impact of this new information is first evaluated using a simplified head model in the next chapter. Then, in chapter 9 a realistic head model is used once again to predict the thermal impact and to suggest methods to account for the temperature during TTFields planning, which is one of the main goals of this thesis.

Chapter 8

Tissue temperature during TTFields treatment planning: simplified head model

Published work

The results presented in this chapter resulted in the following work:

1. **Nichal Gentilal**, Ariel Naveh, Tal Marciano, Ze'ev Bomzon, Yevgeniy Telepinsky, Yoram Wasserman, and Pedro Cavaleiro Miranda. The impact of scalp's temperature in the predicted LMiPD in the tumor during TTFields treatment for glioblastoma multiforme. *Brain and Human Body Modeling 2021* (*in press*) – **Book chapter #2**

2. **Nichal Gentilal**, Ariel Naveh, Tal Marciano, Ze'ev Bomzon, Yevgeniy Telepinsky, Yoram Wasserman, and Pedro Cavaleiro Miranda. Optimization of TTFields planning: the importance of scalp's temperature in the predicted treatment efficacy. *Brain and Human Body Modeling conference: from fast and accurate computational modeling to clinical practice*, 19th-20th August 2021, virtual conference – **Oral presentation #8**

8.1 Introduction

In order to evaluate and quantify treatment efficacy, the percentage of the tumor volume above 1 V/cm has been used throughout this work. This metric proved to be very useful to verify whether a certain pair was able to induce the therapeutic EF intensity at the tumor and which of the two array pairs contributed the most to treatment.

Most recently, a different metric was suggested to quantify the effectiveness of the therapy. By definition, the electric field quantifies the force induced by the field on charged particles and not the energy that is actually deposited in tissues, as it occurs in other cancer treatment planning techniques, such as radiotherapy, where the dose is measured in terms of energy absorbed per kilogram of tissue (SI units: Gy or J/kg). Thus, to make

TTFields planning framework more similar to other techniques, the power density (PD) in the tumor was suggested by Ballo et al [98] to evaluate treatment effectiveness instead of the electric field. This metric is mathematically expressed by:

$$PD = \sigma ||\boldsymbol{E}||^2 \tag{8.1}$$

where, as before, σ is the electric conductivity, $\boldsymbol{E}$ is the electric field vector, and PD is the power density (in W/m^3).

As seen in the work by Ballo et al [98], there is a spatial correlation between the EF and the PD distribution in the head. However, one of the main differences between these two is that the electric field tends to be lower in regions with a high electric conductivity, such as the CSF and ventricles, whereas the PD remains relatively high in these regions thus indicating that the energy deposited is still significant. Similarly to the therapeutic threshold of 1 V/cm in terms of EF, a threshold for the PD can also be deduced. To account for the fact that the fields are applied in two perpendicular directions, the same work suggested to use the local minimum power density (LMiPD). This metric was defined as the lowest of the two power densities induced by each pair in each voxel of the tumor. An investigation was conducted by Ballo et al [98] to find the value for the LMiPD that best divided TTFields patients that participated in the EF-14 clinical trial into two groups with the greateast statistical difference in the overall survival. To deduce this threshold, head models were created for each one of 340 patients with the arrays placed at the same positions as the ones used during treatment. The average monthly compliance and the average electric current injected were retrieved from the log files. Then, the power density distribution for each patient was obtained through computational simulations. Based on that data, the LMiPD value that best divided patients in the two aforementioned groups was 1.15 mW/cm^3. A similar analysis in terms of local minimum electric field intensity (LMiFI) yielded 1.06 V/cm, which was very close to the 1 V/cm seen in *in-vitro* studies [16]. Patients whose LMiPD was below the threshold had an OS of 21.5 months and a PFS of 7.9 months, whereas those who were in the complementary group had an increase of 3.4 and 0.3 months in these two endpoints, respectively.

By comparing equation (8.1) with the Joule heating term, equation (3.9), that was added to Pennes' equation, one can conclude that they are mathematically equivalent. On one hand, the power density in the tumor should be maximized to enhance treatment outcomes. On the other hand, to increase the PD it is necessary to inject more current into the arrays, which in turn increases the Joule effect and leads to a quicker temperature rise on the scalp and consequently to a reduction on the current injected. This negative feedback highlights the need to find a trade-off between treatment efficacy and patient's safety to optimize how TTFields are applied and planned. The importance of accounting for these temperature increases during planning might even lead to the choice of a different treatment layout compared to the suggestion made by the NovoTAL system.

8.2 Aim

The goals of this work were:

1. Analyse the variation of the LMiPD in the tumor as a function of array positioning following the same methodology as the one implemented in the NovoTAL system;

2. Investigate new metrics to predict treatment efficacy and compare those results with the ones obtained using the LMiPD;

3. Consider the temperature increases in the head following the approach described in the previous chapter;

4. Study how the conclusions drawn in terms of treatment efficacy and choice of the best treatment layout vary when the temperature is also accounted for;

8.3 Methods

8.3.1 The simplified head model

As time-transient simulations using realistic head models are very time-consuming and in order to maximize the number of layouts that could be tested, a simplified head model (SHM) was used in this chapter. This was the same model as the one used by Novocure in other studies for internal validation of results. It can be mathematically expressed by the general ellipsoid equation:

$$\frac{(x-x_0)^2}{a^2}+\frac{(y-y_0)^2}{b^2}+\frac{(z-z_0)^2}{c^2}=1 \tag{8.2}$$

where (x_0, y_0, z_0) are the coordinates of the center of the ellipsoid and a, b and c are the three main semi-axes lengths.

More specifically, this model is a particular case where two of these semi-axes have the same length, thus describing a spheroid model. If this model is centered at $(0, 0, 0)$, the general equation is simplified to:

$$\frac{x^2}{a^2}+\frac{y^2}{b^2}+\frac{z^2}{a^2}=1 \tag{8.3}$$

Each one of the tissues of interest (scalp, skull, CSF, brain and ventricles, which were assumed to be filled with CSF) was considered to be a spheroid shell with specific a and b values. These values were chosen based on the head measurements of patient 17015 that participated in the EF-14 clinical trial. A spherical virtual lesion, with a diameter of 15.2 mm, was also added to the model to mimic a tumor, as depicted in figure 8.1.

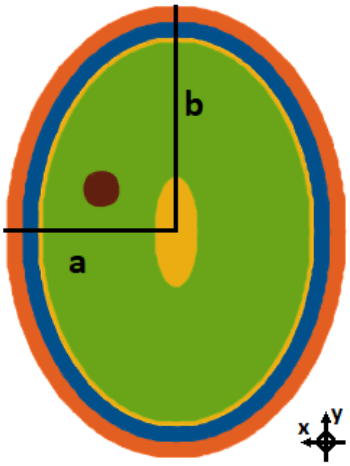

Tissue	a	b
Scalp	75	100
Skull	68	93
CSF	61	86
Brain	59	84
Ventricles	10	25

Figure 8.1: Axial cut through the center of the model (plane z=0). Each tissue was represented as a spheroid shell with the values of the main semi-axes, a and b, shown in the table on the right, in mm. The scalp is represented in orange, the skull in blue, the CSF, which also fills the ventricles, in yellow and the brain in green. The values assigned to each layer were based on the dimensions of the head of patient 17015 that participated in the EF-14 clinical trial. A spherical lesion, with the center at (34,18,0) mm and diameter of 15.2 mm, in brown, was also added to the model to mimic a GBM.

8.3.2 Array placement

Given the goal of this work, several array positionings were provided by Novocure and tested. The distances between the center of the transducers were the ones of the new generation of arrays, which were discussed in section 7.1. The positions to place each transducer were provided as an STL file. In order to build the models for finite element studies, it was necessary to use Materialise 3-matic. This design tool allows to manipulate STL files to create a single geometry and a volume mesh that can be imported into COMSOL Multiphysics. Briefly, a surface mesh composed by several small triangles was created in a semi-automatic manner for each tissue, gel and transducer layers. A maximum triangle edge length of 2.0 mm for the latter two and of 3.0 mm for tissues was set and, whenever it was necessary, small corrections were made (e.g.: surface smoothing, improving mesh quality, etc). After surface meshes were sucessfully created for each component, they were assembled two a time, from the inner to the outermost surface using the non-manifold assembly operator. Surface meshes for the whole geometry were generated every time a non-manifold assembly was created. Furthermore, this operation required for the gel radius to be slightly bigger than the radius of the transducers. As the latter was 10 mm, the former was considered to be 10.3 mm.

For clarity of discussion, throughout this chapter the arrays will be named after their rotation in regard to the reference pair, pair 0°, instead of anterior-posterior and left-right. The arrays were only rotated around the z-axis. In total, 12 different pairs could be placed in the scalp spaced by 15°. This rotation interval was the same one used by Korshoej et al [94], in which the authors studied the impact of array positioning on the average EF in the tumor. In all cases, the line that connected the two central transducers of each pair, hereinafter referred to as the array vector (AV), passed through the center of the tumor. The direction of the array vector was 0° when it pointed along the y-axis and 90° when it pointed along the x-axis. As it was necessary to ensure that the arrays were as perpendicular as possible, the number of combinations for each pair was limited

to the ones rotated by 90°±15° from each other. In total, there were 18 possible layouts that could be built that respected these conditions. However, in 4 of them there was an overlap between some transducers of the two pairs, which decreased the total number of possible layouts to 14. Out of these, 7 layouts were randomly selected and built for the purpose of this study (figure 8.2).

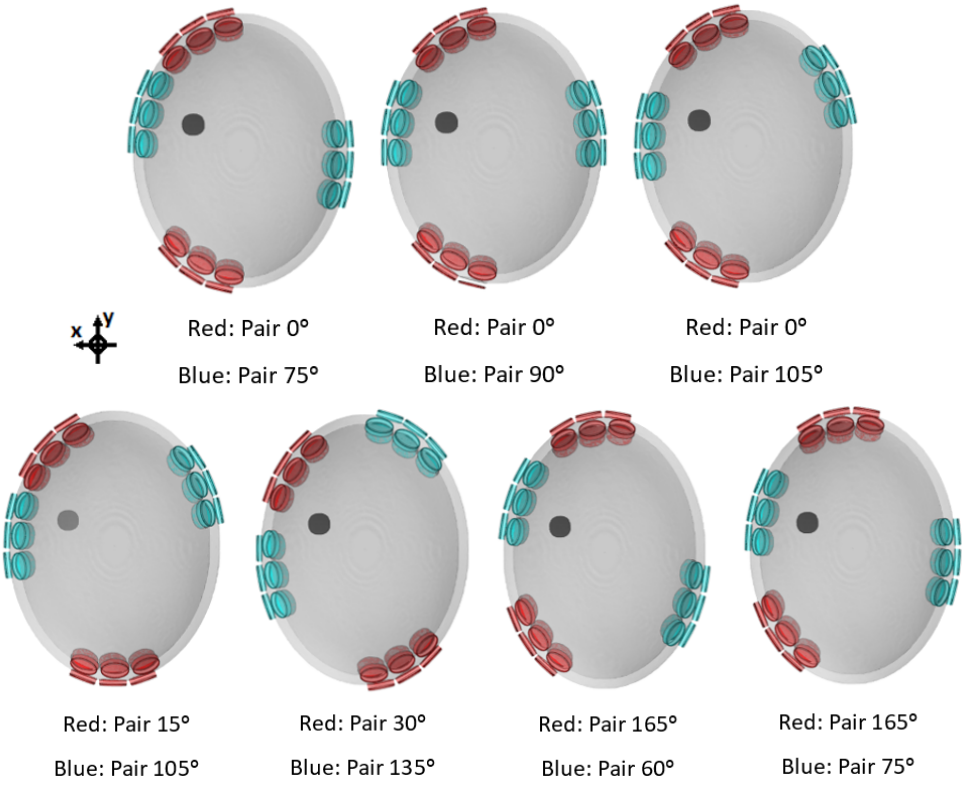

Figure 8.2: Top view of the seven spheroid models used. For each pair there was a maximum of three possible complementary pairs that could be used. For pair 0° these three pairs were rotated by 75° (upper row, left), 90° (upper row, middle) and 105° (upper row, right). For all layouts, the array vector of each pair passed through the center of the tumor, which is represented in black. The pair with the longest array vector is colored in red, whereas the pair with the shortest array vector is colored in blue. The position of the tumor was the same for all layouts.

8.3.3 Physical properties, metrics and predictors

8.3.3.1 Physical properties

As this work was made in collaboration with Novocure and to better compare the results of this study with the ones reported by Ballo et al [98], the electric properties were changed to the same ones reported by these authors. Compared to the standard values presented in table 4.1, the electric conductivity of the skull was increased to 0.080 S/m, whereas the electric conductivity of the scalp was augmented to 0.30 S/m and its relative permittivity was reduced from 10 000 to 5 000. According to the work by Wenger et al [93], an increased scalp conductivity leads to a lower electric field strength in the tumor as more current is shunted through the scalp. However, when skull's electric conductivity is increased more current flows into the cranial cavity. Given that σ_{skull} was increased by six-fold while scalp's electric conductivity remained practically the same, the electric

field in the tumor will be higher for this new set of values compared to what would be obtained if the previous set was used. Following the conclusions of the same work, the value of the relative permittivity of the scalp does not significantly affect the EF in the tumor. It is also important to note that the sensitivity analysis (chapter 4) showed that higher σ_{scalp} and σ_{skull} values lead to lower predictions of temperature maxima in every tissue.

The values of the remaining electric parameters and the thermal ones were the standard values reported in table 4.1. The physical parameters of the brain were obtained by averaging the values of the GM with a contribution of 60%, and of the WM whose contribution was 40% [133]. The length of the array vector for each pair and the impedance of the model seen through that pair are presented in table 8.1.

Table 8.1: Array vector and head impedance for each pair. As expected, the further apart the arrays the higher the impedance.

Pair	0°	15°	30°	60°	75°	90°	105°	135°	165°
Array vector (cm)	18.5	18.7	18.4	16.5	15.8	15.3	15.2	16.0	17.6
Impedance (Ω)	92	93	90	82	78	77	78	84	91

In this table, it is possible to verify that there is a strong relationship between the length of the array vector and the impedance of the head. The values obtained for the latter were within the range seen in the log files, according to what was discussed in the previous chapter.

8.3.3.2 Metrics used

As mentioned previously, the LMiPD in the tumor was used in this work as a metric to evaluate and rank the different layouts. According to Wenger et al [134], the images used for TTFields treatment planning should have a minimum resolution of 1 mm^3. Thus, the values of the power density produced by each pair in the active tumor were exported from COMSOL by defining a regular grid with 1 mm spacing in every direction. Then, the lowest of the two power densities in each voxel was considered and the average LMiPD for each layout was calculated.

Two additional metrics were used in this study:

1. The local average power density (LAPD) was defined and calculated following the same rationale as the LMiPD, but considering the average of the two power densities in each voxel in the tumor, instead of the minimum.

2. The third metric used was the SAR, which was already discussed in chapter 2. Contrary to the other two metrics, it was quantified in the scalp instead of the tumor, in the same point where the maximum temperature was reached. The rationale behind the use of this metric was to investigate how a layout ranking based on it might correlate with the ones obtained with the other two. As discussed before, the SAR is typically used to evaluate if the electromagnetic radiation can be harmful to the human body for higher frequencies, in the order of MHz, and it has not been

reported in TTFields, in which the frequency used is between 100-500 kHz. Thus, there is not any SAR threshold above which it is possible to assert that TTFields are harmful or not safe. In this work, SAR is also used to study the variability of the results in terms of relative safety between different layouts. For each layout, the highest local SAR in the scalp was quantified in two points: one underneath the pair with the highest impedance and one underneath the pair with the lowest impedance. As a complete TTFields duty cycle corresponds to current being injected alternately, SAR values were averaged for comparison between layouts.

8.3.3.3 Predictors used

Each one of the three metrics previously mentioned, LMiPD, LAPD and SAR, were quantified using two different predictors:

1. Predictor A was based on the same methodology implemented in the NovoTAL system where 900 mA of current are injected into each array pair [39].

2. To account for the thermal limitations of the therapy, information about the temperature was added when using predictor B. As discussed in the previous chapter, equation (6.2) can be used to predict the maximum steady-state temperature that the scalp will reach as a function of the injected current. Through an iterative process, it was possible to investigate the maximum current that could be injected and that led to the desired temperature on the scalp.

Each electric study took around 10 min in workstation 3, whereas each thermal time-transient study took around 10 hours to simulate the first five minutes of treatment.

8.4 Results and discussion

8.4.1 LMiPD, LAPD and SAR based on predictor A

The average values of the LMiPD, LAPD and SAR when predictor A was used are presented in table 8.2.

Table 8.2: Average LMiPD and LAPD in the tumor and average maximum local SAR values in the scalp when current was injected following the same approach as the one implemented in the NovoTAL system (900 mA in each pair). Each layout was named after the two pairs that compose it, where the first pair is the one with the longest array vector and consequently the highest impedance.

Layout	I (mA) First pair	I (mA) Second pair	LMiPD (mW/cm^3)	LAPD (mW/cm^3)	SAR (W/kg)
0/75	900	900	6.63	7.01	2274
0/90	900	900	6.61	6.88	2106
0/105	900	900	6.57	6.81	2012
15/105	900	900	6.88	7.12	2497
30/135	900	900	6.71	7.18	2517
165/60	900	900	6.31	6.96	3448
165/75	900	900	6.30	6.84	3213

The values of the LMiPD were very similar for all layouts (range: 6.30-6.88 mW/cm^3), mainly due to simplicity of the geomery used. The worst layout in terms of LMiPD, layout 165/75, induced a value that was only 8% lower than the one induced by layout 15/105, which was the best one. In this SHM, the local minimum power density values were mainly limited by the low PD produced by the pair with the longest AV. In general, a longer array vector corresponds to a more resistive current path, as shown in table 8.1. However, given that the impedance of this pair only varied between 90 and 93 Ω, the PD induced in the tumor was pratically the same regardless of the layout. The layout that induced the highest value was the one in which the distance between the tumor and the closest array of the most resistive pair was minimized. In layout 15/105, this distance was 55 mm, whereas this value increased to 78 mm in layout 165/75. Thus, the LMiPD was higher for the former compared to the latter, for the same injected current. It is noteworthy that due to the simplicity of the geometry and to the fact that the temperature was not accounted for, the values of the LMiPD were way above the therapeutic threshold of 1.15 mW/cm^3 reported by Ballo et al [98].

To overcome the limitations of the LMiPD, the LAPD was defined and calculated. In general, when one pair is placed in a region that maximizes the EF induced in the tumor in that direction, the arrays of the complementary pair are placed in regions that lead to the lowest EF, as perpendicularity between the two pairs has to be sought. The distance between the tumor and the center of the closest array of the least resistive pair was 48 mm in layout 15/105, whereas this value decreased to 36 mm in layout 165/75. This explains why the latter layout now induced a value higher than the former compared to when the criterion used was the LMiPD. In general, the average power density when the contribution of both pairs was considered varied less, which explains why an even lower sensitivity to array positioning was obtained when the LAPD was used (range: 6.81-7.18 mW/cm^3). The layout that induced the lowest LAPD, layout 0/105, produced a value only 5% lower than the best one, layout 30/135.

As for the maximum local SAR, the values obtained were much higher than the thresholds defined by the international agencies as safety limits for MR imaging (table 2.1). Although the values presented in table 8.2 represent local maxima in the scalp, measured in specific points, and were not averaged over one or 10 grams of tissue, it is not straightforward to deduce that TTFields are harmful or not safe for the patient, as discussed in more detail in the next chapter with data obtained using a realistic head model. According to the data presented in table 8.2, it is only possible to conclude that, based on the points where the SAR was measured, the safest layout, i.e., the one that induced the lowest SAR, is layout 0/105, which yielded a value 42% lower than layout 165/60, which was the least safe one.

Figure 8.3 is a visual representation of the variation of which layout is the best one based on the criterion used. Due to the reasons mentioned above, the differences in the order between the LMiPD and the LAPD values were few and small. However, when SAR was used major variations occurred in some cases.

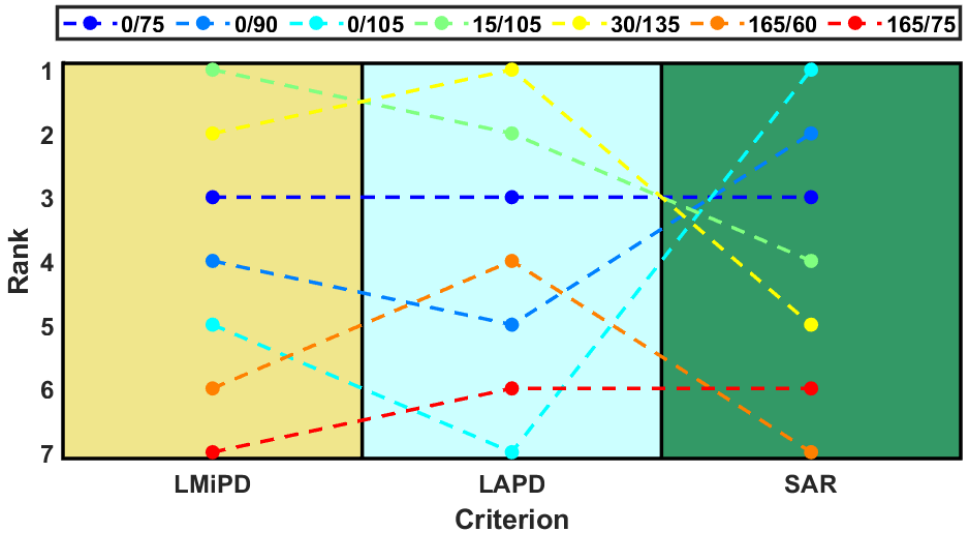

Figure 8.3: Ranking of the 7 different layouts based on three different criteria when predictor A was used. Under these conditions, the same current, 900 mA, was injected into each pair and in all layouts. A value of 1 in the y-axis means that that layout is the best choice, whereas a value of 7 means that it is the worst option. Each rectangle corresponds to an analysis based on a different metric: LMiPD (yellow) and LAPD (blue), both quantified in the tumor, and local SAR in the scalp (green).

8.4.2 LMiPD, LAPD and SAR based on predictor B

To find out how much current could be injected into each pair when the temperature was also considered, an iterative approach was followed based on the maximum temperature that the scalp would reach for specific amounts of current injected, as explained in chapter 6. Based on what was described in chapter 7, the conditions of the simulations were fine-tuned to:

1. The temperature was monitored at the interface between the scalp and the gel. In each array, the only temperature that was not measured was the one that corresponded to the central transducer as there is no thermistor there;

2. The temperature was controlled independently for each pair. This means that the maximum current that could be injected into each pair did not have to be necessarily the same value.

For this study in particular, the maximum steady-state temperature predicted for the scalp when the lowest injectable current, 400 mA, was considered already surpassed the 39.5 ℃ underneath the pair with the highest impedance (the red pairs in figures 8.2). Thus, the critical temperature was considered to be 40.5 ℃ in the studies presented in this chapter. The average current injected considering both pairs was maximized in each study. As an example of the data obtained, figure 8.4 shows the variation of the maximum temperature of the scalp for different amounts of current injected using layout 0/75.

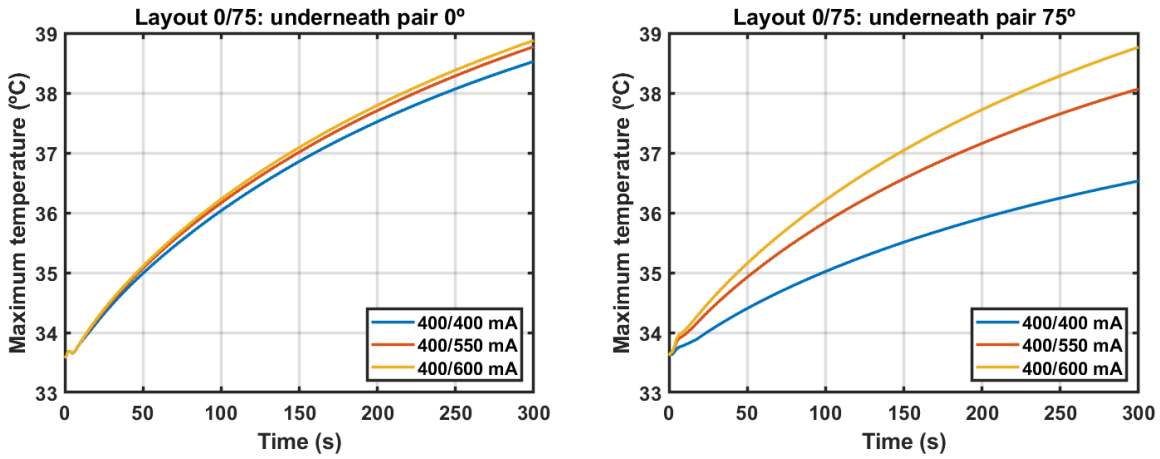

(a) Underneath pair 0°

(b) Underneath pair 75°

Figure 8.4: Variation of the maximum temperature of the scalp underneath pair 0° (left) and pair 75° (right) for different sets of injected currents using layout 0/75. Each set is identified as X1/X2 mA, where X1 is the current injected in pair 0 ° pair and X2 the current injected in the complementary pair. The switching time between X1 and X2 was one second. As clearly seen, varying how much current was injected into one pair also affected scalp's temperature underneath the other pair.

Equation (6.2) was fitted to the data presented in the previous figure and the maximum steady-state temperature that the scalp would reach underneath each pair was then predicted using equation (6.3) (table 8.3).

Table 8.3: Maximum steady-state temperature predicted on the surface of the scalp underneath each pair of arrays when different sets of current were injected alternately with a switching time of one second. Changing how much current was injected into pair 75° also led to a variation of scalp's temperature underneath pair 0° .

Injected current (mA) Pair 0° /Pair 75°	Maximum temperature underneath pair 0° (℃)	Maximum temperature underneath pair 75° (℃)
400/400	40.1	37.7
400/550	40.4	39.5
400/600	40.5	40.4

An increase of 200 mA of current into pair 75° from 400 mA to 600 mA, led to a temperature increase of 2.7 ℃ on the scalp underneath this pair and of 0.4 ℃ underneath pair 0° as the two pairs were placed very close to each other (figure 8.2). A more detailed discussion of the impact of the distance between array pairs is provided in the next subsection. The values of current that led to values around 40.5 ℃ on the scalp underneath both pairs were 400 mA in pair 0° and 600 mA in pair 75°. In table E.1 in appendix E the values of the fitted coefficients C_1, C_2 and C_3 are presented for these currents, as well as for the currents that led to values as close as possible to 40.5 ℃ on the scalp for the remaining layouts. For these sets of current injected, the LMiPD, LAPD and SAR were quantified in the same regions as before and are presented in table 8.4. All values reported decreased compared to the ones presented in table 8.2 as less than 900 mA were injected in all cases. In parentheses the relative decrease is presented.

Table 8.4: Average LMiPD and LAPD in the tumor and average maximum local SAR values in the scalp when the amount of current injected into each pair depended on the temperature of the scalp. In parentheses the relative decrease compared to the respective values presented in table 8.2 is given.

Layout	I (mA) First pair	I (mA) Second pair	T+LMiPD (mW/cm^3)	T+LAPD (mW/cm^3)	T+SAR (W/kg)
0/75	400 (-56%)	600 (-33%)	1.31 (-80%)	2.29 (-67%)	710 (-69%)
0/90	410 (-54%)	625 (-31%)	1.38 (-79%)	2.40 (-65%)	677 (-68%)
0/105	423 (-53%)	600 (-33%)	1.48 (-78%)	2.28 (-67%)	645 (-68%)
15/105	400 (-56%)	575 (-36%)	1.44 (-79%)	2.14 (-70%)	755 (-70%)
30/135	425 (-53%)	600 (-33%)	1.71 (-75%)	2.35 (-67%)	887 (-65%)
165/60	423 (-53%)	600 (-33%)	1.39 (-78%)	2.38 (-66%)	1069 (-69%)
165/75	423 (-53%)	625 (-31%)	1.39 (-78%)	2.47 (-64%)	1019 (-68%)

As expected, accounting for the temperature led to a decrease in how much current was injected into each layout. The current injected into the most resistive pair ranged between 400 and 425 mA, whereas more current could be injected into the least resistive pair (575-625 mA). As the decrease in the former was more or less uniform (54%, range: 53-56%) and given that it was the pair that limited the most the LMiPD values, the reduction on that metric was practically the same for all layouts (78%, 75-80%). However, this small variation was enough to increase the range seen for LMiPD to 31% (1.31-1.71 mW/cm^3). This range of values is much closer to the therapeutic threshold of 1.15 mW/cm^3, which was also deduced when the thermal restrictions of the therapy were accounted for [98]. On the other hand, the range for the LAPD augmented to 13% (2.14-2.47 mW/cm^3), whereas for the SAR it increased to 40% (645-1069 W/kg).

Figure 8.5 depicts a qualitatively comparison of the best layout according to the metric used.

Given the low variation in the LMiPD values across layouts when 900 mA were injected (table 8.2), it was expected that the layouts that would induce the highest values when the temperature was accounted for would be the ones in which more current was injected into the most resistive pair (table 8.4, first column), which was what occurred. In terms of LAPD, the layout that induced the highest value was layout 165/75, in which the highest average current was injected, whereas in layout 15/105 the opposite occurred and it was thus the worst option. As for SAR values, the conclusions drawn in the previous subsection did not vary and the safest layout was still layout 0/105.

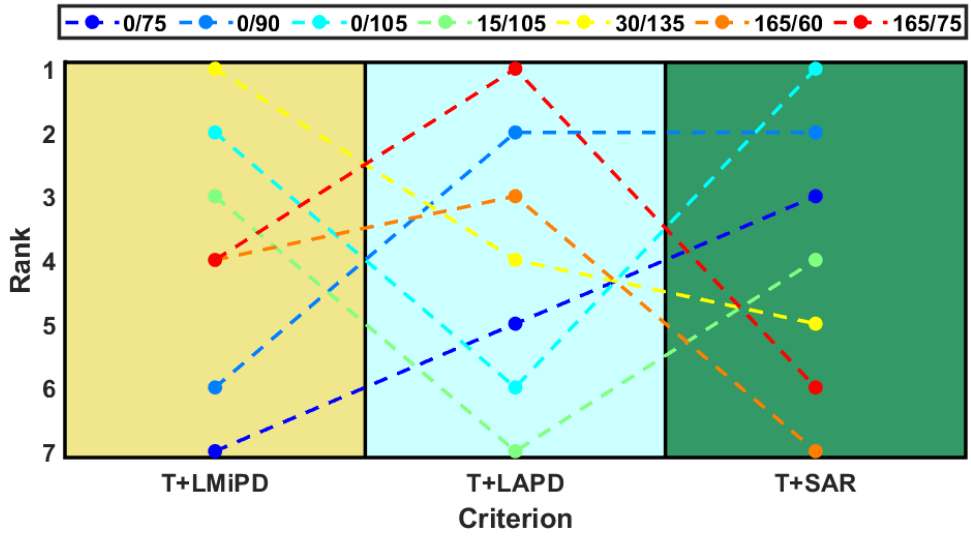

Figure 8.5: Ranking of the 7 different layouts based on three different criteria when predictor B was used. Under these conditions, different amounts of current were injected into each pair and into each layout. Each rectangle corresponds to an analysis based on a different metric: LMiPD (yellow) and LAPD (blue), both quantified in the tumor, and local SAR in the scalp (green).

8.4.3 Importance of accounting for scalp's temperature

Based on the data presented in subsections 8.4.1 and 8.4.2, it was possible to conclude that accounting for the temperature led to significant decreases in all metrics considered. On average, the current injected into the most resistive pair decreased by 54% (range: 400-425 mA, first column of table 8.4), whereas the average current injected into the complementary pair was reduced by 33% (575-625 mA, second column). The decrease on the first significantly affected the average LMiPD values due to the reasons mentioned above. On average, the latter values reduced around 78% across layouts (75-80%, third column), whereas the LAPD values were less, but still significantly affected by accounting for the temperature as, on average, a decrease of 67% (64-70%, fourth column) was seen. Lastly, SAR values decreased by 68% (65-70%, fifth column). These results highlight the importance of considering the temperature in TTFields computational studies. The threshold of 1.15 mW/cm^3 in terms of LMiPD was obtained from experimental data, in which the temperature was inherently considered. However, due to all the complications associated with considering this additional parameter in *in-silico* work, it has been neglected, even in the NovoTAL system, and its importance has never been quantified. The results obtained using this SHM showed that the current injected into each pair, and consequently the metrics, might be significantly reduced. For realistic head models, this might also lead to meaningful decreases in the metrics used and consequently the therapeutic threshold might not be reached.

Despite the almost uniform decrease in the several metrics in all layouts, the range of values for each one of them increased compared to what was reported in table 8.2, which indicates that accounting for the temperature might allow to differentiate more the layouts in terms of effectiveness. Figure 8.6 combines the information of figure 8.3 and 8.5 and depicts a relative comparison of the layouts as a function of the metric used. In this figure, it is easily observable that there is a significant variation of the results based not only on the metric chosen, but also on the addition of information concerning the

temperature.

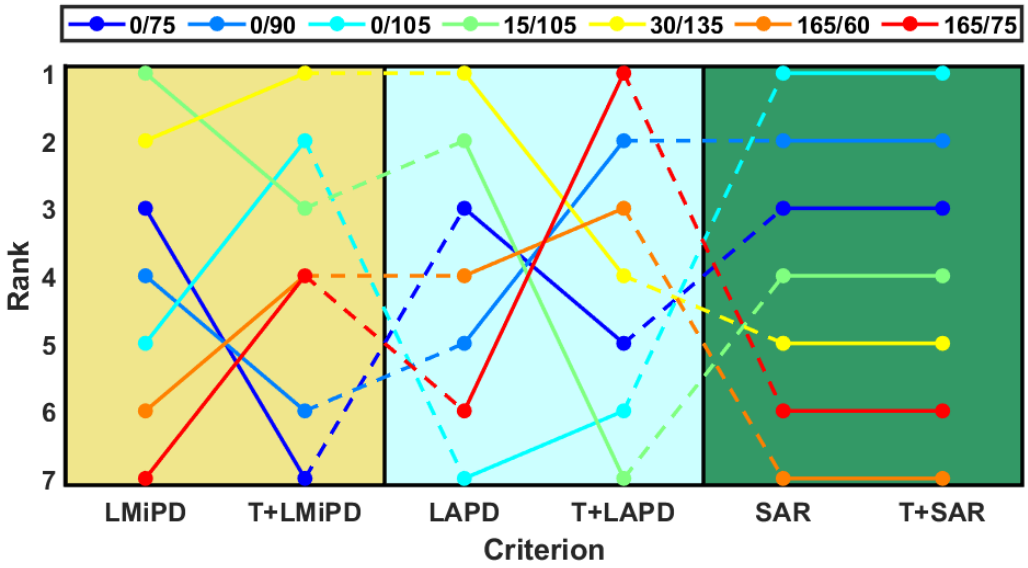

Figure 8.6: Ranking of the 7 different layouts based on three different criteria using predictor A (LMiPD, LAPD and SAR) and predictor B (T+LMiPD, T+LAPD, T+SAR). The amount of current injected into each layout was the same for the first, but it varied for the second. Each rectangle corresponds to an analysis based on a different metric: LMiPD (yellow) and LAPD (blue), both quantified in the tumor, and local SAR in the scalp (green).

In general, accounting for the temperature benefited the layouts whose array pairs were far enough from each other. Due to the geometry of the model, the closest transducers of different pairs in layouts 0/75 and 15/105 were only separated by 2.2 mm. Consequently the temperature increases on the scalp underneath both pairs led to the appearence of a common temperature hotspot (figure 8.7, black arrows) that limited how much current could be injected into each pair. As the rationale to choose the values of the current was to increase as much as possible the average current injected into each layout, the least resistive pair was benefited. As seen in table 8.3 an increase in the current injected in pair 75° by 200 mA led to an increase of 0.4 ℃ in the maximum temperature predicted for the scalp underneath pair 0°. This explains why both these layouts ranked worse in terms of LMiPD when the temperature was considered during planning. In layout 0/90, the distance between these transducers was 10.0 mm, which created a weaker but still significant hotspot (figure 8.7).

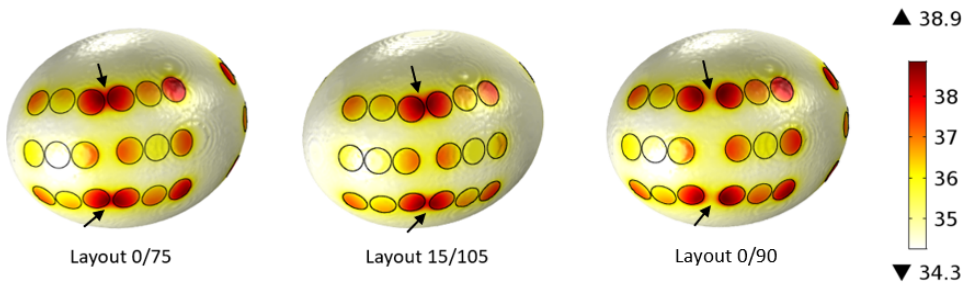

Figure 8.7: Temperature distribution at the end of the simulation (t=5 minutes) in layouts 0/75 (left), 15/105 (middle) and 0/90 (right). Due to the proximity of some transducers of different pairs in these three layouts temperature hotspots occurred (black arrows), which limited how much current could be injected into each pair. In the first two the shortest distance between transducers of different pairs was 2.2 mm, whereas in the third it was 10.0 mm. Temperature scale is in ℃.

Layouts in which the pairs were relatively far from each other improved their position in the ranking. In general, the layouts ranked better when the current injected into the most resistive pair was higher, when the criteria used was T+LMiPD, or when the average current injected in both pairs was higher, when the criteria used was T+LAPD. When these values were similar for different layouts, the distance between the arrays and the tumor played a major role. For instance, the same current was injected in both pairs in layouts 0/105 and 165/60. The average distance between the tumor and the most resistive pair's closest array in the first was 62 mm, whereas it increased to 78 mm in the second, which explains why layout 165/60 was worse in terms of induced LMiPD. The distance between the tumor and the least resistive pair's closest array was 48 mm in both these layouts, but given that pair 60° (in layout 165/75) was more centered above the tumor the average PD induced was higher than the one produced by pair 105° (in layout 0/105). Thus, layout 165/60x was better in terms of LAPD. Lastly, including information concerning the temperature when SAR was used did not change the ranking. As all layouts had a similar decrease in the injected current in both pairs and given that the range of values obtained for this metric was high enough across layouts when predictor A was used, accounting for the temperature did not lead to any variation in the ranking when predictor B was considered.

8.5 Limitations and conclusions

The results presented here have some limitations that are important to address. For the lowest current that is injected in patients, 400 mA, the temperature of the scalp in this SHM already surpassed the optimal limit of 39.5 ℃ and thus the temperature threshold had to be increased to 40.5 ℃. This might lead to an overcontribution of the Joule heating effect to the temperature increases. As seen in chapter 4, this effect explains pratically 100% of the heating in the scalp during TTFields treatment. An alternative path that could be followed to avoid this issue would be to use values of current lower than 400 mA. Although it would not mimic the real conditions in which treatment is performed, the temperature values would be within the range of interest. Under these conditions, the values of the LMiPD, LAPD and SAR when predictor B was used would also decrease as less current would be injected in both array pairs.

In terms of the different metrics considered, the values of the LMiPD and LAPD varied less than 10% across layouts when predictor A was used. This result was not unexpected as the geometry used was very simple and the arrays were only rotated around the z-axis. However, such a small variation also makes the results very sensitive to small computational errors, which might significantly affect the conclusions. When predictor B was used there was also an additional source of error. As shown in table E.1 in appendix E, the maximum steady-state temperature predicted on the surface of the scalp was not exactly 40.5 ℃ for all layouts but it varied between 40.3 and 40.7 ℃. This led to small variations in the value of the injected current, which might affect the order in which the layouts were ranked, especially considering the low range of values reported in table 8.4.

Nonetheless, this SHM allowed to gain some important insights on how accounting for the temperature of the scalp might affect the predicted therapy efficacy and allowed to fine-tune the protocol when similar calculations are performed using a realistic head model in the next chapter. In general, a significant decrease in the current injected into each pair, and consequently in all metrics used to evaluate treatment effectiveness, was observed

when the temperature was considered. The layouts that were more affected were the ones in which two arrays pairs were separated by 1 cm or less, as a common temperature hotspot occurred which affected how much current could be injected in both pairs. Ensuring a minimum distance between arrays during planning and when the physician or caregiver are placing them on patient's head might be one important way of optimizing treatment benefits.

These results also showed that the choice of the best treatment layout strongly depends on the metric used to evaluate it. The LMiPD is a conservative approach to predict treatment effectiveness as it might be limited by the pair that induces the lowest PD in the tumor. On the other hand, the LAPD is more informative in terms of overall treatment efficacy, but it might mask the ineffectiveness of one pair, if the other one is placed in an optimal region. As for the SAR, its quantification and clinical applicability still needs more investigation when used to evaluate the safest layout. One possible approach that might help to improve a ranking based on the SAR is using virtual observation points, as discussed in the next chapter.

Chapter 9

Tissue temperature during TTFields treatment planning: realistic head model

Published work

The results presented in this chapter resulted in the following work:

1. **Nichal Gentilal**, Ariel Naveh, Tal Marciano and Pedro Cavaleiro Miranda. The impact of scalp's temperature on the choice of the best layout for TTFields treatment. Submitted to *Innovation and Research in Biomedical Engineering* – **Peer-reviewed paper #3**

2. **Nichal Gentilal**, Eyal Abend, Ariel Naveh, Tal Marciano, Igal Balin, Yevgeniy Telepinsky, and Pedro Cavaleiro Miranda. Temperature and impedance variations during Tumor Treating Fields (TTFields) treatment. *Frontiers in Human Neuroscience*, 16:931818, 2022. DOI: 10.3389/fnhum.2022.931818 – **Peer-reviewed paper #4**

3. **Nichal Gentilal**, Ariel Naveh, Tal Marciano, Ze'ev Bomzon, Yevgeniy Telepinsky, Yoram Wasserman, and Pedro Cavaleiro Miranda. A computational study of the relation between the power density in the tumor and the maximum temperature in the scalp during Tumor Treating Fields (TTFields) therapy. *2021 43rd Annual International Conference of the IEEE Engineering in Medicine and Biology Society (EMBC)*, 4192-4195, 2021. DOI: 10.1109/EMBC46164.2021.9630071 – **4-page abstract #3**

4. **Nichal Gentilal**, Ariel Naveh, Tal Marciano, Ze'ev Bomzon, Yevgeniy Telepinsky, Yoram Wasserman, and Pedro Cavaleiro Miranda. A computational study of the relation between the power density in the tumor and the maximum temperature in the scalp during Tumor Treating Fields (TTFields) therapy. *IEEE Engineering in Medicine and Biology Society (EMBC 2021)*, 1st-5th November 2021, virtual conference – **Oral presentation #9**

9.1 Introduction

In the literature, the EF has been widely used to investigate the best array positioning for each patient and for each tumor [82, 94]. Subsequent work took this comparison further and studied the impact of different layouts based on the average EF strength induced in the tumor, which might be a better approach as it gives an overall idea of how effective a treatment can be as a function of array placement. In general, it is not possible to maximize the EF in both directions simultaneously while still ensuring the perpendicularity between the two pairs. The study by Wenger et al [82] was the first work to quantify the importance of creating personalized treatment maps for each patient based on the position of the tumor. In general, the average field intensity in the this tissue increased between 32 and 45% when array positioning was adjusted to the tumor location. Smaller improvements were seen in the work by Korshoej et al [94], in which adapted layouts led to an enhancement of the average field strength in the tumor between 9 and 23%. The latter study also suggested that treatment outcomes could be significantly enhanced when the AP pair was oriented 45°, and consequently the LR 135°, to the sagittal plane, for most tumor locations. These angular positions were the ones that minimized the distance between the two arrays of the same pair, i.e., the array vector, and thus that decreased the impedance of the head in both directions. However, it might not always be practicle to place the arrays with these angular positions and it is necessary to find a trade-off between the choice of where to place them and the EF intensity in the tumor in both directions.

The NovoTAL system is the FDA-approved software used by the certified physician during treatment planning to find the positions of the arrays on the scalp that optimize the EF in the tumor in both directions. The workflow followed by this software is shown in figure 9.1.

As glioblastoma is a fast-growing disease, optimal treatment planning would imply acquiring a new set of MR data regularly (step S11 in figure 9.1), which is time-consuming and cost-ineffective. Thus, the most recent MR images are typically used. Ideally, structural data, such as standard T1 and T2 MRI sequences, and data from which electric conductivity maps can be deduced, such as diffusion-weighted imaging (DWI), DTI or gradient echo sequences (GRE) are used. Structural data is used in the second step (step S12) to downgrade the complexity of treatment planning. At this stage, a more rough segmentation of the scalp, skull and CSF is performed by considering these three tissues as three different shells or convex hulls which allows for a quicker but still accurate representation of the head [134]. This process can be done using standard algorithms and software or by allowing the physician to measure the thickness of these three tissues in regions of interest using the MR images. This simplification allows to reduce the time that it takes to plan treatment.

A similar approach is not recommended for the brain and tumor. On one hand, the geometry of the brain is extremely complex and a rougher segmentation of this tissue could significantly impact the EF predicted in the brain and in the tumor. On the other hand, as treatment effectiveness is based on the EF values foreseen in the latter an oversimplification of its representation is not desirable. DTI measurements can be used to estimate diffusion tensors to map the electric conductivity values for each voxel of the brain and tumor (step S13) and to create conductivity maps (step S14). This approach is one possible way to distinguish between tissues during segmentation due to their different dielectric properties. The inclusion of the electric conductivity anisotropy led to

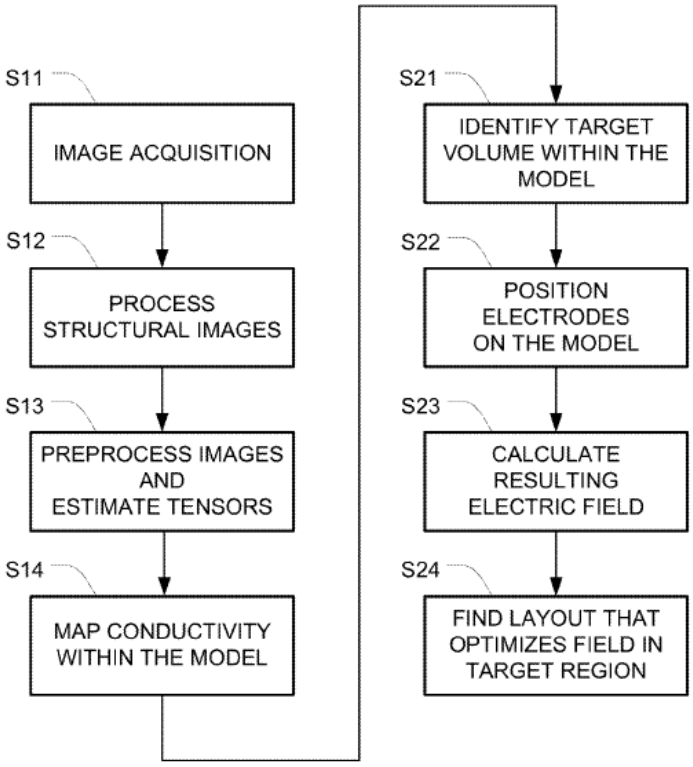

Figure 9.1: Schematic of how TTFields treatment planning is carried out in the NovoTAL system. MR images are firstly acquired, during step S11, and processed. The representation of the outermost tissues (scalp, skull and CSF) is simplified during step S12, whereas images that allow to segment the grey matter, white matter and tumor are pre-processed during step S13. Electric conductivity maps are then obtained for the latter three tissues, while isotropic and homogeneous values are assumed for the most superficial ones during step S14. After the target volume is identified in step S21, several layout positionings are chosen in step S22 and the electric field is calculated for each one of them in step S23. The choice of which layout to use is made in step S24 and it is based on the electric field in the tumor. Image taken from [134].

differences in the predicted EF in the brain by up to 34% in electroconvulsive therapy [116] and by up to 50% in tDCS [117] compared to when isotropic electric conductivities were assumed. These were local variations quantified in regions of interest. In TTFields, the EF in the brain is studied in terms of average variations as the values in the tumor are more relevant. In the study by Wenger et al [93] adding brain's anisotropy yielded an average EF variation of only 4% in the brain and 10% in the tumor for TTFields therapy. This shows that even if isotropic electric conductivities were used for healthy tissues, the predictions on treatment effectiveness would be reasonably accurate. However, the dielectric properties of the tumor were shown to be patient-specific and vary depending on the histological class of this tissue. Due to this intratumoral heterogeneity, the electric properties obtained for each voxel allow to improve the accuracy of the predictions [135, 136].

At the end of this stage, a computational model is obtained in which the target volume is identified (step 21). Akin to what is done in radiotherapy treatment planning, this target volume can be the gross tumor volume (GTV), i.e., the tumor that is seen in the MR images, or the clinical target volume (CTV), which also includes any other tissue with presumed tumor. To find the best array layout, different approaches can be used as extensively described in [134] (step 22). One of them comprehends testing a finite number

of layouts, available in the NovoTAL database, and the one that yields the highest average EF in the tumor is chosen. These simulations are typically performed by injecting 900 mA in each array pair [39] (step S23). The simulations can be done in different software such as COMSOL Multiphysics, Sim4Life, Ansys, or Matlab. Another optimization approach consists in placing a dipole at the center of the tumor and aligned with the direction of the expected field and then solving for the electric field potential. The regions of the scalp where the EF is the highest are used as a starting point to place the arrays. Then, iteratively, it is possible to fine-tune their position until a practical solution is reached.

At the end of this process, the physician gets a personalized 3D map that helps him, the patient and the caregiver in placing the arrays on the scalp throughout treatment (step S24) (figure 9.2).

Additional details on TTFields planning can be found in [134, 137, 138].

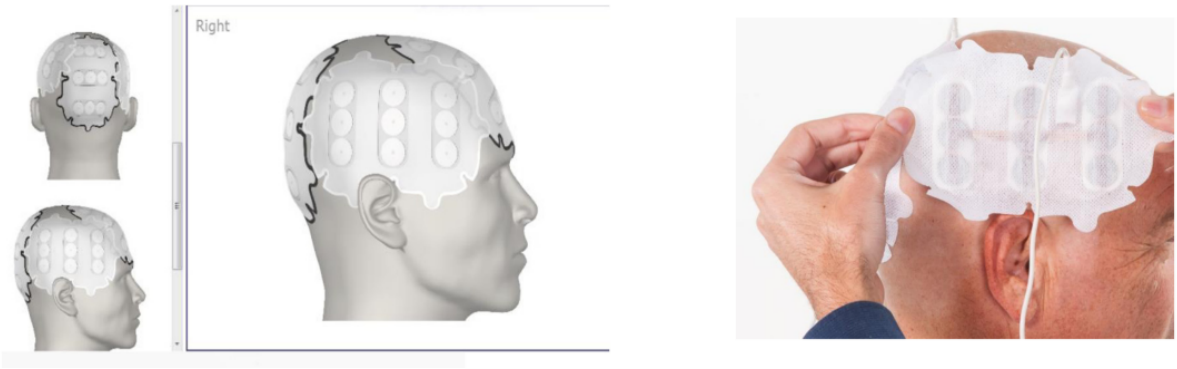

Figure 9.2: Left: output of the NovoTAL system that indicates the best regions to place the arrays in a patient. The array positions are the ones that yield the highest average EF in the tumor. Right: the arrays are placed on patient's head based on this output. Image taken from [39].

The workflow presented in figure 9.1 shows that NovoTAL does not include information about the temperature increases in any part of treatment planning. Ideally, this should be accounted for during step S23 when the electric field distribution is predicted, in a similar way as the one described in the previous chapter.

9.2 Aim

The goals of this work were:

1. Investigate how the choice of the best layout varies in a realistic head model based on different criteria: average EF, LMiPD, LAPD, and SAR;
2. Study how those conclusions vary when the temperature is also accounted for;
3. Investigate ways to improve TTFields treatment planning in the NovoTAL system by considering the temperature;
4. Predict the temperature increases in the head and TTFields thermal impact. Compare those results with the ones reported during clinical trials and with the predictions made in in section 2.2;

9.3 Methods

9.3.1 Realistic head models

The same realistic head model as the one presented in section 3.1, Colin27, was used. Given the goal of this work and the changes in array dimensions discussed in section 7.1, the layouts used were changed compared to the one presented in figure 3.2.

Novocure used the NovoTAL system to create personalized array layouts for this head model. Out of the 10 different layouts suggested by the system, 5 of them were randomly selected for the purpose of this work. Similarly to what was done in subsection 8.3.2, information about the location of each transducer was provided as an STL file and was worked on in Materialise 3-matic, following the same methodology. The distance between the center of the transducers was 44 mm in one direction and 22 mm in the other, which represents the most recent generation of arrays. The thickness of the transducers was 1 mm and the radius was 10.0 mm. The average thickness of the layer of gel in each model was 0.7 mm, which is very close to the 0.6 mm of gel that comes embedded in the arrays [132], whereas the radius was 10.3 mm. The maximum edge length was 2.0 mm for the gel and transducers and of 3.0 mm for tissues. The total number of degrees of freedom was around 6 millions, which was similar to the model presented in figure 3.2. The whole process of creating surface meshes took around two days for each layout, whereas the final volume mesh took 5 minutes to be created.

9.3.2 Physical properties, metrics and predictors

As the NovoTAL system ranks the layouts based on the average EF induced in the tumor, in this work this additional metric was also studied alongside with the ones used in the previous chapter: LMiPD, LAPD and SAR. These four metrics were quantified using predictor A, in which 900 mA were injected into each pair, and using predictor B, in which the current injected depended on the temperature of the scalp. Compared to what was considered in the previous chapter, the latter predictor was slightly changed:

1. The maximum temperature allowed in the scalp was 39.5 ℃, which is the same threshold as the one considered in real treatments, and not 40.5 ℃;

2. In this RHM the AP pair was the one that contributed the least to treatment. Thus, in order to enhance the predicted treatment efficacy the criterion used in this work to choose how much current to inject into each pair was to first maximize the current injected into the AP pair and only then in the LR pair. This means that the current that leads to 39.5 ℃ in the scalp underneath the former pair is investigated first and after that value is found and fixed, the current that leads to the same temperature value on the scalp, or as close as possible to it, is looked for for the LR pair. The values of the injected currents were bounded by 400 mA and 1000 mA. This approach is different than the one followed with the SHM, in which the criterion used was to maximize the average current injected considering both pairs and not the current injected into the least effective pair.

The same physical properties as the ones used in the SHM were considered.

Each frequency-domain study took around 2 hours, whereas each time-transient simulation took around 40 h in workstation 3 to simulate the first five minutes of treatment.

9.4 Results and discussion

9.4.1 Impact of the new electric parameters

As a new set of electric parameters was used in this study ($\sigma_{scalp} = 0.30$ S/m, $\sigma_{skull} = 0.080$ S/m), a preliminary investigation was made in which the ATV1 in the active tumor was quantified and compared with what was obtained when the previous set was used ($\sigma_{scalp} = 0.25$ S/m, $\sigma_{skull} = 0.013$ S/m), using the realistic head model. The relative permittivity of the scalp was also reduced from 10 000 to 5 000, although this does not significantly affect the electric field in the tumor, as discussed by Wenger et al [93]. The electric properties of the remaining tissues were the same in both cases. To allow for a direct comparison with the results presented throughout this thesis, the array layout that was used was the one shown in figure 3.2, and not any of the ones that were suggested by the NovoTAL system. In table 9.1 the ATV1s are presented when 900 mA of current were injected into each pair, alongside with the respective head impedance.

Table 9.1: ATV1 when 900 mA were injected into the AP and LR pairs for each set of electric parameters using the old array layout. The only differences in both sets were the values specified in this table. The remaining physical properties were the same in both cases. The impedance of the head in both directions is also presented for each set of values.

Set of electric values		ATV1 AP (%)	Impedance AP (Ω)	ATV1 LR (%)	Impedance LR (Ω)
Old	$\sigma_{scalp} = 0.25$ S/m $\sigma_{skull} = 0.013$ S/m $\epsilon_{r,scalp} = 10\ 000$	13	104	72	77
New	$\sigma_{scalp} = 0.30$ S/m $\sigma_{skull} = 0.080$ S/m $\epsilon_{r,scalp} = 5\ 000$	17	60	82	50

These values show that increasing the electric conductivity of these two tissues simultaneously led to more current flowing into the cranial cavity and thus to a higher ATV1 in the tumor in both directions. Due to the reasons explained before, the increase was higher for the LR pair (+10%) than for AP's (+4%). As expected, the impedance of the head decreased in both directions and reached 50 Ω in the first (-35%) and 60 Ω in the second (-42%). Based on what was discussed in section 7.3, these two values are at the low-end of the range seen in patients, which might indicate that the EF in the tumor is overestimated or that this head model only represents a small fraction of the patients treated with TTFields. Nonetheless, given that this work was made in collaboration with Novocure and to better compare the results obtained with those reported by Ballo et al [98], in which the new set of values was used, this new set of electric parameters was still considered in the studies presented in this chapter.

9.4.2 Layouts

The five different layouts are shown in figure 9.3 from different perspectives. Due to practical reasons and contrary to what occurred with the SHM, the array vector does not

pass through the center of the tumor in all arrays. The new array dimensions provide more head coverage compared to what was observed when the previous layout was used. The anterior-posterior pair is colored in red, the left-right in blue and the tumor location, which remained unaltered, is represented in black. For the new set of electric parameters used, the impedance of the head in the AP direction varied between 59 and 61 Ω and between 46 and 48 Ω in the LR direction. These values are even lower than what was obtained for the old layout using the new set of electric parameters (table 9.1). This might be another indication that the electric parameters are being overestimated.

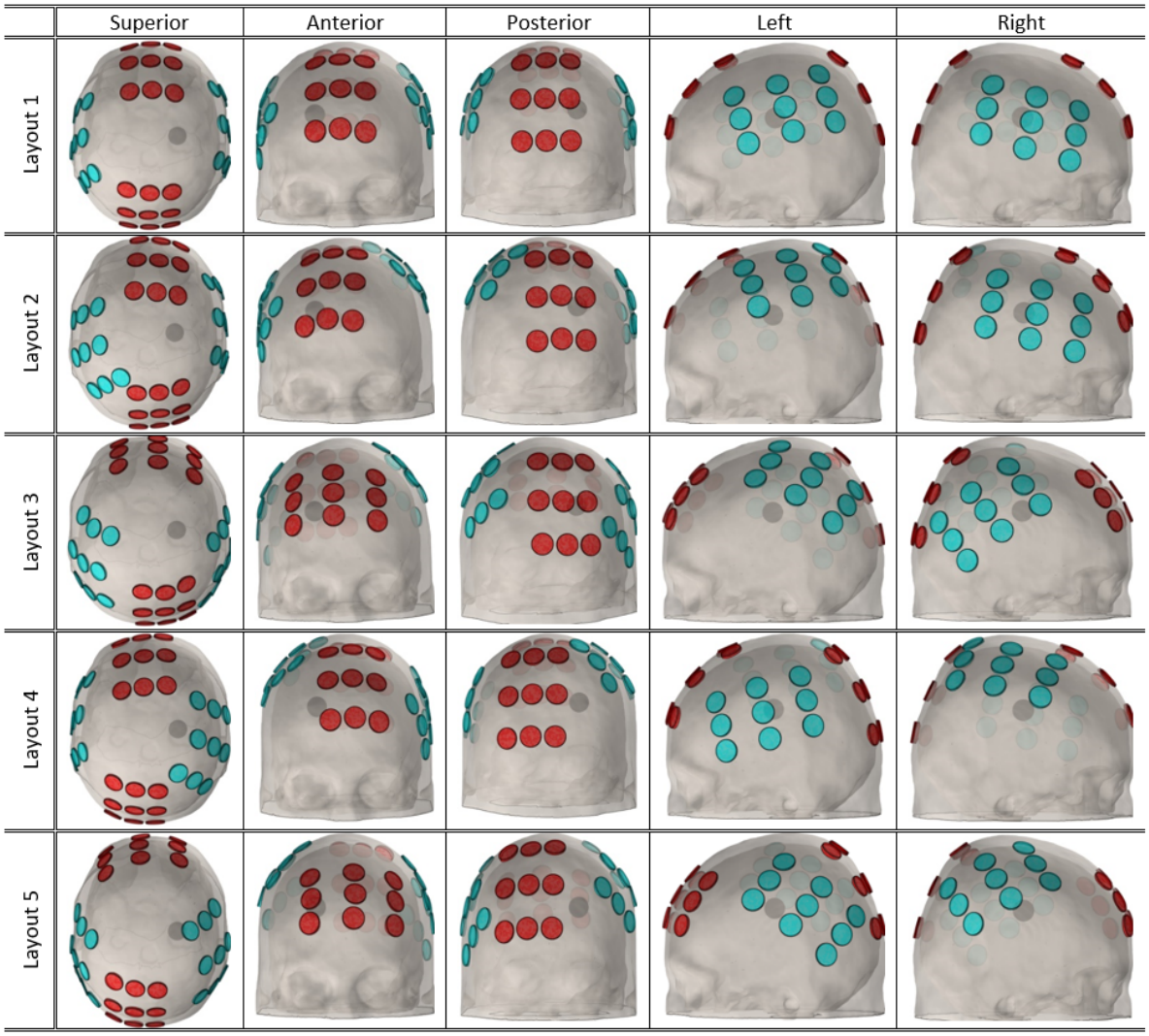

Figure 9.3: Different perspectives of the five realistic head models created with five different array layouts obtained through the NovoTAL system. The anterior-posterior pair is colored in red, the left-right pairs in blue and the tumor in black. The location of the latter was the same for all layouts.

Contrary to what was considered in previous published computational studies (e.g.: [43, 80, 82, 93, 111]), the transducers in the layouts shown in the previous figure are placed in a variety of different ways. For instance, the anterior array in layout 1 is placed vertically and in the middle of the forehead thus theoretically allowing to focus more the electric field in tumors close to the corpus callosum. This tumor location represented 3% of the patients that participated in the EF-14 clinical trial [17]. On the other hand, the anterior array in layout 3 is placed horizontally, which makes it possible to increase the

electric field magnitude in tumors located in the hemispheres. Furthermore, given that the head is larger in the anterior-posterior direction than in the left-right one, there are more possibilities to place the LR pair. For example, layout 3 might be more suitable for tumors located in the parietal lobe (34% of the patients that participated in the EF-14 trial had a tumor in this lobe [17]), whereas layout 4 might be better for tumors appearing in the temporal lobe (40%, [17]). This highlights the high degree of flexibility of solutions that the NovoTAL system can provide.

9.4.3 The best layout based on the NovoTAL system

For each layout, the average EF and the respective ATV1 in the tumor, as well as the array vector, are presented in table 9.2 for each pair. The first two values were obtained following the same approach as the one considered in the NovoTAL system, where 900 mA were injected independently into each pair. Average values considering both pairs are also shown for these three quantities.

Table 9.2: Average electric field, ATV1 and array vector for each layout and for each pair obtained using the new set of electric parameters.

Layout	EF (V/cm)			ATV1 (%)			AV (cm)		
	AP	LR	Average	AP	LR	Average	AP	LR	Average
1	0.84	1.57	1.21	24	93	59	16.8	16.7	16.8
2	0.90	1.55	1.23	32	93	63	16.3	15.9	16.1
3	0.93	1.41	1.17	37	82	60	17.7	15.5	16.6
4	0.76	1.59	1.18	15	86	51	16.7	15.8	16.3
5	0.76	1.56	1.16	16	85	51	17.9	15.9	16.9

Among the five different options to place the arrays, layout 3 was the best one in terms of electric field induced in the tumor in the AP direction (0.93 V/cm), whereas layout 4 produced the highest value when current was injected in the LR pair (1.59 V/cm). Even though there is a strong correlation between the EF induced in the tumor and the ATV1, the data presented in the previous table indicates that the layout that induced the highest EF was not the one that also yielded the highest ATV1. For instance, the average 1.59 V/cm reached in the tumor when current was injected into the LR pair in layout 4 did not translate into the highest ATV1 in that direction among the five different layouts. In layouts 1 and 2, EF maxima reached lower values when current was injected into the LR pair, but the field was more uniform and thus a higher tumor volume surpassed 1 V/cm. In general, shorter array vectors also did not lead to higher EFs or ATV1s in the tumor. Although the distance between the two pairs is an important factor, the relative difference across layouts was not high enough to significantly affect the predicted treatment effectiveness. Instead, the location of each array was more meaningful. This can be quantitatively seen comparing the values of the AV for the AP pair in layouts 3 and 4 and the position of the arrays in figure 9.3. The AV in the first was 17.7 cm, whereas in the second it was 16.7 cm. However, the EF and the ATV1 were higher for the former because the tumor was directly underneath both arrays of this pair in layout 3. The same did not occur for layout 4.

As expected, the values of the EF were higher for the LR pair compared to AP's due to tumor's location. Considering all layouts, the average EF induced by the former

was 1.54 V/cm with the values ranging between 1.41-1.59 V/cm, which corresponds to a variation of 11%. In the complementary pair, the average EF was 0.84 V/cm and the range observed was 0.76-0.93 V/cm, a variation of 18%. As NovoTAL ranks the layouts in terms of average EF induced, the best layout for this tumor location and head model would be layout 2, with a predicted value of 1.23 V/cm. The worst choice would be layout 5, which induced an average EF of 1.16 V/cm. It is noteworthy that the relative difference between these two values is only 6%. This indicates that all five different options suggested by NovoTAL have practically the same effectiveness if the criterion used to rank the layouts is the average EF when 900 mA are injected into each pair. The data presented in table 9.2 indicates that the average ATV1 might be a better option as the values predicted vary over a wider range. The relative difference between the best option, layout 2, and the worst options, layouts 4 and 5, was around 19%.

The values of the ATV1 for these layouts were very similar or higher than what was obtained with the old layout (table 9.1, third row), which indicates that they represent better solutions. Based on the criterion used by the NovoTAL system, layout 2 would be the best choice for treatment when the temperature is not accounted for.

9.4.4 LMiPD, LAPD and SAR based on predictor A

Following the same approach as the one presented in subsection 8.4.1, the average LMiPD and LAPD were quantified in the tumor and the maximum local SAR in the scalp when 900 mA of current were injected into each pair independently (table 9.3).

Table 9.3: Average LMiPD and LAPD in the active tumor and maximum local SAR in the scalp for each layout when 900 mA of current were injected into each pair independently.

Layout	I (mA) AP	I (mA) LR	LMiPD (mW/cm^3)	LAPD (mW/cm^3)	SAR (W/kg)
1	900	900	0.81	2.10	3570
2	900	900	0.93	2.10	2982
3	900	900	0.93	1.89	3936
4	900	900	0.70	2.13	3354
5	900	900	0.69	2.06	4038

Contrary to what was seen with the spheroid model, there is now a wider range of variation in these metrics. The values for the LMiPD varied by up to 26%, between 0.69 and 0.93 mW/cm^3. The two layouts that led to the lowest LMiPD in the active tumor were layouts 4 and 5, which yielded 0.70 and 0.69 mW/cm^3, respectively, whereas layouts 2 and 3 induced the highest value, 0.93 mW/cm^3. These values are correlated with the ones obtained for the ATV1 when current was injected into the AP pair (table 9.2) as this is the pair that limits the values of the LMiPD the most. Thus, the layouts that can induce the highest and the most uniform electric field in the tumor, which can be quantified by the ATV1, are also the ones that will most likely lead to the highest LMiPD. However, it is noteworthy that as this metric is based on the value of the power density in each voxel of the tumor, the value of the LMiPD might also be reduced when changing the position of the LR pair given that in certain regions of the tumor the power density induced by the AP pair is higher than the one produced by LR's. A similar rationale is

presented in figure 2.4 for the EF distribution, where it can be observed that the regions where the active tumor reaches the therapeutic threshold of 1 V/cm are different for each pair. All the LMiPD values are below the therapeutic threshold of 1.15 mW/cm^3 deduced by Ballo et al [98] that best divides EF-14 patients in two groups with the most statistical difference in the overall survival. This is explained by tumor's location, which was placed in a region of the head where the EF and PD induced by the AP pair were low.

In terms of LAPD, the range of values obtained was narrower (11%) than for the LMiPD (26%), but it was still higher than what was seen for the SHM (5%, table 8.2). The lowest value obtained was 1.89 mW/cm^3 for layout 3, whereas the highest was 2.13 mW/cm^3 for layout 4. Contrary to what occurred with the spheroid model, here one of the best layouts in terms of LMiPD, layout 3, is now the worst in terms of LAPD, whereas the opposite occurred for layout 4. In the latter, the anterior and posterior arrays are placed in the worst positions compared to the other layouts. However, as the left and right arrays are placed in regions that increase the value of the power density in this direction, the LAPD was significantly enhanced.

The analysis based on the SAR also led to a wider range of values than those seen using the spheroid model. For this RHM, the SAR values varied by 26% of the maximum value and ranged between 2982 W/kg, in layout 2, and 4038 W/kg, in layout 5. As discussed before, these results might only be used qualitatively as these are SAR values measured in only two specific points. This means that layout 2 is probably the safest out of the five layouts.

Figure 9.4 depicts a qualitative comparison of the best layout to use depending on the criterion selected. Based on this analysis, layout 2 would be chosen based on the EF, on the LMiPD (layout 3 produced the same value), and on the SAR, whereas layout 4 would be the best option based on the LAPD. The choice made by the NovoTAL system based on the EF, layout 2, would thus be the best option in 2 out of the other 3 criteria evaluated and would rank second using the LAPD with a predicted value only 1.4% lower than layout 4.

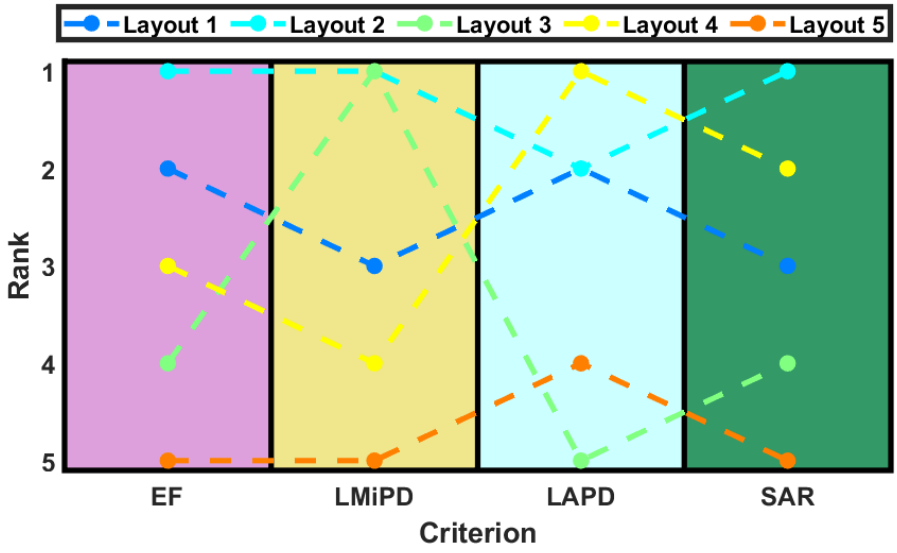

Figure 9.4: Ranking of the 5 different layouts based on four different criteria when predictor A was used. Under these conditions, the same current, 900 mA, was injected into each pair and in all layouts. Each rectangle corresponds to an analysis based on a different metric: EF (purple), which is how the NovoTAL system ranks the layouts, LMiPD (yellow) and LAPD (blue), all quantified in the tumor, and local SAR in the scalp (green).

9.4.5 EF, LMiPD, LAPD and SAR based on predictor B

The results obtained with the spheroid model indicated that layouts in which transducers of different pairs were very close to each other might rank worse when the temperature is accounted for. This might be a limitation on how much current is injected in layouts 2 to 5, in which there are transducers of different pairs close to each other (figure 9.3). The same analysis as the one presented in subsection 8.4.2 was carried out to rank the layouts based on the temperature of the scalp using predictor B. To find how much current could be injected into each pair a similar iterative approach was followed with the adjustments described in subsection 9.3.2. The maximum temperature variation of the scalp underneath the AP and LR pairs in layout 1 for a 5-minute simulation is shown in figure 9.5 for different sets of injected current.

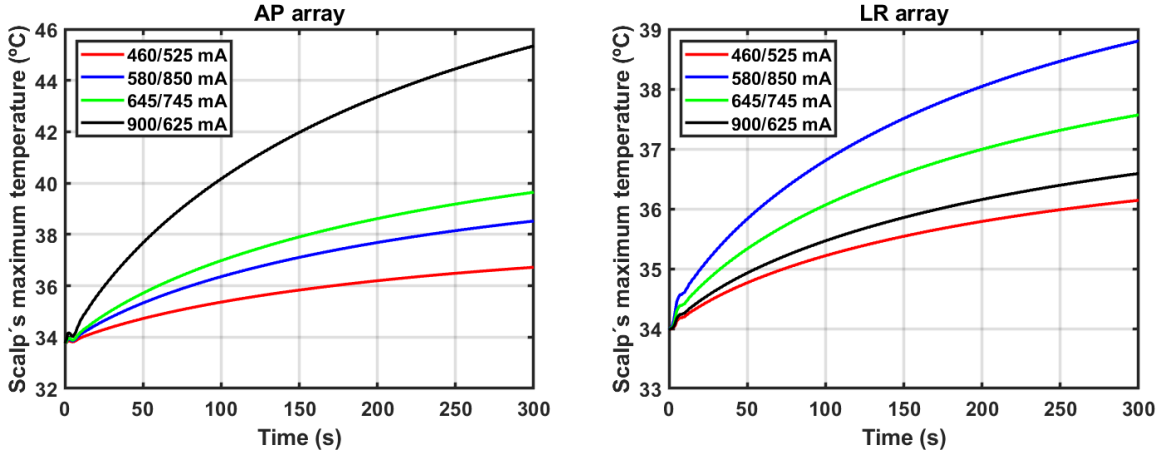

(a) AP pair (b) LR pair

Figure 9.5: Variation of the maximum temperature of the scalp underneath the AP (left) and the LR (right) pairs for different sets of injected current in layout 1. Each set is identified as X1/X2 mA, where X1 is the current injected in the AP pair and X2 is the current injected in the LR pair. Current was injected alternately into each pair with a switching time of one second. The y-axis is different for each plot.

Equation (6.2) was fitted to the data presented in this figure and the maximum steady-state temperature that the scalp would reach underneath each pair was then predicted using equation (6.3). The results are presented in table 9.4.

Table 9.4: Maximum steady-state temperature predicted on the scalp surface underneath each pair of arrays when different sets of current were injected. Each set is identified as X1/X2 mA, where X1 is the current injected in the AP pair and X2 is the current injected in the LR pair. Current was injected alternately into each pair with a switching time of one second.

Injected current (mA) AP/LR	Maximum temperature underneath AP pair (°C)	Maximum temperature underneath LR pair (°C)
460/525	37.3	36.4
580/850	39.4	39.4
645/745	40.7	38.1
900/625	47.3	37.0

Based on the data of the previous table and on what was discussed before, it is possible to conclude that if this head model with this layout represented a patient treated with TTFields, in average, 580 mA of current would be injected in the AP pair and 850 mA into the LR pair with a switching of one second. This set of values are the ones that leads to a maximum steady-state temperature predicted on the surface of the scalp around 39.5 ℃ underneath both pairs. The minimum adjusted-R^2 for the data shown in the previous table was 0.9992. For this set of currents, the temperature of all tissues at the end of the simulation (t=5 minutes) can be viewed in figure 9.9 in subsection 9.4.7. Following the same rationale, the maximum current that could be injected into each pair in the remaining 4 layouts to induce a maximum steady-state temperature of 39.5 ℃ on the scalp, or as close as possible to it, was also predicted and it is presented in table 9.5, alongside with the values of the EF, LMiPD, LAPD and SAR for those currents. The values of the coefficents C_1, C_2 and C_3, as well as the A-R^2 are shown in table F.1, in appendix F. As seen in this table, the maximum temperature predicted for the scalp underneath each pair was not exactly 39.5 ℃ for all layouts, but it varied between 39.3 and 39.8 ℃. As each simulation took around 42 hours to compute, it was necessary to find a trade-off between the accuracy of the results and the time invested in these studies. Additional considerations on these approximations are made in section 9.5. Layout 2 was the only one in which it was not possible to induce 39.5 ℃ underneath both pairs simultaneously due to the occurence of a temperature hotspot, as discussed in more detail in the next subsection. The temperature distribution on each tissue surface for layouts 2 to 5 is presented in figures F.1 to F.4, respectively, in appendix F. The temperature increases and the prediction of the thermal impact are discussed in detail in subsection 9.4.7.

Table 9.5: Average EF, LMiPD and LAPD in the tumor and maximum local SAR values in the scalp when the temperature was also accounted for. The current injected into each pair was the one that led to a maximum steady-state temperature on scalp's surface of 39.5 ℃ underneath the AP pair and as close as possible to that value underneath the LR pair. In parentheses the relative decrease compared to the respective values obtained using predictor A are given.

Layout	I (mA) AP	I (mA) LR	T+EF V/cm	T+LMiPD mW/cm^3	T+LAPD mW/cm^3	T+SAR W/kg
1	580 (-36%)	850 (-6%)	1.01 (-17%)	0.36 (-56%)	1.66 (-21%)	2374 (-34%)
2	580 (-36%)	650 (-28%)	0.85 (-31%)	0.40 (-57%)	1.04 (-51%)	1384 (-54%)
3	580 (-36%)	775 (-14%)	0.91 (-22%)	0.44 (-53%)	1.22 (-35%)	2346 (-40%)
4	550 (-39%)	800 (-11%)	0.94 (-20%)	0.27 (-61%)	1.53 (-28%)	2002 (-40%)
5	565 (-37%)	800 (-11%)	0.93 (-20%)	0.29 (-58%)	1.48 (-28%)	2280 (-44%)

As expected, accounting for the temperature led to a decrease in the value of the current injected in both pairs compared to the 900 mA that the NovoTAL system considers when choosing the best layout. On average, the current injected into the AP pair decreased by 37% (range: 36-39%), whereas in the LR pair this value was only 14% (6-28%). More current could be injected into the latter as the impedance was lower in that direction.

Inevitably, the reduction in these values was accompanied by a decrease in all the metrics evaluated as well. On average, the EF dimished by 22% (17-31%), the LMiPD by 57% (53-61%), the LAPD by 33% (21-51%), and the SAR by 42% (34-54%). The current injected into the AP pair was reduced by practically the same amount in all layouts due to the fact that this current was optimized first (see subsection 9.3.2). This indicates that, for this criterion, the amount of current injected might be more influenced by head's geometry and physical properties than by the layout chosen when the temperature is also considered in the calculations. The current injected into the LR pair varied more across layouts as a result of the choice of optimizing current in the AP pair first. For the LR pair, the lowest current injected was 650 mA in layout 2, due to the occurrence of a temperature hotspot.

The choice of which layout to use changed significantly depending on the criterion considered, as shown in figure 9.6. Based on this analysis, layout 1 would be chosen based on the EF and LAPD, layout 3 based on the LMiPD, and layout 2 based on the SAR. The latter layout, which was the best in almost every criteria when the temperature was not accounted for, is now the worst in 2 out of the 4 of them.

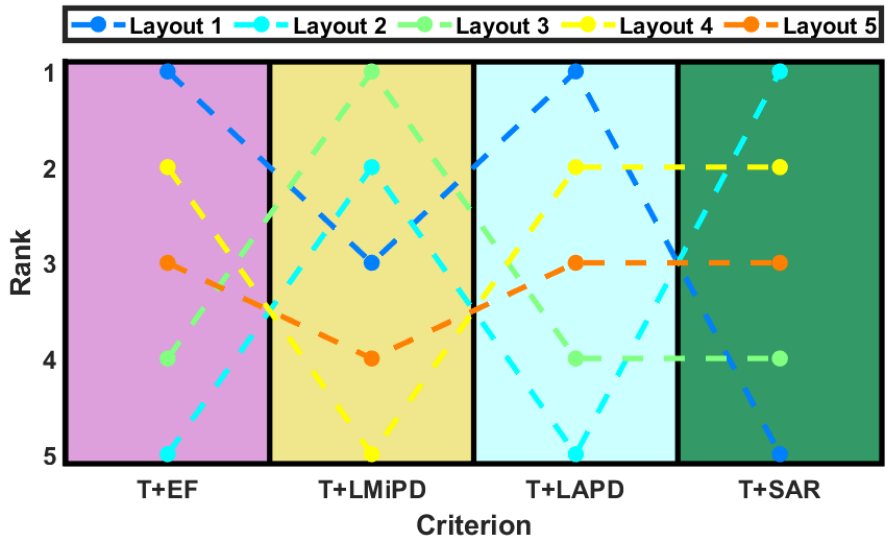

Figure 9.6: Ranking of the 5 different layouts based on four different criteria when predictor B was used. Under these conditions, different amounts of current were injected into each pair and into each layout. Each rectangle corresponds to an analysis based on a different metric: EF (purple), LMiPD (yellow) and LAPD (blue), all quantified in the tumor, and local SAR in the scalp (green).

9.4.6 Importance of accounting for the temperature

As discussed in subsection 8.4.3, accounting for the temperature of the scalp is relevant in two different ways: it decreases the values of the metrics used to predict treatment effectiveness by decreasing the injected current, and it shows that there is a distance between transducers of different pairs below which temperature hotspots might occur. These two parameters are strongly correlated with each other, as the second might significantly impact the first.

In terms of metrics, accounting for the temperature led to a significant reduction in the values obtained regardless of the layout. Similarly to what was observed with the simplified head model, the amount of current injected had to be lower than the 900 mA

typically assumed in the NovoTAL system. Figure 9.7 depicts a qualitatively comparison of which layout would be chosen for this tumor position and for this head model based on the analysis presented in the two previous subsections.

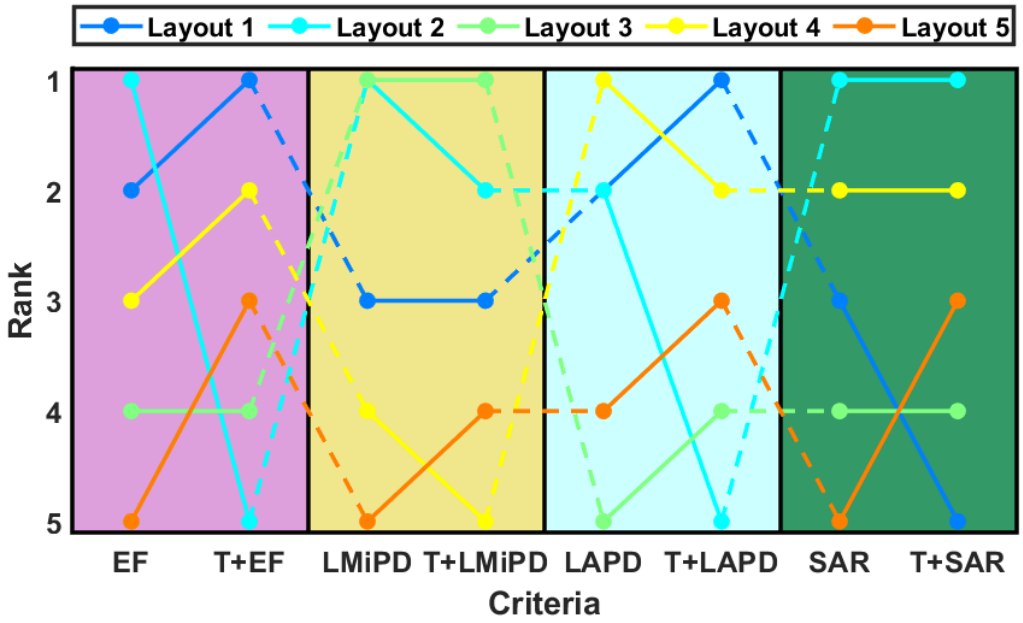

Figure 9.7: Ranking of the 5 different layouts based on four diferent criteria using predictor A (EF, LMiPD, LAPD and SAR) and predictor B (T+EF, T+LMiPD, T+LAPD, T+SAR). The amount of current injected into each layout was the same for the first, but it varied for the second. Each rectangle corresponds to an analysis based on a different metric: EF (purple), LMiPD (yellow) and LAPD (blue), all quantified in the tumor, and local SAR in the scalp (green).

The LMiPD and the SAR were the ones in which the least variations were seen due to the reasons explained above. The calculations of the EF and the LAPD were most affected by the lowest current injected in the LR pair using layout 2. This layout was the only one in which it was not possible to simultaneously induce the desired temperature on the scalp underneath both pairs (table F.1, appendix F). Underneath AP's the maximum steady-state temperature that the scalp reached was indeed 39.5 ℃, but underneath the second it was only 38.3 ℃. If more current was injected into the LR pair the temperature of the scalp underneath the AP's would also increase and surpass the 39.5 ℃. This occurred because one transducer of the left array was only 3 mm apart from one of the posterior array and thus a temperature hotspot occurred (figure 9.8a), similarly to what was reported with the simplified head model. Consequently, the EF and the LAPD for this layout decreased significantly when the temperature was also accounted for. The rank of the remaining layouts was not significantly affected by adding information about the temperature as the minimum distance between transducers of different pairs was enough to avoid it. As an example, figure 9.8b depicts the temperature distribution on scalp's surface using layout 5 at the end of the simulation. The shortest distance between transducers of different pairs was 8 mm, which was not enough to create a visible temperature hotspot. In the remaining three layouts this distance was 8 mm or higher.

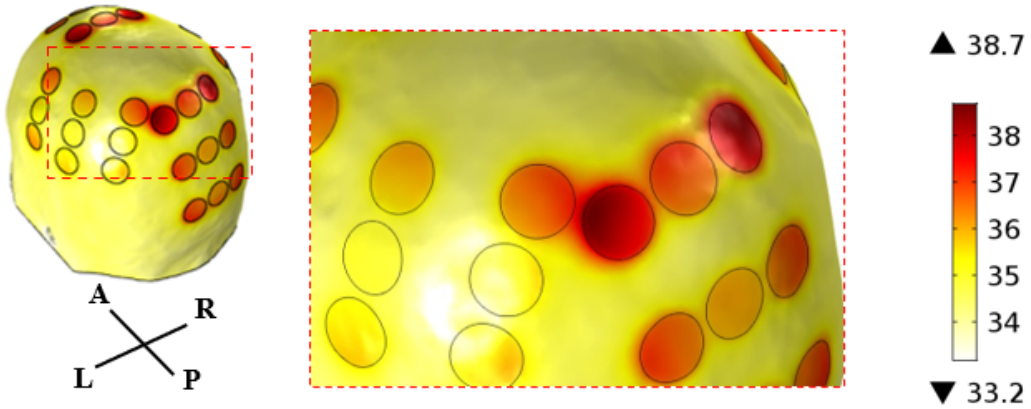

(a) Layout 2

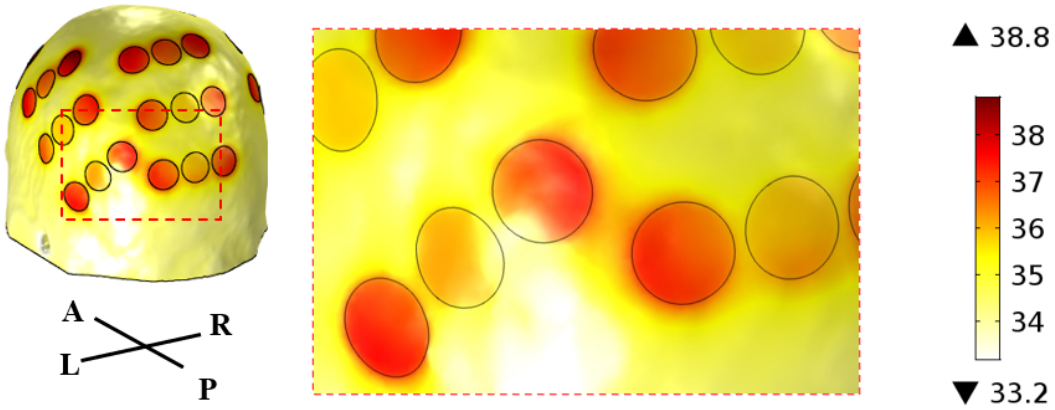

(b) Layout 5

Figure 9.8: Temperature distribution on the surface of the scalp at the end of simulation (t=5 minutes) when current was injected alternately into the AP and LR pairs with a switching time of one second in (a) layout 2 and (b) layout 5. The circles represent the interface between the scalp and the gel and they correspond to the regions where the maximum temperature was reached and measured. In layout 2 one transducer of the posterior array was placed only 3 mm apart from one transducer of the left array which created a significant temperature hotspot there, thus limiting how much current could be injected in the LR pair. In layout 5, the distance between the two closest transducers from the posterior and left pairs was 8 mm, which was enough to not create a visible temperature hotspot between the transducers of different arrays. Temperature scales are in ℃.

Even though layout 2 was the only one in which there was a visible temperature hotspot on the surface of the scalp, the data presented in table 9.5 suggests that there might still be a small contribution of the current injected in the AP pair on the temperature increases underneath the LR pair and vice-versa. In layout 1, in which the arrays were the most separated, the current injected into the LR pair was only reduced by 6% compared to when the temperature was not accounted for. In layouts 3 to 5, this decrease was higher, between 11 and 14%, but it was still lower than the 28% seen in layout 2. Nonetheless, it was still possible to predict a maximum steady-state temperature of 39.5 ℃ on the scalp underneath both pairs in all layouts except in layout 2.

Based on these results it can be concluded that adding information about the temperature leads to a similar decrease in all metrics provided that the arrays are sufficiently apart from each other (table 9.5, excluding data from layout 2). The minimum distance to avoid a significant reduction in the current injected seems to be 8 mm. This explains why

in figure 9.7, the position of each layout did not vary significantly within each rectangle (i.e., EF vs. T+EF, LMiPD vs. T+LMiPD, LAPD vs. T+LAPD and SAR vs. T+SAR, excluding data from layout 2).

After investigating the impact of the temperature on these metrics it is important to discuss which might be the most appropriate one to use. The metric used by the NovoTAL system, the average EF, has been reported since the first study on TTFields was published by Kirson et al in 2004 [16]. The large majority of the following work that investigated TTFields efficacy and that suggested ways to improve its application was also based on this metric (e.g.: [43, 82, 94]). The therapeutic threshold of 1 V/cm was already validated, which is one of the strongest arguments in favor of using it. In 2019, an alternative metric was suggested by Ballo et al [98] based on *in-silico* data. In an attempt to make TTFields planning more similar to other cancer treatment planning techniques, such as radiotherapy, a metric that quantified the energy absorbed by tissues was suggested: the LMiPD. The same authors investigated the equivalent therapeutic threshold of 1 V/cm in terms of this new metric and the results yielded 1.15 mW/cm^3. Among the four metrics used in this study, the EF and the LMiPD are the only ones that were investigated in the literature to quantify treatment effectiveness. The LAPD, which was first defined and calculated in this thesis, is a less conservative approach to predict the efficacy of TTFields compared to the LMiPD. As it provides information in terms of the overall contribution of both pairs, it might mask the inefficacy of one pair if the other one is placed in an optimal position. The local SAR value, which was measured locally in the points in the scalp where temperature maxima were reached, is the only metric that was not used to predict how effective a layout might be, but rather to evaluate which might be the safest one. However, the points where they were measured are not necessarily the same ones in which the highest SAR values will be reached, as the temperature also depends on other parameters such as the blood perfusion rate. One interesting alternative that could be used based on the SAR is to evaluate the safety of each layout following a similar approach as the one suggested by Eichfelder and Gebhardt [139]. In that work, the authors calculated and validated a new method called the virtual observation points to estimate a maximum SAR value during a MRI procedure. Extrapolating this method for TTFields, this would mean that local SAR would be measured in a pre-defined and fixed number of points in the head, regardless of the position of the layouts. Then all the values measured would be averaged and the layout that induced the lowest SAR would be considered the safest one. In MRI, it was shown that the values measured in those specific regions, which do not have to be necessarily the same for TTFields, can set a maximum estimation for the total SAR in the head [139].

As validated thresholds for some of these metrics are lacking, one possible approach to rank the layouts is to use the LMiPD first, as it is the most conservative approach and thus it sets a minimum value for the expected treatment effectiveness. In the case that two layouts yield similar values, the LAPD could be used as a second criterion, as it provides more information about the combined contribution of both pairs. As a starting point, the same therapeutic threshold of 1.15 mW/cm^3 could also be used for the LAPD, due to the similarity in the calculation of this metric with the LMiPD. Nonetheless, it would be important to do a similar analysis to the one performed by Ballo et al [98] but for the average value in each voxel instead of the minimum. In the unlikely case that the combined PD metrics are not sufficient to determine the best layout, the one that induced the lowest SAR in the scalp could be the optimal choice. In this context, it would be useful to follow a more rigorous method than the one considered in this work

to measure the SAR. The limits defined by the international agencies for MRI (table 2.1) might not be applicable to TTFields due to the differences in the application of these techniques and on the final goal. Regardless of which metric is used, thresholds should be defined considering that the current injected is not constant and that it depends on the temperature of the scalp.

9.4.7 The temperature variation in the remaining tissues and a more realistic prediction of the thermal impact

The initial goal of this thesis was to improve the model in order to predict the thermal impact of TTFields treatment more accurately. Based on the results described in the previous chapters, it is now possible to study the temperature increases in a much more realistic manner compared to what was known in the beginning of the PhD. Figure 9.9 depicts the temperature distribution when layout 1 was used, whereas figures F.1 to F.4 (appendix F) illustrate the same information for layouts 2 to 5, respectively. As expected, temperature maxima in each tissue always occurred at its surface and quickly decreased with depth. In these five temperature distributions, an additional superior view was also added for a clearer view of the increases. Due to the current control conditions, the maximum temperature that tissues reached at the end of the simulation was practically the same for all layouts. Scalp was the one whose temperature reached the highest value, whereas the brain was the tissue whose temperature varied the least. Due to the independent current injection mode, temperature maxima in each tissue was reached in two different regions when layouts 1, 3, 4 and 5 were used, one underneath the AP pair and another underneath the LR pair. In layout 2, due to the temperature hotspot the maximum temperature in each tissue was reached only underneath the AP pair.

By comparing the temperature distribution obtained using any of these layouts with the one shown in figure 2.7, one can easily see that there are some differences. Firstly, the maximum temperature values when layouts 1 to 5 were used are lower partly because those distributions were evaluated after a shorter exposure to the EFs (5 minutes instead of 6) and partly because the current control mode was different. In the first study on heat transfer during TTFields it was assumed that the temperature of the transducers, whose critical limit was assumed to be 41 ℃, was the current controller. Thus, as the scalp heats more than the transducers, after just six minutes of application of the EFs, the temperature on this tissue surface had reached 42 ℃, whereas the maximum temperature of the skull was 39.4 ℃, CSF's 39 ℃ and brain's 38.1 ℃ (figure 2.7, page 31). Another difference concerns the area in which these increases occurred. As the distance between the transducers was augmented in one direction, from 33 to 44 mm, in layouts 1 to 5, the arrays covered a larger area of the head. This led to the appearance of cooler regions between the lines of transducers separated by 44 mm

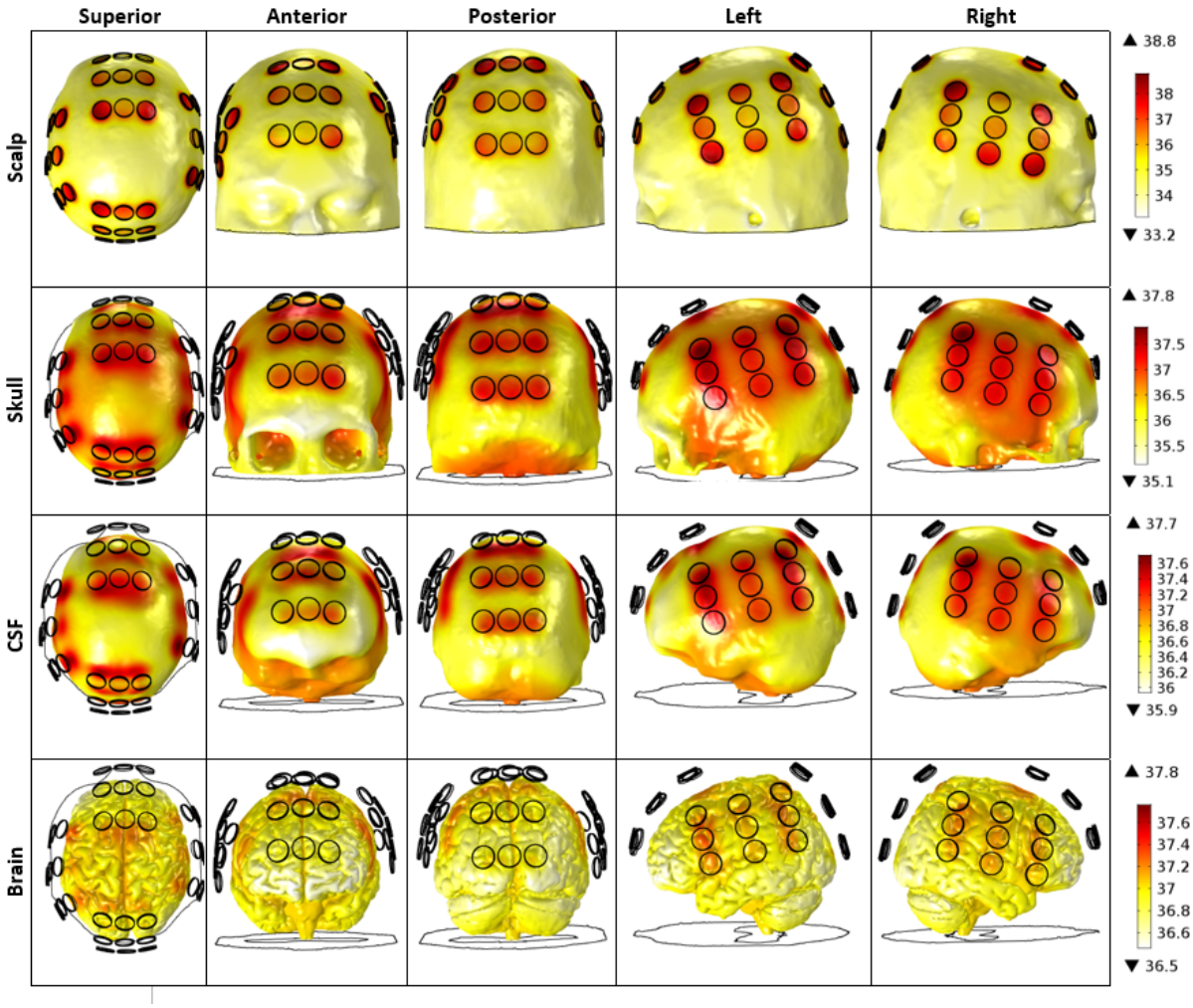

Figure 9.9: Temperature distribution, from five different perspectives, on each tissue surface at the end of the simulation (t=300 seconds) when layout 1 was used. Current was injected alternately into each pair with a switching time of one second. The current injected into the AP pair was 580 mA, whereas in the LR's it was 850 mA. For these values of current the maximum steady-state temperature predicted on the scalp surface underneath both pairs is 39.5 ℃. The temperature increases occurred mainly underneath the arrays as clearly seen by the regions in red. Each circle represents the region where a transducer was placed. First row: scalp; Second row: skull; Third row: CSF; Fourth row: Brain. In the latter, the maximum temperature was reached at the GM surface. Scales are different for each row. All values are in ℃.

As similar temperatures distributions were predicted for all layouts, it is possible to predict the thermal impact for all of them based only on the temperature variations observed in one. Figure 9.10 depicts the maximum temperature variation for the skull, CSF, brain and tumor when layout 1 was used. These variations follow the same exponential expression (equation (6.2)) as the scalp, although with different coefficients. Thus, curve fitting was performed to each one of these curves to predict the maximum steady-state temperature that each tissue will reach. The temperature variation obtained with the fitted expression is presented in dashed lines in the same figure.

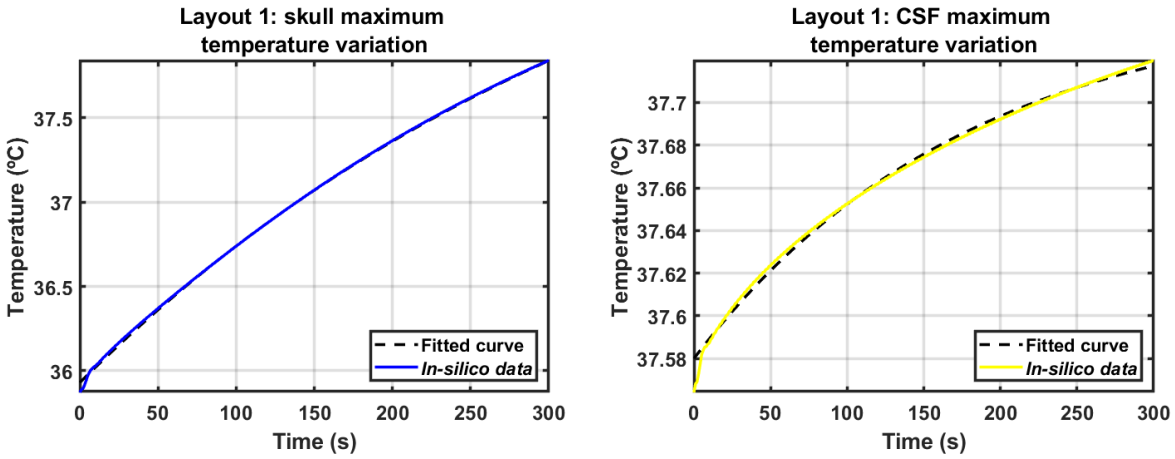

(a) Skull

(b) CSF

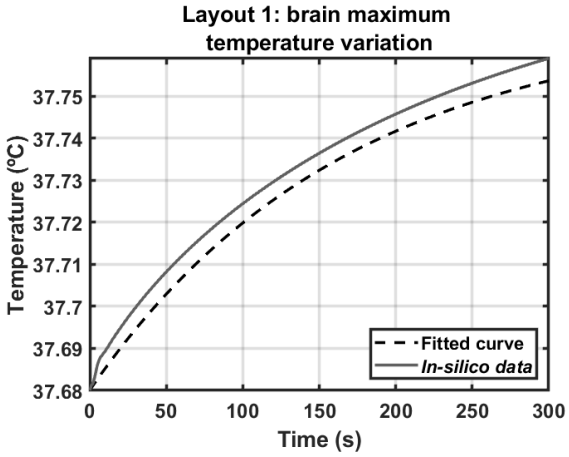

(c) Brain

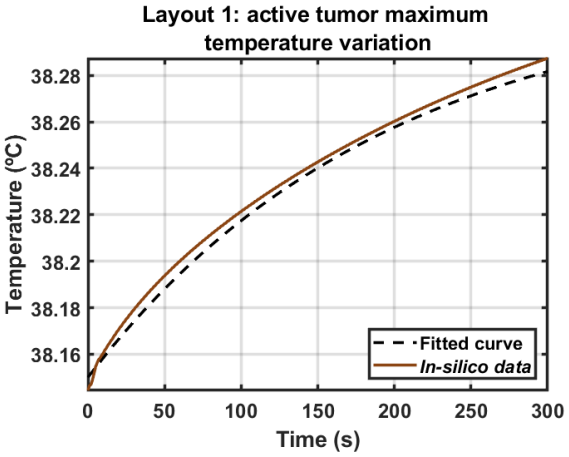

(d) Tumor

Figure 9.10: Variation of the maximum temperature of the skull (upper row, left), CSF (upper row, right), brain (lower row, left), and active tumor (lower row, right) when 580 mA were injected into the AP pair and 850 mA into the LR pair with a switching time of one second using layout 1 (solid lines). Similarly to the scalp, all these tissues follow an exponential temperature variation when TTFields are applied. Thus, in each plot the temperature variation obtained with the fitted expression is also presented in black dashed lines. In the skull, the fitted curve is not well observed as it is overlapped by the *in-silico* data. In the CSF, brain and tumor, the behaviour of the fitted curve suggests an underestimation of the temperature variation. The y-axis are different for each tissue.

The values of the fitted coefficients are presented in table 9.6 for each case.

Table 9.6: Coefficients obtained when fitting an exponential function to the temperature variation of the skull, CSF, brain and active tumor. In the scalp, the maximum steady-state temperature predicted under these conditions is 39.5 ℃. The high values of the A-R^2 indicate that the general expression used can explain well the temperature variations observed.

Tissue	C_1 (℃)	C_2 (s)	C_3 (℃)	A-R^2	T_{max} (℃)
Skull	3.50	380	35.9	0.9998	39.4
CSF	0.17	178	37.6	0.9970	37.8
Brain	0.09	167	37.7	0.9990	37.8
Tumor	0.17	194	38.2	0.9983	38.4

The values of C_1 indicate that the deeper the tissue, the lower the contribution of the EFs in increasing its temperature. After the scalp, the skull is the tissue whose temperature varies the most. According to the predictions made, these fields are responsible for increasing skull's temperature by 3.5 ℃, thus reaching a temperature of 39.4 ℃, which is very close to scalp's 39.5 ℃. In the CSF and tumor this increment was only 0.17 ℃, whereas in the brain was even lower, 0.09 ℃. These results are in accordance with the heat transfer pathways shown in figure 4.2, in which it was seen that in the scalp, skull and CSF the Joule effect is the main source of heating, but in the brain it explains only a small fraction of the temperature increases. However, as depicted by the dashed lines in the previous figure, and as discussed in appendix D, the temperature predicted based on equation (6.3) might be underestimating the real contribution of the EFs.

Based on the values of C_2 it is possible to extrapolate the maximum temperature reached in each tissue after 5 minutes to the values that would be reached after 6 minutes. This allows for a comparison with the temperature increases after 6 minutes of treatment with 900 mA that are shown in figure 2.7 (page 31) and which were obtained based on what was known at the beginning of this thesis. Under these conditions, the maximum temperature of the scalp would be 39.0 ℃ (based on the data of table F.1 appendix F), skull's 38.1 ℃, CSF's 37.9 ℃ and brain's 37.8 ℃. All these values are lower than what is reported in figure 2.7 due to modifications made based on what was discussed in chapter 7.

As discussed at the end of subsection 2.2.4, the thermal impact is only predicted based on the temperature variations and maximum temperature reached by each tissue. These new predictions indicate that none of the thresholds defined in the literature for thermal harm were surpassed in any healthy tissue. In the brain, where most of the thermal impact was predicted, the maximum temperature increase due to the EFs is now less than 0.1 ℃, which is not high enough to cause significant physiological changes according to the literature. In all these tissues, an increase of the blood perfusion rate and variations in the metabolic activity might occur to help dissipate heat more efficiently. These are biophysical mechanisms that help to dissipate heat more efficiently and thus they are not unexpected. The temperature dependence of these two mechanisms was not considered in the simulations performed, but it would most likely improve the predictions in terms of treatment efficacy, as the scalp would cool down more quickly. As for the tumor, the temperature increases due to the application of the EFs are not high enough to attribute TTFields efficacy to a phenomenom similar to the one considered in local hyperthermia treatments. It is unclear if the increment of 0.17 ℃ has any impact in sensitising tumoral cells to the action of other medical techniques such as radiotherapy. Overall, the results from this analysis indicate that Tumor Treating Fields seem to be safe from a thermal point of view.

9.4.8 Importance of the results derived in the previous chapters

All the work developed in the previous chapters allowed to gradually improve some parts of Tumor Treating Fields modelling. Those results gave insights on how to account for the temperature during treatment planning and which factors could change the results the most. Ideally, the predictions made through *in-silico* work would be based on Optune's current injection algorithm, which was discussed in chapter 7. However, due to its complexity, a different approach that could simplify it but still lead to accurate predictions was needed. The current injection algorithm studied in chapter 6, whose initial

intent was to investigate if it was possible to reach a continuous treatment, proved to be a viable option to predict the average current that is injected into each pair in patients. It was based on this approach that it was possible to take the first step towards a more accurate and realistic treatment planning using a simplified head model in chapter 8. In that chapter, it was shown that maximizing the average current injected into each model would favour the least resistive pair and consequently produce lower LMiPD values in the tumor because of the low current injected into the most resistive pair. Due to that reason, current was maximized in the AP pair first in the realistic head model. The different criteria considered to rank the layouts used in the RHM model were also justified by the results obtained with the simplified head model, as significant variations in what is considered to be the best option were observed depending on the metric chosen. Thus, based on the output of chapters 6 to 8, it was possible to improve TTFields modelling, investigate the best way to account for the temperature increases during treatment and evaluate the sensitivity of the choice of the best layout on the criterion used.

The results of the sensitivity analysis of the physical parameters, presented in chapter 4, showed that increasing the thermal conductivity and blood perfusion rate of the scalp decreased temperature maxima in every tissue. A variation in the same direction was observed when the electric conductivity of the scalp and skull were increased. More specifically, skull's electric conductivity was increased to the maximum value reported in the literature, which, as shown in table 4.2, leads to the lowest temperature maxima predicted in almost every tissue, including the scalp. Table C.1 in appendix C indicates that the maximum temperature predicted for the scalp decreased from 41.6 to 38.6 ℃ (-3.0 ℃) when skull's electric conductivity was increased from 0.013 to 0.080 S/m. As current injection depends on the temperature of this tissue, it is expected that the values found in this chapter for each layout that induced a maximum steady-state temperature of 39.5 ℃ correspond to the best-case scenario. Furthermore, it was shown that when the arrays were at least 8 mm apart, there were no visible temperature hotspots that could significantly impact the current injected into each pair. This conclusion might not hold if the electric conductivity of the skull, or even of the scalp, are reduced as the Joule effect in each tissue would be higher. In those cases, less current would be injected into each pair to induce the same temperature in the scalp, which could decrease the predicted treatment effectiveness when this additional parameter was considered during treatment planning.

One possible way to decrease the temperature, even if less favorable physical parameters are used for the scalp, is to consider other relevant cooling mechanisms in the simulations. In chapter 5, it was seen that sweat represents one additional path to cool down the scalp and that depending on the values assigned to the parameters that model it, it could be the main one. If this mechanism was considered in simulations presented in this chapter, the values of the fitted coefficients would most likely be different. As the temperature would vary more slowly, more simulation time would also be needed to perform a reliable curve fitting. Adding sweat could also decrease the minimum distance between transducers as the scalp would cool down more quickly.

9.5 Limitations and conclusions

Throughout this chapter an investigation of the impact of adding information regarding the temperature in the NovoTAL system was carried out. Temperature maxima on the

scalp was reached underneath the outer transducers of each array, as more current was injected there due to the edge effects discussed previously. Underneath these transducers, at the interface between the scalp and the gel, the temperature distribution was not uniform. Within each one of these interfaces, the maximum temperature was reached in the periphery and in regions further away from the center of the transducer, as depicted by the darker colors in those regions in figure 9.9. However, the arrays used in patients have a thermistor placed in the center of the transducer and thus current control is made based on the temperature at the center of this interface. To improve the accuracy of the results deduced in this chapter, a circular interface with a diameter of 2 mm should have been represented. This is the size of the thermistor used in the Optune system and it would most likely lead to a more optimistic prediction of treatment efficacy, as the reported temperature would be lower and more current could be injected into each pair to induce a maximum temperature of 39.5 ℃ in that region. This more realistic approach might also lead to a more intense temperature hotspot in layouts in which transducers of different pairs are close to each other.

The predictions made in terms of how much current could be injected into each pair were also based on the assumption that the time simulated in each study to predict the maximum temperature variation was representative enough to extrapolate the conclusions for the whole treatment time. The high values of the adjusted-R^2 indicate a very good agreement for the first five minutes of treatment between the fitted coefficients and the data used to obtain them. However, similarly to what occurred for the deepest tissues (figure 9.10), an underestimation of the temperature of the scalp using the fitted curve was also observed (data not shown). To minimize the error associated with these predictions, the value of C_3, which was known for every tissue, was not kept constant during curve fitting as it would lead to a more pronounced underestimation of the temperature. This underestimation leads to a lower maximum temperature predicted for the scalp and consequently to a more optimistic prediction of treatment effectiveness as more current is injected into each pair. One way to test this hypothesis is to perform additional studies under the same conditions but simulating more than just the first five minutes of treatment. Based on the data presented, the skull is the tissue that takes the longest to reach a steady-state temperature when the EFs are applied (C_2 = 380 seconds, table 9.6). If three time constants were simulated based on this value (i.e., 19 minutes), the contribution of the EFs in increasing the temperature of this tissue would have already reached 95% of its maximum. Thus, the fitted coefficients could be more accurate and possibly less biased by simulation time. It would also help to improve the accuracy of the results if more validation tests were made to investigate if the general expression used, equation (6.2), can predict the average current injected in other patients and for the new set of electric parameters used. As discussed before, this equation was validated in chapter 7 by comparing the current injected in the head model used with data from one patient's log files when the old set was still being used. Ideally, the maximum temperature predicted for the scalp underneath each pair should also be exactly 39.5 ℃. However, due to time constraints, it was not possible to run enough iterations to induce exactly that value in all layouts. As shown in table F.1 (appendix F) the maximum temperature predicted for the scalp varied between 39.3 and 39.8 ℃, which could slightly influence the injected current.

One of the main challenges when trying to consider the temperature during planning is the time that it takes to run the simulations. In workstation 3, each iteration took more than 1.5 days to compute and at least 4 iterations were performed for each layout. This implies that it was necessary at least 1 week per layout to determine how much current

could be injected into each pair to induce a maximum of 39.5 ℃ on the scalp. As there were five different possibilities to place the arrays, it took more than one month just to find the best array positioning for this model and tumor location. This makes this approach unpractical to use in patients, especially considering that GBM is a fast-growing tumor and treatment planning should be as quick as possible. Even if more powerful workstations that could significantly reduce simulation time were used, accounting for the temperature would most likely require changing TTFields planning workflow in stages prior to step S23 (figure 9.1). As mentioned previously, in step S12, the representation of the scalp, skull and CSF is downgraded and these tissues are represented as simple shells or convex hulls to reduce the time that it takes to plan treatment. This approach might not be viable when the temperature is of interest as it could change the results in terms of temperature distribution on the surface of the scalp.

In the case that it is not feasible to perform time-transient simulations to predict the temperature, indirect ways to account for its impact might also help to optimize treatment planning. One of the quickest ways to do this is ensuring a minimum distance between the arrays of at least 1.0 or 1.5 cm to prevent the occurrence of temperature hotspots. Even though in the head models used 0.8 cm were enough to not observe any hotspots on the surface of the scalp, there might still be some influence of the current injected into one pair in increasing the temperature of the head underneath the complementary pair. Ideally, temperature-wise, the arrays should be placed as separated apart as possible. However, if the minimum distance between the arrays is ensured, the decrease in the metrics will be pratically the same regardless of the layout used and therefore the ranking will not be very affected by taking the temperature into account. Nonetheless, results might vary significantly depending on the criterion used. Even for the two metrics reported in the literature, the average EF and the LMiPD, the choice of the best layout was not in agreement when the temperature was considered (figure 9.7), which highlights the need to investigate in more detail the best way to rank layouts.

Chapter 10

Final considerations

10.1 Main outcomes of this work

The results obtained during the MSc thesis, which were the starting point for the work developed in this PhD, showed the relevance of studying the temperature variations during TTFields therapy. In that work, it was shown that in each tissue heating occurred mainly underneath the arrays and temperature maxima was always reached on the surface. In this PhD thesis, these predictions were improved and further investigated by adding information regarding the real current injection algorithm. This was accomplished by following an approach that simplified its complexity but that maintained the accuracy of the results for the data analysed. Based on the results obtained it was shown that the temperature variation of each tissue could be modelled by an exponential expression with coefficients that could be deduced by curve fitting *in-silico* data. To the best of author's knowledge, this was the first study that quantified the temperature increases during therapy using an approximation to the real algorithm and that predicted how these increases might affect treatment planning. Based on the results obtained, it was also shown that accounting for this additional parameter is of the utmost importance when predicting treatment efficacy as the current injected has to be lower than the 900 mA that the NovoTAL system typically considers in simulations. Even though the current injection algorithm is independent for each pair, the occurrence of common temperature hotspots between arrays might indirectly influence how much current is injected in both pairs. This highlights the need to ensure a minimum distance between the arrays and, ideally, to place them as far possible from each other. Arrays that are very close to each other might lead to a significant decrease in the current injected and consequently the therapeutic threshold of 1 V/cm might not be reached.

Another important outcome of this work is related with the criterion used to rank layouts. It was shown that what is considered to be the best layout depends on the parameter that one wants to prioritize. In this work, the ones that were analysed were the average electric field, the minimum PD (LMiPD), the average PD (LAPD), and head safety (SAR), although other options could be considered. Adding information about the temperature might lead to significant variations in this choice, which is an additional argument in favor of considering this parameter during planning. The results obtained also showed the importance of a more thorough investigation of how modelling should be performed. The values assigned to the physical parameters play an important role in the

maximum temperature values predicted for each tissue. More specifically, it was shown that the electric conductivity of the scalp and skull, and the thermal conductivity and the blood perfusion rate of the scalp are the parameters that lead to the highest uncertainty on the temperature predicted for each tissue and transducers and thus these should be the ones that are more carefully chosen in this type of studies. In terms of energy transfer mechanisms, it was shown that sweat might be a relevant cooling path although there is still not any equation that accurately models it. Thus, in future heat transfer studies this mechanism should be included only after more validation tests are performed.

Despite these uncertainties, the thermal investigation carried out throughout this thesis allowed to study in detail the temperature variations during treatment and showed, for the first time, that Tumor Treating Fields seem to be safe for the patient from a thermal point of view.

10.2 General limitations of this work

The results presented in this thesis and the conclusions drawn from them were based solely in *in-silico* work. This is the only way to non-invasively study how the electric fields interact with the head and to assess the efficacy of different treatment methodologies. In the last two decades, there was a quick development in the computational resources used to perform this type of studies and, nowadays, practical results can be obtained in a matter of few hours as a result of the increasing power of computer processors and optimized algorithms. Inevitably, there will always be limitations when models are used to reproduce and investigate what occurs in living biological systems. The goal is to find the best trade-off between the simplifications made and the accuracy of the results drawn through this approach. This work is no exception and thus, there are some limitations that are important to address. Some of them were already discussed at the end of each chapter, whereas the most general ones are discussed here.

The number of healthy tissues that were segmented in the head model used consisted in scalp, skull, CSF, grey matter, white matter, and lateral ventricles. Typically, these are the only tissues that are represented in the large majority of computational studies to predict the EF distribution in the head. However, the impact of adding more anatomical detail is still unclear when the temperature is considered during TTFieds therapy. In electroconvulsive therapy, adding a layer of fat between the scalp and the skull was shown to have a significant impact both in the electric field distribution and in the maximum temperature predicted for tissues [97]. The work by Hershkovich et al [132] also showed that adding a layer of fat affects the EF when TTFields are applied to the torso. As the electric conductivity of the scalp is much higher than fat's, the current density in the first increases and consequently the Joule effect is also augmented. Thus, if this additional layer is accounted for in TTFields heat transfer studies a meaningful decrease in the current that can be injected into each pair might occur, as scalp's temperature might increase more quickly. Likewise, even more detail can be added to the model. For example, the scalp could be further divided into epidermis, dermis and fat, and a layer of muscle could be represented between the scalp and skull. The more superficial the tissue added, the more likely it is to affect the temperature distribution, although other factors such as the thickness of the layer and the values of the physical parameters also play an important role.

Another limitation of this work was the representation of the tumor. The virtual

lesion consisted in a spherical necrotic core, with a diameter of 1.4 cm, surrounded by a concentric active shell, with a diameter of 2.0 cm. In the EF-11 clinical trial, patients who received TTFields therapy had a tumor whose largest diameter at randomisation was, on average, 6.1 cm (maximum: 15.2 cm) [8]. The work by Wenger et al [82] indicated that the EF in the active shell might not change significantly as a result of tumor's shape and size for volumes by up to 26.6 cm^3 due to the large coverage of the individual arrays. Nonetheless, it would increase the reliability of the results presented here if a sensitivity analysis concerning the size, morphology and position of the tumor was carried out. Most likely, the results in terms of temperature increases in the scalp would hold as the tumor is much smaller than this tissue, but the conclusions in regard to treatment effectiveness might change drastically. To improve the accuracy of the predictions in terms of EF in the tumor, more tissues could also be represented. It is known that the occurrence of a peritumoral edema is common in GBM and that it will most likely decrease the EF in the tumor if considered in computational simulations [136]. Other studies indicated that there is a high intratumoral GBM heterogeneity, with perinecrotic regions having lower electric conductivity values compared to the solid tumor compartments [135]. In the NovoTAL system, these regions are accounted for by assigning dielectric properties to each voxel of the tumor using diffusion tensor images in steps S13 and S14 of the treatment planning workflow (figure 9.1).

The lack of representation of the medical tape that covers the arrays might also lead to less accurate temperature predictions. This medical tapes covers a significant area of the scalp and it makes energy transfer with the environment more difficult compared to when this tissue is in direct thermal contact with the surroundings. Furthermore, the physical properties of this tape might also vary throughout treatment due to patient's sweating. The degree of variation of the results in terms of temperature is still uncertain, but most likely it has a negative impact on the predicted treatment efficacy as there is an additional barrier to heat removal from the head.

10.3 Future work

Based on the general limitations discussed above and on the specific limitations discussed at the end of each chapter, it is possible to define future work that would allow to improve the predictions made so far, and ultimately to enhance how Tumor Treating Fields treatments are planned and delivered to patients.

One of the aspects that is still necessary to investigate is the sensitivity of the results to the model used. In this context, using different head models and different tumor positions, but the same physical parameters as the ones considered in the previous chapter, would be a good first approach to the problem. This would help to quantify the inter-subject variability of the temperature distribution and study how the predictions made in terms of current injected vary from patient to patient. Based on what was discussed in the previous section, segmentation of more tissues, such as fat, and a detailed study of its impact on temperature maxima on the scalp would also be an interesting study to perform.

Experimental work would also help to improve the computational results. As the sensitivity analysis presented in chapter 4 indicated there are four physical parameters whose uncertainty leads to the highest variation on the temperature predicted for each tissue. These parameters were scalp and skull's electric conductivity and scalp's thermal conductivity and blood perfusion rate. However, measuring these properties in humans

is very difficult due to several experimental and ethical constraints. Thus, experiments in animals might be the best alternative. In the literature, there are several studies that reported different approaches to measure tissues dielectric properties (e.g.: [132, 140]), thermal conductivity (e.g.: [141, 142]), and blood perfusion rate (e.g.: [143]). Out of these four most significant parameters, the electric conductivities of the scalp and the skull should be measured first as their impact in the temperature predicted is more relevant compared to the thermal parameters, and also because they might significantly alter the EF in the tumor.

One of the tasks that was initially planned for this thesis was an experimental validation of the heat transfer model. Preliminary work was done toward this goal, but due to the pandemic and subsequent alterations on the initial workplan the advances were limited. Some *in-silico* work was done in which the electric fields were applied first to an aquarium with water and then to a simplified representation of the forearm. At the same time, Novocure did the experiments under similar conditions and the results were compared with each other. The conclusions drawn from these analysis showed some discrepancies between the temperature predicted and measured. This does not necessarily mean that Pennes' equation provides wrong predictions, as the experimental setup and the conditions of the simulations in the two experiments had some differences. Thus, in the future, a thorough investigation is needed under more controlled conditions. The main aim is to study the accuracy of the predictions made through Pennes' equation when TTFields are applied.

Whether information about tissues temperature is added to the NovoTAL system through a similar methodology as the one considered in this work or by an indirect application of the conclusions drawn from it, it is still necessary to investigate the clinical applicability of these studies. This includes, e.g., examining if the layouts already considered in this software have all arrays separated apart by, at least, 0.8 cm. The choice of the best metric to evaluate treatment efficacy is also one of the aspects that should receive more attention in the near future, as it may impact significantly which layout is used. Lastly, information about the temperature of the scalp was incorporated in the model by fitting the data of the temperature variation to an exponential equation. Even though this method proved to be a good estimator for the average current injected in patients, a sensitivity analysis on how the fitted coefficients might vary for longer simulation times and for other set of physical parameters is still needed. Ultimately, the most important future work is a validation of the main findings of this thesis by incorporating the relevant information in the NovoTAL system and comparing the outcome with the results presented here.

10.4 The future of Tumor Treating Fields

Tumor Treating Fields were first reported in the study by Kirson et al in 2004 [16] and have been used for the treatment of recurrent glioblastoma since 2011 following the results of the EF-11 clinical trial [8]. Since then, this technique was also FDA-approved for newly-diagnosed glioblastoma in 2014, following the results of the EF-14 clinical trial [17], and for malignant pleural mesothelioma in combination with chemotherapy in 2019, following the stellar clinical trial results [144]. As of 2021, TTFields are also being investigated for the treatment of advanced small-cell lung carcinoma (EF-15 clinical trial) [145], in recurrent ovarian cancer (innovate) [146], pancreatic cancer (panova) [147], and

hepatocellular carcinoma (hepanova) [148]. These clinical trials are either at phase I, II or III and are applied jointly with chemotherapy as an alternative to chemoterapy alone.

The increasing number of clinical trials in different types of cancer suggests that TTFields might be a reliable option not only in glioblastoma treatment, but in oncology in general. As of 2021, TTFields are used in the USA, some countries in Europe, Israel, Japan, and China [29]. However, it is not likely that this technique will be available in lower-middle, or even in upper-middle, income countries in the next few years, as its monthly cost is around 21 000 USD [20]. This value covers the rent of the Optune system, the arrays, treatment planning in the NovoTAL system, patient and physician training, and 24 hours technical support. The *post-hoc* analysis of the EF-14 clinical trial data carried out by Connock et al [149] estimated that adding TTFields to patient's treatment costs, on average, 453 848 € and it gives patients additional 0.604 years to live. A similar analysis was also performed by Guzauskas et al [150] and the results yielded 188 637 USD and 1.25 years, respectively. One of the main differences in these analysis is that the calculations performed by the first authors were based on the french healthcare system, whereas the second based their calculations on the USA system. Regardless of which is the best way to calculate the cost/effectiveness ratio of TTFields, the high monthly amount that is necessary to pay for it makes TTFields acceptance more difficult. Currently, only Japan, Israel, Sweden, and in some cases Germany, have included this technique in the national reimbursement system [20]. Besides its cost, there are other aspects that might contribute for more countries to not consider TTFields as a viable option, as pointed by Rominiyi et al [20]. Among these, the lack of a control group in clinical trials, the burden of carrying the device, the daily compliance and the fact that the mechanisms of action are not completely understood, might be the most significant ones. In countries where this technique is available, only 30% of the eligible GBM patients are treated with it [150], most of which in the USA [20]. As of 2021, the number of patients that were or still are being treated with TTFieds worldwide is around 18 000 [151].

Despite these challenges, the results seen in other studies might help to increase TTFields acceptance in the future. The computational work by Korshoej et al [111] showed that TTFields efficacy for GBM is enhanced when a craniectomy is performed prior to treatment. In somes cases, the EF in the tumor might increase by up to 70%. These results led to a phase I clinical trial, in which part of the skull of 15 recurrent GBM patients was strategically removed during surgery. Patients were then treated concomitantly with TTFields and chemotherapy. The outcomes showed an OS of 15.5 months and a PFS of 4.6 months, with no additional treatment toxicity [152]. These results were better than what was found in the literature when no craniectomy was performed. This led to the approval of a phase II clinical trial with 70 patients, randomized at a ratio of 1:1, to receive the best practice medical oncology therapy either with or without skull remodeling surgery. The estimated study completion date is on the 1st of March, 2024. Another study that might allow to increase TTFields visibility and acceptance was performed by Giladi et al [24]. This *in-vitro* and *in-vivo* work showed that applying TTFields immediately after radiotherapy could impair the reparation of radiation-induced DNA damage. This led to a phase I/II clinical trial, the PriCoTTF trial, which started in 2020, to test a similar hypothesis [153]. The goal is to investigate the benefits of starting TTFields therapy at the same time as radiochemotherapy in 33 newly-diagnosed GBM patients. The outcome of these two studies performed by Korshoej et al [152] and Guberina et al [153] might lead to the approval of TTFields in earlier stages of treatment in the next few years and thus to increase its acceptance.

Chapter 11

Scientific output: Full list of published and presented work

11.1 Peer-reviewed papers, book chapters and 4-page abstracts

Peer-reviewed papers:

1. * **Nichal Gentilal** and Pedro Cavaleiro Miranda. Temperature control in TTFields therapy of GBM: impact on the duty cycle and tissue temperature. *Physics in Medicine and Biology*, 64(22):225008, 2019. DOI: 10.1088/1361-6560/ab5323

2. **Nichal Gentilal** and Pedro Cavaleiro Miranda. Heat transfer during TTFields treatment: Influence of the uncertainty of the electric and thermal parameters on the predicted temperature distribution. *Computer Methods and Programs in Biomedicine*, 196:105706, 2020. DOI: 10.1016/j.cmpb.2020.105706

3. **Nichal Gentilal**, Ariel Naveh, Tal Marciano and Pedro Cavaleiro Miranda. The impact of scalp's temperature on the choice of the best layout for TTFields treatment. Submitted to *Innovation and Research in Biomedical Engineering*

4. **Nichal Gentilal**, Eyal Abend, Ariel Naveh, Tal Marciano, Igal Balin, Yevgeniy Telepinsky, and Pedro Cavaleiro Miranda. Temperature and impedance variations during Tumor Treating Fields (TTFields) treatment. *Frontiers in Human Neuroscience*, 16:931818, 2022. DOI: 10.3389/fnhum.2022.931818

Book chapters:

1. **Nichal Gentilal**, Ricardo Salvador, and Pedro Cavaleiro Miranda. A thermal study of Tumor Treating Fields for glioblastoma multiforme. *Brain and Human Body Modeling 2020*, chap. 3:37-62, 2020. DOI: 10.1007/978-3-030-45623-8_3

*This paper was submitted and published after the PhD had started, but the main content of this work was developed during the master thesis.

2. **Nichal Gentilal**, Ariel Naveh, Tal Marciano, Ze'ev Bomzon, Yevgeniy Telepinsky, Yoram Wasserman, and Pedro Cavaleiro Miranda. The impact of scalp's temperature in the predicted LMiPD in the tumor during TTFields treatment for glioblastoma multiforme. *Brain and Human Body Modeling 2021* (*in press*)

4-page abstracts:

1. **Nichal Gentilal** and Pedro Cavaleiro Miranda. The impact of the uncertainty of biological tissue thermal parameters on the estimated maximum temperature during TTFields therapy. *2020 42nd Annual International Conference of the IEEE Engineering in Medicine and Biology Society (EMBC)*, 2283-2286, 2020. DOI: 10.1109/EMBC44109.2020.9175372

2. **Nichal Gentilal** and Pedro Cavaleiro Miranda. Continuous versus intermittent application of electric fields during TTFields for glioblastoma treatment. *2021 Global Medical Engineering Physics Exchanges/Pan American Health Care Exchanges*, 1-4, 2021. DOI: 10.1109/GMEPE/PAHCE50215.2021.9434835

3. **Nichal Gentilal**, Ariel Naveh, Tal Marciano, Ze'ev Bomzon, Yevgeniy Telepinsky, Yoram Wasserman, and Pedro Cavaleiro Miranda. A computational study of the relation between the power density in the tumor and the maximum temperature in the scalp during Tumor Treating Fields (TTFields) therapy. *2021 43rd Annual International Conference of the IEEE Engineering in Medicine and Biology Society (EMBC)*, 4192-4195, 2021. DOI: 10.1109/EMBC46164.2021.9630071

11.2 Oral presentations

1. **Nichal Gentilal** and Pedro Cavaleiro Miranda. A review on Tumor Treating Fields: a novel modality in cancer treatment. *4th International congress of CiiEM: health, well-being and ageing in the XXI century*, 2nd-5th June 2019, Setúbal, Portugal. DOI: 10.1080/07853890.2021.1896891

2. **Nichal Gentilal**, Ricardo Salvador, and Pedro Cavaleiro Miranda. A computational study of Joule heating during TTFields therapy. *IEEE Engineering in Medicine and Biology Society (EMBC 2019)*, 23rd-27th July 2019, Berlin, Germany (oral presentation in a minisymposium: "The science and engineering of Tumor Treating Fields (TTFields)")

3. Cornelia Wenger, Hadas Sara Hershkovich, Catherine Tempel-Brami, Moshe Giladi, and Ze'ev Bomzon. Creating conductivity maps at 200 KHz of brain and tumor tissue of glioblastoma patients with water-content based electric properties tomography. *American Society for Radiation Oncology (ASTRO 2019)*, 15th-18th September 2019, Chicago, Illinois, USA (oral presentation on behalf of Novocure); DOI: 10.1016/j.ijrobp.2019.06.591

4. Ariel Naveh, Hadas Sara Hershkovich, Noa Urman, and Ze'ev Bomzon, Tumor Treating Fields therapy to the abdomen is unlikely to cause thermal tissue damage: results of an extensive computational simulation. *American Society for Radiation*

Oncology (ASTRO 2019), 15th-18th September 2019, Chicago, Illinois, USA (oral presentation on behalf of Novocure); DOI: 10.1016/j.ijrobp.2019.06.357

5. **Nichal Gentilal** and Pedro Cavaleiro Miranda. Current injection during TTFields therapy: new methods to increase the effective treatment time. *IEEE Engineering in Medicine and Biology Society (EMBC 2020)*, 20th-24th July 2020, virtual conference (oral presentation in a minisymposia: "The evolving science and engineering of Tumor Treating Fields Part I")

6. **Nichal Gentilal** and Pedro Cavaleiro Miranda. The impact of the uncertainty of biological tissue thermal parameters on the estimated maximum temperature during TTFields therapy. *IEEE Engineering in Medicine and Biology Society (EMBC 2020)*, 20th-24th July 2020, virtual conference

7. **Nichal Gentilal** and Pedro Cavaleiro Miranda. Continuous versus intermittent application of electric fields during TTFields for glioblastoma treatment. *15th Global Medical Engineering Physics Exchanges (GMEPE) and Pan American Health Care Exchanges (PAHCE)*, 15th-20th March 2021, virtual conference

8. **Nichal Gentilal**, Ariel Naveh, Tal Marciano, Ze'ev Bomzon, Yevgeniy Telepinsky, Yoram Wasserman, and Pedro Cavaleiro Miranda. Optimization of TTFields planning: the importance of scalp's temperature in the predicted treatment efficacy. *Brain and Human Body Modeling conference: from fast and accurate computational modeling to clinical practice*, 19th-20th August 2021, virtual conference

9. **Nichal Gentilal**, Ariel Naveh, Tal Marciano, Ze'ev Bomzon, Yevgeniy Telepinsky, Yoram Wasserman, and Pedro Cavaleiro Miranda. A computational study of the relation between the power density in the tumor and the maximum temperature in the scalp during Tumor Treating Fields (TTFields) therapy. *IEEE Engineering in Medicine and Biology Society (EMBC 2021)*, 1st-5th November 2021, virtual conference

10. **Nichal Gentilal**, Ariel Naveh, Tal Marciano, Ze'ev Bomzon, Yevgeniy Telepinsky, Yoram Wasserman, and Pedro Cavaleiro Miranda. Towards a simplified head phantom to validate computational heat transfer results for TTFields therapy. *IEEE Engineering in Medicine and Biology Society (EMBC 2021)*, 1st-5th November 2021, virtual conference (oral presentation in a minisymposia: "Science and technology of Tumor Treating Fields 1: Basic science and innovation")

11. **Nichal Gentilal** and Pedro Cavaleiro Miranda. The relevance of tissue temperature in planning Tumor Treating Fields (TTFields) treatment for glioblastoma. *Jornadas Doutorais do Departamento de Física*, 16th-17th February 2022, Lisbon, Portugal

11.3 Poster presentations

1. **Nichal Gentilal** and Pedro Cavaleiro Miranda. Tumor Treating Fields: a new modality in cancer treatment. *Encontro Ciência 2019*, 8th-10th July 2019, Lisbon, Portugal

2. **Nichal Gentilal** and Pedro Cavaleiro Miranda. A thermal study of Tumor Treating Fields for glioblastoma treatment. *Ciências research day 2019*, 30th October 2019, Lisbon, Portugal

3. **Nichal Gentilal** and Pedro Cavaleiro Miranda. Influence of the thermal and electric properties of biological tissues on the maximum temperature during TTFields therapy. *American Association for Cancer Research 2020 (AACR 2020)*, 22nd-24th June 2020, virtual conference. DOI: 10.1158/1538-7445.AM2020-5484

4. **Nichal Gentilal** and Pedro Cavaleiro Miranda. The impact of the electric conductivity of tissues on the electric field intensity and power density during TTFields therapy for glioblastoma. *American Society for Radiation Oncology (ASTRO 2020)*, 23rd-29th October 2020, virtual conference. DOI: 10.1016/j.ijrobp.2020.07.715

5. **Nichal Gentilal** and Pedro Cavaleiro Miranda. A thermal study of Tumor Treating Fields (TTFields) for glioblastoma treatment. *Ciências research day 2020*, 28th October 2020, virtual conference

6. **Nichal Gentilal** and Pedro Cavaleiro Miranda. A thermal study of Tumor Treating Fields for glioblastoma treatment. *Encontro Ciência 2021*, 28th-30th June 2021, virtual conference

11.4 Invited seminars

1. **Nichal Gentilal** and Pedro Cavaleiro Miranda. The thermal impact of Tumor Treating Fields. Seminar at the *10th Workshop on Biomedical Engineering*, 6th April 2019, Lisbon, Portugal

2. **Nichal Gentilal** and Pedro Cavaleiro Miranda. Tumor Treating Fields: A new modality in cancer treatment. Seminar of *New Tecnologies in Diagnosis and Therapy*, 15th April 2019, Lisbon, Portugal

3. **Nichal Gentilal** and Pedro Cavaleiro Miranda. The thermal impact of Tumor Treating Fields. Seminar to Novocure's physics, experimental and engineering teams, 2nd December 2019, Haifa, Israel

4. **Nichal Gentilal** and Pedro Cavaleiro Miranda. Tumor Treating Fields: A new modality in cancer treatment. Seminar of *New Tecnologies in Diagnosis and Therapy*, 6th April 2020, virtual presentation

5. **Nichal Gentilal** and Pedro Cavaleiro Miranda. Heat transfer when delivering TTFields. Seminar at the *Neuroelectrics-Novocure workshop*, 10th June 2020, virtual workshop

6. **Nichal Gentilal** and Pedro Cavaleiro Miranda. The thermal impact of Tumor Treating Fields. Seminar to Novocure's physics team, 10th November 2020, virtual presentation

7. **Nichal Gentilal** and Pedro Cavaleiro Miranda. Tumor Treating Fields: A new modality in cancer treatment. Seminar of *New Tecnologies in Diagnosis and Therapy*, 22nd March 2021, virtual presentation

8. **Nichal Gentilal** and Pedro Cavaleiro Miranda. Tumor Treating Fields: A new modality in cancer treatment. Seminar of *New Tecnologies in Diagnosis and Therapy*, 4th April 2022, Lisbon, Portugal

References

[1] David N. Louis, Arie Perry, Guido Reifenberger, Andreas von Deimling, Dominique Figarella-Branger, Webster K. Cavenee, Hiroko Ohgaki, Otmar D. Wiestler, Paul Kleihues, and David W. Ellison. The 2016 World Health Organization classification of tumors of the central nervous system: A summary. *Acta Neuropathologica*, 131 (6):803–820, 2016. doi: 10.1007/s00401-016-1545-1.

[2] Michael V. Sofroniew and Harry V. Vinters. Astrocytes: Biology and pathology. *Acta Neuropathologica*, 119(1):7–35, 2010. doi: 10.1007/s00401-009-0619-8.

[3] Marc R. Freeman and David H. Rowitch. Evolving concepts of gliogenesis: A look way back and ahead to the next 25 years. *Neuron*, 80(3):613–623, 2017. doi: 10.1016/j.neuron.2013.10.034.

[4] Bujung Hong, Manolis Polemikos, Hans E. Heissler, Christian Hartmann, Makoto Nakamura, and Joachim K. Krauss. Challenges in cerebrospinal fluid shunting in patients with glioblastoma. *Fluids and Barriers of the CNS*, 15(1):1–9, 2018. doi: 10.1186/s12987-018-0101-x.

[5] Quinn T. Ostrom, Haley Gittleman, Peter Liao, Toni Vecchione-Koval, Yingli Wolinsky, Carol Kruchko, and Jill S. Barnholtz-Sloan. CBTRUS statistical report: Primary brain and other central nervous system tumors diagnosed in the United States in 2010-2014. *Neuro-oncology*, 19(S5):1–88, 2017. doi: 10.1093/neuonc/nox158.

[6] John D. Mathews, Anna V. Forsythe, Zoe Brady, Martin W. Butler, Stacy K. Goergen, Graham B. Byrnes, Graham G. Giles, Anthony B. Wallace, Philip R. Anderson, Tenniel A. Guiver, Paul McGale, Timothy M. Cain, James G. Dowty, Adrian C. Bickerstaffe, and Sarah C. Darby. Cancer risk in 680 000 people exposed to computed tomography scans in childhood or adolescence: Data linkage study of 11 million Australians. *BMJ*, 346(7910):1–18, 2013. doi: 10.1136/bmj.f2360.

[7] Fonnet E. Bleeker, Remco J. Molenaar, and Sieger Leenstra. Recent advances in the molecular understanding of glioblastoma. *Journal of Neuro-Oncology*, 108(1): 11–27, 2012. doi: 10.1007/s11060-011-0793-0.

[8] Roger Stupp, Eric T. Wong, Andrew A. Kanner, David Steinberg, Herbert Engelhard, Volkmar Heidecke, Eilon D. Kirson, Sophie Taillibert, Zvi Ram, J. Lee Villano, Nikolai Rainov, Frank Liebermann, Vladimir Dbalý, Uri Weinberg, David Schiff, Lara Kunschner, Jeffrey Raizer, Jerome Honnorat, Andrew Sloan, Mark Malkin, Joseph C. Landolfi, Franz Payer, Maximilian Mehdorn, Robert J. Weil, Susan C. Pannullo, Manfred Westphal, Martin Smrcka, Lawrence Chin, Herwig Kostron, Silvia Hofer, Jeffrey Bruce, Rees Cosgrove, Nina Paleologous, Yoram Palti, Philip H. Gutin, and Claude Bernard. NovoTTF-100A versus physician ' s choice chemotherapy in recurrent glioblastoma: A randomised phase III trial of a novel treatment modality. *European Journal of Cancer*, 48(14):2192–2202, 2012. doi: 10.1016/j.ejca.2012.04.011.

[9] Derek Richard Johnson. Rising incidence of glioblastoma and meningioma in the United States: Projections through 2050. *2012 Annual Meeting of the American Society of Clinical Oncology*, 30(S15):2065, 2012. doi: 10.1200/jco.2012.30.15_suppl.2065.

[10] Chris McKinnon, Meera Nandhabalan, Scott A. Murray, and Puneet Plaha. Glioblastoma: Clinical presentation, diagnosis, and management. *The BMJ*, 374 (1560):1–9, 2021. doi: 10.1136/bmj.n1560.

[11] Antoine Verger and Karl-Josef Langen. PET imaging in glioblastoma : Use in clinical practice. In Steven De Vleeschouwer, editor, *Glioblastoma*, chapter 9, pages 155–174. Codon Publications, Brisbane (AU), 1st edition, 2017. doi: 10.15586/codon.glioblastoma.2017.ch9.

[12] Roger Stupp, Warren P. Mason, Martin J. van den Bent, Michael Weller, Barbara Fisher, Martin J.B. Taphoorn, Karl Belanger, Alba A. Brandes, Christine Marosi, Ulrich Bogdahn, Jürgen Curschmann, Robert C. Janzer, Samuel K. Ludwin, Thierry Gorlia, Anouk Allgeier, Denis Lacombe, J. Gregory Cairncross, Elizabeth Eisenhauer, and René O. Mirimanoff. Radiotherapy plus concomitant and adjuvant temozolomide for glioblastoma. *New England Journal of Medicine*, 352 (10):987–996, 2005. doi: 10.1056/NEJMoa043330.

[13] Jacob P. Fisher and David C. Adamson. Current FDA-approved therapies for high-grade malignant gliomas. *Biomedicines*, 9(324):1–13, 2021. doi: 10.3390/biomedicines9030324.

[14] Catarina Fernandes, Andreia Costa, Lígia Osório, Rita C. Lago, Paulo Linhares, Bruno Carvalho, and Cláudia Caeiro. Current standards of care in glioblastoma therapy. In Steven De Vleeschouwer, editor, *Glioblastoma*, chapter 11, pages 73–

80. Codon Publications, Brisbane (AU), 1st edition, 2017. doi: 10.15586/codon.glioblastoma.2017.ch11.

[15] U. S. National Institutes of Health. National Cancer Institute (NCI) (accessed: 18/12/2021). URL `https://www.cancer.gov/publications/dictionaries/cancer-terms/def/`.

[16] Eilon D. Kirson, Zoya Gurvich, Rosa Schneiderman, Erez Dekel, Aviran Itzhaki, Yoram Wasserman, Rachel Schatzberger, and Yoram Palti. Disruption of cancer cell replication by alternating electric fields. *Cancer Research*, 64(9):3288–3295, 2004. doi: 10.1158/0008-5472.can-04-0083.

[17] Roger Stupp, Sophie Taillibert, Andrew Kanner, William Read, David M. Steinberg, Benoit Lhermitte, Steven Toms, Ahmed Idbaih, Manmeet S. Ahluwalia, Karen Fink, Francesco Di Meco, Frank Lieberman, Jay Jiguang Zhu, Giuseppe Stragliotto, David D. Tran, Steven Brem, Andreas F. Hottinger, Eilon D. Kirson, Gitit Lavy-Shahaf, Uri Weinberg, Chae Yong Kim, Sun Ha Paek, Garth Nicholas, Jordi Burna, Hal Hirte, Michael Weller, Yoram Palti, Monika E. Hegi, and Zvi Ram. Effect of tumor-treating fields plus maintenance temozolomide vs maintenance temozolomide alone on survival in patients with glioblastoma a randomized clinical trial. *Journal of the American Medical Association*, 318(23):2306–2316, 2017. doi: 10.1001/jama.2017.18718.

[18] Eilon D Kirson, Vladimir Dbalý, František Tovarys, Josef Vymazal, Jean F Soustiel, Aviran Itzhaki, Daniel Mordechovich, Shirley Steinberg-Shapira, Zoya Gurvich, Rosa Schneiderman, Yoram Wasserman, Marc Salzberg, Bernhard Ryffel, Dorit Goldsher, Erez Dekel, and Yoram Palti. Alternating electric fields arrest cell proliferation in animal tumor models and human brain tumors. *Proceedings of the National Academy of Sciences*, 104(24):10152–10157, 2007. doi: 10.1073/pnas.0702916104.

[19] Jack A. Tuszynski, Cornelia Wenger, Douglas E. Friesen, and Jordane Preto. An overview of sub-cellular mechanisms involved in the action of TTFields. *International Journal of Environmental Research and Public Health*, 13(11):1–23, 2016. doi: 10.3390/ijerph13111128.

[20] Ola Rominiyi, Aurelie Vanderlinden, Susan J. Clenton, Caroline Bridgewater, Yahia Al-Tamimi, and Spencer James Collis. Tumour treating fields therapy for glioblastoma: current advances and future directions. *British Journal of Cancer*, 124(4): 697–709, 2021. doi: 10.1038/s41416-020-01136-5.

[21] Nidhi Gera, Aaron Yang, Talia S. Holtzman, Sze X. Lee, Eric T. Wong, and Kenneth D. Swanson. Tumor treating fields perturb the localization of septins and

cause aberrant mitotic exit. *PLoS ONE*, 10(5):1–20, 2015. doi: 10.1371/journal.pone.0125269.

[22] Andrew A. Bridges and Amy S. Gladfelter. Septin form and function at the cell cortex. *Journal of Biological Chemistry*, 290(28):17173–17180, 2015. doi: 10.1074/jbc.R114.634444.

[23] Lukas Berkelmann, Almke Bader, Saba Meshksar, Anne Dierks, Gökce Hatipoglu Majernik, Joachim K. Krauss, Kerstin Schwabe, Dirk Manteuffel, and Anaclet Ngezahayo. Tumour-treating fields (TTFields): Investigations on the mechanism of action by electromagnetic exposure of cells in telophase/cytokinesis. *Scientific Reports*, 9(7362):1–11, 2019. doi: 10.1038/s41598-019-43621-9.

[24] Moshe Giladi, Mijal Munster, Rosa S. Schneiderman, Tali Voloshin, Yaara Porat, Roni Blat, Katarzyna Zielinska-Chomej, Petra Hååg, Ze'ev Bomzon, Eilon D. Kirson, Uri Weinberg, Kristina Viktorsson, Rolf Lewensohn, and Yoram Palti. Tumor treating fields (TTFields) delay DNA damage repair following radiation treatment of glioma cells. *Radiation Oncology*, 12(206):1–13, 2017. doi: 10.1186/s13014-017-0941-6.

[25] Edwin Chang, Chirag B. Patel, Christoph Pohling, Caroline Young, Jonathan Song, Thomas Anthony Flores, Yitian Zeng, Lydia Marie Joubert, Hamed Arami, Arutselvan Natarajan, Robert Sinclair, and Sanjiv S. Gambhir. Tumor Treating Fields increases membrane permeability in glioblastoma cells. *Cell Death Discovery*, 4 (113):1–13, 2018. doi: 10.1038/s41420-018-0130-x.

[26] Wei Yung Ding, Jiawen Huang, and Hongyan Wang. Waking up quiescent neural stem cells: Molecular mechanisms and implications in neurodevelopmental disorders. *PLoS Genetics*, 16(4):1–26, 2020. doi: 10.1371/journal.pgen.1008653.

[27] Fransje A. Castelijns, Janine Ezendam, Mieke A. Latijnhouwers, Ivonne M. Van Vlijmen-Willems, Patrick L. Zeeuwin, Marie-Jeanne Gerritsen, Peter C. Van de Kerkhof, and Piet E. Van Erp. Epidermal cell kinetics by combining in situ hybridization and immunohistochemistry. *The Histochemical journal*, 30(12):869–877, 1998. doi: 10.1023/a:1003457709690.

[28] Moshe Giladi and Rosa Schneiderman. WO 2017/175116 A1: Reducing motility of cancer cells using Tumor Treating Fields (TTFields), 2017.

[29] Roni Blatt, Shiri Davidi, Mijal Munster, Anna Shteingauz, Shay Cahal, Adel Zeidan, Tal Marciano, Zeev Bomzon, Adi Haber, Moshe Giladi, Uri Weinberg, Adrian

Kinzel, and Yoram Palti. In-vivo safety of Tumor Treating Fields (TTFields) applied to the torso. *Frontiers in Oncology*, 11(670809):1–10, 2021. doi: 10.3389/fonc.2021.670809.

[30] Adrian Kinzel, Michael Ambrogi, Michael Varshaver, and Eilon D. Kirson. Tumor Treating Fields for glioblastoma treatment: Patient satisfaction and compliance with the second-generation optune® system. *Clinical Medicine Insights: Oncology*, 13:1–7, 2019. doi: 10.1177/1179554918825449.

[31] Novocure. Optune: Patient information and operation manual (accessed: 21/12/2021). URL `https://www.optune.com/instructions-for-use`.

[32] Andrew A. Kanner, Eric T. Wong, John L. Villano, and Zvi Ram. Post hoc analyses of intention-to-treat population in phase III comparison of NovoTTF-100A™ system versus best physician's choice chemotherapy. *Seminars in Oncology*, 41(5 Suppl 6): S25–S34, 2014. doi: 10.1053/j.seminoncol.2014.09.008.

[33] Maciej M. Mrugala, Herbert Engelhard, David Dinh Tran, Yvonne Kew, Robert Cavaliere, John L. Villano, Daniela Annenelie Bota, Jeremy Rudnick, Ashley Love Sumrall, Jay Jiguang Zhu, and Nicholas Butowski. Clinical practice experience with NovoTTF-100A™ system for glioblastoma: the patient registry dataset (PRiDe). *Seminars in Oncology*, 41(S6):S4–S13, 2014. doi: 10.1053/j.seminoncol.2014.09.010.

[34] Eilon D Kirson, Rosa S. Schneiderman, Vladimir Dbalý, František Tovaryš, Josef Vymazal, Aviran Itzhaki, Daniel Mordechovich, Zoya Gurvich, Esther Shmueli, Dorit Goldsher, Yoram Wasserman, and Yoram Palti. Chemotherapeutic treatment efficacy and sensitivity are increased by adjuvant alternating electric fields (TTFields). *BioMed Central Medical Physics*, 9(1):1–13, 2009. doi: 10.1186/1756-6649-9-1.

[35] Steven A. Toms, Chae Yong Kim, Garth Nicholas, and Zvi Ram. Increased compliance with Tumor Treating Fields therapy is prognostic for improved survival in the treatment of glioblastoma: a subgroup analysis of the EF-14 phase III trial. *Journal of Neuro-Oncology*, 141(2):467–473, 2019. doi: 10.1007/s11060-018-03057-z.

[36] Zvi Ram, Chae Yong Kim, Andreas F. Hottinger, Ahmed Idbaih, Garth Nicholas, and Jay Jiguang Zhu. Efficacy and Safety of Tumor Treating Fields (TTFields) in Elderly Patients with Newly Diagnosed Glioblastoma: Subgroup Analysis of the Phase 3 EF-14 Clinical Trial. *Frontiers in Oncology*, 11(671972):1–12, 2021. doi: 10.3389/fonc.2021.671972.

[37] Mario E. Lacouture, Mary Elizabeth Davis, Grace Elzinga, Nicholas Butowski, David Tran, John L. Villano, Lucianna Dimeglio, Angela M. Davies, and Eric T.

Wong. Characterization and management of dermatologic adverse events with the NovoTTF-100A system, a novel anti-mitotic electric field device for the treatment of recurrent glioblastoma. *Seminars in Oncology*, 41(3 Suppl. 4):S1–S14, 2014. doi: 10.1053/j.seminoncol.2014.03.011.

[38] Mario E. Lacouture, Milan J. Anadkat, Matthew T. Ballo, Fabio Iwamoto, Suriya A. Jeyapalan, Renato V. La Rocca, Margaret Schwartz, Jennifer N. Serventi, and Martin Glas. Prevention and management of dermatologic adverse events associated with Tumor Treating Fields in patients with glioblastoma. *Frontiers in Oncology*, 10(1045):1–13, 2020. doi: 10.3389/fonc.2020.01045.

[39] Aafia Chaudhry, Laura Benson, Michael Varshaver, Ori Farber, Uri Weinberg, Eilon Kirson, and Yoram Palti. NovoTTF™-100A system (Tumor Treating Fields) transducer array layout planning for glioblastoma: A NovoTAL™ system user study. *World Journal of Surgical Oncology*, 13(316):1–7, 2015. doi: 10.1186/s12957-015-0722-3.

[40] Yung-Shin Sun. Direct-current electric field distribution in the brain for Tumor Treating Field applications: A simulation study. *Computational and Mathematical Methods in Medicine*, (3829768):1–13, 2018. doi: 10.1155/2018/3829768.

[41] Quim Castellví, Mireia M. Ginestà, Gabriel Capellà, and Antoni Ivorra. Tumor growth delay by adjuvant alternating electric fields which appears non-thermally mediated. *Bioelectrochemistry*, 105:16–24, 2015. doi: 10.1016/j.bioelechem.2015.04.006.

[42] Nichal Gentilal. *Heating of head tissues during TTFields therapy: a computational study (MSc thesis)*. Faculdade de Ciências da Universidade de Lisboa, 2018.

[43] Nichal Gentilal, Ricardo Salvador, and Pedro Cavaleiro Miranda. Temperature control in TTFields therapy of GBM: impact on the duty cycle and tissue temperature. *Physics in Medicine and Biology*, 64(22):225008, 2019. doi: 10.1088/1361-6560/ab5323.

[44] Alessandra Finisguerra, Renato Borgatti, and Cosimo Urgesi. Non-invasive brain stimulation for the rehabilitation of children and adolescents with neurodevelopmental disorders: A systematic review. *Frontiers in Psychology*, 10(135):1–24, 2019. doi: 10.3389/fpsyg.2019.00135.

[45] Antoni Valero-Cabré, Julià L. Amengual, Chloé Stengel, Alvaro Pascual-Leone, and Olivier A. Coubard. Transcranial magnetic stimulation in basic and clinical neuroscience: A comprehensive review of fundamental principles and novel

insights. *Neuroscience and Biobehavioral Reviews*, 83(9):381–404, 2017. doi: 10.1016/j.neubiorev.2017.10.006.

[46] Preet Minhas, Varun Bansal, Jinal Patel, Johnson S. Ho, Julian Diaz, Abhishek Datta, and Marom Bikson. Electrodes for high-definition transcutaneous DC stimulation for applications in drug delivery and electrotherapy, including tDCS. *Journal of Neuroscience Methods*, 190(2):188–197, 2010. doi: 10.1016/j.jneumeth.2010.05.007.

[47] Hayley Thair, Amy L. Holloway, Roger Newport, and Alastair D. Smith. Transcranial direct current stimulation (tDCS): A beginner's guide for design and implementation. *Frontiers in Neuroscience*, 11(641):1–13, 2017. doi: 10.3389/fnins.2017.00641.

[48] Marilia Menezes de Oliveira, Peng Wen, and Tony Ahfock. Heat transfer due to electroconvulsive therapy: Influence of anisotropic thermal and electrical skull conductivity. *Computer Methods and Programs in Biomedicine*, 133:71–81, 2016. doi: 10.1016/j.cmpb.2016.05.022.

[49] Antoni Valero-Cabré, Richard J. Rushmore, and Bertram Payne. Low frequency transcranial magnetic stimulation on the posterior parietal cortex induces visuotopically specific neglect-like syndrome. *Experimental Brain Research*, 172(1):14–21, 2006. doi: 10.1007/s00221-005-0307-4.

[50] Kaspar Schindler, Thomas Nyffeler, Roland Wiest, Martinus Hauf, Johannes Mathis, Ch W. Hess, and René Müri. Theta burst transcranial magnetic stimulation is associated with increased EEG synchronization in the stimulated relative to unstimulated cerebral hemisphere. *Neuroscience Letters*, 436(1):31–34, 2008. doi: 10.1016/j.neulet.2008.02.052.

[51] Simone Rossi, Mark Hallett, Paolo Maria Rossini, Alvaro Pascual-Leone, and The safety of TMS Consensus Group. Safety, ethical considerations, and application guidelines for the use of transcranial magnetic stimulation in clinical practice and research. *Clinical Neurophysiology*, 120(12):323–330, 2009. doi: 10.1016/j.clinph.2009.08.016.

[52] Simone Rossi, Andrea Antal, Sven Bestmann, Marom Bikson, Carmen Brewer, Jürgen Brockmöller, Linda L. Carpenter, Massimo Cincotta, Robert Chen, Jeff D. Daskalakis, Vincenzo Di Lazzaro, Michael D. Fox, Mark S. George, Donald Gilbert, Vasilios K. Kimiskidis, Giacomo Koch, Risto J. Ilmoniemi, Jean Pascal Lefaucheur, Letizia Leocani, Sarah H. Lisanby, Carlo Miniussi, Frank Padberg, Alvaro Pascual-Leone, Walter Paulus, Angel V. Peterchev, Angelo Quartarone, Alexander Rotenberg, John Rothwell, Paolo M. Rossini, Emiliano Santarnecchi, Mouhsin M. Shafi,

Hartwig R. Siebner, Yoshikatzu Ugawa, Eric M. Wassermann, Abraham Zangen, Ulf Ziemann, and Mark Hallett. Safety and recommendations for TMS use in healthy subjects and patient populations, with updates on training, ethical and regulatory issues: Expert guidelines. *Clinical Neurophysiology*, 132(1):269–306, 2021. doi: 10.1016/j.clinph.2020.10.003.

[53] Risto J. Ilmoniemi, Ruohonen Jarmo, and Karhu Jari. Transcranial Magnetic Stimulation - A new tool for functional imaging of the brain. *Critical Reviews in Biomedical Engineering*, 27(3-5):241–284, 1999.

[54] Abhishek Datta, Maged Elwassif, and Marom Bikson. Bio-heat transfer model of transcranial DC stimulation: Comparison of conventional pad versus ring electrode. *Proceedings of the 31st Annual International Conference of the IEEE Engineering in Medicine and Biology Society: Engineering the Future of Biomedicine, EMBC 2009*, 5:670–673, 2009. doi: 10.1109/IEMBS.2009.5333673.

[55] Jennifer Frankel, Jonna Wilén, and Kjell Hansson Mild. Assessing exposures to Magnetic Resonance Imaging's complex mixture of magnetic fields for in vivo, in vitro, and epidemiologic studies of health effects for staff and patients. *Frontiers in Public Health*, 6(66):1–10, 2018. doi: 10.3389/fpubh.2018.00066.

[56] Frank G. Shellock and John V. Crues. MR procedure: Biologic effects, safety, and patient care. *Radiology*, 232(3):635–652, 2004. doi: 10.1148/radiol.2323030830.

[57] Frank G. Shellock and Daniel J. Schaefer. Radiofrequency energy-induced heating during magnetic resonance procedures: Laboratory and clinical experiences. In Frank G. Shellock, editor, *Magnetic resonance procedures: Health effects and safety*, chapter 4, pages 75–95. CRC Press, 1st edition, 2001. ISBN 0849308747.

[58] Lawrence P. Panych and Bruno Madore. The physics of MRI safety. *Journal of Magnetic Resonance Imaging*, 47(1):28–43, 2018. doi: 10.1002/jmri.25761.

[59] Andreas Boss, Hansjörg Graf, Alexander Berger, Ulrike A. Lauer, Hanne Wojtczyk, Claus D. Claussen, and Fritz Schick. Tissue warming and regulatory responses induced by radio frequency energy deposition on a whole-body 3-Tesla magnetic resonance imager. *Journal of Magnetic Resonance Imaging*, 26(5):1334–1339, 2007. doi: 10.1002/jmri.21156.

[60] William P. Shuman, David R. Haynor, Arthur W. Guy, George E. Wesbey, Daniel J. Schaefer, and Albert A. Moss. Superficial- and deep-tissue temperature increases in anesthetized dogs during exposure to high specific absorption rates in a 1.5-T MR imager. *Radiology*, 167(2):551–554, 1988. doi: 10.1148/radiology.167.2.3357971.

[61] Brian J. Barber, Daniel J. Schaefer, Christopher J. Gordon, David C. Zawieja, and Jamie Hecker. Thermal effects of MR imaging: Worst-case studies on sheep. *American Journal of Roentgenology*, 155(5):1105–1110, 1990. doi: 10.2214/ajr.155.5.2120944.

[62] Christopher M. Collins, Wanzhan Liu, Jinghua Wang, Rolf Gruetter, J. Thomas Vaughan, Kamil Ugurbil, and Michael B. Smith. Temperature and SAR calculations for a human head within volume and surface coils at 64 and 300 MHz. *Journal of Magnetic Resonance Imaging*, 19(5):650–656, 2004. doi: 10.1002/jmri.20041.

[63] FDA. Medical Devices: BSD-2000 Hyperthermia System – H090002 (accessed: 25/12/2021), 2011. URL `https://www.accessdata.fda.gov/scripts/cdrh/cfdocs/cfhde/hde.cfm?id=375550`.

[64] Niloy R. Datta, Silvia G. Ordóñez, Udo Gaipl, Margarethus M. Paulides, Hans Crezee, Johanna Gellermann, Dietmar Marder, Emsad Puric, and Stephan Bodis. Local hyperthermia combined with radiotherapy and-/or chemotherapy: Recent advances and promises for the future. *Cancer Treatment Reviews*, 41(9):742–753, 2015. doi: 10.1016/j.ctrv.2015.05.009.

[65] Martin H. Falk and Rolf D. Issels. Hyperthermia in oncology. *International Journal of Hyperthermia*, 17(1):1–18, 2001. doi: 10.1080/02656730118511.

[66] Adam Chicheł, Janusz Skowronek, Magda Kubaszewska, and Marek Kanikowski. Hyperthermia - description of a method and a review of clinical applications. *Reports of Practical Oncology and Radiotherapy*, 12(5):267–275, 2007. doi: 10.1016/S1507-1367(10)60065-X.

[67] Petra P. Kok, Cressman Erik, Ceelen Wim, Brace Christopher L., Ivkov Robert, Grüll Holger, Ter Haar Gail, Wust Peter, and Crezee Johannes. Heating technology for malignant tumors: A review. *International Journal of Hyperthermia*, 37(1):711–741, 2020. doi: 10.1080/02656736.2020.1779357.

[68] Stephen A. Sapareto and William C. Dewey. Thermal dose determination in cancer therapy. *International Journal of Radiation Oncology, Biology, Physics*, 10(6):787–800, 1984. doi: 10.1016/0360-3016(84)90379-1.

[69] Mark W. Dewhirst, Benjamin L. Viglianti, Michaël Lora-Michiels, Michael Hanson, and Jack P. Hoopes. Basic principles of thermal dosimetry and thermal thresholds for tissue damage from hyperthermia. *International Journal of Hyperthermia*, 19(3):267–294, 2003. doi: 10.1080/0265673031000119006.

[70] Pavel S. Yarmolenko, Eui Jung Moon, Chelsea Landon, Ashley Manzoor, Daryl W. Hochman, Benjamin L. Viglianti, and Mark W. Dewhirst. Thresholds for thermal damage to normal tissues: An update. *International Journal of Hyperthermia*, 27 (4):320–343, 2011. doi: 10.3109/02656736.2010.534527.

[71] Sebastián A. Leon, Sucha Asbell, Hyder Husain Arastu, Gerald Edelstein, A. J. Packel, S. Sheehan, Ierachmiel Daskal, Gad G. Guttmann, and I. Santos. Effects of hyperthermia on bone. II. Heating of bone in vivo and stimulation of bone growth. *International Journal of Hyperthermia*, 9(1):77–87, 1993. doi: 10.3109/02656739309061480.

[72] Maria Frosini. Changes in CSF composition during heat stress and fever in conscious rabbits. *Progress in Brain Research*, 162(6):449–457, 2007. doi: 10.1016/S0079-6123(06)62022-0.

[73] Gerard C. Van Rhoon. Is CEM43^{o}C still a relevant thermal dose parameter for hyperthermia treatment monitoring? *International Journal of Hyperthermia*, 32 (1):50–62, 2016. doi: 10.3109/02656736.2015.1114153.

[74] Nobuhiko Katunuma. Mechanism and regulation of bone resorption by osteoclasts. *Current Topics in Cellular Regulation*, 35:179–192, 1997. doi: 10.1016/S0070-2137(97)80008-8.

[75] Huan Wang, Bonnie Wang, Kieran P. Normoyle, Kevin Jackson, Kevin Spitler, Matthew Sharrock, Claire M. Miller, Catherine Best, Daniel Llano, and Rose Du. Brain temperature and its fundamental properties: A review for clinical neuroscientists. *Frontiers in Neuroscience*, 8(307):1–17, 2014. doi: 10.3389/fnins.2014.00307.

[76] Brian S. Meldrum. Glutamate and glutamine in the brain glutamate as a neurotransmitter in the brain: Review of physiology and pathology. *Journal of Nutrition*, 130(Suppl 4S):1007S–1015S, 2000. doi: 10.1093/jn/130.4.1007S.

[77] Michael Roslin, Roger Henriksson, Per Bergström, Urban Ungerstedt, and A. Tommy Bergenheim. Baseline levels of glucose metabolites, glutamate and glycerol in malignant glioma assessed by stereotactic microdialysis. *Journal of Neuro-Oncology*, 61(2):151–160, 2003. doi: 10.1023/A:1022106910017.

[78] Nobuhiko Matsumi, Kengo Matsumoto, Nobuya Mishima, Eiji Moriyama, Tomohisa Furuta, Akira Nishimoto, and Kohji Taguchi. Thermal damage threshold of brain tissue - Histological study of heated normal monkey brains. *Neurologia Medico-Chirurgica*, 34(4):209–215, 1994. doi: 10.2176/nmc.34.209.

[79] Surendar S. Nathan, Saurabh R. Sinha, Barry Gordon, Ronald P. Lesser, and Nitish V. Thakor. Determination of current density distributions generated by electrical stimulation of the human cerebral cortex. *Electroencephalography and Clinical Neurophysiology*, 86(3):183–192, 1993. doi: 10.1016/0013-4694(93)90006-H.

[80] Nichal Gentilal and Pedro Cavaleiro Miranda. Heat transfer during TTFields treatment: Influence of the uncertainty of the electric and thermal parameters on the predicted temperature distribution. *Computer Methods and Programs in Biomedicine*, 196:105706, 2020. doi: 10.1016/j.cmpb.2020.105706.

[81] Pedro Cavaleiro Miranda, Abeye Mekonnen, Ricardo Salvador, and Peter J. Basser. Predicting the electric field distribution in the brain for the treatment of glioblastoma. *Physics in Medicine and Biology*, 59(15):4137–4147, 2014. doi: 10.1088/0031-9155/59/15/4137.

[82] Cornelia Wenger, Ricardo Salvador, Peter J. Basser, and Pedro Cavaleiro Miranda. Improving Tumor Treating Fields treatment efficacy in patients with glioblastoma using personalized array layouts. *International Journal of Radiation Oncology Biology Physics*, 94(5):1137–1143, 2016. doi: 10.1016/j.ijrobp.2015.11.042.

[83] TME Electronic Components. Temperature sensors (accessed: 15/06/2018). URL `https://www.tme.eu/gb/`.

[84] IFM. Temperature sensors (accessed: 15/06/2018). URL `https://www.ifm.com/gb/en`.

[85] Fatemeh Adibzadeh, Margarethus M. Paulides, and Gerard C. van Rhoon. SAR thresholds for electromagnetic exposure using functional thermal dose limits. *International Journal of Hyperthermia*, 34(8):1248–1254, 2018. doi: 10.1080/02656736.2018.1424945. URL `https://doi.org/10.1080/02656736.2018.1424945`.

[86] Alan R. Moritz and F. C. Henriques. Studies of thermal injury: II. The relative importance of time and surface temperature in the causation of cutaneous burns. *The American journal of pathology*, 23(5):695–720, 1947. ISSN 00029440.

[87] William L. Lanier. Cerebral metabolic rate and hypothermia: Their relationship with ischemic neurologic injury, 1995.

[88] Hubert L Rosomoff and Duncan A. Holaday. Cerebral blood flow and cerebral oxygen consumption during hypothermia. *American Journal of Physiology*, 179(1): 85–88, 1954. doi: 10.1152/ajplegacy.1954.179.1.85.

[89] Maxim Volgushev, Trichur R. Vidyasagar, Marina Chistiakova, and Ulf T. Eysel. Synaptic transmission in the neocortex during reversible cooling. *Neuroscience*, 98 (1):9–22, 2000. doi: 10.1016/S0306-4522(00)00109-3.

[90] Maxim Volgushev, Igor Kudryashov, Marina Chistiakova, Mikhail Mukovski, Johannes Niesmann, and Ulf T. Eysel. Probability of transmitter release at neocortical synapses at different temperatures. *Journal of Neurophysiology*, 92(1):212–220, 2004. doi: 10.1152/jn.01166.2003.

[91] Peter J. Joris, Ronald P. Mensink, Tanja C. Adam, and Thomas T. Liu. Cerebral blood flow measurements in adults: A review on the effects of dietary factors and exercise. *Nutrients*, 10(530):1–15, 2018. doi: 10.3390/nu10050530.

[92] Pedro Cavaleiro Miranda, Abeye Mekonnen, Ricardo Salvador, and Giulio Ruffini. The electric field in the cortex during transcranial current stimulation. *NeuroImage*, 70:48–58, 2013. doi: 10.1016/j.neuroimage.2012.12.034.

[93] Cornelia Wenger, Ricardo Salvador, Peter J. Basser, and Pedro Cavaleiro Miranda. The electric field distribution in the brain during TTFields therapy and its dependence on tissue dielectric properties and anatomy: A computational study. *Physics in Medicine and Biology*, 60(18):7339–7357, 2015. doi: 10.1088/0031-9155/60/18/7339.

[94] Anders Rosendal Korshoej, Frederik Lundgaard Hansen, Nikola Mikic, Gorm von Oettingen, Jens Christian Hedemann Sørensen, and Axel Thielscher. Importance of electrode position for the distribution of tumor treating fields (TTFields) in a human brain. Identification of effective layouts through systematic analysis of array positions for multiple tumor locations. *PLoS ONE*, 13(8):1–16, 2018. doi: 10.1371/journal.pone.0201957.

[95] Jaakko Malmivuo and Robert Plonsey. *Bioelectromagnetism: Principles and applications of bioelectric and biomagnetic fields*. Oxford University Press, 1st edition, 1995. ISBN 9780195058239. doi: 10.1093/acprof:oso/9780195058239.001.0001.

[96] Harry H. Pennes. Analysis of tissue and arterial blood temperatures in the resting human forearm. *Journal of Applied Physiology*, 1(2):93–122, 1948.

[97] Marilia Menezes de Oliveira, Paul Wen, and Tony Ahfock. Bio-heat transfer model of electroconvulsive therapy: Effect of biological properties on induced temperature variation. *38th Annual International Conference of the IEEE Engineering in Medicine and Biology Society (EMBC)*, pages 3997–4000, 2016. doi: 10.1109/EMBC.2016.7591603.

[98] Matthew T. Ballo, Noa Urman, Gitit Lavy-Shahaf, Jai Grewal, Ze'ev Bomzon, and Steven Toms. Correlation of Tumor Treating Fields Dosimetry to survival outcomes in newly diagnosed glioblastoma: A large-scale numerical simulation-based analysis of data from the phase 3 EF-14 randomized trial. *International Journal of Radiation Oncology Biology Physics*, 104(5):1106–1113, 2019. doi: 10.1016/j.ijrobp.2019.04.008.

[99] Philippe Hasgall, Francesco Di Gennaro, Christian Baumgartner, Esra Neufeld, Bryan Lloyd, Marie-Christine Gosselin, and Niels Kuster. IT'IS Database for thermal and electromagnetic parameters of biological tissues (accessed: 17/02/2020). URL `https://itis.swiss/virtual-population/tissue-properties/database/`.

[100] Francis A. Duck. *Physical properties of tissue: A comprehensive reference book*. Academic Press, London, 1st edition, 1990. ISBN 0122228006. doi: 10.1016/0141-5425(91)90034-5.

[101] Alan R. Moritz and F. C. Henriques. Studies of thermal injury. I: The conduction of heat to and through skin and the temperatures attained therein. A theoretical and an experimental investigation. *The American Journal of Pathology*, 23(4):530–549, 1947.

[102] Suleyman Biyikli, Michael F. Modest, and Richard Tarr. Measurements of thermal properties for human femora. *Journal of Biomedical Materials Research*, 20(9):1335–1345, 1986. doi: 10.1002/jbm.820200908.

[103] Gerard M. J. Van Leeuwen, Jeff W. Hand, Jan J. W. Lagendijk, Denis V. Azzopardi, and A. David Edwards. Numerical modeling of temperature distributions within the neonatal head. *Pediatric Research*, 48(3):351–356, 2000. doi: 10.1203/00006450-200009000-00015.

[104] Robert L. McIntosh and Vitas Anderson. A comprehensive tissue properties database provided for the thermal assessment of a human at rest. *Biophysical Reviews and Letters*, 5(3):129–151, 2010. doi: 10.1142/S1793048010001184.

[105] Avtar S. Ahuja, Kedar N. Prasad, William R. Hendee, and Paul L. Carson. Thermal conductivity and diffusivity of neuroblastoma tumor. *Medical Physics*, 5(5):418–421, 1978. doi: 10.1118/1.594434.

[106] Kjetil G. Brurberg, Ilana C. Benjaminsen, Liv M.R. Dørum, and Einar K. Rofstad. Fluctuations in tumor blood perfusion assessed by dynamic contrast-enhanced MRI. *Magnetic Resonance in Medicine*, 58(3):473–481, 2007. doi: 10.1002/mrm.21367.

[107] Peter Vaupel, Friedrich Kallinowski, and Paul Okunieff. Blood flow, oxygen and nutrient supply, and metabolic microenvironment of human tumors: A review. *Cancer Research*, 49(23):6449–6465, 1989.

[108] Obdulia Ley and Yildiz Bayazitoglu. Effect of physiology on the temperature distribution of a layered head with external convection. *International Journal of Heat and Mass Transfer*, 46(17):3233–3241, 2003. doi: 10.1016/S0017-9310(03)00100-5.

[109] Jeffery Steketee. Spectral emissivity of skin and pericardium. *Physics in Medicine and Biology*, 18(5):686–694, 1973. doi: 10.1088/0031-9155/18/5/307.

[110] Eugene. A. Kiyatkin and Hari S. Sharma. Permeability of the blood-brain barrier depends on brain temperature. *Neuroscience*, 161(3):926–939, 2009. doi: 10.1016/j.neuroscience.2009.04.004.

[111] Anders Rosendal Korshoej, Guilherme Bicalho Saturnino, Line Kirkegaard Rasmussen, Gorm Von Oettingen, Jens Christian Hedemann Sørensen, and Axel Thielscher. Enhancing predicted efficacy of tumor treating fields therapy of glioblastoma using targeted surgical craniectomy: A computer modeling study. *PLoS ONE*, 11(10):1–25, 2016. doi: 10.1371/journal.pone.0164051.

[112] Sitaramanjaneya R. Guntur, Kang Il Lee, Dong Guk Paeng, Andrew John Coleman, and Min Joo Choi. Temperature-dependent thermal properties of ex-vivo liver undergoing thermal ablation. *Ultrasound in Medicine and Biology*, 39(10):1771–1784, 2013. doi: 10.1016/j.ultrasmedbio.2013.04.014.

[113] Chang W. Song, Lisa M. Chelstrom, and Daniel J. Aumschild. Changes in human skin blood flow by hyperthermia. *International Journal of Radiation Oncology, Biology, Physics*, 18(4):903–907, 1990. doi: 10.1016/0360-3016(90)90415-G.

[114] Christian Rossmanna and Dieter Haemmerich. Review of temperature dependence of thermal properties, dielectric properties, and perfusion of biological tissues at hyperthermic and ablation temperatures. *Critical Reviews in Biomedical Engineering*, 42(6):467–492, 2014. doi: 10.1615/CritRevBiomedEng.2015012486.

[115] Cornelia Wenger, Hadas Sara Hershkovich, Catherine Tempel-Brami, Moshe Giladi, and Ze'ev Bomzon. Water-content electrical property tomography (wEPT) for mapping brain tissue conductivity in the 200-1000 kHz range: Results of an animal study. In Sergey Makarov, Marc Horner, and Gregory Noetscher, editors, *Brain and Human Body Modeling 2019: computational human models presented at EMBC 2018*, chapter 20, pages 367–393. Springer, Cham, 1st edition, 2019. ISBN 9783030212933. doi: 10.1007/978-3-030-21293-3_20.

[116] Won Hee Lee, Zhi De Deng, Andrew F. Laine, Sarah H. Lisanby, and Angel V. Peterchev. Influence of white matter conductivity anisotropy on electric field strength induced by electroconvulsive therapy. *Proceedings of the Annual International Conference of the IEEE Engineering in Medicine and Biology Society, EMBS*, pages 5473–5476, 2011. doi: 10.1109/IEMBS.2011.6091396.

[117] Salman Shahid, Peng Wen, and Tony Ahfock. Numerical investigation of white matter anisotropic conductivity in defining current distribution under tDCS. *Computer Methods and Programs in Biomedicine*, 109(1):48–64, 2013. doi: 10.1016/j.cmpb.2012.09.001.

[118] Chin Leong Lim, Chris Byrne, and Jason K. W. Lee. Human thermoregulation and measurement of body temperature in exercise and clinical settings. *Annals of the Academy of Medicine Singapore*, 37(4):347–353, 2008.

[119] Arthur C. Guyton and John E. Hall. *Textbook of medical physiology*. Saunders Elsevier, Philadelphia, 12 edition, 2006. ISBN 9781416045748.

[120] Yair Shapiro, Kent B. Pandolf, and Ralph F. Goldman. Predicting sweat loss response to exercise environment and clothing. *European Journal of Applied Physiology*, 48(1):83–96, 1982. doi: 10.1007/BF00421168.

[121] Baruch Givoni and Ralph F. Goldman. Predicting rectal temperature response to work, environment, and clothing. *Journal of Applied Physiology*, 32(6):812–822, 1972. ISSN 00218987. doi: 10.1152/jappl.1972.32.6.812.

[122] Refrigerating American Society of Heating and Air conditioning Engineers. Thermal comfort. In *2013 ASHRAE Handbook—Fundamentals*, chapter 9. Atlanta, GA, si edition, 2013. ISBN 1936504472.

[123] Ricard R. Gonzalez, Samuel N. Cheuvront, Scott J. Montain, Daniel A. Goodman, Laurie A. Blanchard, Larry G. Berglund, and Michael N. Sawka. Expanded prediction equations of human sweat loss and water needs. *Journal of Applied Physiology*, 107(2):379–388, 2009. doi: 10.1152/japplphysiol.00089.2009.

[124] 3M Science Applied to Life. 3M Medical tapes and films (accessed: 17/11/2019). URL `https://www.3m.com/3M/en{_}US/company-us/search/?Ntt=medical+tapes`.

[125] Vitality Medical. Medical adhesive tape (accessed: 17/11/2019). URL `https://www.vitalitymedical.com/tape.html`.

[126] Emanuele Russo, Hans Kuerten, Cornelis W. M. van der Geld, and Bernard J. Geurts. Water droplet condensation and evaporation in turbulent channel flow. *Journal of Fluid Mechanics*, 749(4):666–700, 2014. doi: 10.1017/jfm.2014.239.

[127] Mark Harker. Psychological sweating: A systematic review focused on aetiology and cutaneous response. *Skin Pharmacology and Physiology*, 26(2):92–100, 2013. doi: 10.1159/000346930.

[128] Şükrü Özen, Selçuk Helhel, and Osman Çerezci. Heat analysis of biological tissue exposed to microwave by using thermal wave model of bio-heat transfer (TWMBT). *Burns*, 34(1):45–49, 2008. doi: 10.1016/j.burns.2007.01.009.

[129] Ahad Mohammadi, Leonardo Bianchi, Somayeh Asadi, and Paola Saccomandi. Measurement of ex-vivo liver, brain and pancreas thermal properties as function of temperature. *Sensors*, 21(12):2–15, 2021. doi: 10.3390/s21124236.

[130] Marin Marin, Aatef Hobiny, and Ibrahim Abbas. Finite element analysis of nonlinear bioheat model in skin tissue due to external thermal sources. *Mathematics*, 9(1459): 1–9, 2021. doi: 10.3390/math9131459.

[131] Yoram Wasserman, Michael Krinitsky, Mikhail Shtotland, and Victor Kaikov. US 2018/0050200 A1: Temperature measurement in arrays for delivering TTFields, 2018.

[132] Hadas Sara Hershkovich, Noa Urman, Ofir Yesharim, Ariel Naveh, and Ze'ev Bomzon. The dielectric properties of skin and their influence on the delivery of tumor treating fields to the torso: A study combining in vivo measurements with numerical simulations. *Physics in Medicine and Biology*, 64(18):185014, 2019. doi: 10.1088/1361-6560/ab33c6.

[133] Yulin Ge, Robert I. Grossman, James S. Babb, Marcie L. Rabin, Lois J. Mannon, and Dennis L. Kolson. Age-related total gray matter and white matter changes in normal adult brain. Part I: Volumetric MR imaging analysis. *American Journal of Neuroradiology*, 23(8):1327–1333, 2002.

[134] Cornelia Wenger, Pedro Cavaleiro Miranda, Ze'ev Bomzon, Noa Urman, Eilon Kirson, Yoram Wasserman, and Yoram Palti. US 2017/0120041 A1: TTFields treatment with optimization of electrode positions on the head based on MRI-based conductivity measurements, 2017.

[135] Martin Proescholdt, Amer Haj, Christian Doenitz, Alexander Brawanski, Ze'ev Bomzon, and Hadas Sara Hershkovich. CMBT-14. The dielectric properties of brain

tumor tissue. In *Neuro-oncology*, pages vi35–vi36, 2019. doi: 10.1093/neuonc/noz175.136.

[136] Stefan T. Lang, Liu Shi Gan, Cael McLennan, Oury Monchi, and John J. P. Kelly. Impact of peritumoral edema during Tumor Treatment Field therapy: A computational modelling study. *IEEE Transactions on Biomedical Engineering*, 67(12): 3327–3338, 2020. doi: 10.1109/TBME.2020.2983653.

[137] Ze'ev Bomzon, Cornelia Wenger, Martin Proescholdt, and Suyash Mohan. Tumor Treating Fields at EMBC 2019: A roadmap to developing a framework for TTFields dosimetry and treatment planning. In Sergey Makarov, Gregory Noetscher, and Aapo Nummenmaa, editors, *Brain and Human Body Modeling 2020: computational human models presented at EMBC 2019*, chapter 1, pages 3–17. Springer, Cham, 1st edition, 2021. ISBN 9783030456221. doi: 10.1007/978-3-030-45623-8_1.

[138] Noa Urman, Shay Levy, Avital Frenkel, Doron Manzur, Hadas Sara Hershkovich, Ariel Naveh, Ofir Yesharim, Cornelia Wenger, Gitit Lavy-shahaf, Eilon Kirson, and Ze'ev Bomzon. Investigating the connection between Tumor Treating Fields distribution in the brain and glioblastoma patient outcomes. A simulation-based study utilizing a novel model creation technique. In Sergey Makarov, Marc Horner, and Gregory Noetscher, editors, *Brain and Human Body Modeling 2019: computational human models presented at EMBC 2018*, chapter 7, pages 139–154. Springer, Cham, 1st edition, 2019. ISBN 9783030212933. doi: 10.1007/978-3-030-21293-3.

[139] Gabriele Eichfelder and Matthias Gebhardt. Local specific absorption rate control for parallel transmission by virtual observation points. *Magnetic Resonance in Medicine*, 66(5):1468–1476, 2011. doi: 10.1002/mrm.22927.

[140] Richard S. Waremra and Philipus Betaubun. Analysis of electrical properties using the four point probe method. *E3S Web of Conferences*, 73(13019):1–4, 2018. doi: 10.1051/e3sconf/20187313019.

[141] Myron L. Cohen. Measurement of the thermal properties of human skin. A review. *The Journal of Investigative Dermatology*, 69(3):333–338, 1977. doi: 10.1111/1523-1747.ep12507965.

[142] Nuno P. Silva, Anna Bottiglieri, Raquel C. Conceição, Martin O'halloran, and Laura Farina. Characterisation of ex-vivo liver thermal properties for electromagnetic-based hyperthermic therapies. *Sensors*, 20(10):1–14, 2020. doi: 10.3390/s20103004.

[143] Patricia L. Ricketts, Ashvinikumar V. Mudaliar, Brent E. Ellis, Clay A. Pullins, Leah A. Meyers, Otto I. Lanz, Elaine P. Scott, and Thomas E. Diller. Non-invasive

blood perfusion measurements using a combined temperature and heat flux surface probe. *International Journal of Heat and Mass Transfer*, 51(23-24):5740–5748, 2008. doi: 10.1016/j.ijheatmasstransfer.2008.04.051.

[144] Giovanni L. Ceresoli, Joachim G. Aerts, Rafal Dziadziuszko, Rodryg Ramlau, Susana Cedres, Jan P. van Meerbeeck, Manlio Mencoboni, David Planchard, Antonio Chella, Lucio Crinò, Maciej Krzakowski, Jörn Rüssel, Antonio Maconi, Letizia Gianoncelli, and Federica Grosso. Tumour Treating Fields in combination with pemetrexed and cisplatin or carboplatin as first-line treatment for unresectable malignant pleural mesothelioma (STELLAR): a multicentre, single-arm phase 2 trial. *The Lancet Oncology*, 20(12):1702–1709, 2019. doi: 10.1016/S1470-2045(19)30532-7.

[145] Miklos Pless, Cornelia Droege, Roger von Moos, Marc Salzberg, and Daniel Betticher. A phase I/II trial of Tumor Treating Fields (TTFields) therapy in combination with pemetrexed for advanced non-small cell lung cancer. *Lung Cancer*, 81(3): 445–450, 2013. doi: 10.1016/j.lungcan.2013.06.025.

[146] Ignace Vergote, Roger von Moos, Luis Manso, Els Van Nieuwenhuysen, Nicole Concin, and Cristiana Sessa. Tumor Treating Fields in combination with paclitaxel in recurrent ovarian carcinoma: Results of the INNOVATE pilot study. *Gynecologic Oncology*, 150(3):471–477, 2018. doi: 10.1016/j.ygyno.2018.07.018.

[147] Fernando Rivera, Manuel Benavides, Javier Gallego, Carmen Guillen-Ponce, José Lopez-Martin, and Marc Küng. Tumor treating fields in combination with gemcitabine or gemcitabine plus nab-paclitaxel in pancreatic cancer: Results of the PANOVA phase 2 study. *Pancreatology*, 19(1):64–72, 2019. doi: 10.1016/j.pan.2018.10.004.

[148] Anca Grosu, Eleni Gkika, Thomas Brunner, J. Strouthos, and Uri Weinberg. Phase 2 HEPANOVA trial of tumor treating fields concomitant with sorafenib for advanced hepatocellular carcinoma. In *Annals of Oncology*, volume 30, pages iv61–iv62. Elsevier Masson SAS, 2019. doi: 10.1093/annonc/mdz155.223.

[149] Martin Connock, Peter Auguste, Claude Dussart, Jacques Guyotat, and Xavier Armoiry. Cost-effectiveness of tumor-treating fields added to maintenance temozolomide in patients with glioblastoma: An updated evaluation using a partitioned survival model. *Journal of Neuro-Oncology*, 143(3):605–611, 2019. doi: 10.1007/s11060-019-03197-w.

[150] Gregory F. Guzauskas, Erqi L. Pollom, Volker W. Stieber, Bruce C.M. Wang, and Louis P. Garrison. Tumor treating fields and maintenance temozolomide for newly-diagnosed glioblastoma: A cost-effectiveness study. *Journal of Medical Economics*, 22(10):1006–1013, 2019. doi: 10.1080/13696998.2019.1614933.

[151] Novocure. Optune system (accessed: 16-01-2022). URL `https://www.optune.com/`.

[152] Anders Rosendal Korshoej, Slavka Lukacova, Yasmin Lassen-Ramshad, Christian Rahbek, Kåre Eg Severinsen, Trine Lignell Guldberg, Nikola Mikic, Mette Haldrup Jensen, Søren Ole Stigaard Cortnum, Gorm von Oettingen, and Jens Christian Hedemann Sørensen. OptimalTTF-1: Enhancing tumor treating fields therapy with skull remodeling surgery. A clinical phase I trial in adult recurrent glioblastoma. *Neuro-Oncology Advances*, 2(1):1–11, 2020. doi: 10.1093/noajnl/vdaa121.

[153] Nika Guberina, Christoph Pöttgen, Sied Kebir, Lazaros Lazaridis, C. Scharmberg, Wolfgang Lübcke, Michael Niessen, Maja Guberina, Björn Scheffler, Verena Jendrossek, Ramazan Jabbarli, Daniela Pierscianek, Ulrich Sure, Teresa Schmidt, Christoph Oster, Peter Hau, Anca L. Grosu, Martin Stuschke, Martin Glas, Youness Nour, and Lutz Lüdemann. Combined radiotherapy and concurrent Tumor Treating Fields (TTFields) for glioblastoma: Dosimetric consequences on non-coplanar IMRT as initial results from a phase I trial. *Radiation Oncology*, 15(83):1–11, 2020. doi: 10.1186/s13014-020-01521-7.

[154] Herman A Haus and James R Melcher. *Electromagnetic fields and energy*. Prentice Hall, 1st edition, 1989. ISBN 9780415475976.

[155] Olgierd Zienkiewicz and Robert L. Taylor. *The Finite Element Method Volume 1: the basis*. Butterworth-Heinemann, Oxford, 5th edition, 2000. ISBN 0 7506 5049 4.

[156] Ricardo Salvador. *Numerical modelling in Transcranial Magnetic Stimulation (PhD thesis)*. Faculdade de Ciências da Universidade de Lisboa, 2009.

[157] Allan F. Bower. *Applied mechanics of solids*. CRC Press, Boca Raton, 1st edition, 2009. ISBN 9789896540821. doi: 10.1201/9781439802489.

[158] COMSOL. COMSOL Multiphysics reference manual v.5.5. pages 1307–1311, 2018.

Appendices

Appendix A

Derivation of Laplace's equation

In this appendix, a brief description of how to deduce Laplace's equation, equation (3.1), that is used to predict the electric field distribution within the head, is provided. A much more detailed discussion of how this equation can be deduced and the conditions in which it is valid can be found in Haus and Melcher [154].

The most general way to represent how electromagnetic radiation and matter interact is through Maxwell's equations. These are mathematically described in their differential form as:

$$\nabla \times \mathbf{H} = \mathbf{J} + \frac{\partial \mathbf{D}}{\partial t} \tag{A.1}$$

$$\nabla \times \mathbf{E} = -\frac{\partial \mathbf{B}}{\partial t} \tag{A.2}$$

$$\nabla \cdot \mathbf{D} = \rho_v \tag{A.3}$$

$$\nabla \cdot \mathbf{B} = 0 \tag{A.4}$$

where $\boldsymbol{H}$ is the magnetic field (A/m), $\boldsymbol{J}$ the current density (A/m^2), $\boldsymbol{D}$ the electric displacement (C/m^2), $\boldsymbol{E}$ the electric field intensity (V/m), $\boldsymbol{B}$ the magnetic field density (T), ρ_v the electric charge density (C/m^3), and t is the time (s). All physical parameters in bold are vectorial quantities.

The first equation, equation (A.1), is commonly known as the Maxwell-Ampère's law and it states that a magnetic field can be generated by an electric current and/or by a time-varying electric field. The second equation, equation (A.2), is Maxwell-Faraday's law of induction, which describes how a time-varying magnetic field induces an electric field. These two equations describe how the electromagnetic waves are generated and propagated through a medium by the interplay between the magnetic and electric fields. The third and fourth equations are known as Gauss' laws for electric and magnetic fields, respectively, and they state how the electric field is related with the electric charge density, equation (A.3), and that there can not be magnetic monopoles, equation (A.4).

The relation between the different physical quantities is further described by the constitutive relations:

$$\mathbf{D} = \epsilon \mathbf{E} \tag{A.5}$$
$$\mathbf{B} = \mu \mathbf{H} \tag{A.6}$$
$$\mathbf{J} = \sigma \mathbf{E} \tag{A.7}$$

where ϵ (F/m) is the absolute permittivity, μ (H/m) is the absolute permeability of the medium and σ is the electric conductivity (S/m). The first two are mathematically given by:

$$\epsilon = \epsilon_0 \epsilon_r \tag{A.8}$$
$$\mu = \mu_0 \mu_r \tag{A.9}$$

where ϵ_0 ($\approx 8.854 \times 10^{-12}$ F/m) is the permittivity of the vaccum, ϵ_r (unitless) the relative permittivity of the medium, μ_0 the permeability of the vaccum ($4\pi \times 10^{-7}$ H/m) and μ_r (unitless) the relative permeability of the medium. In equations (A.5) to (A.9) it was assumed that the medium is isotropic and thus that ϵ_r, ϵ, μ_r, μ, and σ could be represented by scalar values. For anisotropic materials, these quantities are replaced by tensors, i.e., 3x3 matrices, and the respective multiplications with the other physical quantities should be replaced by the dot product.

In some cases, based on the nature of the problem being studied, it is possible to simplify equations (A.1) to (A.4) by neglecting some terms, especially the ones that involve time derivatives, that would not contribute significantly to the final solution. The quasistatic approximations of Maxwell's equations were defined accounting for this, which proved to be very useful in solving complex problems. These simplified equations can be obtained by either neglecting the magnetic induction (the electroquasistatic approximation) or the electric displacement current (the magnetoquasistatic approximation), depending on the conditions of the problem. For the purpose of the study of the electric field distribution within the human head at a frequency between 100 and 500 kHz, the first approximation can be considered given that the electromagnetic wavelength, ≈15 m, is significantly larger than the size of the head, ≈ 20 cm. This condition is necessary and sufficient for the time delay between the changes in the sources of the fields and the changes in the induced fields to be ignored and thus to allow to use the electroquasistic approximation, as explained in detail in Haus and Melcher [154]. Under these conditions, Maxwell's equations can be simplified and rewritten as:

$$\nabla \times \mathbf{H} = \mathbf{J} + \epsilon \frac{\partial \mathbf{E}}{\partial t} \tag{A.10}$$
$$\nabla \times \mathbf{E} = -\mu \frac{\partial \mathbf{H}}{\partial t} \approx 0 \tag{A.11}$$
$$\nabla \cdot \mathbf{E} = \frac{\rho_v}{\epsilon} \tag{A.12}$$
$$\nabla \cdot \mathbf{H} = 0 \tag{A.13}$$

These are some of the equations that are already implemented in the software used throughout this thesis, COMSOL Multihysics. The electric currents (ec) interface of the

AC/DC module is used to compute the potential distribution and thus to predict the electric field and current distributions within the geometry used. A fully defined system is obtained by including the equation of continuity:

$$\nabla \cdot \mathbf{J} + \frac{\partial \rho_v}{\partial t} = 0 \tag{A.14}$$

This equation states that the variation of the electric charge contained within a volume can only change by the amount of electric current flowing through the boundaries of that same volume.

Under the EQS approximation, the second term on the left-hand side of equation (A.14) is set to zero and thus using the constitutive relation expressed by equation (A.7) it follows that:

$$\nabla \cdot \sigma \boldsymbol{E} = 0 \tag{A.15}$$

From equation (A.11) the electric field is irrotational and therefore it can be represented as a function of the electric potential in the following form:

$$\nabla \times \boldsymbol{E} = 0 \Leftrightarrow \boldsymbol{E} = -\nabla \phi \tag{A.16}$$

where ϕ is the electrostatic potential (V).

Combining the previous equation with equation (A.15) the following is deduced:

$$\nabla \cdot (\sigma \nabla \boldsymbol{\phi}) = 0 \tag{A.17}$$

This is a particular case of Poisson's equation and it is known as Laplace's equation for electrostatics. This equation allows to predict the electric field distribution for TTFields studies using the EQS approximation of Maxwell's equations.

Appendix B

The Finite Element Method (FEM)

In this appendix, a very brief description of the finite element method (FEM) is presented based on a much more extensive discussion of it that can be found in [155, 156]. The same nomenclature and methodology as the one presented in Zienkiewicz and Taylor [155] is followed. All the variables in bold refer to vectorial or matricial quantities.

The FEM is a powerful numerical tool used to solve physical problems that can be described by differential equations, which is the case of the equations that describe the electric potential and the temperature variation, presented in chapter 3. In this method, it is assumed that the equations in a given domain Ω (a volume, an area, etc) can be described by a set of differential equations of the form:

$$\boldsymbol{A}(\boldsymbol{u}) = \begin{Bmatrix} A_1(\boldsymbol{u}) \\ A_2(\boldsymbol{u}) \\ \vdots \end{Bmatrix} = \boldsymbol{0} \tag{B.1}$$

where $\boldsymbol{A}$ contains the differential equations that describe the problem of interest and $\boldsymbol{u}$ is a scalar (e.g.: the scalar electric potential, the temperature) or a vector function (e.g.: the electric field vector) that satisfies the equations and whose values are the solution of the problem.

At the boundaries, Γ, of each domain, an additional set of equations has to be imposed so the problem is completely defined:

$$\boldsymbol{B}(\boldsymbol{u}) = \begin{Bmatrix} B_1(\boldsymbol{u}) \\ B_2(\boldsymbol{u}) \\ \vdots \end{Bmatrix} = \boldsymbol{0} \tag{B.2}$$

In FEM, an approximate solution for $\boldsymbol{u}$, $\hat{\boldsymbol{u}}$, is sought in the form of:

$$\boldsymbol{u} \approx \hat{\boldsymbol{u}} = \sum_{i=1}^{n} \boldsymbol{N_i} \boldsymbol{a_i} = \boldsymbol{N}\boldsymbol{a} \tag{B.3}$$

where $\boldsymbol{N_i}$ are the shape functions, which are known, and $\boldsymbol{a_i}$ are the nodal displacements. These nodal displacements are the solution to the problem and can be determined as described below. The degrees of freedom are given by n and they correspond to the

number of nodal displacements that must be determined to obtain the solution.

The discretization implicit in equation (B.3) allows to solve equations (B.1) and (B.2) by using an equivalent system of linear equations:

$$\boldsymbol{K}\boldsymbol{a} = \boldsymbol{f} \tag{B.4}$$

In the latter, $\boldsymbol{K}$ is often referred to as the stiffness matrix and $\boldsymbol{f}$ is column vector known as the force vector. The parameters $\boldsymbol{a}$, necessary to calculate the approximate solution $\hat{\boldsymbol{u}}$, can be obtained by inverting $\boldsymbol{K}$.

There are two different approaches that can be followed to calculate $\hat{\boldsymbol{u}}$: the method of weigthed residuals and the method of determination of a variational functional, as explained in detail in chapter 3 of Zienkiewicz and Taylor [155]. As the first is the one implemented in the software used throughout this thesis, COMSOL Multiphysics, it is also the one that is discussed here.

The starting point for this approach consists in expressing equations (B.1) and (B.2) in their integral form. As these sets of equations have to be zero at each point of the domain Ω, and at the boundaries Γ, it follows that:

$$\int_{\Omega} \boldsymbol{v}^T \boldsymbol{A}(\boldsymbol{u}) \partial\Omega + \int_{\Gamma} \bar{\boldsymbol{v}}^T \boldsymbol{B}(\boldsymbol{u}) \partial\Gamma = 0, \quad \forall \boldsymbol{v}, \bar{\boldsymbol{v}} \tag{B.5}$$

where $\boldsymbol{v}$ and $\hat{\boldsymbol{v}}$ are column vectors of arbitrary weighting functions defined in the domain and boundaries of the problem, respectively. The only restriction imposed on the latter two is that they are bounded, so the two previous integrals are finite. For the same reason, it is necessary that the $p-1$ derivatives of $\boldsymbol{u}$ to be continuous, where p is the maximum order of the derivatives occuring in $\boldsymbol{A}$ or $\boldsymbol{B}$.

In the method of weigthed residuals, $\boldsymbol{v}$ and $\hat{\boldsymbol{v}}$ are rewritten as:

$$\boldsymbol{v} = \sum_{j=1}^{n} \boldsymbol{w}_j \delta \boldsymbol{a}_j \tag{B.6}$$

$$\bar{\boldsymbol{v}} = \sum_{j=1}^{n} \bar{\boldsymbol{w}}_j \delta \boldsymbol{a}_j \tag{B.7}$$

where $\delta \boldsymbol{a}_j$ are arbitrary parameters and $\boldsymbol{w_j}$ and $\bar{\boldsymbol{w}}_{\boldsymbol{j}}$ are known functions.

Inserting equations (B.6) and (B.7) into equation (B.5) and considering equation (B.3) one obtains the following:

$$\delta \boldsymbol{a}_j^{\boldsymbol{T}} \Big[\int_{\Omega} \boldsymbol{w}_j^T \boldsymbol{A}(\boldsymbol{N}\boldsymbol{a}) \partial\Omega + \int_{\Gamma} \bar{\boldsymbol{w}}_j^T \boldsymbol{B}(\boldsymbol{N}\boldsymbol{a}) \partial\Gamma \Big]_{\Omega} = 0, \quad \forall j = 0, 1, ..., n \tag{B.8}$$

As $\delta \boldsymbol{a}_j$ are arbitrary, the last expression can be simplified to:

$$\int_{\Omega} \boldsymbol{w}_j^T \boldsymbol{A}(\boldsymbol{Na})\partial\Omega + \int_{\Gamma} \bar{\boldsymbol{w}}_j^T \boldsymbol{B}(\boldsymbol{Na})\partial\Gamma = 0, \quad \forall j = 0, 1, ..., n \tag{B.9}$$

The quantity $\boldsymbol{A}(\boldsymbol{Na})$ is the residual of the approximation of $\boldsymbol{u}$ by equation (B.3) and $\boldsymbol{B}(\boldsymbol{Na})$ is the residual of the boundary conditions. Thus, equation (B.9) is the weigthed integral of the residuals, hence the name of the method. The choice of $\boldsymbol{w}_j$ and $\bar{\boldsymbol{w}}_j$ depends on the method used, being the Galerkin method one of the most common ones. In the latter, it is assumed that the weighting functions are the same as the shape functions, $\boldsymbol{N}_j$.

In some cases, it is still possible to simplify the calculation of equation (B.5). If one integrates it by parts an alternative form of that equation is obtained:

$$\int_{\Omega} \boldsymbol{C}(\boldsymbol{v})^T \boldsymbol{D}(\boldsymbol{u})\partial\Omega + \int_{\Gamma} \boldsymbol{E}(\bar{\boldsymbol{v}})^T \boldsymbol{F}(\boldsymbol{u})\partial\Gamma = 0, \quad \forall \boldsymbol{v}, \bar{\boldsymbol{v}} \tag{B.10}$$

where the matrices $\boldsymbol{C}$, $\boldsymbol{D}$, $\boldsymbol{E}$ and $\boldsymbol{F}$ contain lower order derivatives than those occuring in equation (B.5). Equation (B.10) is then less restrictive than equation (B.5) and that is why the former is known as the weak version of the latter. Following the same approach as before, equation (B.10) can be written as:

$$\int_{\Omega} \boldsymbol{C}(\boldsymbol{w}_j)^T \boldsymbol{D}(\boldsymbol{Na})\partial\Omega + \int_{\Gamma} \boldsymbol{E}(\bar{\boldsymbol{w}}_j)^T \boldsymbol{F}(\boldsymbol{Na})\partial\Gamma = 0, \quad \forall j = 0, 1, ..., n \tag{B.11}$$

The advantage of the latter formula is that $\boldsymbol{C}$, $\boldsymbol{D}$, $\boldsymbol{E}$ and $\boldsymbol{F}$ are linear operators which allow to represent equation (B.11) as a linear system of equations similar to equation (B.4).

The shape functions, $\boldsymbol{N}_j$, that appeared in most of the equations described above, are defined locally for each finite element. In computational simulations that use the FEM, the geometry is divided into several finite elements, in which equation (B.11) is solved (figure B.1).

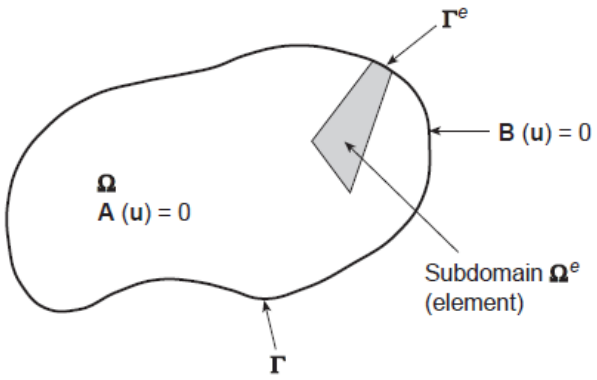

Figure B.1: In the FEM, the geometry of the problem is divided into several elements, e. Instead of solving the equations in the whole domain, Ω, and boundaries, Γ, at once, they are solved in the domain, Ω_e, and boundaries, Γ_e, of each element. The final solution is then obtained by the sum of the solution of all elements of the whole domain. Adapted from [155].

In 2D, these elements are typically triangles and in 3D tetrahedrons, although other shapes can be considered. The ensemble of all elements forms the mesh. To ensure that an accurate solution is obtained through the FEM, it is necessary that the mesh is fine enough, i.e., that the elements are small enough, so that the geometry is well represented. Elements with a small size also ensure that a low order for the shape functions can be used (linear or quadratic), that can accurately represent the variation of the solution. In figure B.2, a simple representation of the importance of the mesh is provided. A coarser mesh leads to a poorer representation of the geometry as less surface and volume elements are used. However, for extremely fine meshes, the number of elements increases significantly which leads to very long simulation times.

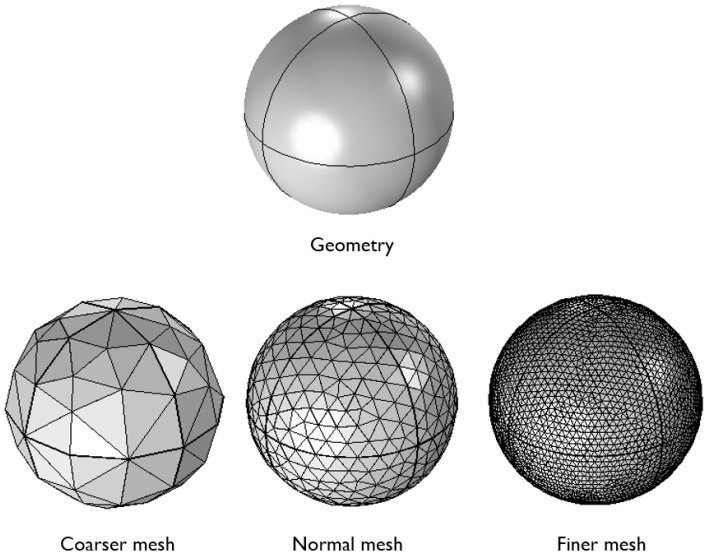

Figure B.2: The geometry of interest (upper figure) is a sphere. The finer the mesh, the more elements are used to represent the geometry and thus the more accurate the final solution. However, the higher the number of elements the longer it takes to run the simulation. Thus, in the FEM there has to be a trade-off between the accuracy of the results and simulation time.

As mentioned previously, $\boldsymbol{N}_j$ is defined locally for each element, e, of the mesh. Thus, equation (B.11) can be rewritten as:

$$\sum_{e=1}^{m} \Big(\int_{\Omega^e} \boldsymbol{C}(\boldsymbol{N}_j)^T \boldsymbol{D}(\boldsymbol{N}\boldsymbol{a}) \partial\Omega + \int_{\Gamma^e} \boldsymbol{E}(\bar{\boldsymbol{N}}_j)^T \boldsymbol{F}(\boldsymbol{N}\boldsymbol{a}) \partial\Gamma \Big) = 0, \quad \forall j = 0, 1, ..., n \tag{B.12}$$

where Ω^e is the domain of each element and Γ^e the respective boundary. The total number of elements in the mesh is given by m.

Thus, the matrices $\boldsymbol{K}$ and $\boldsymbol{a}$ in equation (B.4) can be obtained by assembling simpler matrices, $\boldsymbol{k}^e$ and $\boldsymbol{a}^e$, respectively, that are specific for each element. Under these conditions, $\boldsymbol{u}$ is given by:

$$\boldsymbol{u} \approx \hat{\boldsymbol{u}} = \sum_{i=1}^{n} \boldsymbol{N_i} \boldsymbol{a_i^e} = \boldsymbol{N}\boldsymbol{a}^e \tag{B.13}$$

The number of points, n, can vary depending on the order of the elements considered during the calculations. For first order elements, $\hat{\boldsymbol{u}}$ is calculated at the vertices of each element. It is possible to increase the accuracy of the solution, at a cost of an increased computational time and memory usage, by considering higher order elements. In that case, the nodes are not only at the vertices of each element, but they might also be on the edges or faces of the element, as depicted in figure B.3. Higher order elements imply using shape functions, $\boldsymbol{N_j}$, with a higher polynomial degree.

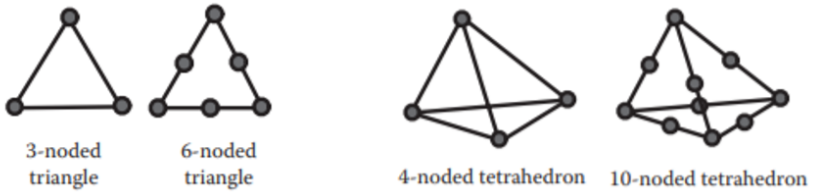

Figure B.3: The total number of points in which the solution is computed, the nodes, can vary depending on the order of the elements. For first-order elements, there are 3 nodes for each triangle (2D) and 4 for each tetraheadron (3D). For higher order elements the number of nodes is higher (in the figure: 6 for the triangle and 10 for the tetraheadron), which increases the accuracy of the solution at a cost of an increased computational time and memory usage. Adapted from [157].

In general, one of the main challenges of the FEM has to do with the calculation of $\boldsymbol{K}$. For 1D, direct methods for inverting $\boldsymbol{K}$ can be used at a low computational cost. However, for the most general applications that use the FEM, a 3D geometry is required, which is divided into several thousands of elements yielding millions of degrees of freedom. Thus, an iterative approach has to be considered instead, which requires less storage and fewer operations to solve the problem. The rationale behind an iterative process is to successively improve the calculated solution until a stopping criterion is reached. Given an initial guess, $\boldsymbol{a^0}$, an iterative solver finds the solution to the following equation:

$$\hat{\boldsymbol{u}}^{\boldsymbol{k+1}} = \boldsymbol{T}\hat{\boldsymbol{u}}^{\boldsymbol{k}} + \boldsymbol{c}, \quad k = 0, 1, ... \tag{B.14}$$

where $\hat{\boldsymbol{u}}^{\boldsymbol{k}}$ is the solution of the problem on iteration k, $\boldsymbol{T}$ is the iteration matrix and $\boldsymbol{c}$ is a vector. In stationary studies, the latter two are fixed. In non-stationary studies, $\boldsymbol{T}$ and $\boldsymbol{c}$ might vary in each iteration and their calculation depends on the solver used. The choice of the best solver for each problem depends on several factors. The most used ones in COMSOL Multiphysics are the generalized minimal residual (GMRES), the flexible generalized minimal residual (FGMRES), the biconjugate gradient stabilized method (BiCGSTab) and the conjugate gradients. The main differences between them can be found elsewhere [158].

In every iterative process, there has to be a condition that allows the solver to stop the calculations. Ideally, the stopping condition corresponds to a case where the relative difference between two consecutive solutions, $\hat{\boldsymbol{u}}^{\boldsymbol{k+1}}$ and $\hat{\boldsymbol{u}}^{\boldsymbol{k}}$, is lower than a predefined tolerance, which indicates that the solution has converged. Very often, a maximum number of iterations is also defined to avoid running the solver *ad aeternum* in the case that it is not converging or its convergence is very slow.

Appendix C

Additional data on the sensitivity analysis of the physical parameters

In this appendix additional data concerning the sensitivity analysis, discussed in chapter 4, is presented. In the following tables the impact that each electric and thermal parameter variation had on the percentile 99.99% of the temperature distribution in each tissue and on the average temperature, T_{avg}, of the most significant transducer are shown. As discussed in that chapter, the percentile 99.99% was considered to be the maximum temperature, T_{max}. The deviation of each result with respect to the value obtained when the standard (std) set of values was used is also presented for each case following the formula:

$$\Delta^{std}_{tissue,MST} = T^{new\,set}_{max,avg} - T^{std}_{max,avg} \tag{C.1}$$

The standard set of values used is presented in table 4.1, but the values changed in each test are repeated in tables C.1 and C.2 for convenience. In total, 57 simulations were performed. The results concerning the variation of the temperature of the tumor are not presented as its maximum temperature did not vary by more than 0.1 ℃ in any simulation.

The highest and lowest temperature predicted when the electric and thermal parameters of biological tissues were changed are highlighted in bold in the tables. These are the same parameters as the ones presented in table 4.2, which is replicated below.

Parameter evaluated	Tissue		T^{-}_{max} / T^{-}_{avg}	T^{+}_{max} / T^{+}_{avg}
Maximum temperature	Scalp	Electric	σ^{max}_{skull}	σ^{min}_{skull}
		Thermal	$\omega^{*,max}_{scalp}$	k^{min}_{scalp}
	Skull	Electric	σ^{max}_{skull}	σ^{min}_{scalp}
		Thermal	$\omega^{*,max}_{scalp}$	k^{min}_{skull}
	CSF	Electric	σ^{max}_{skull}	σ^{min}_{scalp}
		Thermal	$\omega^{*,max}_{scalp}$	k^{min}_{scalp}
	Brain	Electric	σ^{max}_{scalp}	σ^{min}_{scalp}
		Thermal	$\omega^{*,max}_{scalp}$	k^{min}_{scalp}
Average temperature	MST	Electric	σ^{max}_{skull}	σ^{min}_{scalp}
		Thermal	$\omega^{*,max}_{scalp}$	k^{min}_{scalp}

Table C.1: Impact of the uncertainty of the value of each electric and thermal parameter on the maximum temperature predicted for each tissue and on the average temperature predicted for the most significant transducer (MST) – part I.

Simulation number	Physical property	Parameter	Std value	New value	Percentile 99.99 % of the temperature ($\equiv T_{max}$) (°C)								Average temperature (°C)	
					Scalp	Δ^{std}_{scalp}	Skull	Δ^{std}_{skull}	CSF	Δ^{std}_{CSF}	Brain	Δ^{std}_{brain}	MST	Δ^{std}_{MST}
1	–	–	Std	Std	41.60	–	40.20	–	39.80	–	38.50	–	40.43	–
2	Electric conductivity σ (S/m)	σ_{scalp}	0.25	0.14	42.94	1.34	**41.56**	1.36	**41.22**	1.42	**39.32**	0.82	**41.62**	1.19
3		σ_{scalp}	0.25	0.45	39.75	-1.85	38.81	-1.39	38.47	-1.33	**37.85**	-0.65	38.86	-1.57
4		σ_{skull}	0.013	0.003	**43.47**	1.87	40.88	0.68	40.01	0.21	38.54	0.04	41.48	1.05
5		σ_{skull}	0.013	0.080	**38.56**	-3.04	**38.33**	-1.87	**38.19**	-1.61	37.86	-0.63	**38.07**	-2.36
6		σ_{CSF}	1.79	1.64	41.60	0.01	40.19	-0.01	39.78	-0.02	38.49	-0.01	40.43	0.00
7		σ_{CSF}	1.79	1.94	41.58	-0.02	40.21	0.00	39.81	0.01	38.50	0.00	40.42	-0.01
8		σ_{GM}	0.25	0.15	41.62	0.03	40.20	0.00	39.78	-0.02	38.49	-0.01	40.44	0.01
9		σ_{GM}	0.25	0.50	41.57	-0.03	40.22	0.02	39.83	0.04	38.52	0.02	40.42	-0.01
10		σ_{WM}	0.12	0.08	41.59	-0.01	40.19	-0.02	39.78	-0.02	38.49	-0.01	40.42	-0.01
11		σ_{WM}	0.12	0.30	41.60	0.00	40.23	0.03	39.84	0.04	38.52	0.02	40.44	0.01
12		$\sigma_{tumor\,shell}$	0.24	0.15	41.60	0.00	40.20	0.00	39.80	0.00	38.50	0.00	40.43	0.00
13		$\sigma_{tumor\,shell}$	0.24	0.50	41.60	0.00	40.20	0.00	39.80	0.00	38.50	0.00	40.43	0.00
14		$\sigma_{tumor\,core}$	1.0	0.5	41.60	0.00	40.20	0.00	39.80	0.00	38.50	0.00	40.43	0.00
15		$\sigma_{tumor\,core}$	1.0	1.50	41.60	0.00	40.20	0.00	39.80	0.00	38.50	0.00	40.43	0.00
16		σ_{gel}	0.10	0.05	43.33	1.73	40.62	0.41	40.08	0.28	38.67	0.17	42.15	1.72
17		σ_{gel}	0.10	0.20	40.52	-1.08	39.92	-0.29	39.59	-0.21	38.38	-0.11	39.38	-1.05
18	Thermal conductivity k (W/(m °C))	k_{scalp}	0.34	0.16	**42.55**	0.95	40.44	0.23	**40.05**	0.25	**38.66**	0.16	**41.08**	0.65
19		k_{scalp}	0.34	0.50	41.10	-0.49	40.05	-0.15	39.66	-0.13	38.43	-0.07	40.11	-0.32
20		k_{skull}	1.16	0.16	42.26	0.66	**41.94**	1.73	39.87	0.07	38.53	0.03	41.03	0.60
21		k_{CSF}	0.60	0.50	41.66	0.06	40.33	0.12	39.96	0.16	38.47	-0.03	40.49	0.06
22		k_{CSF}	0.60	0.62	41.59	-0.01	40.18	-0.02	39.77	-0.03	38.50	0.00	40.42	-0.01
23		k_{GM}	0.565	0.503	41.61	0.01	40.22	0.02	39.82	0.03	38.54	0.05	40.44	0.01
24		k_{GM}	0.565	0.576	41.60	0.00	40.20	0.00	39.79	0.00	38.49	-0.01	40.43	0.00
25		k_{WM}	0.503	0.460	41.60	0.00	40.20	0.00	39.80	0.00	38.50	0.00	40.43	0.00
26		k_{tumor}	0.550	0.495	41.60	0.00	40.20	0.00	39.80	0.00	38.50	0.00	40.43	0.00
27		k_{tumor}	0.550	0.605	41.60	0.00	40.20	0.00	39.80	0.00	38.50	0.00	40.43	0.00
28		k_{gel}	0.6	0.3	41.79	0.19	40.22	0.02	39.80	0.01	38.50	0.00	40.40	-0.03
29		k_{gel}	0.6	1.2	41.45	-0.15	40.19	-0.01	39.79	0.00	38.50	0.00	40.42	-0.01
30		$k_{transducers}$	6	3	41.91	0.32	40.21	0.01	39.79	0.00	38.50	0.00	40.43	0.00
31		$k_{transducers}$	6	12	41.33	-0.27	40.20	0.00	39.80	0.01	38.50	0.00	40.43	0.00

Table C.2: Impact of the uncertainty of the value of each electric and thermal parameter on the maximum temperature predicted for each tissue and on the average temperature predicted for the most significant transducer (MST) – part II.

Simulation number	Physical property	Parameter	Std value	New value	Percentile 99.99 % of the temperature ($\equiv T_{max}$) (°C)								Average temperature (°C)	
					Scalp	Δ^{std}_{scalp}	Skull	Δ^{std}_{skull}	CSF	Δ^{std}_{CSF}	Brain	Δ^{std}_{brain}	MST	Δ^{std}_{MST}
1	–	–	Std	Std	41.60	–	40.20	–	39.80	–	38.50	–	40.43	–
32	Blood specific heat c (W/(m °C))	c_b	3600	3300	41.73	0.13	40.32	0.11	39.90	0.10	38.60	0.10	40.55	0.13
33		c_b	3600	3930	41.47	-0.13	40.09	-0.12	39.69	-0.10	38.40	-0.10	40.30	-0.13
34	Blood density ρ (kg/m^3)	ρ_b	1050	1025	41.63	0.04	40.24	0.03	39.82	0.03	38.52	0.03	40.46	0.04
35		ρ_b	1050	1064	41.58	-0.02	40.19	-0.02	39.78	-0.02	38.48	-0.01	40.41	-0.02
36	Blood perfusion rate ω^* (10^{-3} 1/s)	ω^*_{scalp}	1.43	0.91	42.11	0.51	40.55	0.35	39.80	0.00	38.63	0.13	40.91	0.49
37		ω^*_{scalp}	1.43	2.20	**41.03**	-0.57	**39.82**	-0.38	**39.52**	-0.27	**38.36**	-0.14	**39.89**	-0.53
38		ω^*_{skull}	0.143	0.040	41.63	0.03	40.26	0.05	39.85	0.05	38.53	0.03	40.46	0.03
39		ω^*_{skull}	0.143	0.180	41.59	-0.01	40.18	-0.02	39.78	-0.02	38.49	-0.01	40.42	-0.01
40		ω^*_{GM}	13.30	11.69	41.62	0.03	40.25	0.05	39.86	0.07	38.59	0.10	40.46	0.03
41		ω^*_{GM}	13.30	14.68	41.58	-0.02	40.17	-0.04	39.75	-0.05	38.43	-0.07	40.41	-0.02
42		ω^*_{WM}	3.70	3.30	41.60	0.00	40.21	0.00	39.80	0.00	38.50	0.00	40.43	0.00
43		ω^*_{WM}	3.70	5.21	41.59	0.00	40.20	-0.01	39.79	-0.01	38.49	-0.01	40.43	0.00
44		$\omega^*_{tumor\,shell}$	1.72	1.55	41.60	0.00	40.20	0.00	39.80	0.00	38.50	0.00	40.43	0.00
45		$\omega^*_{tumor\,shell}$	1.72	1.89	41.60	0.00	40.20	0.00	39.80	0.00	38.50	0.00	40.43	0.00
46	Metabolic rate Q_{met} (W/m^3)	$Q_{met\,scalp}$	363	271	41.59	-0.01	40.20	-0.01	39.79	0.00	38.50	0.00	40.43	0.01
47		$Q_{met\,scalp}$	363	2294	41.76	0.16	40.33	0.13	39.90	0.10	38.56	0.06	40.59	0.16
48		$Q_{met\,skull}$	70	542	41.61	0.01	40.23	0.03	39.82	0.02	38.51	0.02	40.44	0.02
49		$Q_{met\,GM}$	16229	10369	41.57	-0.03	40.15	-0.06	39.73	-0.07	38.41	-0.08	40.40	-0.02
50		$Q_{met\,GM}$	16229	17859	41.61	0.01	40.22	0.02	39.81	0.02	38.52	0.02	40.44	0.02
51		$Q_{met\,WM}$	4518	2491	41.60	0.00	40.20	0.00	39.79	0.00	38.49	-0.01	40.43	0.01
52		$Q_{met\,WM}$	4518	5018	41.60	0.00	40.20	0.00	39.80	0.00	38.50	0.00	40.43	0.01
53		$Q_{met\,active\,shell}$	58000	52200	41.60	0.00	40.20	0.00	39.80	0.00	38.50	0.00	40.43	0.01
54		$Q_{met\,active\,shell}$	58000	63800	41.60	0.00	40.20	0.00	39.80	0.00	38.50	0.00	40.43	0.01
55	Convection factor h (W/(m^2 °C))	h_{gel} $h_{transducers}$	4	2	42.08	0.49	40.34	0.14	39.90	0.11	38.55	0.06	40.98	0.55
56		h_{gel} $h_{transducers}$	4	8	40.71	-0.89	39.96	-0.24	39.60	-0.19	38.39	-0.10	39.43	-1.00
57	Emissivity ϵ (1)	ϵ_{gel} $\epsilon_{transducers}$	1.0	0.5	42.41	0.82	40.43	0.22	39.97	0.18	38.59	0.09	41.34	0.91

Appendix D

Analysis of the equation used to predict the temperature variations

In chapter 6, equation (6.2) was used to predict the temperature variation of the most significant transducer when TTFields were applied. As the head was in thermal equilibrium with the environment before current injection began, the temperature increases occurred only due to the Joule effect. In those studies, the first six minutes of treatment were simulated to predict how much current could be injected into both pairs to induce a maximum steady-state temperature, T_{max}, predicted through equation (6.3), of 40.4 ℃ in the MST. These two equations are replicated below for convenience:

$$T = C_1(1 - exp(-t/C_2)) + C_3 \tag{6.2}$$

$$T_{max} \equiv \lim_{t\to\infty} T = C_1 + C_3 \tag{6.3}$$

In this appendix two different studies were performed to investigate two different aspects discussed in that chapter. The goal of study A was to investigate the sensitivity of the coefficients C_1, C_2 and C_3 to the simulation time. For the purpose of this work, the first eight minutes of treatment were simulated. The upper plot in figure D.1 depicts the temperature variation of the MST when the critical current, 675 mA, was injected. This simulation took around 45 hours in workstation 1. Curve fitting of the data was performed to the temperature variation considering only the first 2 (A1), 4 (A2), 6 (A3), and 8 (A4) minutes of treatment (figure D.1, middle row). Study A3 corresponds to the data used to drawn the conclusions presented in chapter 6. In all cases, the value of C_3 is known to be equal to 33.38 ℃, as it represents the temperature of the transducer in the beginning of the simulation. The reason why it was not kept constant during the curve fitting process was because it led to a more pronounced underestimation of the temperature variation at the end of the simulation compared to when it was set as a free parameter.

Study B was performed to investigate why the coefficients C_4 and C_6 (table 6.2), predicted using equation (6.4), and which modelled the temperature variation when the fields were shut down, did not match the values of C_1 and C_3 presented in table 6.1 for the same injected current. When current injection was ceased, the head was still not in thermal equilibrium with the environment (figure 6.3) and thus what was simulated was not the beginning of the exponential decay. To mimic this situation, curve fitting of the

temperature variation of the MST was performed considering the temperature variation in different time intervals: 1-5 (B1), 2-6 (B2), 3-7 (B3), and 4-8 (B4) minutes (figure D.1, lower row).

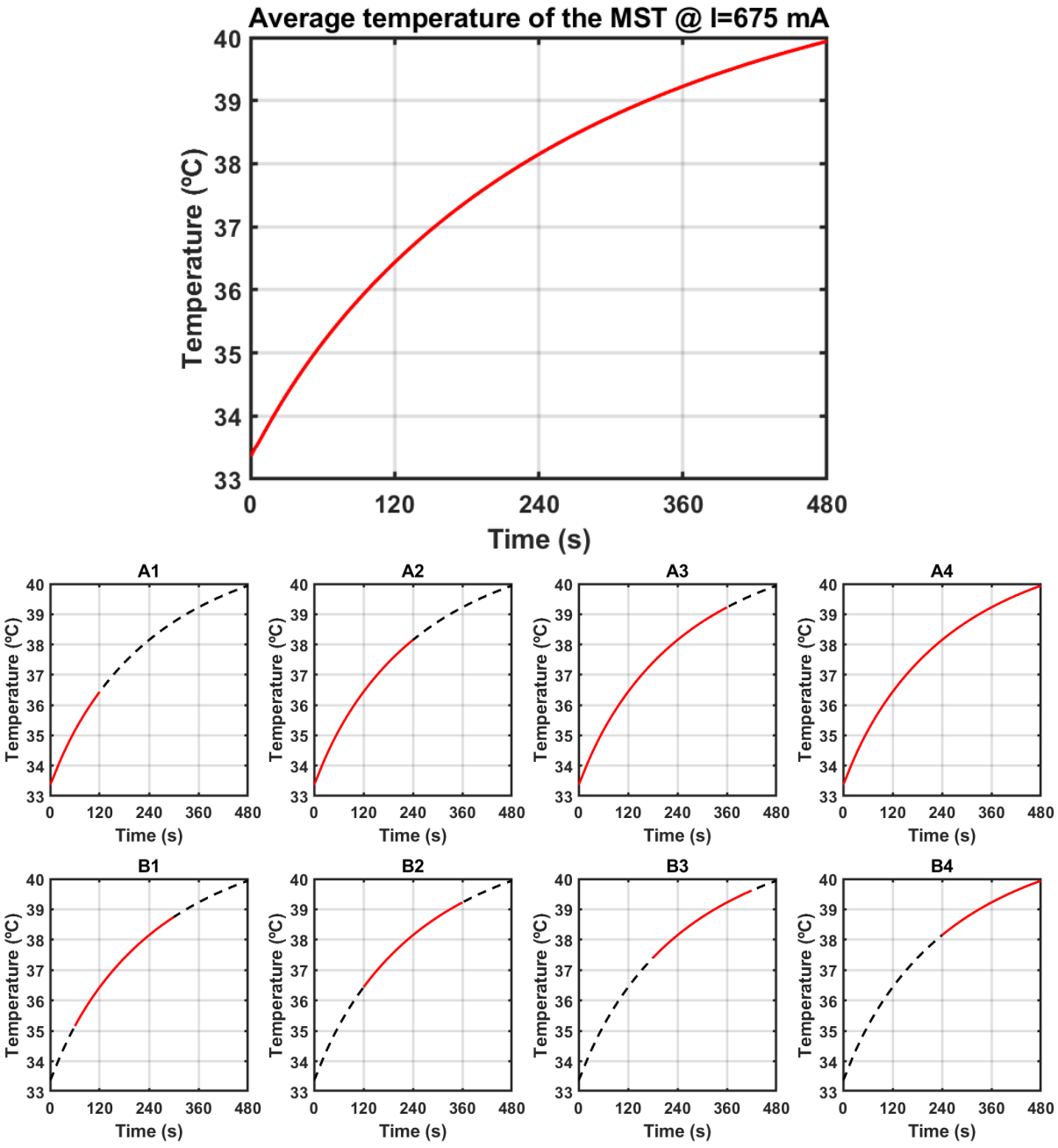

Figure D.1: Variation of the average temperature of the MST for an 8-minute simulation when 675 mA were injected into each array alternately with a switching time of one second (upper row). In study A, the importance of the simulation time was investigated by analysing different portions of this variation (middle row). In study A1, only the first 2 minutes were considered, whereas this value was increased to 4 minutes in study A2, to 6 minutes in A3, and 8 minutes in A4. In study B, the significance of which time interval is studied was investigated (lower row). In study B1, only the temperature variation between 1 and 5 minutes was considered, whereas in the other studies this 4-minute time window was shifted 1 minute between consecutive studies and it included data from the time interval 2 to 6 minutes in study B2, 3 to 7 minutes in B3, and 4 to 8 minutes in B4. In all cases, the red line indicates the data that was analysed.

The coefficents obtained for each one of these studies through curve fitting are presented in table D.1.

Table D.1: Curve fitting coefficients for each test. In study A (A1-A4) the goal was to investigate the impact of the simulation time on the curve fitting parameters. In study B (B1-B4) the aim was to investigate the influence of using data from different time periods in the values of the coefficients.

Study	Time interval (s)	C_1 (℃)	C_2 (s)	C_3 (℃)	A-R^2	T_{max} (℃)
A1	0-120	6.07	170	33.35	1	39.42
A2	0-240	6.79	201	33.38	0.9999	40.17
A3	0-360	7.17	222	33.42	0.9998	40.59
A4	0-480	7.40	237	33.46	0.9997	40.86
B1	60-300	7.22	235	33.52	1	40.74
B2	120-360	7.33	257	33.69	1	41.02
B3	180-420	7.34	275	33.86	1	41.20
B4	240-480	7.36	280	33.89	1	41.25

The results obtained in study A suggest that longer simulations yield a higher T_{max}. In study A1 only the first 2 minutes were simulated and this value was 39.4 ℃, but it increased by around 1.5 ℃ when the first 8 minutes were simulated in study A4. These values were mainly affected by the estimation of C_1, which quantifies the contribution of the EFs. The value of C_3 varied by 0.1 ℃, whereas C_2 varied by more than one minute between studies A1 and A4. It is expected that the more time is simulated, the more accurate and reliable the fitted coefficients are. This can also be observed comparing the values of T_{max} between consecutive studies. From A1 to A2 this value varied by 0.75 ℃, from A2 to A3 by 0.42 ℃ and from A3 to A4 by 0.27 ℃, which indicates that T_{max} is becoming less sensitive to the treatment time simulated. Ideally, simulations should be done in which the MST reaches a value very close to its steady-state. Based on the value of C_3 in study A4, at t=711 seconds the contribution of the EFs in increasing the temperature of the MST would reach 95% of its maximum value. Curve fitting performed with that data would be more reliable to predict T_{max}, but it would also lead to a computational time of roughly 3 days. This highlights that there has to be a trade-off between the accuracy of the results and simulation time.

To the analysis of the the results obtained in study B, the data concerning study A2 can also be added as the evaluation period was four minutes as well. In general, these results indicate that shifting the time-window to later times leads to higher values predicted for T_{max} mainly because the value of C_3 was progressively more overestimated the more this time-window was moved to the right. Even though the value of C_1 approximated the one obtained in study A4, in which data for the whole 8 minutes was considered, this was not enough to compensate the increases in C_3. As the time-derivative is higher for the initial time periods, curve fitting with data that corresponds to a time-window such as the one used in study B4, in which the temperature is varying less, might lead to less accurate predictions of the value of the coefficients. These conclusions are representative of what occurred in chapter 6 when the values of C_4 and C_6 were predicted.

Appendix E

Simplified head model: curve fitting data

In this appendix the coefficients obtained when equation (6.2) was fitted to the temperature variation of the scalp using the simplified head model (chapter 8) are presented for each layout. These data concern only the current that led to a maximum steady-state temperature, T_{max}, predicted through equation (6.3), as close as possible to 40.5 ℃ on the surface of the scalp, based on 5-minute simulations. These two equations are replicated below for convenience:

$$T = C_1(1 - exp(-t/C_2)) + C_3 \tag{6.2}$$

$$T_{max} \equiv \lim_{t \to \infty} T = C_1 + C_3 \tag{6.3}$$

Table E.1: Curve fitting coefficients for the simplified head model and for each layout. The current injected into each pair was the one that led to a maximum steady-state temperature predicted on scalp's surface, T_{max}, as close as possible to 40.5 ℃. The values of the adjusted-R^2 suggest that the equation used for curve fitting can explain very well the temperature variation of the scalp when TTFields are applied to a simplified head model.

Layout	Pair	Injected current (mA)	C1 (℃)	C2 (s)	C3 (℃)	A-R^2	T_{max} (℃)
0/75	0°	400	6.85	209	33.6	0.9995	40.5
	75°	600	6.65	219	33.8	0.9996	40.5
0/90	0°	410	6.80	217	33.7	0.9996	40.5
	90°	625	6.73	216	33.9	0.9995	40.6
0/105	0°	423	6.70	211	34.0	0.9997	40.7
	105°	600	6.51	209	33.9	0.9994	40.4
15/105	15°	400	6.79	205	33.7	0.9995	40.5
	105°	575	6.60	212	33.8	0.9996	40.4
30/135	30°	425	6.82	211	33.7	0.9996	40.5
	135°	600	6.66	206	33.9	0.9994	40.6
165/60	165°	423	6.97	215	33.6	0.9997	40.6
	60°	600	6.39	208	33.9	0.9994	40.3
165/75	165°	423	6.70	212	33.6	0.9997	40.3
	75°	625	6.50	205	33.9	0.9994	40.4

Appendix F

Realistic head model: additional data

F.1 Realistic head model: curve fitting data

In this section of the appendix the coefficients obtained when equation (6.2) was fitted to the temperature variation of the scalp using the realistic head model (chapter 9) are presented for each layout. These data concern only the current that led to a maximum steady-state temperature, T_{max}, predicted through equation (6.3), as close as possible to 39.5 ℃ on the surface of the scalp. These two equations are replicated below for convenience:

$$T = C_1(1 - exp(-t/C_2)) + C_3 \tag{6.2}$$

$$T_{max} \equiv \lim_{t \to \infty} T = C_1 + C_3 \tag{6.3}$$

Table F.1: Curve fitting parameters for the realistic head model and for each layout. The current injected into each pair was the one that led to a maximum steady-state temperature predicted on scalp's surface, T_{max}, as close as possible to 39.5 ℃. The values of the adjusted-R^2 suggest that the equation used for curve fitting can explain very well the temperature variation of the scalp when TTFields are applied.

Layout	Pair	Injected current (mA)	C1 (℃)	C2 (s)	C3 (℃)	A-R^2	T_{max} (℃)
1	AP	580	5.53	166	33.8	0.9993	39.3
	LR	850	5.11	151	34.3	0.9981	39.4
2	AP	580	5.73	177	34.0	0.9991	39.7
	LR	650	4.51	196	33.8	0.9996	38.3
3	AP	580	5.66	170	33.9	0.9995	39.6
	LR	775	5.20	155	34.3	0.9983	39.4
4	AP	550	5.31	177	34.0	0.9991	39.3
	LR	800	5.34	151	34.0	0.9989	39.3
5	AP	565	5.49	159	34.3	0.9987	39.8
	LR	800	5.41	148	34.1	0.9987	39.5

F.2 Temperature distribution: layout 2

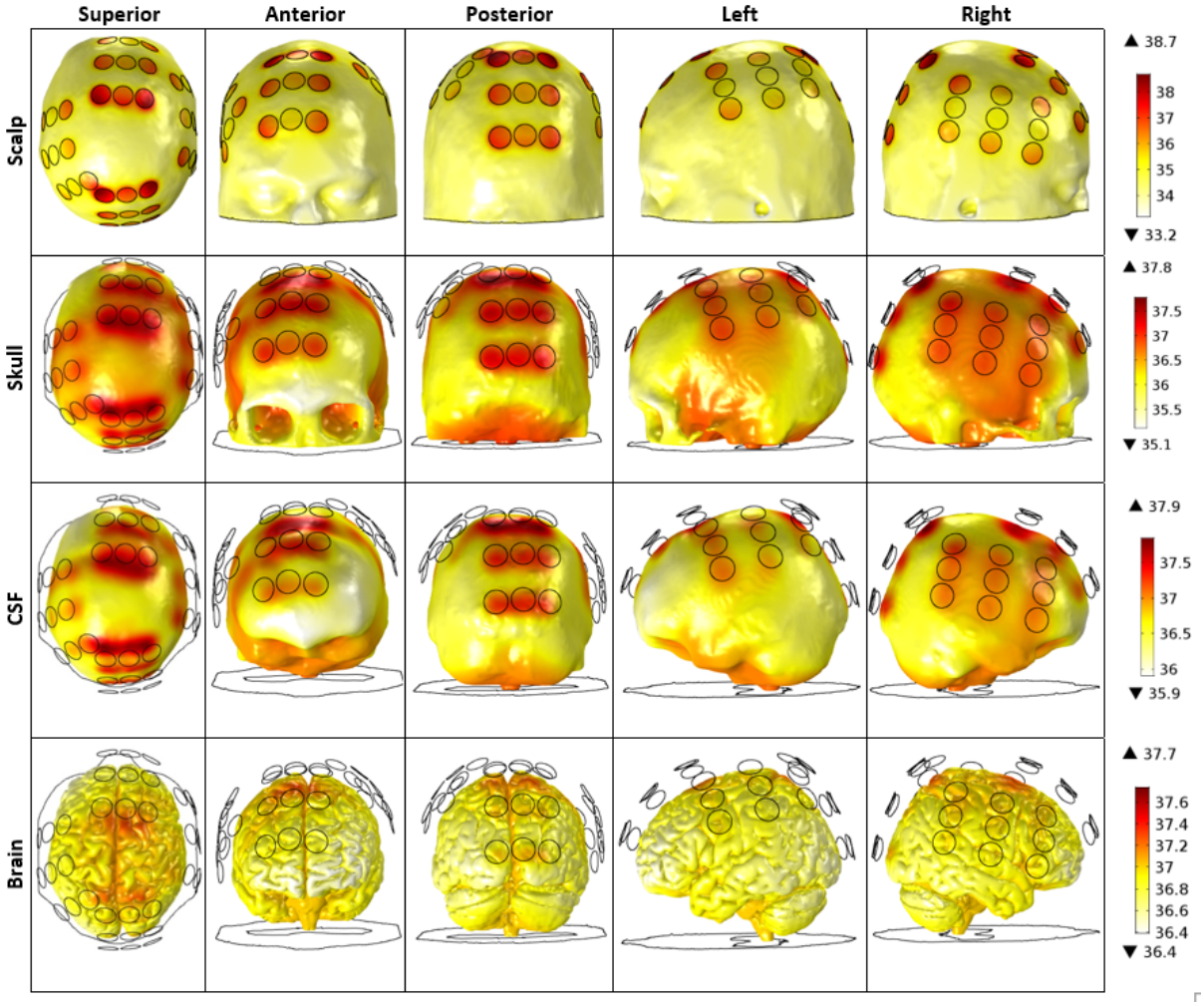

Figure F.1: Temperature distribution, from five different perspectives, on each tissue surface at the end of the simulation (t=300 seconds) when layout 2 was used. Current was injected alternately into each pair with a switching time of one second. The current injected into the AP pair was 580 mA, whereas in the LR's it was 650 mA. For these values of current the maximum steady-state temperature predicted on the scalp surface underneath the first pair is 39.5 ℃, but underneath the second is only 38.3 ℃. If more current was injected into the LR pair, the temperature of the scalp underneath AP's would have been higher than the desired 39.5 ℃. The temperature increases occurred mainly underneath the arrays as clearly seen by the regions in red. Each circle represents the region where a transducer was placed. First row: scalp; Second row: skull; Third row: CSF; Fourth row: Brain. In the latter, the maximum temperature was reached at the GM surface. Scales are different for each row. All values are in ℃.

F.3 Temperature distribution: layout 3

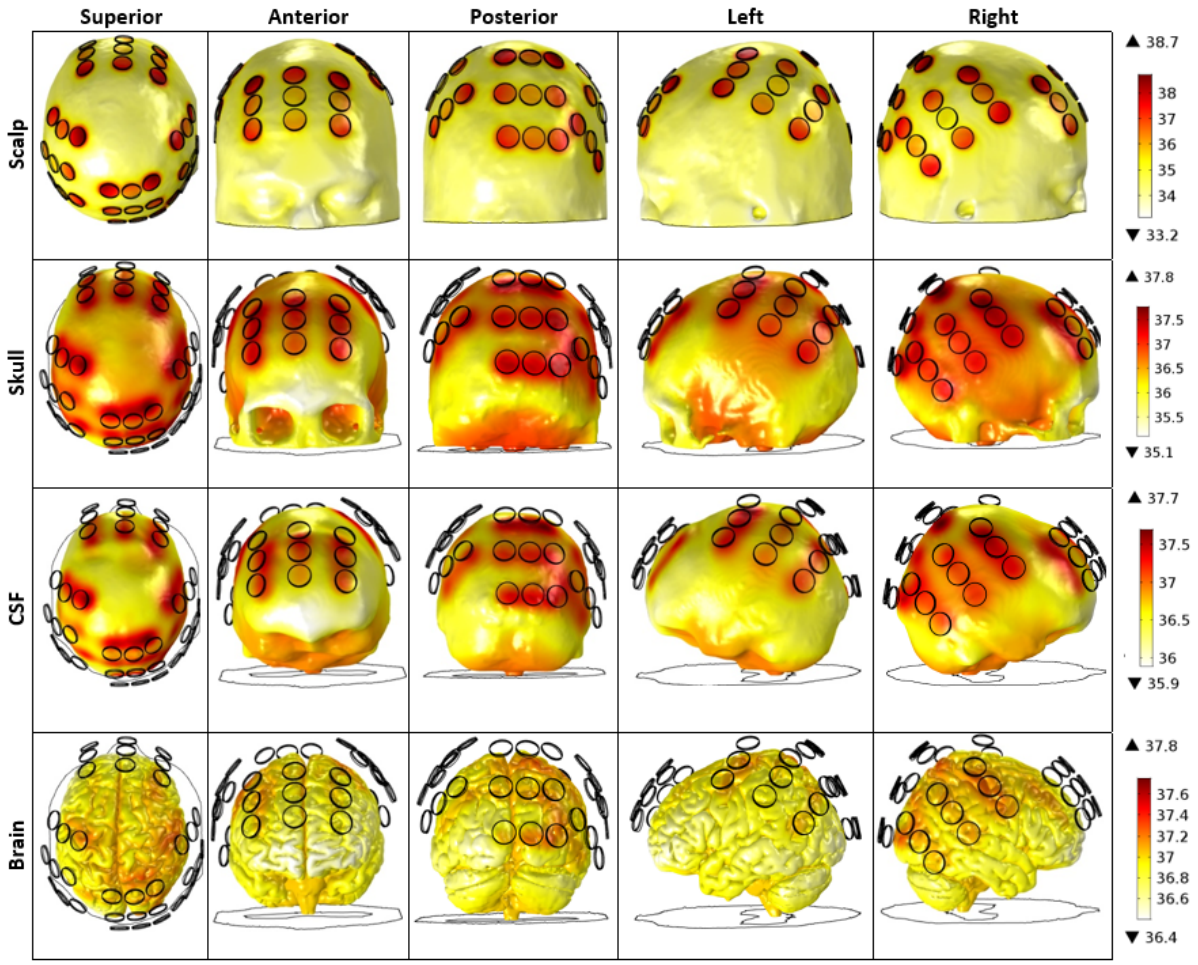

Figure F.2: Temperature distribution, from five different perspectives, on each tissue surface at the end of the simulation (t=300 seconds) when layout 3 was used. Current was injected alternately into each pair with a switching time of one second. The current injected into the AP pair was 580 mA, whereas in the LR's it was 775 mA. For these values of current the maximum steady-state temperature predicted on the scalp surface underneath both pairs is 39.5 ℃. The temperature increases occurred mainly underneath the arrays as clearly seen by the regions in red. Each circle represents the region where a transducer was placed. First row: scalp; Second row: skull; Third row: CSF; Fourth row: Brain. In the latter, the maximum temperature was reached at the GM surface. Scales are different for each row. All values are in ℃.

F.4 Temperature distribution: layout 4

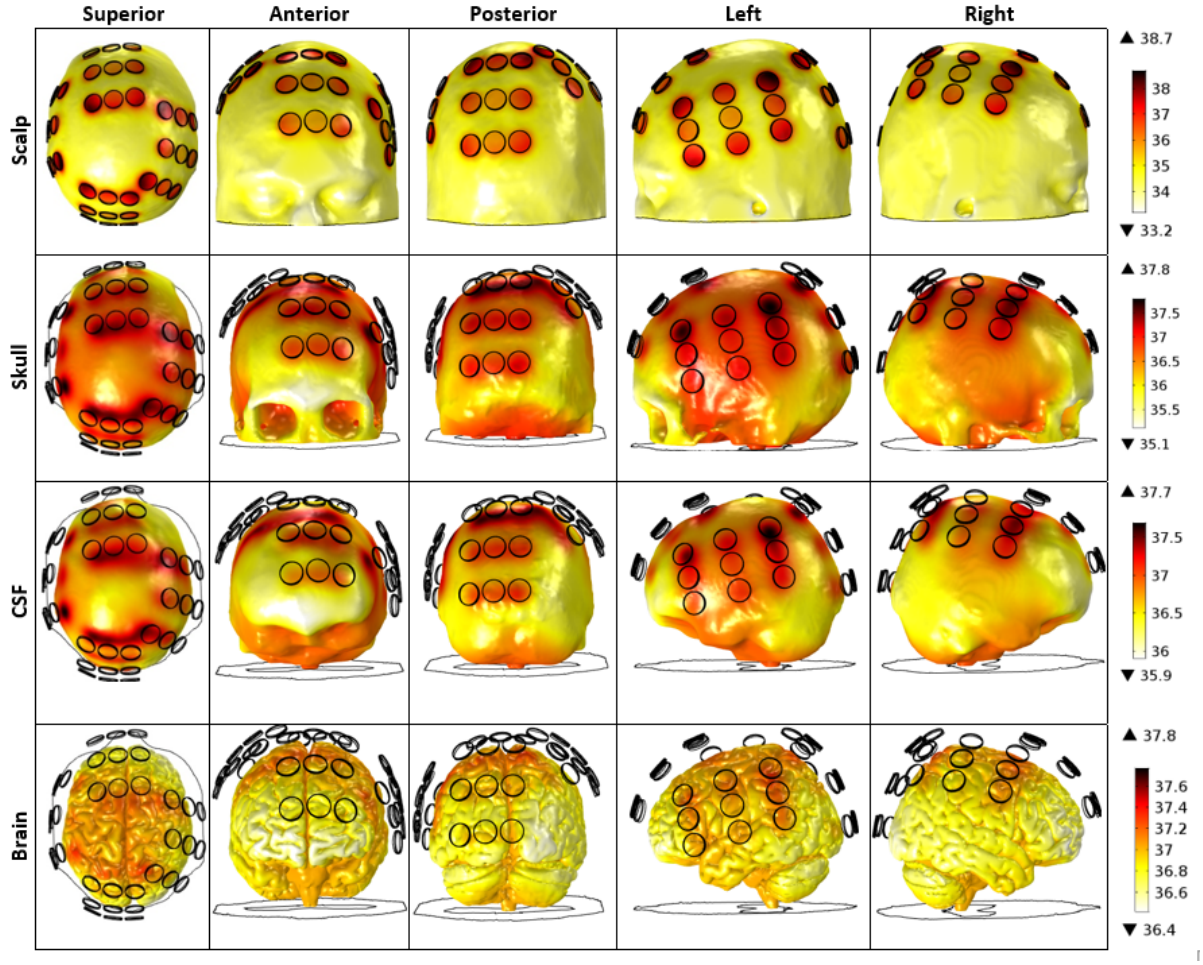

Figure F.3: Temperature distribution, from five different perspectives, on each tissue surface at the end of the simulation (t=300 seconds) when layout 4 was used. Current was injected alternately into each pair with a switching time of one second. The current injected into the AP pair was 550 mA, whereas in the LR's it was 800 mA. For these values of current the maximum steady-state temperature predicted on the scalp surface underneath both pairs is 39.5 ℃. The temperature increases occurred mainly underneath the arrays as clearly seen by the regions in red. Each circle represents the region where a transducer was placed. First row: scalp; Second row: skull; Third row: CSF; Fourth row: Brain. In the latter, the maximum temperature was reached at the GM surface. Scales are different for each row. All values are in ℃.

F.5 Temperature distribution: layout 5

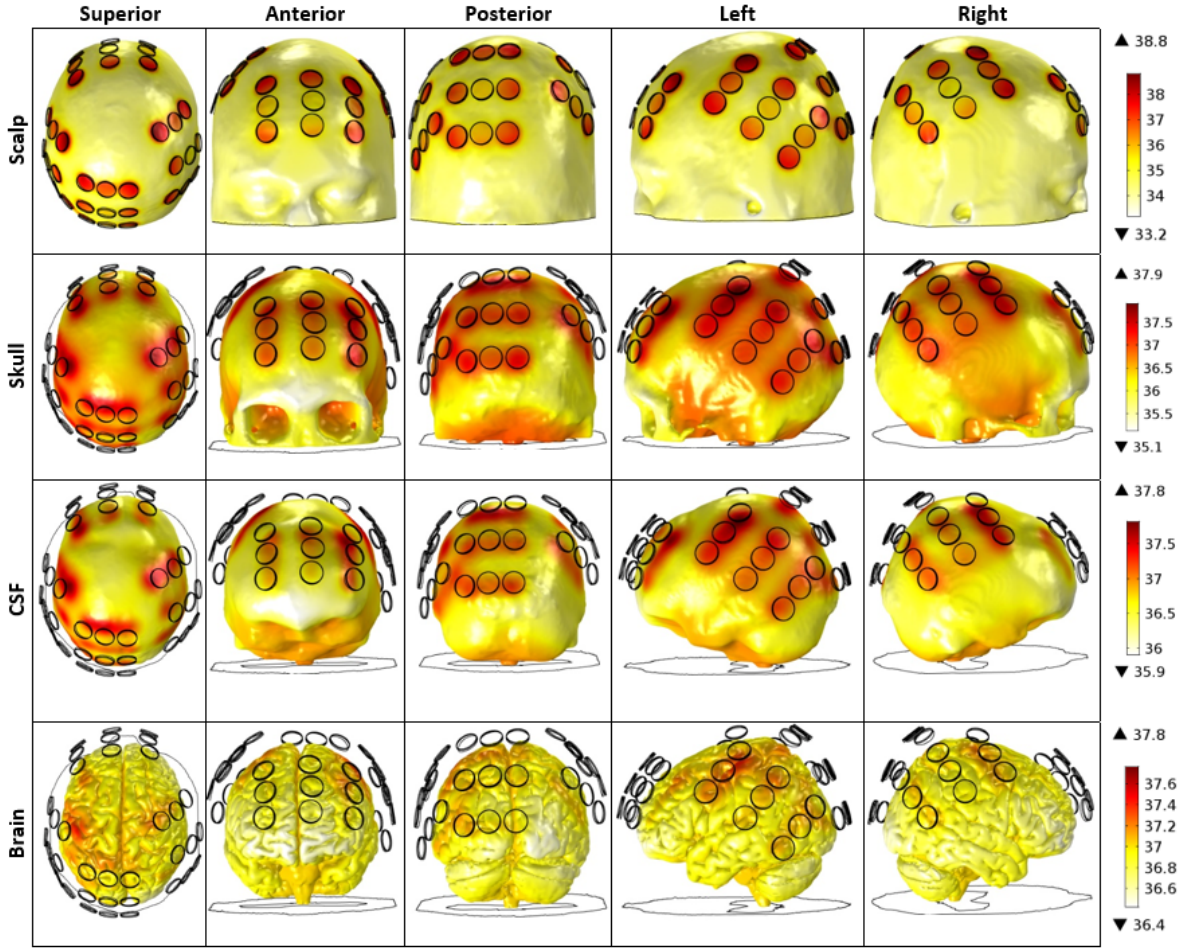

Figure F.4: Temperature distribution, from five different perspectives, on each tissue surface at the end of the simulation (t=300 seconds) when layout 5 was used. Current was injected alternately into each pair with a switching time of one second. The current injected into the AP pair was 565 mA, whereas in the LR's it was 800 mA. For these values of current the maximum steady-state temperature predicted on the scalp surface underneath both pairs is 39.5 ℃. The temperature increases occurred mainly underneath the arrays as clearly seen by the regions in red. Each circle represents the region where a transducer was placed. First row: scalp; Second row: skull; Third row: CSF; Fourth row: Brain. In the latter, the maximum temperature was reached at the GM surface. Scales are different for each row. All values are in ℃.